J. Hydrol. Hydromech., 66, 2018, 4, 357–359
DOI: 10.2478/johh-2018-0037

65th Anniversary of the Institute of Hydrology, Slovak Academy of Sciences

The Institute of Hydrology, Slovak Academy of Sciences is one of the Journal of Hydrology and Hydromechanics co-publishers and in this year celebrates its 65th anniversary. For this reason I afford, as the Director of the Institute of Hydrology, to write some words about the history of our institution and the history of the journal, as well.

The necessity to understand basic laws of water cycle as a precondition to improve water management of Slovakia was the reason of establishing the Institute of Hydrology, Slovak Academy of Sciences (SAS), 65 years ago. The resolution of the Presidium of the Slovak Academy of Sciences in 1953 established the institute as the Water Management Laboratory of SAS. Founder of the Institute – and its first director – was Prof. Dr. Oto Dub. Since then eight people have held the position of director of the Institute. There are: Prof. E. Mäsiar (1963–1974), Prof. M. Dzubák (1974–1981), Prof. J. Benetin (1981–1990), Dr. K. Kosorin (1990–1991), Dr. J. Šútor (1991–2004), Dr. V. Štekauerová (2004–2012), Dr. P. Pekárová (2012–2016) and me (2016-up to now).

The aim of the Water Management Laboratory of SAS was to develop theoretical hydrology and solution of actual problems related to surface and subsurface water. In 1959 the Water Management Laboratory was renamed (again by the resolution of the Presidium of SAS) to the Institute of Hydrology and Hydrotechnics SAS. The relatively good equipment for the theoretical and experimental studies was reflected in many research activities. Since 1963 Presidium of SAS decided to change the name of the institution again according to its new tasks. Its new name – Institute of Hydrology and Hydraulics SAS – better represented its research topics. It is necessary to mention the year 1989, after which significant changes of the Institute were performed. The number of employees decreased from 108 to 50 and funding of the Institute was changed from budgetary to those which activity are covered from the state budget only partially (since 1993). To characterize contemporary institute's activity focused to hydrology, its name has been changed to the Institute of Hydrology SAS since 1993.

Institute of Hydrology SAS is now a scientific research institution which conducts a comprehensive research and teaching in the field of environmental science and water management to improve and disseminate knowledge on the circulation and quality of water in the nature. The activity of the Institute is focused on:

– water balance components and their changes in catchments;
– transport processes of water and dissolved matters in the atmosphere–plant canopy–soil water–groundwater system with special focus on the subsurface water formation and its quality;
– flow of surface water, groundwater and transported substances;
– impact of human activities on hydrological processes, including processes of surface and subsurface water pollution;
– changes in hydrological regime of surface and subsurface waters caused by expected climatic changes;
– solving problems connected with environmental management, ecology, utilization and protection of environment, hydrogeology, pedology
– solving problems connected with water constructions and their impact on the environment, hydromelioracy, hydrotechnical applications, water modifications, flood protection, water morphology, integrated water management, water planning and water resources protection;
– solving problems connected with landscape engineering, plants and soil protection and with securing water supply during drought seasons.

The Institute provides consultancy and expertise services related to its main activity and also performs PhD study in accordance to valid legal regulations.

Since its establishment, the mission of the Institute of Hydrology SAS is the acquirement and transfer of new scientific knowledge in the fields of hydrology, hydrodynamics and water hydraulics to water management practise, mainly in Slovakia. The Institute elaborates methodologies and manuals to provide the society with powerful tools to solve urgent and perspective water-related problems using the contemporary scientific knowledge. Simulation models are designed and used in analyses and predictions of water dynamics and quality. Special attention is paid to building databases of input data characterizing the regions of Slovakia.

Different sub-disciplines of hydrology are using specific methodological approaches and equipment; this is reflected even in structure of the Institute. Institute is divided into two departments:

– Department of Surface Water Hydrology,
– Department of Subsurface Water Hydrology.

Territory of Slovakia is morphologically diversified and research under different natural conditions also needs specific methodology and equipment. There was one of reasons to establish remoted workplaces for particular regions, which are focused on research in the field conditions:

– Research Base of Mountain Hydrology, Liptovský Mikuláš, (research of water movement and runoff formation in condition of mountainous catchments),
– Research Base of Lowland Hydrology, Michalovce (soil hydrology of lowlands, with accent to East Slovakia Lowland).

The aim of research conducted by the Institute of Hydrology SAS is to acquire new knowledge about quantitative and qualitative characteristics of water movement in ecosystems influenced by human activity and global changes (climate change is one of many global changes).

Those goals can be reached by the combined laboratory and field activities; field research is the source of primary information about the system and allows designing mathematical and simulation models and its results also can be used for their validation.

By all manners of means, one of the significant activities of the Institute of Hydrology SAS consists in the issue of the Journal of Hydrology and Hydromechanics. History of this journal reached or is linked with the establishment of the Institute. The first volume of the journal antecedent, which name at that time was the Vodohospodársky časopis, was published in 1953, when the Institute was founded, and contained one double issue. Since 1955 the journal was issued quarterly and since 1969 in 6 issues per year. Since 1961, the journal is issued by the Institute of Hydrology SAS (Slovakia) in co-operation with the Institute of Hydrodynamics AS CR (Czech Republic). During the years the quality of journal has increased, from relatively modest beginnings with small group of authors and

subscribers up to the significant international journal. In 1993 the Journal changed its name to the todays form: Journal of Hydrology and Hydromechanics. Nowadays, the journal is an international open access journal for the basic disciplines of water sciences. The scope of hydrology is limited to biohydrology, catchment hydrology and vadose zone hydrology, primarily of temperate zone. The hydromechanics covers theoretical, experimental and computational hydraulics and fluid mechanics in various fields, two- and multiphase flows, including non-Newtonian flow, and new frontiers in hydraulics. The Journal publishes original research papers, short communications/technical notes, and reviews that have been thoroughly peer reviewed. Hundreds of papers published in the journal prove that, within the mentioned scientific disciplines, it has become an important mediator of research results from all over the world.

This thematic issue summarizes and presents latest results of cooperation among researchers from the Institute of Hydrology SAS and from other research institutions. This issue includes papers from more than 50 authors from 11 European countries. It was designed to communicate contributions on the current state of catchment hydrology, vadose zone hydrology and also hydromechanics.

Iovino et al. (this issue) analyse the extent (determined by the repellency indices RI and RIc) and persistence (determined by the water drop penetration time, WDPT) of soil water repellency (SWR) induced by pines in different geographic regions - in clay loam soil at Ciavolo, Italy (CiF), sandy soil at Culbin, United Kingdom (CuF), silty clay soil at Javea, Spain (JaF), and sandy soil at Sekule, Slovakia (SeF). For Culbin soil, the potential SWR characteristics were also determined after oven-drying at 60°C (CuD). They found out that RI and RIc increased in the order: JaF < CuF < CiF < CuD < SeF, reflecting nearly the same order of WDPT increase. RI correlated closely with WDPT, which was used to develop a classification of RI that showed a robust statistical agreement with WDPT classification according to three different versions of Kappa coefficient.

Bebej et al. (this issue) study of flow type dynamics at pedon scale via morphometric parameter analysis of dye-pattern profile. The application of Brilliant Blue FCF tracer enables to identify flow types in multi-domain porous systems of soils. They analysed the vertical dye pattern profiles exposed for different time lengths, and revealed temporal evolution of dye solution redistribution leading to changes in flow types. The analyses of the dyed patterns profiles allowed to specify three stages of dye solution redistribution history: (i) a stage of preferential macropore flow, (ii) a stage of strong interaction between macropore-domain and soil matrix leading to the generation of heterogeneous matrix flow and fingering flow types, and (iii) a final stage of dye redistribution within the soil body connected with leaching of BB caused by meteoric water.

Soil compaction leads to the decrease in infiltration rates, in saturated hydraulic conductivity and in porosity, as well as causes an increase in soil bulk density. Detailed determination of soil compaction and the investigation of a compaction impact on water content, water penetration depth and potential change in water storage in sandy loam soil under sunflower was carried out by Nagy et al. (this issue) at 3 plots (K1, K2 and K3) within an experimental site (field) near Kalinkovo village (Slovakia). The vertical bulk density distribution was similar to the vertical soil penetration resistance distribution, i.e. the highest values were estimated at the plot K1 in 15–20 cm depths and the lowest values at the plot K2. Soil water storage measured at the plot K2 (in the ridge) was 1.17-times higher than the soil water storage measured at the plot K3 (in the furrow) and 4.2-times higher than the soil water storage measured at the most compacted plot K1 on the edge of the field.

During the last decade, biochar has captured the attention of agriculturalists worldwide due to its positive effect on the environment. To verify the biochar effects on organic carbon content, soil sorption and soil physical properties under the mild climate of Central Europe, Igaz et al. (this issue) established a set of field experiments. Applied biochar increased total and available soil water content in all fertilized treatments. Based on the results from the spring soil sampling (porosity and water retention curves), they found a statistically significant increase in the soil water content for all fertilized treatments. Furthermore, biochar (with or without N fertilization) significantly decreased hydrolytic acidity and increased total organic carbon.

Šimanský et al. (this issue) also present how biochar improves physical properties of soils and contributes to the carbon sequestration. In their study the effects of biochar alone and in a combination with N-fertilizer (i) on the content of water-stable aggregates (WSA) as well as soil structure parameters; and (ii) on the contents of soil organic carbon (SOC) and labile carbon (CL) in water-stable aggregates was investigated. The results indicate that the biochar significantly decreased the structure vulnerability by 25%. The content of SOC in WSA in all size classes and the content of CL in WSA 3–1 mm significantly increased after applying 20 t ha^{-1} of biochar. Their results showed that biochar might have beneficial effects on soil structure parameters.

Sleziak et al. (this issue) focus on quantification of the factors that control change in the hydrological model efficiency over time by using the TUW rainfall-runoff model over the whole territory of Austria. The effect of the temporal change of at-site climatic conditions is expressed by the mean catchment precipitation and the air temperature in two large groups of catchments representing diverse physiographic/climatic zones. The results indicate that the main controlling factor of changes in simulated runoff volumes is the magnitude of the change in precipitation for both groups of catchments.

The research of Fendeková et al. (this issue) was oriented on droughts occurrence in discharge time series in twelve Slovak river basins within the period 1981–2015. Results showed that drought parameters in evaluated river basins of Slovakia differed in respective years, most of the basins suffered more by 2003 and 2012 drought than by the 2015 one. Water balance components analysis for the entire period 1931–2016 showed that because of continuously increasing air temperature and balance evapotranspiration there is a decrease of runoff in the Slovak territory.

The erosion, transport and deposition of sediments in small valley reservoirs represent a significant impact on their operations, mainly with regard to reducing the volume of their accumulation. The aim of the study by Hlavčová et al. (this issue) is a comparison and uncertainty analysis of two modelling concepts for assessment of soil loss and sediment transport in a small agricultural catchment, with an emphasis on estimating the off-site effects of soil erosion resulted in sedimentation of a small water reservoir. The small water reservoir (polder) of Svacenicky Creek which was built in 2012, is a part of the flood protection measures in Turá Lúka and is located in the western part of Slovakia, close to the town of Myjava. The town of Myjava in recent years has been threatened by frequent floods, which have caused heavy material losses and significantly limited the quality of life of the local residents. To estimate the amount of soil loss and sediments transported from the basin, there were applied two modelling concepts and the results were validated with the actual bathymetry of the polder.

The results show that in the given area, there has been a gradual clogging of the bottom of the polder caused by water erosion. It was estimated that within the four years of the acceptance run, 10,494 m^3 of bottom sediments on the Svacenicky Creek polder have accumulated. It therefore follows that repeated surveying of the sedimentation is very important for the management of the water reservoir.

Next paper, by Sokáč et al. (this issue), presents a new approximate method for 1-D simulation of pollution transport in streams with "dead zones". Analytical solutions describing the 1D substance transport in streams have many limitations and factors, which determine their accuracy. One of the very important factors is the presence of the transient storage ("dead zones") that deform the concentration distribution of the transported substance. For better adaptation to such real conditions, a simple 1D approximation method, based on the asymmetric probability distribution (Gumbel's distribution), was proposed and verified on three streams in southern Slovakia. Tracer experiments on these streams confirmed the presence of dead zones to various extents, depending mainly on the vegetation extent in each stream. Statistical evaluation confirms that the proposed method approximates the measured concentrations significantly better than methods based upon the Gaussian distribution.

Velísková et al. (this issue) deal with studying of two topics – measuring of velocity profile deformation behind an overflooded construction and modelling of this velocity profile deformation by computational fluid dynamics (CFD). Numerical simulations with an unsteady RANS models - Standard k-ε, Realizable k-ε, Standard k-ω and Reynolds stress models (ANSYS Fluent v.18) and experimental measurements in a laboratory flume (using ADV) were performed. Results of both approaches showed and affirmed presence of velocity profile deformation behind the obstacle, but some discrepancies between the measured and simulated values were also observed. With increasing distance from the obstacle, the differences between the simulation and the measured data increase and the results of the numerical models are no longer usable.

Mentioned collection of original articles represents latest dissemination outcomes of mainly international cooperation activities of the Institute of Hydrology SAS. I would like to thank all authors for their contributions and I wish the readers of Journal of Hydrology and Hydromechanics a procuration of next knowledge and a lot of new inspiration not only from this issue, but from all next ones.

Yvetta Velísková, Director
Institute of Hydrology, Slovak Academy of Sciences
Dúbravská cesta 9, 841 04 Bratislava, Slovakia
http://www.uh.sav.sk
Email: veliskova@uh.savba.sk

J. Hydrol. Hydromech., 66, 2018, 4, 360–368
DOI: 10.2478/johh-2018-0024

Extent and persistence of soil water repellency induced by pines in different geographic regions

Massimo Iovino[1*], Pavla Pekárová[2], Paul D. Hallett[3], Ján Pekár[4], Ľubomír Lichner[2], Jorge Mataix-Solera[5], Vincenzo Alagna[1], Richard Walsh[3], Annette Raffan[3], Karsten Schacht[6], Marek Rodný[2]

[1] Dipartimento di Scienze Agrarie, Alimentari e Forestali, Università degli Studi di Palermo, Viale delle Scienze, Ed. 4 Ingr. E, 90128 Palermo, Italy.
[2] Slovak Academy of Sciences, Institute of Hydrology, Dúbravská cesta 9, 84104 Bratislava, Slovakia.
[3] University of Aberdeen, Institute of Biological & Environmental Sciences, Aberdeen AB24 3UU, United Kingdom.
[4] Comenius University, Faculty of Mathematics, Physics and Informatics, Mlynská dolina 1, 842 48 Bratislava, Slovakia.
[5] Departamento de Agroquímica y Medio Ambiente, Universidad Miguel Hernández, Edificio Alcudia, Avda de la Universidad, 03202 Elche Alicante, Spain.
[6] Department of Soil Science and Soil Ecology, Institute of Geography, Ruhr-Universitat Bochum, Universitatsstrasse 150, 44801 Bochum, Germany.
[*] Corresponding author. Tel.: +39 091 23897070. Fax: +39 091 484035. E-mail: massimo.iovino@unipa.it

Abstract: The extent (determined by the repellency indices RI and RI_c) and persistence (determined by the water drop penetration time, WDPT) of soil water repellency (SWR) induced by pines were assessed in vastly different geographic regions. The actual SWR characteristics were estimated *in situ* in clay loam soil at Ciavolo, Italy (CiF), sandy soil at Culbin, United Kingdom (CuF), silty clay soil at Javea, Spain (JaF), and sandy soil at Sekule, Slovakia (SeF). For Culbin soil, the potential SWR characteristics were also determined after oven-drying at 60°C (CuD). For two of the three pine species considered, strong (*Pinus pinaster* at CiF) and severe (*Pinus sylvestris* at CuD and SeF) SWR conditions were observed. *Pinus halepensis* trees induced slight SWR at JaF site. RI and RI_c increased in the order: JaF < CuF < CiF < CuD < SeF, reflecting nearly the same order of WDPT increase. A lognormal distribution fitted well to histograms of RI_c data from CuF and JaF, whereas CiF, CuD and SeF had multimodal distributions. RI correlated closely with WDPT, which was used to develop a classification of RI that showed a robust statistical agreement with WDPT classification according to three different versions of Kappa coefficient.

Keywords: Pine; Soil; Water repellency; Water drop penetration time; Repellency index.

INTRODUCTION

Pines are widely planted for sand dune stabilization (CAB International, 2002; Islam et al., 2011; Janusauskaite et al., 2013), but there is a common misconception discounted by scientific evidence that pure coniferous forests cause serious and irreversible soil deterioration. Where deterioration on soils by coniferous forests has been observed it has largely been caused by man's mismanagement and exploitation (Will and Raliard, 1976).

Pine species, having considerable quantities of resins, waxes and aromatic oils in their needles and bark, can induce soil water repellency (SWR) (Doerr et al., 2000; Garcia et al., 2005), resulting in a change to soil hydrophysical properties. Pine root excreted mucilages containing aliphatic compounds may also contribute to SWR (Rumpel et al., 1998). SWR can develop in soils of different textural composition and structural properties, and has been found all over the world (Beatty and Smith, 2010, 2013; Fér et al., 2016; Ward et al., 2015). It can impede infiltration of water, promote surface runoff and erosion, and give rise to preferential flow of water and accelerated transport of chemicals into the groundwater (Doerr et al., 2000; Lichner et al., 2013; Orfánus et al., 2008). Moreover, by modifying water availability, SWR indirectly affects seed germination, seedling establishment and plant growth (Siteur et al., 2016). The impact of pines on soil properties is the result of interactions between the trees and the different components of the ecosystem (Bens et al., 2006, 2007). SWR in forest soils depends on tree species, age of the forest, season of the year, soil water content, organic matter content and type, clay content, wetting and drying history of the soil, frequency of fires, temperature, and relative ambient air humidity (Buczko et al., 2002, 2005, 2006; Diehl, 2013; Doerr et al., 2000; Flores-Mangual et al., 2013). The impacts can be spatially variable, as observed by Gerke et al. (2001) for potential water repellency in a lignitic mine soil afforested with *Pinus nigra.*

SWR is characterized by its persistence (estimated by the water drop penetration time (WDPT) test), severity (measured by the molarity of an ethanol droplet (MED) test, as well as from the water-solid contact angle and capillary rise measurements), and extent (determined by the repellency index RI) (Haas et al., 2018; Krueger et al, 2018; Lichner et al., 2018). The SWR characteristics can be both spatially and temporally variable. From small-scale (centimetre and decimetre) measurements using micro- (disk radius of 1.4 mm) and mini-disk infiltrometers (disk radius of 22.5 mm) at sampling interval of 5 cm and 10 cm, respectively, found water sorptivity S_w could vary by an order of magnitude between neighbouring measuring points (Hallett et al., 2004; Lichner et al., 2012). Such as large amount of spatial variability hinders the measurements of RI as paired measurements of S_w and ethanol S_e sorptivity are needed (Keck et al., 2016; Lichner et al., 2007, 2010). This can be overcome using a combined repellency index RI_c (Alagna et al., 2017), calculated according to Pekárová et al.'s (2015) method by taking into account all the combinations of the measured S_w and S_e pairs. Orfánus et al. (2008) found similar small-scale variation of WDPT.

An assessment of different methods to measure SWR has not yet been reported. For pine soils this is important due to widespread occurrence of SWR, which Rodriguez-Alleres and Beni-

to (2011) found to vary considerably both spatially and temporally on the surface of sandy loam soils of NW Spain under *Pinus pinaster* plantations. The relationship between different measurements and their spatial variability is also important, as RI and MED measure the extent, whereas WDPT reports the persistence of water repellency. Doerr (1998) determined the comparability of MED and WDPT results using air-dried soils with a broad particle size and hydrophobicity range. A close relationship between the two tests was found for highly hydrophobic soils, but not for moderately hydrophobic soils. Whether different SWR measurements are comparable spatially is not known.

The objective of this study was to assess the extent and persistence of soil water repellency induced by pines in vastly different geographic regions. The actual water repellency characteristics were estimated in situ in Ciavolo, Italy, Culbin, United Kingdom, Javea, Spain, and Sekule, Slovakia. Due to its high wettability in the field, the potential water repellency characteristics were also determined after oven-drying at 60°C for Culbin soil. The second objective of this study was to propose a classification of the repellency index RI and determine the comparability of RI and WDPT results.

MATERIAL AND METHODS

Study sites

The first experimental site is located in Ciavolo on the island of Sicily, Italy (37°45'40.6" N, 12°34'09.0" E), under a 30 years old *Pinus pinaster* tree canopy that fully covers the soil surface (site CiF). This area is representative of the reforestations widely applied in the past decades to tackle land degradation. According to the Köppen-Geiger climate classification, the region is classified as Mediterranean, hot summer (Csa) (Kottek et al., 2006). Warm and dry periods in summer alternate with heavy rainfalls mostly occurring in autumn and winter. The average annual rainfall is 632 mm. The elevation at the experimental site is 105 m a.s.l. and the surface slope is shallow (4.4%). The soil is a Rhodoxeralf (Soil Survey Staff, 2014) with a depth of 0.40–0.60 m and the parent material is calcareous sandstone. According to USDA classification, the soil texture is clay loam (Gee and Bauder, 1986). The mean volumetric soil water content at the time of sampling was 0.160 $cm^3\ cm^{-3}$.

The second experimental site was Culbin forest located in the north of Scotland on the southern shore of the Moray Firth (57.63° N, 3.72° W). According to the Köppen-Geiger climate classification, the region is classified as temperate oceanic climate (Cfb) (Kottek et al., 2006) with average annual rainfall of 665 mm. Elevation at the experimental site is 5 to 20 m a.s.l. with slopes ranging from 0 to 18%. Culbin forest was once an area of unstable sand dunes produced by windblown sand from raised beaches west of the site (Ovington, 1950). The forest was planted in 1888 to physically stabilise dune sands. The primary species planted in Culbin forest are Scots pine (*Pinus sylvestris*) and Corsican pine (*Pinus nigra*). The soil is an Ustoxic Quartzipsamments (Soil Survey Staff, 2014) comprised of an organic surface layer overlaying windblown sand. According to USDA classification, the soil texture is sandy (Gee and Bauder, 1986). Soils were sampled at the interface between the organic layer and mineral soil, at a depth of 50 mm from the surface. An assessment of the actual water repellency characteristics was conducted *in situ* (CuF) whereas potential water repellency characteristics were determined in laboratory after oven-drying at 60°C (CuD).

The third experimental site is located at Javea close to Alicante, Spain (38°48'15.0" N, 0°09'18.8" E, elevation 213 m a.s.l.), in a 40 years old afforested plantation of *Pinus halepensis* (Site JaF). The region is classified as Mediterranean, hot summer (Csa) (Kottek et al., 2006). The average annual rainfall is 583 mm, which is mainly winter-dominant. In the past, the site was cultivated as shown by the presence of abandoned agricultural terraces. The soil is a Lithic Rhodoxeralf (Soil Survey Staff, 2014) developed over a karstified limestone with variable depth, generally lower than 0.5 m. According to USDA classification, the soil is silty clay (Gee and Bauder, 1986). The mean volumetric soil water content at the time of sampling was 0.082 $cm^3\ cm^{-3}$.

The fourth experimental site is located at Sekule (48°37'10'' N, 17°00'10'' E) in the Borská nížina lowland (southwest Slovakia), under a 30 years old Scots pine (*Pinus sylvestris*) tree canopy that fully covers the soil surface (site SeF). The region is classified as warm temperate, full humid, cool summer (Cfc) (Kottek et al., 2006). Mean annual precipitation is 550 mm, which is mainly summer-dominant. Elevation is 158 m a.s.l. and surface slope is negligible. The soil is formed by aeolian sand, and it is classified as Aridic Ustipsamments (Soil Survey Staff, 2014). According to USDA classification, soil texture is sandy (Gee and Bauder, 1986). The mean volumetric soil water content at the time of sampling was lower than 0.035 $cm^3 cm^{-3}$. Soil physical and chemical properties of all four sites are presented in Table 1.

Field methods

Field measurements of infiltration were performed with the minidisk infiltrometer (Decagon, 2012) under a negative tension $h_0 = -2$ cm. The soil sorptivity S (L $T^{-0.5}$) was estimated from the cumulative infiltration, I (L), during early-time infiltration process (Philip, 1957):

$$S(-2\ \text{cm}) = I / t^{1/2} \quad (1)$$

Equation (1) was used to calculate both the water sorptivity, S_w, and ethanol sorptivity, S_e, i.e., the soil sorptivity when, respectively, water or ethanol is used as infiltrating fluid.

Two methods were used to estimate the repellency index, RI. In the first method of estimating the repellency index, S_e and S_w were measured in pairwise arrangements (Keck et al., 2016; Lichner et al., 2007, 2010) and only one value of the standard

Table 1. Physical and chemical properties of soil samples from the experimental sites: clay loam soil under *Pinus pinaster* trees at Ciavolo, Italy (CiF), sandy soil under *Pinus sylvestris* trees at Culbin, UK (CuF), silty clay soil under *Pinus halepensis* trees at Javea, Spain (JaF), and sandy soil under *Pinus sylvestris* trees at Sekule, Slovakia (SeF) (NA – not available).

Site	Sand (%)	Silt (%)	Clay (%)	$CaCO_3$ (%)	C_{org} (%)	pH (H_2O)	pH ($CaCl_2$)
Ciavolo	23.6	43.0	33.4	2.05	2.49	7.39	6.76
Culbin	97.1	0.7	1.0	0.04	1.23	NA	4.81
Javea	15.7	43.3	40.8	4.11	4.95	7.55	6.78
Sekule	95.1	2.3	2.6	<0.05	0.83	5.65	4.39

repellency index RI was calculated from one pair of S_e and S_w measurements as follows (Hallett et al., 2001):

$$RI = 1.95\ S_e / S_w \quad (2)$$

In the second method of estimating the repellency index, the combination of all the ethanol and water sorptivities was used to calculate a combined repellency index, RI_c, i.e., $m \times n$ values of RI_c were calculated from m values of S_w and n values of S_e (Pekárová et al., 2015).

The persistence of SWR was assessed using the WDPT by placing a drop of distilled water from a standard medicine dropper or pipette on the soil surface and recording the time to complete penetration. A standard droplet release height of approximately 10 mm above the soil surface was used to minimise the cratering effect on the soil surface. The following classes of the persistence of SWR were distinguished: wettable or non-water-repellent soil (WDPT < 5 s), slightly (WDPT = 5–60 s), strongly (WDPT = 60–600 s), severely (WDPT = 600–3600 s), and extremely (WDPT > 3600 s) water repellent soil (Dekker et al., 2000).

To find the relationship between RI/RI_c and WDPT, the number of plots was increased using the results published in Lichner et al. (2012, 2017). The same field methods as outlined above were used in both studies to obtain WDPT and sorptivity data. Data from Lichner et al. (2012) were collected at Sekule in a bare soil with sandy texture. Two depths were sampled: i) surface soil covered with biological soil crust (SeC), and ii) 50 cm depth soil to exclude the impact of vegetation or organic matter (SeS). At each depth, 10 replicated measurements for WDPT and 9 for S_w and S_e were conducted. Five sites were considered in the second study (Lichner et al., 2017) including a loamy sand soil under avocado trees (HaA) at Ha Ma´apil, Israel, a loamy sand soil (NeP1) and a silty clay soil (NeP2) under date palms at Neve Etan, Israel, and a uncultivated bare sandy soil (ShB1, ShB2) at Shafdan, Israel. From 9 to 15 replicated measurements for WDPT and from 7 to 8 for S_w and S_e were conducted depending on the site. An overall set of WDPT, RI, and RI_c data collected from 12 plots was thus considered to find the relationship between RI/RI_c and WDPT.

Statistical methods

To determine the comparability of RI_c results, estimated according to the Pekárová et al. (2015) method, and WDPT results, a wide set of statistical methods were used (e.g. regression analysis, theory of distribution functions, their transformation and characteristics – like means and quantiles). The statistical software STATGRAPHICS (Statgraphics, 2014) was used for computations.

The values of the paired samples were tested by Cohen's unweighted Kappa coefficient, as well as weighted Kappa coefficients (Friendly and Meyer, 2015). Cohen's Kappa (κ) is a commonly used measure of agreement that compares the observed agreement to agreement expected by chance if the two observer's ratings were independent. If p_{ij} is the probability that a randomly selected subject is rated in category i by the first observer and in category j by the other, then the observed agreement is the sum of the diagonal entries, $P_0 = \sum_i p_{ii}$. If the ratings were independent, this probability of agreement (by chance) would be the sum of the products of the corresponding row totals and column totals, $P_c = \sum_i p_{i+} p_{+i}$. Here, row totals p_{i+} and column totals p_{+j} are marginal frequencies for observations i and j, respectively, so, $p_{i+} = \sum_j p_{ij}$ and $p_{+j} = \sum_i p_{ij}$. Cohen's κ is then the ratio of the difference between actual agreement and chance agreement, $P_0 - P_c$, to the maximum value this difference could obtain:

$$\kappa = \frac{P_0 - P_c}{1 - P_c} \quad (3)$$

When agreement is perfect, κ = 1; when agreement is no better than would be obtained from statistically independent ratings, κ = 0. Coefficient κ could conceivably be negative, but this rarely occurs in practice. The minimum possible value depends on the marginal totals. The original (unweighted) κ only counts strict agreement (the same category is assigned by both observers). A weighted version of κ may be used when one wishes to allow for partial agreement. Weighted κ uses weights, $0 \le w_{ij} \le 1$ for each cell in the table, with $w_{ii} = 1$ for the diagonal cells. In this case P_0 and P_c are defined as weighted sums:

$$P_0 = \sum_i \sum_j w_{ij} p_{ij} \quad (4)$$

$$P_c = \sum_i \sum_j w_{ij} p_{i+} p_{+j}. \quad (5)$$

For a $r \times r$ contingency table, two commonly-used patterns of weights are used, namely those based on equal spacing of weights (linear weighting) for a near-match,

$$w_{ij} = 1 - \frac{|i - j|}{r - 1} \quad (6)$$

and Fleiss-Cohen weights (quadratic weighting), based on an inverse-square spacing,

$$w_{ij} = 1 - \frac{|i - j|^2}{r - 1}. \quad (7)$$

For estimation of Kappa coefficient, the VassarStats-Website for Statistical Computation (Lowry, 2017) was used.

The Landis and Koch (1977) classification of the Kappa coefficient was used to assess the strength of agreement. The following classes of the strength of agreement are distinguished in this classification: poor (Kappa coefficient < 0.00), slight (0.00 ≤ Kappa coefficient < 0.20), fair (0.20 ≤ Kappa coefficient < 0.40), moderate (0.40 ≤ Kappa coefficient < 0.60), substantial (0.6 ≤ Kappa coefficient < 0.80), and almost perfect (0.8 ≤ Kappa coefficient ≤ 1.00).

RESULTS AND DISCUSSION

Characteristics of the extent and persistence of actual SWR of clay loam soil under *Pinus pinaster* trees at Ciavolo, Italy (CiF), sandy soil under *Pinus sylvestris* trees at Culbin, UK (CuF), silty clay soil under *Pinus halepensis* trees at Javea, Spain (JaF), and sandy soil under *Pinus sylvestris* trees at Sekule, Slovakia (SeF), as well as the extent and persistence of potential SWR of sandy soil samples taken under *Pinus syl-*

vestris trees at Culbin, UK, and estimated in the laboratory after oven-drying at 60°C (CuD), are presented in Table 2.

According to the classification proposed by Dekker et al. (2000), it was found that two of three pine species observed in this study induced strong (*Pinus pinaster* trees in clay loam soil at CiF site) to severe (*Pinus sylvestris* trees in sandy soil at CuD and SeF sites) SWR. *Pinus halepensis* trees induced slight SWR in silty clay soil at JaF site. This result is in agreement with the findings of Rodriguez-Alleres and Benito (2011) who found slight to severe repellency in sandy loam soil under *Pinus pinaster* trees at Fontáns, NW Spain. Sandy soil at Culbin, UK, was wettable under field conditions (0.104 ± 0.014 g g^{-1}, gravimetric water content) and became severely repellent after drying in the laboratory. It is in agreement with the findings of Dekker and Ritsema (1994), de Jonge et al. (1999) and Dekker et al. (2001) that SWR increases with a decrease in water content and that the soil becomes wettable above a certain water content called the critical water content. Mean values of RI and RI_c increase in the order: JaF < CuF < CiF < CuD < SeF. Mean values of WDPT increased in nearly the same order: CuF < JaF < CiF < CuD < SeF (Table 2). Thus the pine trees affected the extent and persistence of soil water repellency to a similar extend independently of the different soil and climate characteristics.

Regression dependence between RI/RI_c and WDPT

Table 3 shows the fitting results of several models that were considered to estimate the regression dependence between RI/RI_c and WDPT. Among the models fitted, the linear model yields the highest R-Squared value with 83.56%. The output shows the results of fitting a linear model to describe the relationship between RI (resp. RI_c) and WDPT. The equations of the fitted models are:

$$RI = 3.33 + 0.0626\ WDPT \quad (8)$$

$$RI_c = 4.73 + 0.0509\ WDPT \quad (9)$$

that are characterized by *P* values lower than 0.01, indicating a statistically significant relationship between RI and WDPT (as well as between RI_c and WDPT) at the 99% confidence level. The R-Squared statistic indicates that the model as fitted explains 83.56% of the variability in RI (resp. 83.64% in RI_c). The correlation coefficient equals 0.914 (0.915), thus indicating a relatively strong relationship between the variables. The relationship between WDPT and RI presented as Eq. (8) is in agreement with that presented by Blanco-Canqui and Lal (2009). Their relationship, found across 11 soils in eastern USA ($RI = 0.761 + 0.337\ WDPT$ ($R^2 = 0.15$)), is also linear, but the parameters are different.

The standard deviation of the residuals is 11.87 (9.61). This value can be used to construct prediction limits for new observations (Fig. 1). Similar statistical results were obtained for RI and RI_c, but equation (8) gives a higher range, and therefore RI_c will be used in our next evaluations.

The empirical data series RI_c were not normally distributed. The theoretical lognormal probability distributions of soil water repellency index estimated by STATGRAPHICS Plus software are depicted in Fig. 2. Several tests were conducted to determine whether statistically significant differences between the empirical and theoretical distributions occurred.

Table 2. Characteristics of the extent (RI and RI_c) and persistence (WDPT) of actual SWR at Ciavolo, Italy (CiF), Culbin, UK (CuF), Javea, Spain (JaF), and Sekule, Slovakia (SeF), as well as of potential SWR at Culbin, UK (CuD).

Site	Attribute	Minimum	Maximum	Median	Mean	Standard deviation	Skewness	Kurtosis	Number of replicates
CiF	WDPT (s)	47	1088	397	443	335	0.68	0.24	9
	RI (–)	11.4	45.2	17.8	22.7	12.3	1.06	–0.25	9
	RI_c (–)	5.9	70.6	18.6	23.6	15.3	1.57	2.77	81
CuF	WDPT (s)	1	1	1	1	0	–	–	9
	RI (–)	0.36	10.06	2.54	3.45	3.03	1.42	2.14	9
	RI_c (–)	0.29	18.47	2.50	3.34	3.40	2.68	8.08	81
CuD	WDPT (s)	94.2	2293	682.2	800.4	501.2	1.38	2.44	27
	RI (–)	7.03	67.6	26.1	26.2	18.4	1.51	2.89	9
	RI_c (–)	6.62	67.6	24.9	25.5	14.8	0.84	0.31	81
JaF	WDPT (s)	1	18	3	8	16	1.41	1.32	29
	RI (–)	0.71	2.95	1.78	1.73	0.73	0.10	–0.90	10
	RI_c (–)	0.43	6.21	1.49	1.92	1.29	1.41	1.70	100
SeF	WDPT (s)	8	7100	425.5	1256	1928	2.18	4.21	22
	RI (–)	3.57	360.2	38.6	100.4	122.4	1.29	0.72	11
	RI_c (–)	2.75	518.7	39.5	79.3	104.4	2.30	5.61	121

Table 3. Comparison of alternative models to fit the RI versus WDPT data.

Model	Correlation (–)	R-Squared (%)
Linear	0.9141	83.56
Square root-Y	0.9049	81.89
Multiplicative	0.8809	77.60
Square root-X	0.8592	73.83
Exponential	0.7701	59.30
Logarithmic-X	0.7500	56.25
Double reciprocal	0.5671	32.16
Reciprocal-X	–0.3400	11.56

It was found that the histograms of RI_c for CuF and JaF data fitted well with a lognormal distribution, while the histograms prepared from CiF, CuD and SeF data have rather a multimodal character (Fig. 2). The multimodal character of histograms prepared from CiF, CuD and SeF data is likely explained by the heterogeneous mixture of organic compounds with hydrophilic and hydrophobic functional groups forming the soil organic matter (Ellerbrock et al., 2005). The compounds were likely derived from hydrophobic tissue and exudates produced by microbes, algae and cyanobacteria, epicuticular waxes detached from pine needles and aliphatic compounds releasing from pine roots (Doerr et al., 2000).

Box-and-Whisker plot of the RI_c data series (Fig. 3) shows important features about the measured data. It is clear that the data range is very large. Series RI_c (and RI) does not have a normal distribution. Therefore, we cannot use Eqs (8) and (9) corresponding to the WDPT thresholds to determine the thresholds of RI_c (or RI).

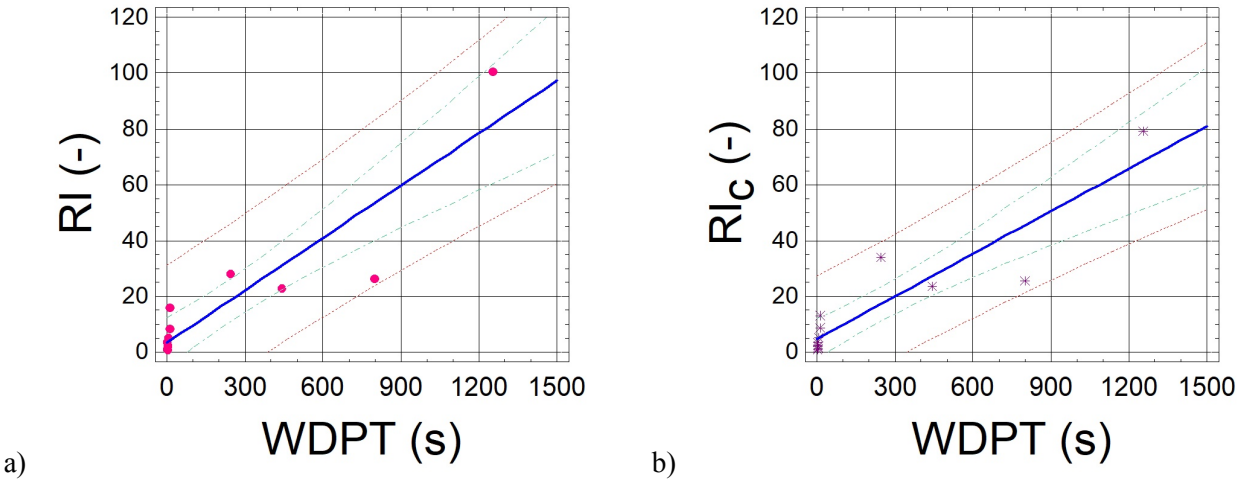

Fig. 1. Plot of fitted model (simple regression) a) RI vs. WDPT, b) RI_c vs. WDPT. The plot includes both 95% confidence limits (green lines) for the means (middle blue line) and 95% prediction limits (outer dotted red lines).

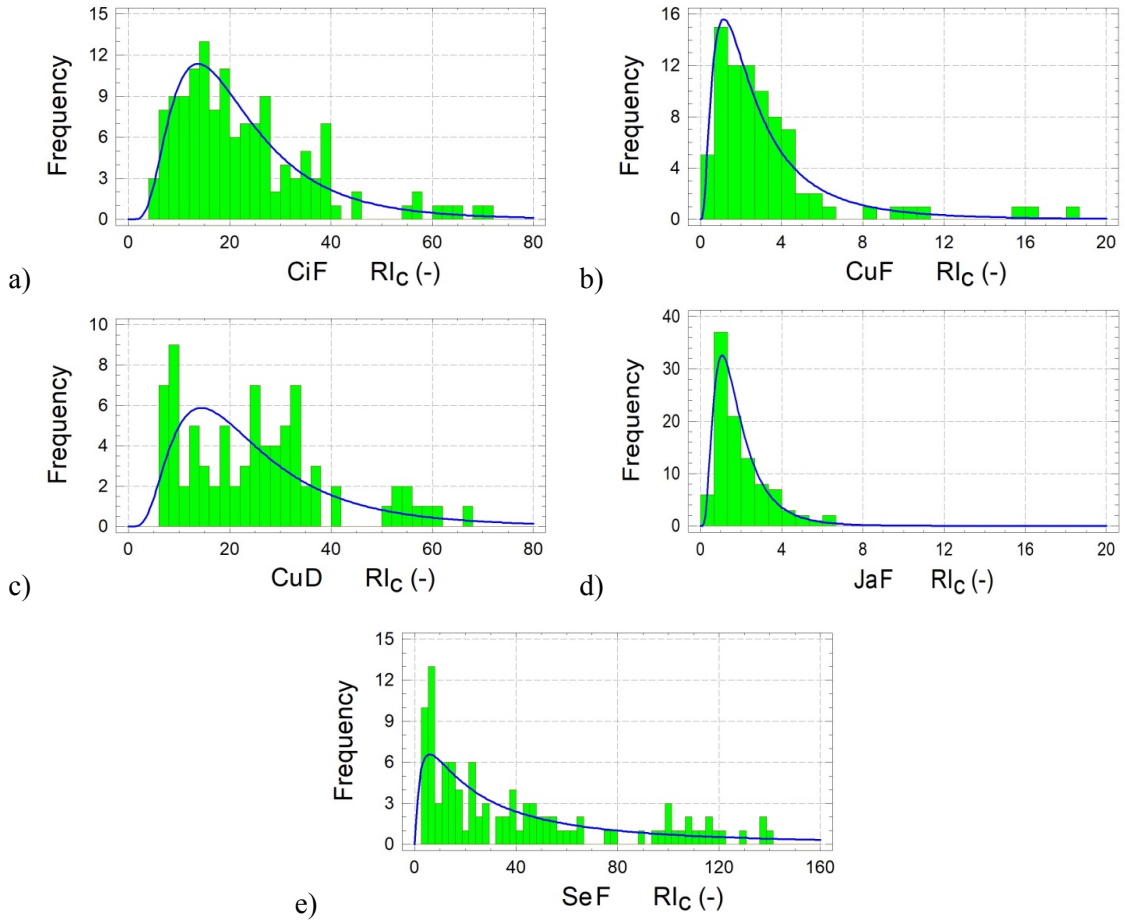

Fig. 2. Histograms and lognormal probability distribution curves of repellency index RI_c estimated at: a) Ciavolo, Italy (CiF); b) Culbin, UK, actual SWR (CuF); c) Culbin, UK, potential SWR (CuD); d) Javea, Spain (JaF); e) Sekule, Slovakia (SeF).

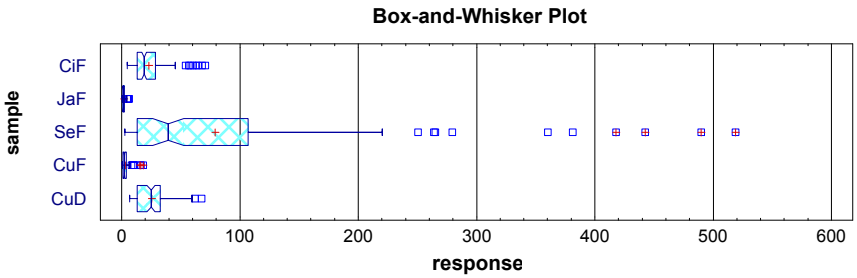

Fig. 3. Box-and-Whisker plots of repellency index RI_c estimated in situ at Ciavolo, Italy (CiF), Javea, Spain (JaF), Sekule, Slovakia (SeF), and Culbin, UK under both actual (CuF) and potential (CuD) SWR conditions (Mean marker – red cross, outlier symbols – blue squares, median – line in the rectangle).

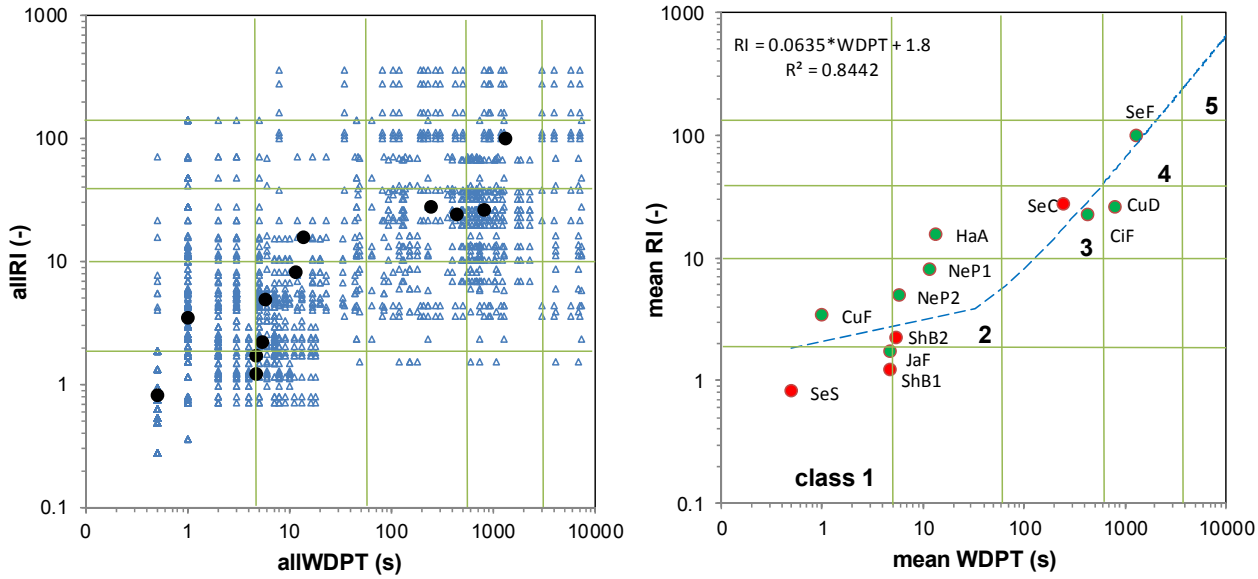

Fig. 4. a) Combined values of allWDPT and allRI data (blue triangles), mean WDPT and mean RI (black points) from each individual experimental site. b) Threshold lines between classes, and linear relationship between mean of RI and mean of WDPT from 12 localities. (Green points: cultivated soils, Red points: bare soils).

Determining thresholds for RI classes

Twelve sets of WDPT and RI values, measured both *in situ* at each of 11 experimental sites and in the laboratory for the dried pine-forest soil taken at Culbin, UK, were combined with one another and 2473 pairs of values (allWDPT, allRI) were obtained (Fig. 4a). The thresholds for five RI classes, corresponding to five WDPT classes were estimated as follows:

1. First, the parameters of theoretical lognormal distribution of the allWDPT data were estimated.
2. Then, the probabilities for tail areas were calculated for the fitted lognormal distribution of allWDPT series. The tail area for allWDPT threshold below 5 s had the probability P = 0.40; tail area below 60 s, P = 0.72; tail area below 600 s, P = 0.93; and tail area below 3600 s had the probability P = 0.98.
3. Next, the threshold values for five classes of the allRI series were estimated from the theoretical lognormal distribution of allRI series, using the probabilities calculated above.
4. Finally, the computed values were adjusted and the final thresholds are presented in Table 4.

The adapted linear relationship between 12 pairs of mean RI and mean WDPT values together with the threshold lines between classes is presented in Fig. 4b.

In the next step, the pairs of allWDPT and allRI were ranked in five classes based on the threshold values in Table 4 and two categorical variables were created, $WDPT_{class}$ and RI_{class} with categorical values 1, 2, 3, 4, and 5. A contingency table of the categorical pairs of $WDPT_{class}$ and RI_{class} is presented in Table 5. The table gives us the frequencies of observations cross-classified by the two variables.

Table 4. Thresholds of the repellency index RI classes corresponding water drop penetration time WDPT classes, and their descriptive labels.

class	descriptive labels	WDPT thresholds (s)	RI thresholds (–)
1	wettable or non-water-repellent soil	WDPT < 5	RI < 1.95
2	slightly water repellent soil	5 ≤ WDPT < 60	1.95 ≤ RI < 10
3	strongly water repellent soil	60 ≤ WDPT < 600	10 ≤ RI < 50
4	severely water repellent soil	600 ≤ WDPT < 3600	50 ≤ RI < 110
5	extremely water repellent soil	3600 ≤ WDPT	110 ≤ RI

To test whether some associations exist, to quantify the strength of association, and to understand the nature of the association among these variables, a three-dimensional histogram of the $WDPT_{class}$ and RI_{class} variables was created (Fig. 5a) from the data of contingency table (Table 5). The compliance between RI_{class} and $WDPT_{class}$ pairs is visually presented in the weighted agreement chart in Fig. 5b (Friendly and Meyer,

2015; Papierowska et al., 2018). The red squares represent the likelihood of ranking in the same class for both variables and corresponds to exact agreement in classification (for example, for class 3 the likelihood is 33). The yellow rectangles correspond to the likelihood of ranking in the same or neighbour class, i.e., partial agreement (e.g., for class 3 it is: 33, 32, 34, 23, and 43). White rectangles represent the likelihood of other rankings.

Behaviour of the characteristics was used to verify the dependence between $WDPT_{class}$ and RI_{class} classes (Table 5). First, the Chi-Square test was used to determine whether both classifications (i.e., row and column in the contingency table) are independent. Since $P < 0.01$, the hypothesis that rows and columns are independent can be rejected at the 99% confidence level. Therefore, the observed row (RI_{class}) for a particular case is related to its column ($WDPT_{class}$).

Then, we estimated the contingency coefficient and lambda of the contingency Table 5. These characteristics express the degree of association on a scale of 0 to 1. Lambda measures how useful the row or column factor is in predicting the other factor. The value of lambda with columns dependent equals 0.0525. This means that there is a 5.25% reduction in error when rows (RI) are used to predict columns (WDPT). For those statistics with P values, P values less than 0.05 indicate a significant association between rows RI and columns WDPT at the 95% confidence level. Contingency coefficient (a version of a Chi-Square test that measures the strength of the dependency between two characteristics) obtained value of 0.5899.

Finally, we computed Kappa coefficient, which provides a measure of the degree to which two judges, $WDPT_{class}$ and RI_{class} concur in their respective sorting's of 5 items into r mutually exclusive categories. Three different versions of Kappa coefficient were calculated, the values according to Eqs. 3–7, and following values of Kappa coefficient were obtained:

- Cohen's unweighted Kappa coefficient = 0.304,
- Kappa coefficient with linear weighting = 0.429,
- Kappa coefficient with quadratic weighting = 0.533.

According to the Landis and Koch (1977) classification of Kappa coefficient, the strength of agreement for the mean WDPT and mean RI pairs is fair for the Cohen's unweighted Kappa coefficient, and moderate for both the Kappa coefficient with linear weighting and the Kappa coefficient with quadratic weighting.

Moreover, we also estimated Kappa coefficient for the mean WDPT and mean RI pairs (contingency table according to Fig. 4b):

- Cohen's unweighted Kappa coefficient = 0.660,
- Kappa coefficient with linear weighting = 0.775,
- Kappa coefficient with quadratic weighting = 0.875.

According to the Landis and Koch (1977) classification of Kappa coefficient, the strength of agreement for the mean WDPT and mean RI pairs is substantial for the Cohen's unweighted Kappa coefficient, substantial for the Kappa coefficient with linear weighting, and almost perfect for the Kappa coefficient with quadratic weighting.

Table 5. Contingency table of all repellency index RI_{class}, corresponding to water drop penetration time $WDPT_{class}$, their descriptive labels, and classes used in this study. (Red colour: exact agreement, yellow: partial agreement).

RI_{class}		$WDPT_{class}$				
		Class 1	Class 2	Class 3	Class 4	Class 5
Class	Value	< 5 s	5–60 s	60–600 s	600–3600 s	> 3600 s
1	<1.95	595	90	0	3	2
2	1.95–10	338	243	62	48	15
3	10–50	243	61	192	190	22
4	50–110	46	7	45	96	5
5	>110	32	14	42	36	46

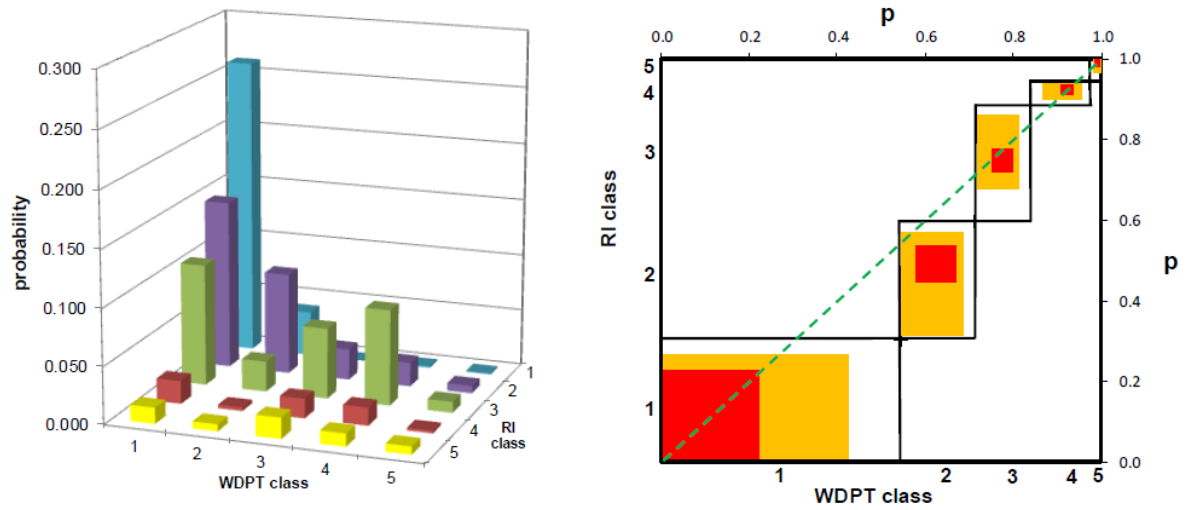

Fig. 5. a) Three-dimensional histogram of the contingency Table 5. b) Weighted agreement chart obtained by comparing $WDPT_{class}$ and RI_{class}. The red colour represents exact agreement and the yellow colour represents partial agreement.

CONCLUSIONS

Pine species observed in this study induced slight (*Pinus halepensis* trees in silty clay soil at Javea, Spain (JaF) site), strong (*Pinus pinaster* trees in clay loam soil at Ciavolo, Italy (CiF) site), and severe (*Pinus sylvestris* trees in sandy soil at Sekule, Slovakia (SeF) site) soil water repellency *in situ*. However, the sandy soil was wettable in situ at Culbin, United Kingdom (CuF), but became severely water repellent after oven-drying at 60°C. Mean values of WDPT increased in nearly the same order as mean values of RI and RI_c thus confirming that these indices are reliable in assessing the persistence (WDPT) and extent (RI and RI_c) of soil water repellency. While the histograms of repellency index RI_c prepared from CuF and JaF data can be fitted well with lognormal distribution, the histograms prepared from CiF, CuD and SeF data have rather a multimodal character due probably to the variable nature of hydrophobic coatings on soil particles and their spatial distribution in soils.

A large set of paired WDPT and RI values, measured both *in situ* and in the laboratory in twelve sites differing for soil type and land use, allowed to propose a new classification for the repellency index RI based on the WDPT classification. The comparability of RI and WDPT results was determined. It was found that the strength of agreement for the mean WDPT and mean RI pairs is substantial for the Cohen's unweighted Kappa coefficient, substantial for the Kappa coefficient with linear weighting, and almost perfect for the Kappa coefficient with quadratic weighting.

Acknowledgements. This work was supported by the Slovak Scientific Grant Agency VEGA Project Nos. 2/0054/14 and 2/0009/2015, the Slovak Research and Development Agency Project No. APVV-15-0160, and it results from the project implementation of the "Centre of excellence for integrated flood protection of land" (ITMS 26240120004).

REFERENCES

Alagna, V., Iovino, M., Bagarello, V., Mataix-Solera, J., Lichner, Ľ., 2017. Application of minidisk infiltrometer to estimate water repellency in Mediterranean pine forest soils. J. Hydrol. Hydromech., 65, 254–363.

Beatty, S.M., Smith, J.E., 2010. Fractional wettability and contact angle dynamics in burned water repellent soils. J. Hydrol., 391, 97–108.

Beatty, S.M., Smith, J.E., 2013. Dynamic soil water repellency and infiltration in post-wildfire soils. Geoderma, 192, 160–172.

Bens, O., Buczko, U., Sieber, S., Hüttl, R.F., 2006. Spatial variability of O layer thickness and humus forms under different pine beech-forest transformation stages in NE Germany. J. Plant Nutr. Soil Sci., 169, 5–15.

Bens, O., Wahl, N.A., Fischer, H., Hüttl, R.F., 2007. Water infiltration and hydraulic conductivity in sandy cambisols: impacts of forest transformation on soil hydrological properties. Eur. J. Forest Res., 126, 101–109.

Blanco-Canqui, H., Lal, R., 2009. Extent of soil water repellency under long-term no-till soils. Geoderma, 149, 171–180.

Buczko, U., Bens, O., Fischer, H., Hüttl, R.F., 2002. Water repellency in sandy luvisols under different forest transformation stages in northeast Germany. Geoderma, 109, 1–18.

Buczko, U., Bens, O., Hüttl, R.F., 2005. Variability of soil water repellency in sandy forest soils with different stand structure under Scots pine (*Pinus sylvestris*) and beech (*Fagus sylvatica*). Geoderma, 126, 317–336.

Buczko, U., Bens, O., Hüttl, R.F., 2006. Water infiltration and hydrophobicity in forest soils of a pine–beech transformation chronosequence. J. Hydrol., 331, 383–395.

CAB International, 2002. Pines of Silvicultural Importance. CABI Publishing, Wallingford.

Decagon, 2012. Mini Disk Infiltrometer User's Manual, Version 10. Decagon Devices, Inc., Pullman, 18 p.

Diehl, D., 2013. Soil water repellency: Dynamics of heterogeneous surfaces. Colloids and Surfaces A: Physicochem. Eng. Aspects, 432, 8–18.

de Jonge, L.W., Jacobsen, O.H., Moldrup, P., 1999. Soil water repellency: effects of water content, temperature, and particle size. Soil Sci. Soc. Am. J., 63, 437–442.

Dekker, L.W., Ritsema, C.J., 1994. How water moves in a water repellent sandy soil. 1. Potential and actual water repellency. Water Resources Research, 30, 2507–2517.

Dekker, L.W., Ritsema, C.J., Oostindie, K., 2000. Extent and significance of water repellency in dunes along the Dutch coast. J. Hydrol., 231–232, 112–125.

Dekker, L.W., Doerr, S.H., Oostindie, K., Ziogas, A.K., Ritsema, C.J., 2001. Water repellency and critical soil water content in a dune sand. Soil Sci. Soc. Am. J., 65, 1667–1674.

Doerr, S.H., 1998. On standardizing the "Water Drop Penetration Time" and the "Molarity of an Ethanol Droplet" techniques to classify soil hydrophobicity: a case study using medium textured soils. Earth Surf. Process. Landforms, 23, 663–668.

Doerr, S.H., Shakesby, R.A., Walsh, R.P.D., 2000. Soil water repellency: its causes, characteristics and hydro-geomorphological significance. Earth-Sci. Rev., 51, 33–65.

Ellerbrock, R.H., Gerke, H.H., Bachmann, J., Goebel, M.-O., 2005. Composition of organic matter fractions for explaining wettability of three forest soils. Soil Sci. Soc. Am. J., 69, 57–66.

Fér, M., Leue, M., Kodešová, R., Gerke, H.H., Ellerbrock, R.H., 2016. Droplet infiltration dynamics and soil wettability related to soil organic matter of soil aggregate coatings. J. Hydrol. Hydromech., 64, 111–120.

Flores-Mangual, M.L., Lowery, B., Bockheim, J.G., Pagliari, P.H., Scharenbroch, B., 2013. Hydrophobicity of Sparta sand under different vegetation types in the Lower Wisconsin River Valley. Soil Sci. Soc. Am. J., 77, 1506–1516.

Friendly, M., Meyer, D., 2015. Discrete Data Analysis with R: Visualization and Modeling Techniques for Categorical and Count Data. Chapman & Hall. ISBN 9781498725835. Web site for book: ddar.datavis.ca

Garcia, F.J.M., Dekker, L.W., Oostindie, K., Ritsema, C.J., 2005. Water repellency under natural conditions in sandy soils of southern Spain. Aust. J. Soil Res., 43, 291–296.

Gee, G.W., Bauder, J.W., 1986. Particle-size analysis. In: Klute, A. (Ed.): Methods of Soil Analysis, Part 1: Physical and Mineralogical Methods. Agron. Monogr. 9. 2nd ed. ASA and SSSA, Madison, WI, pp. 383–411.

Gerke, H.H., Hangen, E., Schaaf, W., Hűttl, R.F., 2001. Spatial variability of potential water repellency in a lignitic mine soil afforested with *Pinus nigra.* Geoderma, 102, 255–274.

Haas, C., Gerke, H.H., Ellerbrock, R.H., Hallett, P.D., Horn, R., 2018. Relating soil organic matter composition to soil water repellency for soil biopore surfaces different in history from two Bt horizons of a Haplic Luvisol. Ecohydrology, 11, Article Number: e1949. https://doi.org/10.1002/eco.1949

Hallett, P.D., Baumgartl, T., Young, I.M., 2001. Subcritical water repellency of aggregates from a range of soil management practices. Soil Sci. Soc. Am. J., 65, 184–190.

Hallett, P.D., Nunan, N., Douglas, J.T., Young, I.M., 2004. Millimeter-scale spatial variability in soil water sorptivity: scale, surface elevation, and subcritical repellency effects. Soil Sci. Soc. Am. J., 68, 352–358.

Islam, K.K., Patricia, S., Rinchen, Y., 2011. Broadleaved regeneration dynamics in the Pine plantation. Journal of Forest

Science, 57, 432–438.
Janusauskaite, D., Baliuckas, V., Dabkevicius, Z., 2013. Needle litter decomposition of native *Pinus sylvestris* L. and alien *Pinus mugo* at different ages affecting enzyme activities and soil properties on dune sands. Baltic Forestry, 19, 50–60.
Keck, H., Felde, V.J.M.N.L., Drahorad, S.L., Felix-Henningsen, P., 2016. Biological soil crusts cause subcritical water repellency in a sand dune ecosystem located along a rainfall gradient in the NW Negev desert, Israel. J. Hydrol. Hydromech., 64, 133–140.
Kottek, M., Grieser, J., Beck, C., Rudolf, B., Rubel, F., 2006. World map of the Köppen-Geiger climate classification updated. Meteorologische Zeitschrift, 15, 259–263.
Krueger, J., Heitkötter, J., Leue, M., Schlüter, S., Vogel, H.-J., Marschner, B., Bachmann, J., 2018. Coupling of interfacial soil properties and bio-hydrological processes: The Flow Cell Concept. Ecohydrology, 11, Article Number: e2024. https://doi.org/10.1002/eco.2024
Landis, J.R., Koch, G.G., 1977. The measurement of observer agreement for categorical data. Biometrics, 33, 159–174. URL: http://www.jstor.org/stable/2529310
Lichner, Ľ., Hallett, P.D., Feeney, D., Ďugová, O., Šír, M., Tesař, M., 2007. Field measurement of the impact of hydrophobicity on soil water transport under different vegetation over time. Biologia, 62, 537–541.
Lichner, L., Hallett, P.D., Orfánus, T., Czachor, H., Rajkai, K., Šír, M., Tesař, M., 2010. Vegetation impact on the hydrology of an aeolian sandy soil in a continental climate. Ecohydrology, 3, 413–420.
Lichner, Ľ., Holko, L., Zhukova, N., Schacht, K., Rajkai, K., Fodor, N., Sándor, R., 2012. Plants and biological soil crust influence the hydrophysical parameters and water flow in an aeolian sandy soil. J. Hydrol. Hydromech., 60, 309–318.
Lichner, Ľ., Capuliak, J., Zhukova, N., Holko, L., Czachor, H., Kollár J., 2013. Pines influence hydrophysical parameters and water flow in a sandy soil. Biologia, 68, 1104–1108.
Lichner, Ľ., Rodný, M., Schacht, K., Marschner, B., Chen, Y., Nadav, Y., Tarchitzky, J., 2017. Comparison of various techniques to estimate the extent and persistence of soil water repellency. Biologia, 72, 982–987.
Lichner, L., Felde, V.J.M.N.L., Büdel, B., Leue, M., Gerke, H.H., Ellerbrock, R.H., Kollár, J., Rodný, M., Šurda, P., Fodor, N., Sándor, R., 2018. Effect of vegetation and its succession on water repellency in sandy soils. Ecohydrology, 11, Article Number: e1991. https://doi.org/10.1002/eco.1991
Lowry, R., 2017. VassarStats - Website for Statistical Computation. http://vassarstats.net/index.html
Orfánus, T., Hallett, P.D., Bedrna, Z., Lichner, Ľ., Kňava, K., Sebíň, M., 2008. Small-scale variation of hydraulic properties in pine forest soil near Sekule, southwestern Slovakia. Soil Water Res., 3, S123–S129.
Ovington, J.D., 1950. The afforestation of Culbin Sands. Journal of Ecology, 38, 303–319.
Papierowska, E., Matysiak, W., Szatyłowicz, J., Debaene, G., Urbanek, E., Kalisz, B., Łachacz, A., 2018. Compatibility of methods used for soil water repellency determination for organic and organo-mineral soils. Geoderma, 314, 221–231.
Pekárová, P., Pekár, J., Lichner, Ľ., 2015. A new method for estimating soil water repellency index. Biologia, 70, 1450–1455.
Philip, J.R., 1957. The theory of infiltration: 1. The infiltration equation and its solution. Soil Science, 83, 345–358.
Rodriguez-Alleres, M., Benito, E., 2011. Spatial and temporal variability of surface water repellency in sandy loam soils of NW Spain under *Pinus pinaster* and *Eucalyptus globulus* plantations. Hydrol. Process., 25, 3649–3658.
Rumpel, C., Knicker, H., Kögel-Knabner, I., Skjemstad, J.O., Hüttl, R.F., 1998. Types and chemical composition of organic matter in reforested lignite-rich mine soils. Geoderma, 86, 123–142.
Siteur, K., Mao, J., Nierop, K.G.J., Rietkerk, M., Dekker, S.C., Eppinga, M.B., 2016. Soil water repellency: a potential driver of vegetation dynamics in coastal dunes. Ecosystems, 19, 1210–1224.
Soil Survey Staff, 2014. Keys to Soil Taxonomy. 12th ed. NRCS, Washington, DC.
Statgraphics, 2014. STATGRAPHICS Centurion XVII User Manual, 311pp. Statpoint Technologies, Inc., The Plains, Virginia, USA. www.STATGRAPHICS.com
Ward, P.R., Roper, M.M., Jongepier, R., Micin, S.F., 2015. Impact of crop residue retention and tillage on water infiltration into a water-repellent soil. Biologia, 70, 1480–1484.
Will, G.M., Raliard, P., 1976. Radiata pine - soil degrader or improver? N.Z. Journal of Forestry, 21, 248–252.

Received 22 January 2018
Accepted 17 May 2018

J. Hydrol. Hydromech., 66, 2018, 4, 369–380
DOI: 10.2478/johh-2018-0029

The study of flow type dynamics at pedon scale via morphometric parameter analysis of dye-pattern profiles

Juraj Bebej[1*], Tomáš Orfánus[2], Marián Homolák[1], Meni Ben-Hur[3], Viliam Pichler[1], Jozef Capuliak[4]

[1] Technical University in Zvolen, Faculty of Forestry, Department of Natural Envirinment, T. G. Masaryka 24, 960 53 Zvolen, Slovakia. E-mails: marian.homolak@tuzvo.sk, viliam.pichler@tuzvo.sk
[2] Institute of Hydrology, Slovak Academy of Sciences, Dúbravská cesta 9, 841 04 Bratislava, Slovakia. E-mail: orfanus@uh.savba.sk
[3] Institute of Soil, Water and Environmental Sciences, The Volcani Center, Agricultural Research Organization, P.O. Box 6, Bet Dagan, 50–250, Israel. E-mail: meni@volcani.agri.gov.il
[4] National Forest Centre, T. G. Masaryka 22, 960 92 Zvolen, Slovak Republic. E-mail: Jozef.Capuliak@nlcsk.org
[*] Corresponding author. E-mail: juraj.bebej@tuzvo.sk

Abstract: The application of Brilliant Blue FCF tracer enables to identify flow types in multi-domain porous systems of soils via analyses of morphologic parameters of stained objects occurring in dye pattern profiles, as they represent the footprint of flow processes which occurred in soil during both the infiltration and the redistribution of dye solution. We analysed the vertical dye pattern profiles exposed for different time lengths, and revealed temporal evolution of dye solution redistribution leading to changes in flow types. The field experiment was performed with the Brilliant Blue tracer (the 10 g l^{-1} concentration) applied on 1m x 1m surface of the Dystric Cambisol. The top litter horizon had been removed before 100 l of the tracer was applied. Four vertical profiles were excavated on the experimental plot (always 20 cm apart) at different times after the irrigation had been finished: 2 hours (CUT 2), 24 hours (CUT 24), 27 hours (CUT 27) and 504 hours (CUT 504). The analyses of the dyed patterns profiles showed the spatio-temporal changes in the dye coverage, surface area density, average BB concentration, and stained path width, which allowed us to specify three stages of dye solution redistribution history: (i) a stage of preferential macropore flow, (ii) a stage of strong interaction between macropore-domain and soil matrix leading to the generation of heterogeneous matrix flow and fingering flow types, and (iii) a final stage of dye redistribution within the soil body connected with leaching of BB caused by meteoric water. With increasing time, the macropore flow types convert to mostly matrix-dominated FTs in the upper part of the soil profile. These results were supported by soil hydrological modelling, which implied that more than 70% of the soil moisture profiles variability among CUT 2–CUT 504 could be explained by the time factor.

Keywords: Dye pattern; Preferential flow; Flow types; Image analysis; Morphometric parameters; Spatio-temporal flow of dye solution.

INTRODUCTION

Dye tracing has become an established way to demonstrate the preferential flow of water in soil and its spatial patterns within soil profiles (Allaire et al., 2009; Capuliak et al., 2010; Flury et al., 1994; Garrido et al., 2014; Ghodrati and Jury, 1990, Vogel et al., 2007). The dye solution transfer in soils can be evaluated by image analysis (Forrer, 2000), which enables to identify the dye solution flow pathways in soils, to measure the morphometric parameters of stained objects, and finally, to determine the flow types (FT) within the observed dye solution pathways (Weiler, 2001; Weiler and Flűhler, 2004).

The preferential flow as a specific kind of water transport in soil is defined as the rapid downward transport of water and solutes via preferred pathways through porous medium (Jury and Horton, 2004). The preferential flow involves rapid flow through large pores termed macropores, that are ubiquitous in structured soils, funnel flow or heterogenous flow (Kung, 1990) and unstable fingered flow (Ritsema and Dekker, 2000), as they arise from distinctively different physical processes (Jury and Horton, 2004). In soils, the above mentioned preferential flow types may occur in tandem, or in the absence of some of them (Jury and Horton, 2004).

Direct measurement of mutual relationships of individual preferential flow types present in field soils is rather difficult because of the tremendous spatial and temporal variability of flow pathways. Tracing with mobile dye is also difficult, because excavation of soil is destructive and experimental results cannot be repeated at the same location (Flury et al., 1994). In consequence, the analysis of dye flow pathways in soils is usually limited to a sole vertical dye pattern soil profile, excavated for 12 or 24 hours after the dye solution application on experimental plots (Bogner et al., 2012; Bundt et al., 2001; Flury and Flűhler, 1994; Flury et al., 1994; Garrido et al., 2014; Hagedorn and Bundt, 2002). In this manner obtained dye pattern profiles represent the snapshots of dye flow pathways in the form of 2-D pictures of 3-D subsurface flow pathways of mobile dye at the time of soil profile excavation. Bundt et al. (2001) excavated a series of five consecutive soil profiles at 10 cm spacing from each other, Alaoui and Goetz (2008) excavated 6 consecutive vertical profiles located 0.20 m apart, Flury et al. (1994) analysed two dye pattern profiles, and Weiler and Flűhler (2004) four or five parallel vertical soil sections of 1m x 1m, while the spacing between the vertical sections was 5–7 cm. The analytical outputs obtained by processing such data enable to calculate the spatial variation of the morphometric parameters of dye pattern soil profiles, and/or to calculate the transport of chemical components around preferred pathways using statistical modelling with regard to spatial soil heterogeneity (Bogner et al., 2012). However, in fact, such data reveal spatio-temporal (not only spatial) variability of the dye patterns.

In consideration of this fact, no field study has tackled with the analyses of dye pattern profiles excavated within one soil pedon at different times. Such a study could have revealed the

dynamic processes of dye solution transport in multimodal and spatially heterogeneous porous body of soil pedon using currently available methods for studying dye pattern profiles.

The problem of the current understanding of water transport in the soil can be seen in the following. The preferential flow, especially in the case of macropore flow, is understood as a temporally and spatially stable flow within the macropore structures (e.g. Bogner et al., 2012). On the other hand, the concept of dynamic dye solution flow says that the macropore preferred flow can be limited for a short period, e.g. when the vertical water flow rates are large in relation to the lateral losses into the surrounding soil matrix due to the prevailing pressure potential gradient either at the soil surface, or the nearly saturated subsurface (Li and Ghodrati, 1997; Weiler, 2005). In the case the water entry pressure decreases, the lateral water flow from the macropore into the surrounding soil matrix increases, the macropore flow will terminate and the soil-matrix water flow becomes dominant (Jarvis and Dubus, 2006; Weiler and Flühler, 2004).

At present, very different approaches exist to parameterise dye pattern profiles based on the measurements of stained object characteristics (Bargués Tobella et al., 2014; Droogers et al., 1998; Perret et al., 1999; Ohrstrom et al., 2002; Shipitalo and Butt, 1999; van Schaik, 2009; Zehe and Flühler, 2001). The approach proposed by Weiler (2001), based on the measurements of the volume and density of stained objects, resulted in the classification of flow types, taking into account different intensity of dye solution-soil interaction, too. The biggest advantage of Weiler (2001) classification of flow types is that this classification is supported by experimental research, results of laboratory modelling, as well as field experiments (Weiler and Flühler, 2004; Weiler and Naef, 2003), which ended in the elaboration of an infiltration model flow variability in macropores (Weiler, 2005).

Our objective was (i) to test the spatio-temporal framework of the dye solution hydrodynamics via the morphometric parameter analyses and flow types identification within the soil profiles excavated at different times, (ii) to analyse mutual relationships between the observed flow types and the outputs of hydrological modelling to examine the pedohydrological similarity concept, and, (iii) based on the obtained results to reconstruct the processes of dye solution infiltration and redistribution within the investigated pedon in a complex spatio-temporal framework.

MATERIALS AND METHODS

Description of the experimental site

The research was performed at Panský diel (N 48° 48' 25.76'', E 19° 09' 20.47'') in the Starohorské Vrchy Mts., a part of the Western Carpathians (Mazúr and Lukniš, 1980), Slovakia, at an altitude of 910 m a.s.l. This area is covered by a 90-year old mixed forest of Norway spruce (*Picea abies* (L.) Karst.), a dominant species, silver fir (*Abies alba* Mill.), European beech (*Fagus sylvatica* L.), Weymouth pine (*Pinus strobus* L.) and European larch (*Larix decidua* Mill). The experimental plot was located on a flat area with negligible inclination, and its geology contained complexes of sediments formed from schist, acidic granitites, arkoses, greenish and reddish mica-slates and quartzite (Andrusov et al., 1985). These rocks were also the forming substrate of the local soil. The climate in the experimental plot is from moderately warm, humid to moderately cold with mean annual temperature of 4.1°C and mean annual precipitation total of 1.023 mm. The soil in the experimental plot is *Dystric Cambisol* (IUSS Working Group WRB, 2015), and its profile description is presented in Table 1.

Experiment Setup

A detailed geophysical survey of the experimental plot area by electric resistivity tomography (ERT) revealed sudden, mosaic changes of hydrophysical properties of soils in the surroundings of the experimental plot, reflecting the changes in both the soil textures and the soil types other than Dystric Cambisol, as well as in mineralogical changes of soil skeleton and its volume abundances within the soil profiles (Fig. 1).

These circumstances had direct impacts on the originally considered design of experiment, as these made it impossible to carry out the experiment on several plots with replications**.** In order to overcome this obstacle, we proceeded to conduct our field experiment only on one experimental plot, via intensively oriented research, based on the comprehensive study of dye solution transport in soil pedon, via utilisation of various and mutually independent methods of study, as specified below.

The air temperature and precipitation at the experimental plot were monitored by an automatic station of the EMS Brno Company (Czech Republic) - Fig. 2. Potential evapotranspiration (PET, mm h^{-1}) was calculated using Penman equation (Penman, 1948).

No rainfall was observed during the period between the BB application and excavation of CUT 2, CUT 24, and CUT 27, but several rainfalls were recorded between CUT 27 and CUT 504 excavation (Fig. 2).

In April 30, 2012, Brilliant Blue (BB) FCF dye solution with 10 g l^{-1} concentration was applied by a sprinkler with 100 mm h^{-1} intensity over a 1 m x 1 m plot. High concentration of dye tracer (BB) was applied to eliminate dye retardation (Kasteel et al., 2002), as well as to increase the visual resolution of stained objects of dye pattern profiles.

The sprinkler consisted of a board supporting 1,600 needles with a 0.5 mm diameter arranged in a 40 x 40 grid. Each needle was individually connected to a liquid distribution vessel

Table 1. Description of soil profile in the experimental site.

	Soil horizons	(cm)	Soil horizon description
Forest-floor litter horizon Oo	Sub-horizon O_{ol}	1.5–7.0	Broad-leaf and needle litter (with sprays, cones…)
	Sub-horizon O_{of}	0.5–1.5	Moderately decomposed plant litter
	Sub-horizon O_{oh}	0.0–0.5	Strongly decomposed plant litter
Umbric horizon	Horizon Au	0–5.0	Umbric, dark brown, sandy loam, wet, loose with slightly nodular structure, with gravel content of approximately 5 %, moderately rooted, apparent transition to Bv horizon
Subsurface horizons	Cambic B_v horizon	5–110	Brown (HUE 5YR, Value 4, Chroma 4) from the upper part tongue-like spots of purplish tone (HUE 5 YR, Value 3, Chroma 3), loamy sand, slightly wet, compacted (less where purple), moderately rooted – slightly in a lower part, gradual transition to C1.
	Horizon C_1	110 +	Light brown, sandy, wet, compacted.

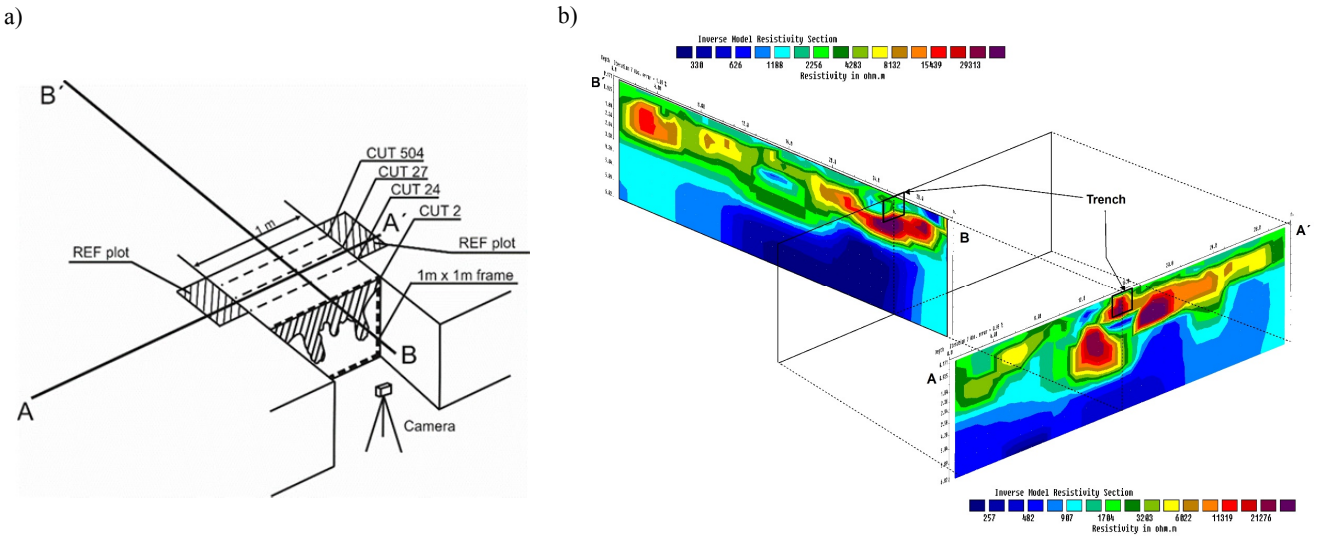

Fig. 1. The location of both the experimental and the REF with projection of CUT2 – CUT 504 soil profiles (a). The lines A-A´ (the contour line), and B-B´ (fall line) represents the orientation of ERT profiles (b), which show the subsurface structures of coloured slates with high electrical resistivity values (11 000–30 000 Ωm) floating on slope deposits with low electrical resistivity values (300–1000 Ωm) (dipole-dipole array).

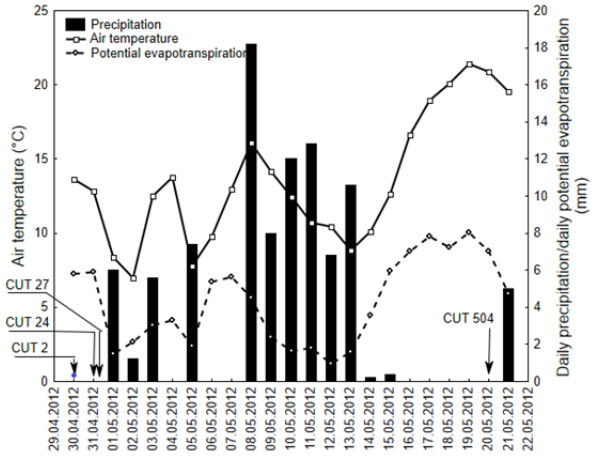

Fig. 2. Temperature, potential evapotranspiration and precipitation at the experimental site.

through the plastic tubings. The tank was supplied with dye solution by a piston diaphragm dosing pump (DME 150, Grundfos Alldos, Reinach, Switzerland) operating in the range of 0.1–140 l h^{-1} with negligible pulsation. The board supporting needles had an industrial vibrator attached to it to assure uniform distribution of droplets over the experimental plot.

We irrigated continuously for 1 hour, so the flooding regime of irrigation was achieved. The tree litter and duff were cleared before irrigation, as organic horizons may have significant influence on flow patterns (Capuliak et al., 2010), as well as on macropore flow initiation process.

As the experimental plot was located on a flat area of the hillslope, the lateral outflow of dye solution from the experimental plot was prevented, and only vertical infiltration of dye solution took place.

After the BB application, a series of four vertical profile cuts, 1 m x 1 m each, were excavated at different times, namely after 2 (CUT 2), 24 (CUT 24), 27 (CUT 27), and 504 hours (CUT 504), revealing the dye pattern profiles for further analysis (Fig. 1). The soil profiles were photographed with a digital camera (Canon EOS 450D) mounted on a stable tripod. Before photographing, the 1 m x 1 m gray frame with a ruler was mounted on the soil profile faces to prevent a geometrical distortion and to assure inhomogeneous illumination correction. The obtained pictures were recorded and stored in the raw format. Afterwards, the sample-extraction sites within the domain of particular profiles were marked, and the profiles were photographed again.

The individual CUT profiles were spaced 20 cm apart, with CUT 2 positioned about 20 cm from the trench bank and the other CUTs were excavated sequentially to the trench front (face uphill). In order to eliminate the dye pattern edge effect, the edge sections of the profiles were excluded from sampling.

The times of excavation events were selected according to the following rules: standard excavation time was considered as 24 hours (CUT 24), the time of 2 hours (CUT 2) was selected to document the dye pattern profile evolved during the infiltration stage (i.e., in time, when thin film of dye solution still remains on the top of irrigated area). The 27-hour profile (CUT 27) was excavated in order to evaluate potential changes in dye pattern profile shortly after standard excavation time (24 hours), when redistribution of dye solution in soil was dominant process in soil pedon. Such an approach enables to access the changes in dye pattern profiles, which emerged during both, the infiltration (CUT 2) and the redistribution stage (CUT 24 and CUT 27) of the dye solution flow in soil profile. The excavation time of the CUT 504 was chosen to record the potential changes in dye pattern as affected by meteoric water imbibition.

After the excavation of CUT 504, additional two vertical profiles were excavated (1 m x 0.5 m each), 35 cm next to the both, left and right edges of the 1 m x 1 m experimental plot. No BB tracer had been applied on the soil surface in this case. These plots are referred as REF ("reference") plots in our study (Fig. 1). The REF profiles served for the comparison with CUT 2 – CUT 504 profiles to reveal physical and chemical changes induced by Brilliant Blue dye solution.

As mentioned, in order to overcome the obstacles resulting from the spatial heterogeneity in soil in the vicinity of the experimental plot area, we proceeded to conduct our field experiment via utilisation of different and mutual independent methods of study:

- Soil reactions changes: It can be expected, that irrigation of acidic soils (pH < 4.0) with abundant BB dye solution (pH = 7) would change the pH (H_2O) values of soil samples on

experimental plot significantly. The intensity of such changes can be judged by comparing them with soil reaction profiles from the REF plots, unaffected by dye solution. With respect to spatio-temporal evolution of the dye infiltration/redistribution process within soil pedon, the temporal changes in soil reaction profiles should be revealed in soil profiles excavated at different times.

- Chemical changes: The sodium represents 5.8% of BB FCF dye molecule weight component; therefore, sodium represents an important agent applied into the soil during the irrigation experiment. The changes of Na^+ concentration ($cmol_c\ kg^{-1}$) in the soil exchangeable complex inside the irrigated part of the pedon (when compared to Na^+ ($cmol_c\ kg^{-1}$) in REF plots) should follow the spatio-temporal redistribution of the dye-solution in the soil pedon in a similar way, as was the case of soil reaction.
- Interaction changes: The process of water transport into the surrounding matrix is referred to as lateral infiltration, or interaction (Weiler and Flühler, 2004; Weiler, 2005). The interaction processes are controlled by water supply into macropores, flow conditions in the macropores and by water transport from macropores into the surrounding matrix (Beven and Germann, 1982; Weiler, 2005). In the case when soil profiles excavated at different times record the spatio-temporal process of dye solution infiltration/redistribution in the soil pedon, the c $Na^{+(IC)}$/c $Na^{+(NC)}$ ratio should reveal the interaction changes between the intensely coloured zones of macropore flow (IC zones) and the surrounding soil matrix of less coloured zones ("soil matrix" – NC zones).

The sampling procedure was adapted to meet the set objectives defined for physical-chemical analyses. Three samples from each 10 cm layer of each CUTs of the experimental plot were taken by Kopecky-cylinder with volume of 100 cm^3, with consideration of colouring intensity: samples labelled as NC (from sites not affected by BB dye), MC (taken from zones with moderate colouring) and IC (samples intensively coloured by BB dye solution). In total, 120 soil samples were taken for physical and chemical analysis from CUT 2 - CUT 504 soil profiles. The soil samples were taken also from the REF plots, where two samples were taken from each 10 cm layer, i.e. in total 20 samples were taken from REF zones.

The results of all above mentioned independent and indirect methods of dye solution flow were summarised and evaluated by Bebej et al. (2017). It was also found that according to the USDA soil taxonomy, the soil samples taken from both the experimental and the REF plots were classified as sandy clay loam (usually, samples from 0.1 to 0.5 m depth), and sandy loam (samples below 0.5 m), and no significant texture differences were found between the experimental and the REF plots. On the other hand, the statistical analysis showed that the depth influenced the percentage content of clay with very high significance ($p = 0.000$) in all soil profiles, and that the lowest clay content was in 100 cm depth. According to the statistical tests, the colouring intensity was significantly related to particle-size distribution, especially to sand fraction, since its content in the intensively coloured zones was significantly higher than in the non-coloured zones ($p = 0.000$). The silt content in the intensively coloured zones was significantly lower than in the samples from the moderately coloured zones ($p = 0.000$), or from the non-coloured zones ($p = 0.001$). It was found that the skeleton content increased with the depth, reaching its maximum in depth interval of 0.4–0.7 m. Generally, no significant differences in the skeleton content were observed among the individual profiles of both, the experimental and the REF plots. From the mineralogical point of view, the soil skeleton is represented by clasts of extremely acid quartzites, sandstones, gray-green-, and red-coloured mica slates. The silicate analyses of fine earth soil samples taken from the soil profiles of REF plots showed no differences in chemical and mineralogical composition of soil. Considering the skeleton composition, its volumetric content, soil textures and chemical composition of fine earth we can propose that the working hypothesis about the spatial representativeness of soil pedon body within the REF and the experimental plots is valid, and that the observed changes in dye pattern profiles will minimally reflect spatial variations existing within the pedon body under investigation (Bebej et al., 2017).

The morphometric parameters chosen for the study of spatio-temporal dye solution transport is based on the measurement of extent and distribution of stained objects within vertical dye pattern profiles excavated at different times (CUT 2 – CUT 504), which can be used for deriving of flow regime characteristics within it. Weiler and Flühler (2004) classified flow processes into five different flow types (FTs), of which three represent the macropore domain, and two the soil matrix FTs. We suppose that predominant flow processes can be deduced from the stained path width (SPW) of stained objects, while SPW limit < 20 mm represents flow pathways, where the dye solution flows primarily in macropores, with minor penetration into the surrounding matrix. In this way, the SPW vertical dye pattern profiles characterised by particular SPW length classes (< 20 mm, 20–200 mm, > 200 mm) can provide information about both, the dominant types of the dye solution flow, and the intensity of macropore-matrix interaction.

The methodology of flow types determination based on SPW evaluation is usually applied without differentiating between the concentration of Brilliant Blue in stained objects. We suggest, that concentration changes should be detected, if the dyed pattern profiles are developing in time.

Specific aspect of our small-scale field experiment relates to the soil water content (SWC) issue. The movement of sorbing solute (Brilliant Blue) is retarded relative to the water flow, because of the partitioning of the solute between the liquid and the solid phases (e.g., Kasteel et al., 2002). The transport processes of dye solution within the soil pedon makes the concentration of Brilliant Blue to be diluted in time course (Germán-Heins and Flury, 2000), and via chromatographic separation of the tracer, the SWC concentration in macropore – soil matrix (i.e. two-domain) system will not spatially coincide with the spatial arrangement of coloured zones. On the other hand, SWC distribution around the zones of preferential flow, and the SWC changes observed in dye pattern profiles exposed at different times, could provide an independent insight on the processes of dye solution flow in the pedon under investigation.

Hydrological modelling (here the HYDRUS dual permeability model) can help to verify the assumption about the temporal dynamics of dye solution transfer processes at the pedon scale. The water balances calculated by the hydrological model include the matrix water content changes, the volumes of water within the fracture domain and the sum of the fluxes on domain boundaries. In our study, the calculated temporal changes of water solution balance can help to understand the dominant macropore flow initiation within the CUT 2 profile (see also Li and Ghodrati, 1997; Weiler and Naef, 2003). In the case of macropore flow initiation on soil surface (CUT 2), the total water content changes in the soil matrix of CUT 2 profile should be very low, because of water bypassing the soil matrix via macropores. By flow initiation theory (Weiler, 2005), an extremely high outflow of dye solution via macropore network should be observed.

Data processing

Evaluation of dye concentration in soil

To calibrate the images for the concentration of BB from the stained flow region, 10 small disturbed soil samples of one to three grams were scraped off the surface of soil profiles from various depths. The sample locations were marked and the soil profile was photographed the second time. The BB concentrations were obtained by extracting BB in the laboratory as described in the following section.

To calibrate the relationship between the colour coordinates and BB concentration, the scraped soil samples were dried at 80ºC for 24 hours. From each homogenised soil sample, a subsample of 0.5 g was weighed in an extraction column (8 ml, empty, glass with PTFE frits), and put in a vacuum vessel. Ten ml of a solution with 4:1 (v : v) ratio of water : acetone was added as an extraction solvent, and the vessel was vapourised under low pressure of ~ –600 Pa for one hour. The extract was filtered through a 0.45 µm filter, the BB concentration in the extract was measured spectrophotometrically (Schimazu UV-1800 Spectrophotometer) at a wavelength of 630 nm (Capuliak, 2008; Capuliak et al., 2010), and the BB concentration in the soil (w : w, BB : soil) was calculated. Based on the calibration graph, dye concentration (C) was calculated for every pixel of the soil profile image and the stained area. For further evaluations, relative dye concentration (C_{rel}) as the ratio between C concentration and the approximate dye concentration of 10 g l^{-1} (C_0) calculated from the dissolution of the total dye tracer amount in 100 l of water used for irrigation.

After taking digital photographs of individual profiles, several procedures were performed to evaluate the spatial concentration of BB in the soil (Forrer et al., 2000): (i) geometric correction; (ii) white-balance and exposure correction; (iii) calibration; (iv) evaluation of the dye concentration. To evaluate the spatial distribution of the various flow types (FTs) in each cut, which was stained by BB, the processing framework in GNU R (R Development Core Team) and C with the help of the ImageMagick image processing library and with a resolution of 500 x 1,000 pixels (i.e., one pixel represents 1 mm x 2 mm) was used (Capuliak et al., 2010).

Morphometric parameter analyses

Two basic parameters describe the morphology of stained objects in space: the volume density (V_v) and the surface area density (S_v). The V_v corresponds to dye coverage (D_c) described by Eq. (1) (Flury et al., 1994):

$$D_c = \left(\frac{D_a}{D_a + ND_a}\right) \cdot 100 \quad (1)$$

where D_a is the surface area in the cut that was stained by dye, and ND_a is the unstained surface area in the cut.

The V_v value represents the total sum of the lengths (L) of stained objects, which are equal to the fraction of pixels (P_p) filled with stained objects in a particular depth determined with a 1-mm step on the depth axis. In doing so, the total count of the pixels divided by the profile width (1,000 pixels) represents the dye coverage for a given depth (Weiler and Flühler, 2004). The increase of the V_v (D_c) value indicates the growth of the macropore: soil matrix interaction (Weiler and Flühler, 2004), too. Hence, volume density values give first impressions of the differences and similarities of the dye patterns between different experimental sites (Weiler and Flühler, 2004), and between the dye pattern profiles exposed to a dye tracer in a given experimental plot for different times.

The S_v value of the profile was estimated from the intercept density calculated as the number of intercepts between the unstained and stained pixels per depth (Weiler and Flühler, 2004).

The V_v and S_v values as functions of the soil depth should be interpreted together, because for a given soil depth in a certain soil profile, the V_v and S_v values can be different. For example, both the S_v and the V_v can be low if small stained areas have also a small surface. However, the V_v can be high and the S_v can be low, if the stained object covering the whole soil volume has a small surface (Weiler and Flühler, 2004).

A stained path width (SPW) represents the width of stained flow pathway in the stained object**.** For each vertical dye pattern, the SPW profile can be calculated as a frequency distribution of three size categories of SPW, <20 mm, 20–200 mm, >200 mm. On the base of the proportion of these SPWs categories, as well as the classification rules of Weiler and Flühler (2004), flow types (FTs) can be distinguished. The mutual relationships among the particular stained object morphometric parameters is presented in Fig. 3.

In order to analyse the spatio-temporal processes of dye solution infiltration and redistribution in soil profiles of the experimental plot, a semi qualitative evaluation of the V_v, S_v, SPW, C_{rel} and the FTs was used as BB dye solution flow during dye solution infiltration and its redistribution in soil profiles should induce the changes in the V_v, S_v, SPW, C_{rel} and FT depth profiles regarding local maxima and minima values of the discussed parameters. Consequently, high V_v, high S_v, and high SPW class >200 mm designate high values of these parameters at a given depth of the soil profile, and the terms high, low, and average indicate visually observed deviations of the particular values from the values recorded in other dye pattern profiles.

Mathematical modelling of soil water content profiles

The rationale for the mathematical simulation of the measured soil water profiles using one single set of hydraulic parameters for each horizontal soil layer was to verify the key assumption of the study, namely that the observed changes within dye patterns of four profiles exposed at different times are rather a result of temporal dynamics of dye solution redistribution processes and succession of various flow types than an intrinsic spatial heterogeneity of the soil pedon. If the evaluated pedon could be considered hydraulically homogeneous in this sense, it should be possible to simulate successfully the SWC profiles at any time with one single set of parameters for each defined soil layer.

Soil water content measurements were performed by a gravimetric method (each 10 cm depth 3 measurements). The parameters of soil hydrophysical characteristics of the matrix domain were estimated from the measured soil water retention curves in pressure chambers (Eijkelkamp, The Netherlands) and saturated hydraulic conductivities estimated by a constant head method on the undisturbed samples (Kopecky cylinders) taken from the profile CUT 2. Then the SWC profile created by averaging of values in particular soil depths in CUT 2 was used to solve the inverse problem for the two-domain (dual permeability) environment to calibrate the parameters of the fracture domain. Once calibrated, the parameters were considered same for all other profiles assuming hydropedological similarity of the soil pedon.

The review of models describing non-equilibrium and preferential flow and transport in the vadose zone has been given e.g. by Šimůnek et al. (2003) and Gerke (2006). While the

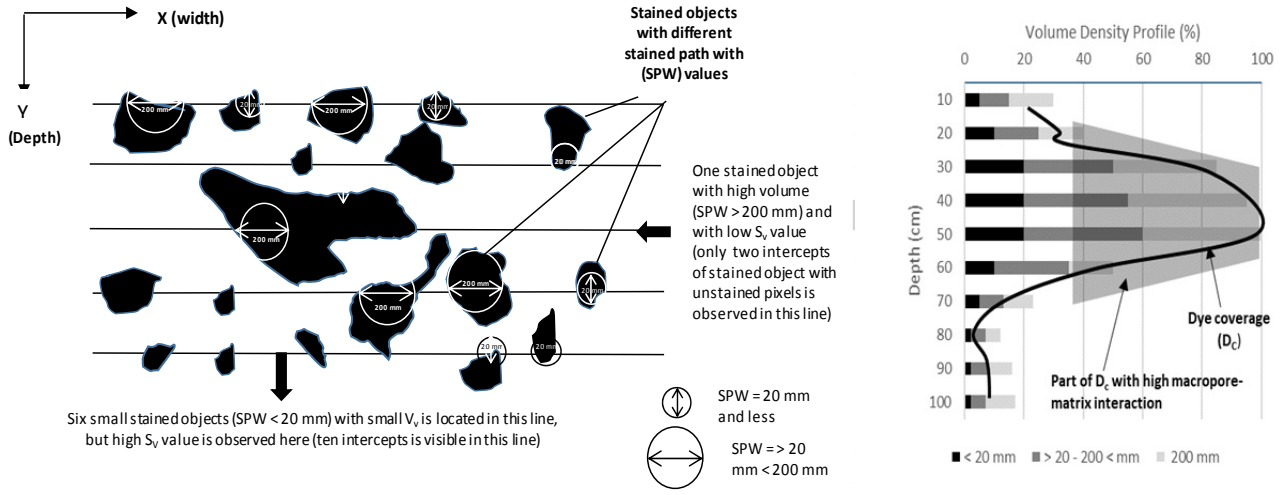

a) b)

Fig. 3. The stained object width measurements in particular vertical sections (Y) provides the information about the V_v, the S_v and the stained path width (SPW) distribution of dye pattern profile (a), which are reflected in the formation of D_c curve, within which a zone with high macropores - soil matrix interaction can be identified, (b).

single-domain model describes the uniform flow in soil porous media, the dual-permeability model can represent a non-equilibrium/preferential flow in a complex system of soil aggregates (matrix) and intermediate spaces (fractures or macropores). In both cases Richards' equation is used to describe the flow in a variably saturated rigid porous medium for one-dimensional isothermal Darcian flow. While in the case of a single-porosity system the Richards' equation is solved for the entire flow domain, in the dual-permeability model, it is applied separately to each of the two pore regions – matrix and fracture domains.

The basic hydraulic functions; i.e. soil water retention curve $\theta(h)$ and hydraulic conductivity function $K(\theta)$ are analytically expressed according to van Genuchten (1980). The initial condition was set as h gradually changing from –500 kPa at the top to –150 kPa at the bottom of the soil profile. The top boundary condition was defined by hourly precipitation (including irrigation with the dye-solution) and calculated evapotranspiration. The bottom boundary condition was defined as free drainage.

RESULTS AND DISCUSSION

Distribution of the Brilliant Blue dye

Dye pattern profiles of particular CUTs, together with their dye coverages are documented in Fig. 4. Highly developed macropore systems within the whole pedon body of the experimental plot show high density of autonomous macropore structures, creating a mutually interconnected system. Nevertheless, some differences between the macropore structures are well visible. Within the CUT 2, macropore pathways are narrow and the top of CUT 2 profile is only slightly covered by BB dye. On the contrary, the top of CUT 24 soil profile is heavily covered with BB dye. In both, the CUT 24 and the CUT 27 profiles, the macropore pathways are broad, indicating increasing macropore-soil matrix interaction. The CUT 504 is different from the other CUTs, and finger-like structures are evident there.

The macropore structures presented in Fig. 4, have arisen due to the existence of structural voids with large apertures of geogenic origin, with minimal presence of biological channels. Due to well-developed periglacial ("cryogenic") phenomena in the area, we propose that the macropores were formed by cycling of freezing and thawing events (Jury and Horton, 2004; Heller, 2012).

The dye coverage values (D_c) as functions of the soil depth for the various 1 m^2 cuts and their zoom in for the 0.1 m soil depth are presented in Figs.5a and 5b, respectively. The low D_c values in certain soil profiles indicate high fractions of the preferential flow, and high values of dye coverage indicate high fractions of the matrix flow. In CUT 2, the dye coverage value was small, from ~40% to 80% at the top (0–0.1 m) soil layer (Figs. 5a and 5b), and then increased to ~80% down to 1 m soil depth. In CUT 24, the dye coverage values were from ~80 to 100% at the top soil layer and slightly decreased downward to ~80%, and became similar to the values of CUT 2 at 1 m soil depth. These results indicate that during the time between 2 hours and 24 hours after the BB application there was an additional infiltration of the dye solution from the dye solution pool located at the top of the soil surface during the dye solution infiltration. In general, the D_c values at the top layer (0–0.1 m) in CUT 24, CUT 27, and CUT 504 were similar. However, these values were higher in CUT 27 and CUT 504 than in CUT 2 and CUT 24 in the ~0.3–0.6 m soil layer. This fact can be explained by lateral dye solution redistribution in the ~0.3–0.6 m soil layer during the time between 24 h to 504 h after the BB application, which caused the increase in the D_c values in CUT 27 and CUT 504 in this soil layer, and simultaneously, the remnant dye solution volume in this stage of dye solution redistribution was not able to increase the D_c values in the CUT 27 and the CUT 504 profiles in the ~0.7–1.0 m soil layer.

The relative BB concentration values (C_{rel}) as functions of soil depth for the various 1 m^2 cuts are presented in Fig. 6. In comparison with Fig. 5, the most significant change in C_{rel} was observed in CUT 504 profile (Fig. 6), where the significant drop in C_{rel} was observed in depth 0.0–0.5 m. The drop in C_{rel} can be related to the impact of rain water invasion into the soil (Fig. 2) accompanied with the leaching of BB from the top and the middle part of the CUT 504 profile.

The proportions of SPW classes within the individual dye pattern profiles (Fig. 7) show that the growth of SPW category > 200 mm from CUT 2 to CUT 504 profiles was accompanied by decrease in abundance of 20–200 mm SPW category. Small abundance of SPW category <20 mm and high abundance of SPW categories >20 mm and <200 mm are observed within the CUT 2 dye pattern profile, which reflects the growth of macropore – soil matrix interaction in time (macropore flow cession) and its gradual switch to the matrix dominated flow

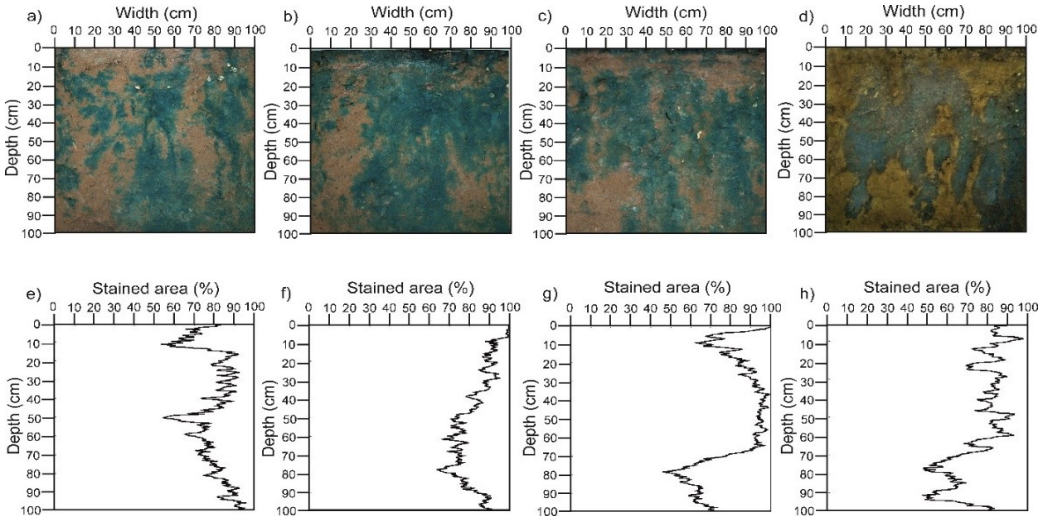

Fig. 4. Dye pattern profiles and corresponding dye pattern coverages (bottom) of CUT 2 (a), CUT 24 (b), CUT 27 (c) and CUT 504 (d) profiles (adapted from Bebej et al., 2017).

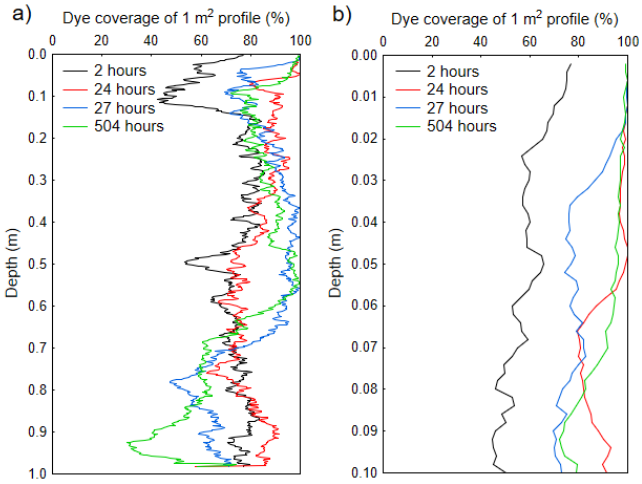

Fig. 5. a) Dye coverage profiles of CUT 2, CUT 24, CUT 27 and CUT 504, b) zoom of dye coverage in depth 0–0.1 m.

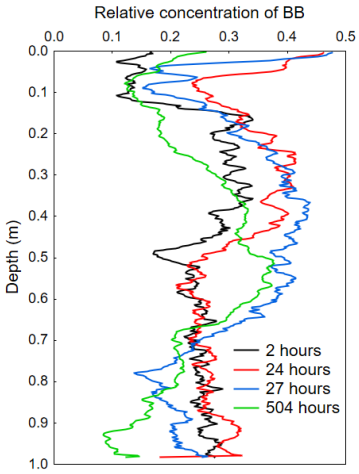

Fig. 6. The average concentration of BB in CUT 2 to CUT 504 soil profiles.

(corresponding also with the time of transition from infiltration to redistribution stage). Dominant abundance of SPW category > 200 mm within the CUT 24 –CUT 504 profiles indicate that

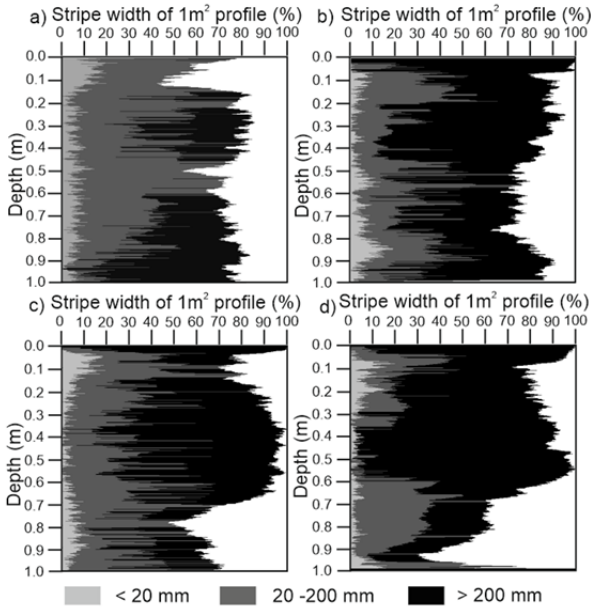

Fig. 7. Relative proportions of three SPW classes in the CUT 2 (a), CUT 24 (b) and CUT 27 (c), and CUT 504 soil profiles.

dye solution is entrapped within stained objects of high volume with small surface, visible in surface density profiles (Fig. 7). It should be noted that the SPW category <20 mm abundance is recorded in all analysed dye pattern profiles, but this SPW objects did not play a significant role in hydrological regime of dye solution during its redistribution in the soil pedon.

The top part of CUT 2 dye pattern profile (Fig. 7, a) provides important information about the initiation processes of macropore flow in the soil body. The low D_c value, as well as the presence of the SPW classes of both < 20 mm, and > 20 mm and < 200 mm, provide strong evidence that the macropore flow was initiated at the soil surface in the case of the experimental plot under investigation. By infiltration model of Weiler (2005), most of the macropores received very little water, while a few macropores received a large proportion of the total volume of dye solution irrigation water. It was proved that the total soil water content change in the soil matrix decreases with an increasing input rate, due to increased bypassing of the soil matrix (Weiler, 2005). This fact is strongly supported in this

study by both the SPW measurements and the dual permeability model simulation results, listed in Chapter 3.3. The other consequence resulting from the ratio of SPW of < 20 mm and > 200 mm classes documented for CUT 2 profile is that the macropore flow was a dominated process, which controlled infiltration of dye solution into the soil body in the time of CUT 2 dye pattern profile generation (Weiler and Flühler, 2004).

The distribution of SPW classes within the particular soil profile exposures enables to calculate flow type distribution (Fig. 8). According to Weiler and Flühler (2004) classification rule, only in the case of CUT 2 profile it is possible to document the abundance of macropore FTs, while in the other CUTs, matrix FTs are dominant (Fig. 8), or even the only FT within the dye pattern profile of CUT 24 is presented.

The surface area densities (S_v) of stained objects in CUT 2 and CUT 24 profiles were very different from those of CUT 27 and CUT 504 (Fig. 9). In the case of CUT 2 profile, the S_v was large in those parts of the soil profile where the dye coverage profile (Fig. 5) reached its minimum. It is noticeable that the maximum S_v values were observed at the top of the CUT2 profile, what indicates direct dye solution flow from the soil surface into the macropore pathways.

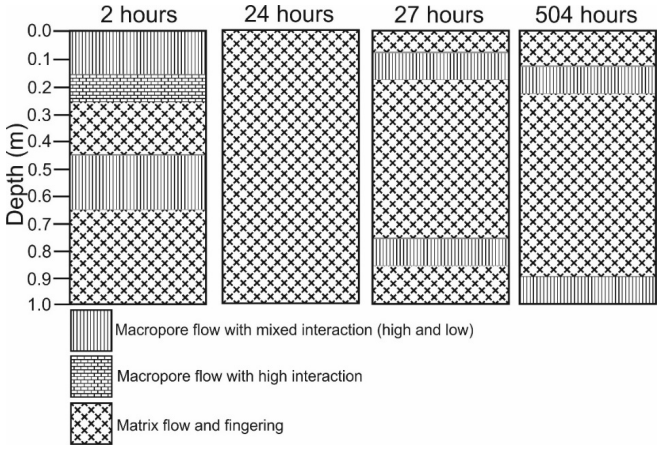

Fig. 8. Flow types categories observed in CUT 2 – CUT 504 profiles.

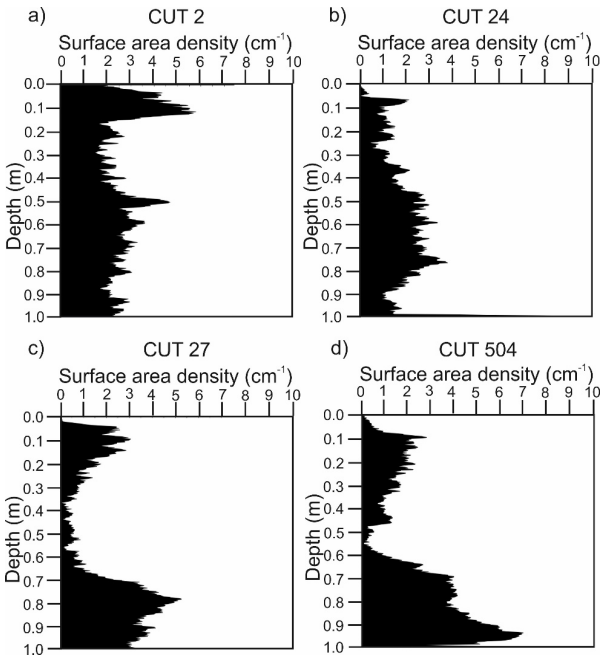

Fig. 9. The surface areal density profiles of vertical dye patterns of CUT 2–CUT 504 profiles.

In the case of the CUT 24 the process of S_v reduction (in comparison to CUT 2) is visible in the upper soil profile, what demonstrates the process of transition zone creation, with developing of matrix FTs, which can be linked with the infiltration of residual dye solution dosage from the surface of the experimental plot in the time between the CUT 2 and CUT 24 profile formations.

In the case of both the CUT 27 and the CUT 504 profiles the S_v started to grow at the upper part of the soil profile, where the dye coverage of profiles reached its local minimum (Fig. 5). The observed growth of S_v in these zones (as well as in the bottom part of the soil profiles, which was even more pronounced) indicates the turnover of the dye solution flow regime characterised by the existence of small stained objects with low volume but high surface density. The origin of high S_v values in the top part of the CUT 27 and CUT 504 profiles (Fig. 9) can be explained by finger propagation of the high-interaction zone, when the matric potential decreases behind the wetting front (Jury and Horton, 2004). In consequence, the SPW stained objects of both <20 mm and >20 mm and <200 mm dominate over >200 mm stained objects in the top parts of the CUT 27 and CUT 504 profiles (Fig. 7), and macropore FTs originated there due to emptying of >200 mm SPW objects (Jardine et al., 1990).

The massive growth of S_v observed in the bottom part of both the CUT 27 and the CUT 504 profiles is caused by a different mechanism than the one observed in the upper parts of the CUT 27 and the CUT 504 profiles. The SWC reached its maximum values in this depth (in contrast to the top parts of CUT 27 and CUT 504 profiles), while the D_c achieved its absolute minimum at these depths of CUT 504 (Fig. 5). Such a situation indicates minimal macropore-soil matrix interaction in deep zones with high volumetric skeleton content, which can be explained by drainage of residual dye solution from the horizons located above, via macropore PF pathways with domination of SPW objects <200 mm.

Fig. 10 summarises the obtained results and provides a general picture about the subsequent stages of dyed solution redistribution within the soil pedon, which are discussed in the following section.

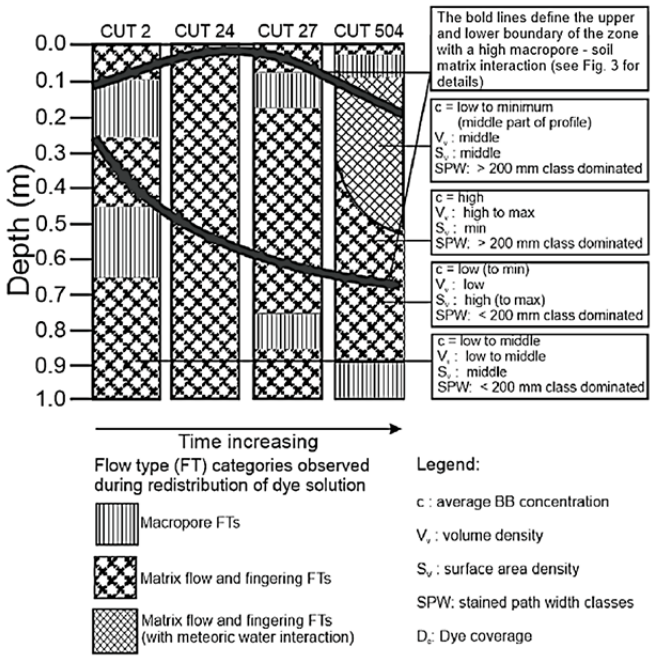

Fig. 10. The spatio-temporal distribution of flow type categories within the CUT 2 –CUT 504 profiles.

Dual-permeability model simulations

A dual permeability model provides the information about the SWC changes within both domains separately. It also calculates the actual and cumulative boundary fluxes on the top and bottom boundary of the modelling domain.

The results of water content profiles within the soil-matrix domain modelled with the simulation setup according to the description in the methodological chapter of this paper are shown in Fig. 11. The van Genuchtens hydraulic parameters of both domains are listed in Table 2.

HYDRUS model simulates SWC profiles within the matrix domain quite well (Fig. 11). Since the SWC was measured by a gravimetric method on undisturbed soil samples, it must be considered as the SWC of soil matrix only. Water within the fracture domain cannot be detected gravimetrically because of fracture-domain volume being void of water during the measurement. This is also the most probable reason for a slight overestimation of SWC in matrix domain by the model. The correlation between the measured and the simulated values of SWC is however very high. Still significant amount of (by time) unexplained variability should be ascribed to intrinsic spatial heterogeneity of the soil at the pedon scale (see R^2 in Table 2). Anyway these results approve the dynamic interpretation of FT changes between the particular soil profiles exposed for different time lengths, since SWC profiles in all particular CUTs were successfully simulated with the same set-up of hydraulic parameters (Table 2).

Table 2. Hydraulic parameters of the porous system domains. (θ_S-m) is saturated soil water content of the matrix domain, θ_r-m is a residual soil water content of the matrix domain, α-m is a shape parameter of the matrix domain, n-m is a shape parameter of the matrix domain, K_S-m is saturated hydraulic conductivity of the matrix domain in cm h^{-1}, θ_S-f is saturated soil water content of the fracture domain, θ_r-f is a residual soil water content of the fracture domain, α-f is a shape parameter of the fracture domain, n-f is a shape parameter of the fracture domain, K_S-f is saturated hydraulic conductivity of the fracture domain in cm h^{-1}, w is the ratio between macropore and matrix regions and measured (SWC-m) and simulated soil water contents (SWC-s) and α_w is the mass transfer coefficient in cm^{-1} h^{-1}.

Hydraulic parameters Depth (cm)		θ_r-m	θ_S-m	α-m	n-m	K_S-m	θ_r-f	θ_S-f	α-f	n-f	K_S-f	w	α_w
0–15		0.10	0.29	0.075	1.180	3.5	0.0	0.8	0.0124	2.0	300	0.2	2.42
15–30		0.16	0.29	0.061	1.120	10.0	0.0	0.8	0.0124	2.0	300	0.2	6.91
30–50		0.17	0.45	0.073	1.178	10.0	0.0	0.8	0.0124	2.0	300	0.2	6.91
50–90		0.12	0.45	0.068	1.150	10.0	0.0	0.8	0.0124	2.0	300	0.2	6.91
90–100		0.15	0.38	0.073	1.178	10.0	0.0	0.8	0.0124	2.0	300	0.2	6.91
CUTs/Depth (cm)		10 cm	20 cm	30 cm	40 cm	50 cm	60 cm	70 cm	80 cm	90 cm	100 cm		
	SWC-measured (vol. %)	16.70	20.20	23.90	24.50	19.90	21.10	20.10	19.10	18.806	21.10		
CUT 2	SWC-simulated (vol. %)	17.00	19.60	24.20	23.80	21.20	21.00	20.90	20.80	19.80	20.00		
	R^2						0.7924						
	SWC-measured (vol. %)	16.00	19.40	21.10	23.60	20.60	20.80	18.50	19.10	17.60	18.90		
CUT 24	SWC-simulated (vol. %)	16.80	19.90	24.00	25.20	24.70	22.30	22.10	22.00	21.80	20.40		
	R^2						0.6956						
	SWC-measured (vol. %)	15.30	19.80	20.90	21.60	20.60	21.70	20.10	20.30	19.50	19.10		
CUT 27	SWC-simulated (vol. %)	16.70	19.90	25.30	24.70	22.40	22.20	22.00	21.80	20.40	20.00		
	R^2						0.7464						
	SWC-measured (vol. %)	14.50	15.10	18.00	17.90	20.40	20.30	20.80	21.10	21.00	19.60		
CUT 504	SWC-simulated (vol. %)	14.60	15.00	21.10	24.20	24.40	23.00	23.10	23.20	21.70	21.90		
	R^2						0.7286						

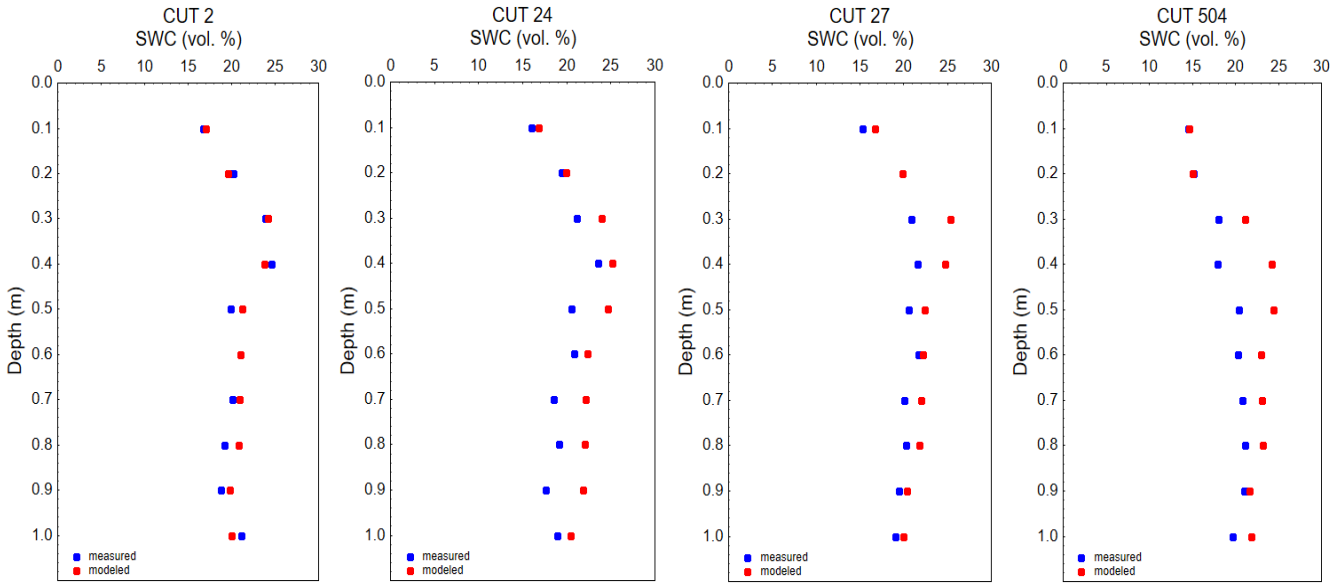

Fig. 11. Average values of measured and simulated (HYDRUS) of soil water content (SWC) within the particular CUT 2 (2-hour), CUT 24 (24-hour), CUT 27 (27-hour) and CUT 504 (504-hour) soil profiles.

The calibrated saturated water content of 0.8 for the fracture domain is relatively high but still a reasonable value (e.g. Gerke et al., 2013; Ireson et al., 2009; Kodešová 2017-personal communication; Mathias et al., 2006). The increase in matrix-domain SWC during the infiltration experiment is not substantial and is located only to particular depths of the soil profile.

From the (by HYDRUS) calculated water balance it follows that only some 30% of the irrigation water was utilised for the matrix SWC increase. The rest of the water either flowed out of the profile via large macropores (fracture domain) or it is actually present within the macropores. This was also supported by mathematical modelling, which shows the distribution of water between two domains and the amount of water which flowed out through the bottom boundary (Table 3).

Table 3. The average values of the SWC present within the particular soil domains (matrix and fractures) in particular times and the cumulative value of the flux through the bottom of soil pedon.

Time (hours)	SWC in matrix domain (m^3 m^{-3})	SWC in fracture domain (m^3 m^{-3})	Cumulative bottom flux (10^{-3} m)
2	0.241	0.0702	10
24	0.22	0.025	50
27	0.22	0.024	51
504	0.22	0.013	110

DISCUSSION

The hydropedological similarity concept used in this study does not mean the same as homogeneity and certainly some changes in porosity, bulk density or skeleton content are still affecting hydrological behaviour even within a single studied soil pedon (Fér et al., 2016; Moreira et al., 2016). Besides almost technical impossibility to make 2-D simulation of such a defined problem (section "Mathematical modelling of soil water content profiles"), also for this reason it was decided to simulate only horizontally averaged water contents within vertical soil profiles and compare them with SWC measured by the gravimetric method, which in fact avoids the fracture domain as the water drains from the largest pores yet immediately during the sampling process.

The variability of the dye coverage, surface density, SPW characteristics, as well as the BB concentration, provides information bases for the reconstruction of dye solution redistribution processes in soil pedon.

The dye flow processes within the experimental soil pedon started immediately after the beginning of irrigation, via macropore-flow pathways, recorded by macropore FTs in CUT 2 profile. Based on modelling with HYDRUS, the dye solution flow at this stage was really concentrated in fracture domain (about 60% of total dye solution applied). As the CUT 2 profile was excavated 2 hours after the completion of the sprinkling experiment, a certain amount of dye solution still remained at the soil surface, which afterwards saturated the top soil layer, as can be seen in CUT 24 profile (Fig. 5). At the same time, the matrix FT category of Weiler and Flühler (2004) began to emerge there (Fig. 8). The D_c, C_{rel} values at the upper part of CUT 24 profile, as well as the SWC data recorded there indicate that the stage preceding the CUT 24 (dye pattern) profile creation, was characterised by maximum quantity of dye solution in this part of the soil profile.

When comparing the dye coverage (D_c) in profiles of CUT 24 and CUT 27 with that of CUT 2, the growth of D_c values observed within the 0.1–0.6 m depth interval of CUT 24 - CUT 27 indicate the growth of macropore-soil matrix interaction, accompanied by the reduction of S_v values. This fact suggests that the dye solution was entrapped within the stained objects of > 20–200 mm with small S_v values typical for soil matrix environment. The comparison of both the shape and the overall geometry of CUT 24 - CUT 27 D_c profiles document the subsidence of this macropore-soil matrix interaction zone into the deeper parts of the soil pedon.

The CUT 504 dye pattern profile manifests the impact of meteoric water on the ultimate dye pattern profile (Fig. 2). The intrusion of meteoric water caused the leaching of BB dye (Fig. 6), evident from the reduction of C_{rel} in the upper part of the CUT 504 profile.

The applied methodology of dye solution redistribution study, as well as the results obtained provide the evidences about the strong temporal control of dye solution flow within the analysed soil pedon. Fast changes were observed within few hours, what illustrates the remarkable dynamics of dye solution redistribution processes. On the other hand, the morphometric parameters of stained objects seemed to be sensitive enough to track these processes.

Bebej et al. (2017) have reported the physical-chemical changes caused by the application of Brilliant Blue dye (pH = 7) on acidic soils (pH < 4.0) from the same experiment. It was found that the application of BB dye solution abruptly increased the pH (H_2O) values in all profiles (CUT 2-CUT 504) of the experimental plot, and that the comparison with REF profiles revealed the gradual drop in pH (H_2O) from CUT 2 to CUT 504 profiles. Bebej et al. (2017) have documented also the changes of Na^+ concentration ($cmol_c$ kg^{-1}) in the soil exchangeable complex extracted from the zones of macropore PF of CUT 2 – CUT 504 profiles, analogous with those described for pH (H_2O).

The obtained results are in line with the findings of Li and Ghodrati (1997), Weiler and Naef (2003) and Weiler (2005) who showed how a surface initiation process can generate extremely dynamic macropore flow.

Alaoui and Goetz (2008) presented dye tracer distribution in six soil profiles that were continuously excavated in steps of every 20 cm. The cited authors declared the soil profiles were excavated one day after irrigation, but unfortunately the reference about timing of individual vertical profile excavation is missing. Nevertheless, the morphometric parameters of the analysed dye objects showed many similarities with our experiment outputs: (i) the dye coverage gradually increased with time, and (ii) the concentration of BB dye increased with depth within the soil profile.

CONCLUSIONS

The knowledge about the character of water redistribution within forest soils during extreme rainfalls or snow-melt situations is crucial for a set of practical applications, such as flood protection, silviculture, forest infrastructure management, etc. It has been proven that dye-tracer irrigation field experiments represent one of the suitable cost-effective tools to manifest and detect the local vadose zone hydrological processes, what is crucial for correct decisions in terms of above mentioned practical problems.

The presented case-study of the (dye solution) pedon-scale flow dynamics showed a key role of the time factor in succession of FTs observable via several vertical soil profiles excavated at different times.

Based on the numerical modelling, the time factor was able to explain from 70% up to 75% of the vertical variability of soil moisture profiles, which supports the assumption of hydropedological similarity of properly selected pedon-scale studies. Notwithstanding, the intrinsic 3-D heterogeneity of soil at the pedon scale may still embed a substantial portion of noise into 2-D result interpretations.

Three stages of dye solution redistribution processes were identified: (i) a stage of preferential macropore flow, (ii) a stage of strong interaction between macropore-domain and soil matrix leading to generation of heterogeneous matrix flow and fingering flow types, and (iii), a final stage of dye redistribution, which was predominantly connected with invasion of meteoric water into the soil pedon, resulting in substantial leaching of BB tracer from dye pattern profiles.

It was shown, how studies based on tracing of flow pathways in soil irrigated by dye solution can support the outputs of hydrological analyses. The question how the selected soil chemical properties (e.g., concentration of exchangeable cations) will reflect the observed spatiotemporal distribution of the dye tracer represents an interesting challenge for further research.

Acknowledgement. This work was supported by the Slovak Research and Development Agency under the contract No. APVV-15-0425 and the project of the scientific agency VEGA no. 2/0152/15. Part of the research was conducted under the project implementation: Centre of excellence for the integrated river basin management in the changing environmental conditions, ITMS code 26220120062; supported by the Research & Development Operational Programme funded by the ERDF.

REFERENCES

Alaoui, A., Goetz, B., 2008. Dye tracer and infiltration experiments to investigate macropore flow. Geoderma, 144, 279–286.

Allaire, S.A., Roulier, S., Cessna, A.J., 2009. Quantifying preferential flow in soils: A review of different techniques. J. Hydrol., 378, 179–204.

Andrusov, D., Began, A., Biely, A., Borza, K., Buday, T., Bystrický, J., Bystrická, H., Cicha, I., Eliáš, M., Eliášová, H., Fusán, O., Gašparíková, V., Gross, P., Hanzlíková, E., KÖhler, E., Houša, V., Lehotayová, R., Leško, B., Ložek, V., Menčík, E., Michalík, J., Mock, R., Pesl, V., Roth, Z., J., Samuel, O., Seneš, J., Slávik, J., Straník, Z., Špička, V., Vašíček, Z., Vaškovský, I., Vozár, J., 1985. Stratigraphic Dictionary of Western Carphatians. Vol. 2. Veda, Bratislava. (In Slovak.)

Bargués Tobella, A., Reese, H., Almaw, A., Bayala, J., Malmer, A., Laundon, H., Ilstedt, A., 2014. The effect of trees on preferential flow and the soil infiltrability in an agroforestry parkland in semiarid Burkina Faso. Water Resources Research, 50, 4, 3342–3354.

Bebej, J., Homolák, M., Orfánus, T., 2017. Interaction of Brilliant Blue dye solution with soil and its effect on mobility of compounds around the zones of preferential flows at spruce stand. Cent. Eur. For. J., 63, 79–90.

Beven, K., Germann, P., 1982. Macropores and water flow in soils. Water Resources Research, 18, 1311–1325.

Bogner, CH., Borken, W., Huwe, B., 2012. Impact of preferential flow on soil chemistry of a podzol. Geoderma, 175–176, 37–56.

Bundt, M., Widmer, F., Pesaro, M., Zeyer, J., Blaser, P., 2001. Preferential flow path: biological "hot spots" in soils. Soil Biol. Biochem., 33, 729–738.

Capuliak, J., Homolák, M., Aschenbrenner, Š., Ahmed, Y.A.R., Královič, R., 2008. Influence of litter on initial water transport in soil under forest stand. In: Šír, M., Tesař, M., Lichner, Ľ. (Eds.): Hydrologie malého povodí. ČVTS, Prague, pp. 59–66.

Capuliak, J., Pichler, V., Flühler, H., Pichlerová, M., Homolák, M., 2010. Beech forest density control on the dominant water flow types in Andic soils. Vadose Zone J., 9, 747–756.

Droogers, P., Stein, A., Bouma, J., de Boer, G., 1998. Parameters for describing soil macroporosity derived from staining patterns. Geoderma, 83, 293–308.

Fér, M., Leue, M., Kodešová, R., Gerke, H.H., Ellerbrock, R.H., 2016. Droplet infiltration dynamics and soil wettability related to soil organic matter of soil aggregate coatings and interiors. J. Hydrol. Hydromech., 64, 2, 111–120.

Forrer, I., Papritz, A., Kasteel, R., Flűhler, H., Luca, D., 2000. Quantifying dye tracer in soil profiles by image processing. Eur. J. Soil Sci., 51, 313–322.

Flury, M., Flühler, H., 1994. Brilliant Blue FCF as a dye tracer for solute transport studies. A toxicological review. J. Environ. Qual., 23, 1108–1112.

Flury, M., Flühler, H., Jury, W.A., Leuenbereger, J., 1994. Susceptibility of Soils to preferential Flow of Water. Water Resour. Res., 30, 1945–1954.

Garrido, F., Serrano, S., Barrios, L., Uruñuela, J., Helmhart, M., 2014. Preferential flow and metal distribution in a contaminated alluvial soil from São Domingos mine (Portugal). Geoderma, 213, 103–114.

Gerke, H.H., 2006. Preferential flow descriptions for structured soils. J. Plant Nutr. Soil Sci., 169, 382–400.

Gerke, H.H., Dusek, J., Vogel, T., 2013. Solute mass transfer effects in two-dimensional dual-permeability modeling of bromide leaching from a tile-drained field. Vadose Zone Journal 12, 2, 1–21.

Germán-Heins, J., Flury, M., 2000. Sorption of Brilliant Blue FCF in soils as affected by pH and ionic strength. Geoderma, 97, 1–2, 87–101.

Ghodrati, M., Jury, W.A., 1990. A field study using dies to characterize preferential flow of water. Soil Sci. Soc. Am. J., 54, 1558–1563.

Hagedorn, F., Bund, M., 2002. The age of preferential flow paths. Geoderma, 208, 119–132.

Heller, K., 2012. Einfluss periglazialer Deckschichten auf die oberflächennahen Fließwege am Hang - eine Prozessstudie im Osterzgebirge, Sachsen. PhD Thesis. Technical University Dresden.

Ireson, A.M., Mathias, S.S., Wheater, H.S., Butler, A.P., Finch, J., 2009. A model for flow in the chalk unsaturated zone incorporating progressive weathering. Journal of Hydrology, 365, 244–260.

IUSS Working Group WRB, 2015. World Reference Base for Soil Resources 2014, update 2015. International soil classification system for naming soils and creating legends for soil maps. World Soil Resources Reports No. 106. FAO, Rome.

Jardine, P.M., Wilson, G.V., Luxmoore, R.J., 1990. Unsaturated solute transport through a forest soil during rain storm events. Geoderma, 46, 103–118.

Jarvis, N.J., Dubus, I.G., 2006. State-of-the-art review on preferential flow. Report DL#6 of the FP6 EU-funded FOOTPRINT project [www.eu-footprint.org], 60p.

Jury, W.A., Horton, R., 2004. Soil Physics. 6th edition. John Wiley & Sons, Inc., Hoboken, New Jersey, USA.

Kasteel, R., Vogel, H.J., Roth, R., 2002. Effect of non-linear

adsorption on the transport behaviour of Brilliant Blue in a field soil. Eur. J. Soil Sci., 53, 231–240.

Kung, K.-J.S., 1990. Preferential flow in a sandy vadose zone. I. Field observation. Geoderma, 46, 51–58.

Li, Y., Ghodrati, M., 1997. Preferential transport of solute transport through soil columns containing constructed macropores. Soil Sci. Soc. Am. J., 61, 1308–1317.

Mathias, S.A., Butler, A.P., Jackson, B.M., Wheater, H.S., 2006. Transient simulations of flow and transport in the Chalk unsaturated zone. Journal of Hydrology, 330, 10–28.

Mazúr, E., Lukniš, M., 1980. Geomorphologic Units Map 1:500 000. Atlas SSR. SÚGK, Bratislava. (In Slovak.)

Moreira, P.H.S., van Genuchten, M.T., Orlande, H.R.B., Cotta, R.M., 2016. Bayesian estimation of the hydraulic and solute transport properties of a small-scale unsaturated soil column. J. Hydrol. Hydromech., 64, 1, 30–44.

Ohrstrom, P., Persson, M., Albergel, J., Zante, P., Nasri, S., Berndtsson, R., Olsson, J., 2002. Field-scale variation of preferential flow as indicated from dye coverage. Journal of Hydrology, 257, 164–173.

Penman, H.L., 1948. Natural evaporation from open water, bare soil and grass. Proceedings of the Royal Society, A193, 120–146.

Perret, J., Prasher, S.O., Kantzas, A., Langford, C., 1999. Three-dimensional quantification of macropore networks in undisturbed soil cores. Soil Sci. Soc. Am. J., 63, 1530–1543.

Ritsema, C.J., Dekker, L.W., 2000. Preferential flow in water repellent sandy soils: principles and modeling implications. J. Hydrol., 231–232, 308–319.

Shipitalo, M.J., Butt, K.R., 1999. Occupancy and geometrical properties of *Lumbricus terrestris* L. burrows affecting infiltration. Pedobiologia, 43, 782–794.

Šimůnek, J., Jarvis, N.J., van Genuchten, M.T., Gärdenäs, A., 2003. Review comparison of models for describing non-equilibrium and preferential flow and transport in the vadose zone. J. Hydrol., 272, 14–35.

van Genuchten, M.T., 1980. A closed-form equation for predicting the hydraulic conductivity of unsaturated soils. Soil Sci. Soc. Am. J., 44, 892–898.

van Schaik, N.L.B.M., 2009. Spatial variability of infiltration patterns related to site characteristics in a semi-arid watershed. Catena, 78, 1, 36–47.

Vogel, T., Lichner, L., Dusek, J., Cipakova, A., 2007. Dual-continuum analysis of a cadmium tracer field experiment. Journal of Contaminant Hydrology, 92, 50–65.

Weiler, M.H., 2001. Mechanisms controlling macropore flow during infiltration. Dye tracer experiments and simulations. PhD Thesis. ETH Zurich.

Weiler, M., 2005. An infiltration model based on flow variability in macropores: development, sensitivity analysis and applications. J. Hydrol., 310, 294–315.

Weiler, M., Flűhler, H., 2004. Inferring flow types from dye patterns in macroporous soils. Geoderma, 120, 137–153.

Weiler, M., Naef, F., 2003. Simulating surface and subsurface initiation of macropore flow. J. Hydrol., 273, 139–154.

Zehe, E., Flühler, H., 2001. Slope scale variation of flow patterns in soil profiles. Journal of Hydrology, 247, 116–132.

Received 29 September 2017
Accepted 5 April 2018

J. Hydrol. Hydromech., 66, 2018, 4, 381–392
DOI: 10.2478/johh-2018-0031

Factors controlling alterations in the performance of a runoff model in changing climate conditions

Patrik Sleziak[1*], Ján Szolgay[1], Kamila Hlavčová[1], Doris Duethmann[2], Juraj Parajka[2], Michal Danko[3]

[1] Department of Land and Water Resources Management, Slovak University of Technology, Radlinského 11, 810 05, Bratislava, Slovakia.
[2] Institute of Hydraulic Engineering and Water Resources Management, Vienna University of Technology, Karlsplatz 13/222, A-1040, Vienna, Austria.
[3] Institute of Hydrology, Slovak Academy of Sciences, Ondrašovská 17, 031 05 Liptovský Mikuláš, Slovakia.
[*] Corresponding author. E-mail: patrik.sleziak@stuba.sk

Abstract: In many Austrian catchments in recent decades an increase in the mean annual air temperature and precipitation has been observed, but only a small change in the mean annual runoff. The main objective of this paper is (1) to analyze alterations in the performance of a conceptual hydrological model when applied in changing climate conditions and (2) to assess the factors and model parameters that control these changes. A conceptual rainfall-runoff model (the TUW model) was calibrated and validated in 213 Austrian basins from 1981–2010. The changes in the runoff model's efficiency have been compared with changes in the mean annual precipitation and air temperature and stratified for basins with dominant snowmelt and soil moisture processes. The results indicate that while the model's efficiency in the calibration period has not changed over the decades, the values of the model's parameters and hence the model's performance (i.e., the volume error and the runoff model's efficiency) in the validation period have changed. The changes in the model's performance are greater in basins with a dominant soil moisture regime. For these basins, the average volume error which was not used in calibration has increased from 0% (in the calibration periods 1981–1990 or 2001–2010) to 9% (validation period 2001–2010) or –8% (validation period 1981–1990), respectively. In the snow-dominated basins, the model tends to slightly underestimate runoff volumes during its calibration (average volume error = –4%), but the changes in the validation periods are very small (i.e., the changes in the volume error are typically less than 1–2%). The model calibrated in a colder decade (e.g., 1981–1990) tends to overestimate the runoff in a warmer and wetter decade (e.g., 2001–2010), particularly in flatland basins. The opposite case (i.e., the use of parameters calibrated in a warmer decade for a colder, drier decade) indicates a tendency to underestimate runoff. A multidimensional analysis by regression trees showed that the change in the simulated runoff volume is clearly related to the change in precipitation, but the relationship is not linear in flatland basins. The main controlling factor of changes in simulated runoff volumes is the magnitude of the change in precipitation for both groups of basins. For basins with a dominant snowmelt runoff regime, the controlling factors are also the wetness of the basins and the mean annual precipitation. For basins with a soil moisture regime, landcover (forest) plays an important role.

Keywords: Climate change; Efficiency of runoff model; TUW model; Regression trees; Austria.

INTRODUCTION

Conceptual rainfall-runoff (r-r) models are useful tools for a wide range of tasks such as flood forecasting (Nester et al., 2016), reservoir and water management (Farkas et al., 2016), climate studies (Merz et. al., 2011), etc. These models are simplifications of the complex processes of runoff generation in a catchment. Components of these models often have to be described by empirical functions based on observations. The models therefore usually contain a number of parameters that do not directly represent measurable entities and thus must be estimated through the model's calibration in order to adjust the behavior of the model to mimic the behavior of an actual system (Valent and Szolgay, 2012). In their practical use such models may be operated under conditions different from those used for the model's calibration and validation, e.g., when we need to simulate the streamflow caused by extreme meteorological conditions or under a changing climate. It is therefore of interest to evaluate a model's performance in situations when the model has to simulate runoff under conditions dissimilar to those observed during the model's calibration (Seibert, 2003) in order to provide trustworthy runoff simulations when running models under conditions that may be significantly different from those used for their calibration. There are still many unknowns concerning the actual extrapolation capacity of particular hydrological models, which in general may depend on the quality and availability of the inputs, the calibration period of the climate model, the degree of the identifiability (sensitivity) of the model parameters, and other factors (Coron et al., 2011). There is also a growing interest in rainfall-runoff modelling over larger spatial domains in a multi-basin manner in order to explore spatial patterns by methods of comparative hydrology (Pechlivanidis and Arheimer, 2015).

A model's performance, for which the term "model efficiency" will also be used throughout this study, can be quantified by many characteristics, such as the runoff volume error, Nash-Sutcliffe efficiency, peak flow errors, the error in the timing of the peaks, etc. (Beven, 2005). The study of model efficiency is important for various reasons; for example, it is important to know how reliable the streamflow and flood forecasts will be, and it is essential to know what the limits of the model efficiency are.

In this paper, we will focus on two aspects of the robustness of the TUW r-r model: the changing climatic conditions (compared to those of the model's calibration) and diverse physiographic/climatic zones (the multi-basin behavior of the model) on the territory of Austria. Both aspects are intended to shed light on the applicability of the model: the first aspect mainly focuses on climate studies, since the model's performance

should remain good under climatically-different simulation periods at the application stage, when the models are used in a climate change context. The second should complement the knowledge gained from modelling a single catchment, and it also substitutes here for an investigation of the uncertainties of the at-site parameters by a spatial comparative analysis in a large number of catchments. The final aim is to detect links between the model's performance and physiographical characteristics in order to understand the inadequacies and strengths of the model's performance for its future use in Austria (and in similar settings).

It is well documented that the efficiency of many models for a given regional application domain depends on the quality of the data (e.g., Andréassian et al., 2001; Coron et al., 2014; Oudin et al., 2006; Perrin et al., 2008), the length of the calibration period (Brath et al., 2004; Coron et al., 2014; Perrin et al., 2007), and the model's structure (Bai et al., 2015; Das et al., 2008; Fenicia et al., 2011; Merz et al., 2011; Perrin et al., 2001, 2003; Valent and Szolgay, 2012; van Esse et al., 2013; Vaze et al., 2010). In this context, quite a few authors have investigated the relationships between the model's efficiency and the climatic and catchment characteristics (e.g., Brigode et al., 2013; Coron et al., 2012; Fowler et al., 2016; Magand et al., 2015; Merz et al., 2009, 2011; Nester et al., 2011; Osuch et al., 2015; Oudin et al., 2006; Seifert et al., 2012; Seiler et al., 2012; Sleziak et al., 2016a, b; Vaze et al., 2010). Nester et al. (2011) calibrated and validated a semi-distributed hydrological model for a set of 57 catchments in Austria and Germany and analyzed how the model efficiency related to various catchment and climatic characteristics. They found a relation between model efficiency (as evaluated by the Nash-Sutcliffe efficiency NSE) and climate characteristics (such as the mean annual precipitation and runoff) and catchment characteristics (the catchment's size). According to their study, the catchment's size was the most significant control on the model efficiency. This is consistent with previous studies (e.g., Das et al., 2008; Merz et al., 2009; van Esse et al., 2013), which showed that model efficiency is mainly controlled by a catchment's size. Along a similar line Bai et al. (2015) evaluated the efficiency (in terms of the NSE and the water balance error) of 12 hydrological models in relation to different catchment and climatic characteristics. According to their study, the model efficiency was mainly influenced by the aridity index, the variability of the runoff, and the catchment's area. Oudin et al. (2006) used two lumped hydrological models (GEJ4 and TOPMODEL) for a sample of 12 US catchments and evaluated their efficiency (in terms of the NSE and the water balance error). They found that the model efficiency was controlled by climatic indicators (mainly precipitation). Similar results have been reported by Vaze et al. (2010), who calibrated four r-r models (SIMHYD, Sacramento, MARG, IHACRES) for 61 catchments in Australia and evaluated their efficiency. They found that the annual precipitation was the main control on the model efficiency.

Investigations of the efficiency of models during periods with contrasting climates has been a frequent topic of recent scientific literature as demonstrated in a review of common problems linked with using r-r models by Coron et al. (2011). Vaze et al. (2010) found that the model efficiency decreases and the bias increases with differences in the annual precipitation between the calibration and validation periods. This is in agreement with Coron et al. (2012), who assessed the efficiency of three lumped r-r models (GRJ4, MORDOR6, and SIMHYD) in relation to various climatic characteristics. The results from their study showed that the model efficiency was mainly affected by changes in the mean rainfall between the calibration and validation periods. Numerous studies have found that the loss of model efficiency can be related to a difference in precipitation (e.g., Coron et al., 2012; Fowler et al., 2016; Oudin et al., 2006; Vaze et al., 2010). There is also evidence that prolonged dry conditions can lead to a degradation in model efficiency over time (Saft et al., 2015; Saft et al., 2016).

Several authors have observed a decreasing trend in model efficiency when the model parameters were transferred over time (Fowler et al., 2016; Merz et al., 2011; Osuch et al., 2015). For example, Merz et al. (2011) found errors in simulations after transferring parameters between climatically different periods. They also revealed significant correlations between model parameters [snow correction factor (SCF), degree-day factor (DDF), the BETA parameter of runoff generation and field capacity (FC)], and climatic characteristics (mean annual precipitation, mean annual air temperature).

One of the possible approaches for evaluating which climatic and catchment characteristics control a model's performance is to use the technique of regression trees. In recent years, this technique has gained great popularity as has been demonstrated in various modeling studies, e.g., Iorgulescu and Beven (2004), Stauer et al. (2010), Seibert et al. (2016), Kuentz et al. (2016), Poncelet et al. (2017). Poncelet et al. (2017) investigated catchment controls on daily runoff simulations in France, Germany, and Austria. They examined how catchment features (i.e., 29 climate and catchment characteristics) and model efficiency criteria (i.e., the Nash-Sutcliffe efficiency, the Kling-Gupta efficiency on inverse streamflow and the mean and deviation biases) are linked. The results from this study showed that the catchment features that most affect a model's performance were the flashiness of precipitation and streamflow, the seasonality of evaporation, and catchment's aridity. While several of the previous studies analyzed the relationship between the hydrological model efficiency and various climatic and catchment characteristics, in this study we intend to focus on a better quantification of the factors that control change in the hydrological model efficiency over time in the context of a case study by using the TUW r-r model over the whole territory of Austria.

The aim of the paper is to evaluate the temporal changes of the efficiency and the factors controlling these changes. In particular, two aspects of the model efficiency are studied, i.e., the effect of the temporal change of at-site climatic conditions as expressed by a) the mean catchment precipitation b) and the air temperature (compared to those of the model's calibration) in two large groups of catchments representing diverse physiographic/climatic zones (the multi-catchment behavior of the model). The two disjunctive catchment groups are delineated by a study of the sensitive parameters of a model and represent catchments with predominantly snow and rain-fed runoff, respectively. Specifically, we address two scientific questions: (1) What factors (i.e., climatic and catchment characteristics) control the temporal changes in the hydrological model efficiency in both groups? (2) To what extent is it possible to quantify and evaluate these factors? We have used a multidimensional analysis by regression trees to evaluate the factors controlling changes in the hydrological model efficiency. This methodology has been tested for 213 catchments, which provide a representative (e.g., Viglione et al., 2013) sample of the different climatic and physiographic conditions in Austria.

The paper is organized as follows: the hydrological model, the calibration strategy, and the regression tree technique are described in Section 2; the study area and catchment set are presented in Section 3; the results are presented and discussed in Section 4; and an overall discussion and conclusions are given in Section 5.

METHODS

The TUW model

Description of the TUW model

A lumped conceptual r-r model at the basin scale (the TUW model, Viglione and Parajka, 2014) was used for the modeling. This model has also previously been used in various modeling studies across Austria (e.g., Parajka and Blöschl, 2008; Parajka et al., 2007; Sleziak et al., 2016a, b; Viglione et al., 2013) and Europe (Ceola et al., 2015). The TUW model has a structure similar to the Hydrologiska Byråns Vattenbalansavdelning (HBV) model (Bergström, 1995). The model works on a daily time step and requires the following catchment inputs: daily precipitation totals, mean daily air temperature, and daily potential evapotranspiration.

The model has 15 calibration parameters (Table 1), and its structure can be divided into three routines: a snow, soil moisture, and runoff routine (Merz and Blöschl, 2004). The role of the snow routine is the accumulation and melting of snow by a degree-day concept, using degree-day factor (mm/°C day) (DDF) and melt air temperature parameter Tm (°C). The catch deficit of precipitation gauges during snowfall is corrected by a snow correction factor SCF (–). A threshold temperature interval Tr – Ts (°C) is used to distinguish between rainfall, snowfall and mix of rain and snow (e.g., Parajka et al., 2005).

The soil moisture routine represents the runoff generation in a basin. Its role is to simulate the processes taking place in the basin's soil profile. This routine includes parameters such as the BETA (–) parameter of runoff generation, the maximum soil moisture storage (FC) (mm), and the limit for potential evapotranspiration Lprat (–).

The runoff routine is used to transform the outflow from upper and lower reservoirs. This routine contains five parameters: parameters related to surface and subsurface runoff (k0, k1, and k2), the threshold storage state (Lsuz) (mm), the constant percolation rate (Cperc) (mm/day), the maximum base and low flows (Bmax) (day), and the Croute transformation parameter (day^2/mm). More details about the model and its structure are given, e.g., in Parajka et al. (2007).

Table 1. The TUW model parameters including lower and upper bounds. The parameter ranges were taken from the literature (e.g. Merz et al., 2011).

Parameter	Abbreviation, unit	Range
Snow correction factor	SCF (–)	0.9–1.5
Degree-day factor	DDF (mm/°C day)	0–5
Rain threshold temperature	Tr (°C)	1–3
Snow threshold temperature	Ts (°C)	–3–1
Melt temperature	Tm (°C)	–2–2
Limit for potential evapotranspiration	Lprat (day)	0–l
Maximum soil moisture storage	FC (mm)	0–600
Nonlinearity parameter	BETA (–)	0–20
Very fast storage coefficient	k0 (days)	0–2
Fast storage coefficient	k1 (days)	2–30
Slow storage coefficient	k2 (days)	30–250
Upper storage coefficient	LSuz (mm)	1–100
Percolation rate	Cperc (mm/day)	0–8
Maximum base parameter	Bmax (days)	0–30
Free scaling parameter	Croute (day^2/mm)	0–50

Calibration strategy

The TUW model was calibrated for three 10-year periods between 1981–2010. The model's parameters are estimated by automatic calibration using the Deoptim differential evolution algorithm (Ardia et al., 2015). This algorithm has also successfully been used in previous modeling studies (e.g., Sleziak et al., 2016a, b). Deoptim belongs to the class of genetics algorithms which use biology-inspired process such as crossover, mutation, and selection on a population. The principle of this algorithm is based on repeated evaluation of the objective function in order to move the population toward a global minimum. For more detailed information regarding the Deoptim algorithm see, e.g., Ardia et al. (2015).

The parameter ranges used in this study were taken from the literature (see, e.g., Merz et al. 2011; Viglione et al., 2013). A warm-up period of one year is used in the calibrations. The objective function combines the Nash-Sutcliffe efficiency (NSE) (Nash and Sutcliffe, 1970) and the logarithmic Nash-Sutcliffe efficiency (logNSE) (Merz et al., 2011). While the NSE puts a greater emphasis on high flows, the logNSE puts a great emphasis on low flows. Mathematically, these criteria can be expressed as follows:

$$NSE = 1 - \frac{\sum_{i=1}^{n}\left(Q_{sim,i} - Q_{obs,i}\right)^2}{\sum_{i=1}^{n}\left(Q_{obs,i} - \overline{Q}_{obs}\right)^2} \quad (1)$$

$$\log NSE = 1 - \frac{\sum_{i=1}^{n}\left(\log(Q_{sim,i}) - \log(Q_{obs,i})\right)^2}{\sum_{i=1}^{n}\left(\log(Q_{obs,i}) - \log(\overline{Q}_{obs})\right)^2} \quad (2)$$

where $Q_{sim,i}$ and $Q_{obs,i}$ represent the simulated and observed mean daily flows on day i, and $\overline{Q}_{obs}$ is the average of the flows observed. The NSE and logNSE coefficients range between $-\infty$ and 1 (NSE = 1 indicates a perfect simulation, i.e., an absolute agreement between the observed and simulated flows). The combination of NSE and logNSE in the objective function (*OF*) is defined as:

$$OF = \frac{1 - NSE}{2} + \frac{1 - \log NSE}{2} \quad (3)$$

The given objective function (Eq. 3) is minimized by the differential evolution algorithm Deoptim (see above).

Performance assessment

In this study, the Differential Split-Sample Test (DSST, Klemeš, 1986) has been adopted to evaluate the ability of the TUW model to simulate runoff under conditions different from those used for the model's calibration. The DSST allows us to evaluate the model's efficiency (performance) in contrasting climatic periods (i.e., in cooler and warmer periods or wetter and drier periods). Some applications of DSST can also be found in, e.g., Seibert (2003), Wilby (2005), Chiew et al. (2009), Vaze et al. (2010), Merz et al. (2011), Brigode et al. (2013), Bai et al. (2015), Sleziak et al. (2016a, b).

The quality of the model simulations is quantified by the Nash-Sutcliffe efficiency (NSE, Eq. 1) and the volume error (VE) (e.g., Merz et al., 2011). The VE is not used in calibration, this metric is used only for the assessment of the model performance. The value VE = 0 means that the simulated mean runoff equals the observed one (i.e., no bias). The values VE < 0 and

VE > 0 denote underestimations and overestimations of the flows.

Multi-dimensional analysis

In this study we applied a multi-dimensional approach using regression trees to identify factors that control changes in volume error between the calibration and validation periods. Here we chose VE values as representative for the comparison because they can be directly comparable between periods and catchments (e.g., Coron et al., 2012). A regression tree is an analytical and visualization method which, via tree-building algorithms, provides information about interactions between various characteristics (i.e., between the variables and the model's features). Based on this technique we can determine the importance of the explanatory variables and also find some common patterns. The principle of this technique is based on the binary splitting of a dataset according to features (i.e., decision variables), which are automatically selected by the algorithm. By implementing the rpart package (Therneau et al., 2017), it is possible to apply one of these algorithms (CART, Breiman et al., 1984) in the R software environment (R Development Core Team, 2011). In general, the CART algorithm creates two main clusters which are further divided into subsets. In order to simplify the structure of the trees we set the minimum number of basins in each final cluster (leaf) to 25. These smaller trees are better suited for capturing general patterns and this way we avoid very complex trees that are difficult to interpret. For more detailed information about regression trees, see, e.g., Kuentz et al. (2016) and Poncelet et al. (2017).

We apply regression trees to identify factors that control changes in bias when a model's parameters are transferred from the calibration to the validation period. As explanatory factors we use (1) climatic characteristics, such as the mean annual precipitation (P), the mean annual air temperature (T), the relative change in mean annual precipitation (Pdif), and the absolute change in mean annual air temperature (Tdif) and, (2) catchment characteristics such as the area, elevation, slope, percentage of forest cover, and aridity (defined as the ratio of the mean annual potential evapotranspiration to the mean annual precipitation).

STUDY REGION AND DATA

Austria was selected as the study region. This region was selected as the test bed region due to (a) the variability of the climate (i.e., an increase in precipitation and air temperatures over recent decades has been observed, Merz et al. 2011), (b) diverse physiographic conditions (i.e., different catchment areas, elevations, geology, etc., Gaál, et al. 2012), (c) the availability of inputs (i.e., precipitation, air temperatures, potential evapotranspiration and streamflow), and the suitability of inputs (i.e., quality of the data) for modeling experiments (e.g., Viglione et al., 2013).

We used a representative sample of 213 catchments in Austria, which represent a large variety of climatic and physiographic conditions of Central Europe. The catchment areas range from 14 to 6200 km^2; mean elevation range from 295 to 2915 m a.s.l. Annual precipitation varies from 400 to 3000 mm/year and mean annual air temperature from –8 to 10°C.

We used daily hydrometeorological catchment data (i.e., the daily precipitation totals, mean daily air temperature, mean daily streamflow, and daily potential evapotranspiration) from the period 1981–2010. These data have also been extensively used in previous modeling studies, e.g., Viglione et al. (2013), Sleziak et al. (2016a, b). Before processing the data, quality flags, missing data, etc., were visually inspected. The precipitation data came from 1091 rainfall gauges. These measurements were used to interpolate the catchments' mean areal precipitation using the external drift kriging method (see Merz et al., 2011). The air temperature data came from 212 climatic stations. The catchments' mean air temperatures were calculated using the least squares trend prediction method (Pebesma, 2001). The mean daily runoff data from 213 gauged catchments were provided by the Austrian Hydrographic Service (HZB). These data were used to calibrate and validate the TUW model. The daily potential evapotranspiration was calculated by a modified Blaney-Criddle method (Parajka et al., 2005). More details about the data (e.g., the methods used to interpolate the data) can be found, e.g., in Merz et al. (2011) and Viglione et al. (2013).

Classification of the basins based on a sensitivity analysis

The selected Austrian basins (213) were classified into two groups using a sensitivity analysis of the TUW model's parameters. This analysis was carried out using a combination of the Latin Hypercube (LH) and one-factor-at-a-time sampling (van Griensven et al., 2006), which allowed us to identify patterns of parameter dominance. The sensitivity analysis is used to detect the most relevant model parameters in relation to the objective functions selected (see calibration strategy, above). The LH subdivides the range of each parameter into N segments, each with a probability of occurrence equal to 1/N. Random values for each parameter are generated such that each of the segments are sampled one time. A detailed description of this method is presented in van Griensven et al., 2006.

In our case, the sensitivity of the model parameters was tested in three specific periods (i.e., 1981–1990, 1991–2000, and 2001–2010). This is documented in Table 2, which gives information about the occurrence of the most sensitive model parameters in these periods. For example, we can see that the degree-day melt parameter (DDF) was 87 times the most sensitive in 1981–1990, 65 times in 1991–2000, and 75 times in 2001–2010 (the value of 0 in the table means that the given parameter did not appear to be the most sensitive in a particular period). With this analysis we identified four model parameters

Table 2. Frequencies of the most sensitive model parameters in three specified calibration periods (1981–1990, 1991–2000, 2001–2010).

Parameter	1981–1990	1991–2000	2001–2010
SCF (–)	0	0	0
DDF (mm/°C day)	87	65	75
Tr (°C)	0	0	0
Ts (°C)	0	0	0
Tm (°C)	0	0	0
Lprat (day)	0	0	0
FC (mm)	91	127	130
BETA (–)	9	2	0
k0 (days)	0	0	0
k1 (days)	0	0	0
k2 (days)	0	0	0
LSuz (mm)	0	0	0
Cperc (mm/day)	20	19	8
Bmax (days)	0	0	0
Croute (day^2/mm)	0	0	0

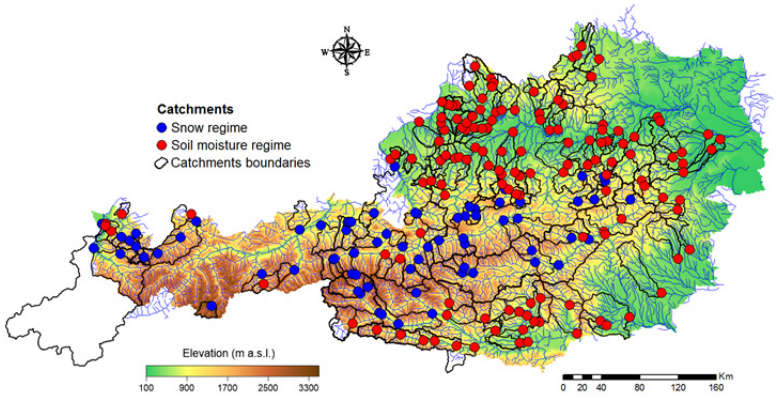

Fig. 1. Map of Austria with the selected catchments (213). The blue circles indicate catchments with a dominant snow regime (71 catchments), and the red circles are catchments with a dominant soil moisture regime (142 catchments). Both groups of catchments were delineated by a model parameter sensitive study.

which have a close relationship with the objective function selected. These results are also presented in Fig. 1 where we can identify two distinct regions showing different sensitivities to the model parameters. In alpine (mountainous) regions, the most sensitive parameters are related to the accumulation and melting of snow (degree-day melt parameter (DDF)). On the contrary, the most sensitive in the flatlands are the parameters related to the soil (maximum soil field capacity (FC), the BETA parameter related to runoff generation, and the percolation rate (Cperc)). These groups were also compared in terms of the hydrological regime. Using this comparison, we classified the 213 Austrian catchments into two main groups of snow (71 catchments, where the DDF was the most sensitive parameter) and soil moisture regimes (142 catchments, where FC, BETA or Cperc was the most sensitive parameter). Table 3 summarizes the main characteristics of these two groups of basins.

Table 3. Basic statistical values (i.e., minimum, median, maximum and mean) computed for the selected characteristics of two group of basins, i.e., basins with a) dominant snow and b) soil moisture regimes.

Area (km^2)	**Min**	**Median**	**Max**	**Mean**
Basins with a snow regime	14.2	150.8	6120	594.8
Basins with a soil moisture regime	13.7	178.2	6214	319.0
Mean elevation (m a.s.l.)	**Min**	**Median**	**Max**	**Mean**
Basins with a snow regime	984	1551	2915	1636
Basins with a soil moisture regime	295	702	1924	795
Forest cover (%)	**Min**	**Median**	**Max**	**Mean**
Basins with a snow regime	2.1	40.3	86.8	43.8
Basins with a soil moisture regime	9	56	98	55.6
Slope (%)	**Min**	**Median**	**Max**	**Mean**
Basins with a snow regime	19.9	38.9	54.2	38.8
Basins with a soil moisture regime	2.6	16.1	47.8	19.3

For a better understanding of the variability between the two different groups of catchments (i.e., catchments with snow and catchments with a soil moisture regime) and also for a better interpretation of the temporal changes in the model parameters, we plotted the changes in the climatic characteristics over three decades for both groups separately (Fig. 2). Figure 2 shows that catchments with a snow-dominant regime are characterized by higher precipitation and lower air temperatures. While the median values of the mean annual precipitation (P) increased from 1032 to 1095 mm/year in catchments with a dominant soil moisture regime, catchments with a dominant snow regime have fairly stable median values (between 1460 and 1455 mm/year). Also, the medians of the mean annual air temperatures (T) show an increasing trend over three decades. The median values of the mean annual air temperatures increased on average by 0.7°C and 0.4°C in catchments with snow and soil moisture regimes, respectively. Interestingly, the medians of the mean annual runoff (Q) practically did not change over three decades.

Based on this analysis, it would be interesting to examine how these changes in climatic characteristics can be linked to changes in the model parameters.

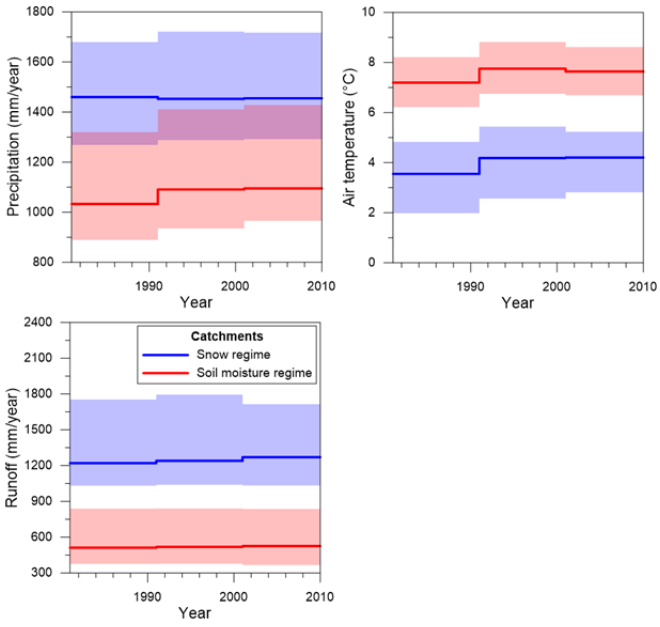

Fig. 2. Changes in the hydroclimatic characteristics (mean annual precipitation, air temperature and runoff) over three decades. The blue line indicates medians for catchments with a snow regime (71 catchments), and the red line shows medians for the catchments with a soil moisture regime (142 catchments). The shaded area represents 75% and 25% percentiles between the catchments.

RESULTS AND DISCUSSION

Assessment of the model's efficiency in different climatic periods

In this section we assess the model's efficiency over different climatic periods (i.e., colder/warmer or drier/wetter periods) for the two groups of catchments. In this study, the period 1981–1990 is considered as colder/drier and the period 2001–2010 as wetter/warmer (see section above).

In the snow-dominated catchments, the mean NSE values during the calibration period were between 0.73 and 0.74 and varied only slightly over the decades (Fig. 3), which means that the model could be calibrated equally well in each period. The average volume errors of –0.02 to –0.07 indicate a tendency to underestimate the simulated runoff volume in the calibration as well as the validation periods.

In the catchments with a dominant soil moisture regime, the median NSE values during the calibration period were between 0.7 and 0.73 for the three calibration periods (Fig. 4), thereby showing a slightly lower model performance in comparison with the snow-dominated catchments. The decrease in the model performance from the calibration to the validation periods is greatest between the calibration from 2001–2010 and the validation from 1981–1990. The assessment of the VE efficiency indicates that the model's calibration is essentially unbiased (the median VE equals 0). Interestingly, the model tends to overestimate flows in warmer validation periods, but underestimates flows in colder and drier decades.

The comparison of the runoff model efficiencies in the two groups of catchments indicates larger NSE efficiencies in catchments with a dominant snow regime for both the calibration and validation periods.

In this context, Schaefli and Gupta (2007) pointed out the correct interpretation of the NSE values. The benchmark model when using NSE is the mean observed flow. In strongly seasonal regimes (like snow-dominated regimes with low flows during winter and high flows during the melting period), a model that can capture the general seasonal regime already achieves a good NSE and therefore often higher NSE values are obtained in snow dominated catchments.

Similar to our study, the Viviroli et al. (2009) focused on calibration of large number of catchments (i.e., 140 catchments in Switzerland) between different calibration periods. They calibrated the distributed r-r model PREVAH (Precipitation-Runoff-EVApotranspiration-HRU model) in hourly time step between 1984–2003. They proposed a robust calibration strategy that combines traditional calibration approach (multiple measures of goodness-of-fit) and a fuzzy approach (used for modeling high flows). They observed a decreasing trend in model performance after transferring parameters between contrasted calibration periods. For example, for 49 representative basins (i.e., with a long record of observations) the median of NSE decreased from 0.75 (calibration period) to 0.72 (validation period). For high flows slightly poorer values of NSE were obtained (i.e., 0.69 in calibration and 0.67 in validation).

Merz et al. (2011) found errors in simulations (overestimation of Q_{95} by about 12%, overestimation of Q_{50} by about 15%, and overestimation of Q_{05} by about 35%) when the model parameters were transferred over time.

Our findings also indicate that in snow-dominated catchments the model tends to systematically underestimate the volume of the flows. On the contrary, in catchments with a soil moisture regime, the model simulates flow volume closer to the observation in the calibration periods, but overestimates flows when the model parameters are transferred from colder/drier to wetter/warmer decades (i.e., from 1981 – 1990 to 2001-2010) . These results contrast with previous findings, e.g., Vaze et al. (2010) or Coron et al. (2012), who observed a tendency to overestimate mean runoff when the calibration period was wetter (i.e., a wet to dry parameter transfer). This can be related to the different regions (i.e., Austria vs Australia) and physiographic conditions studied.

Generally, for hydrological simulations under varying conditions, physically based distributed models are usually preferred over conceptual r-r models (like TUW), because of their process foundation they are valid for conditions outside the calibration period and also allow a better description of spatial heterogeneity (e.g., Finger et al., 2012). However, they require more input data, which is often not available, and have more parameters. Furthermore, the higher complexity of these models demands a longer computation time (Sun, et al., 2017). While conceptual models like HBV have minimal data requirements, require minimal computing time, they may not be well suited under changing conditions.

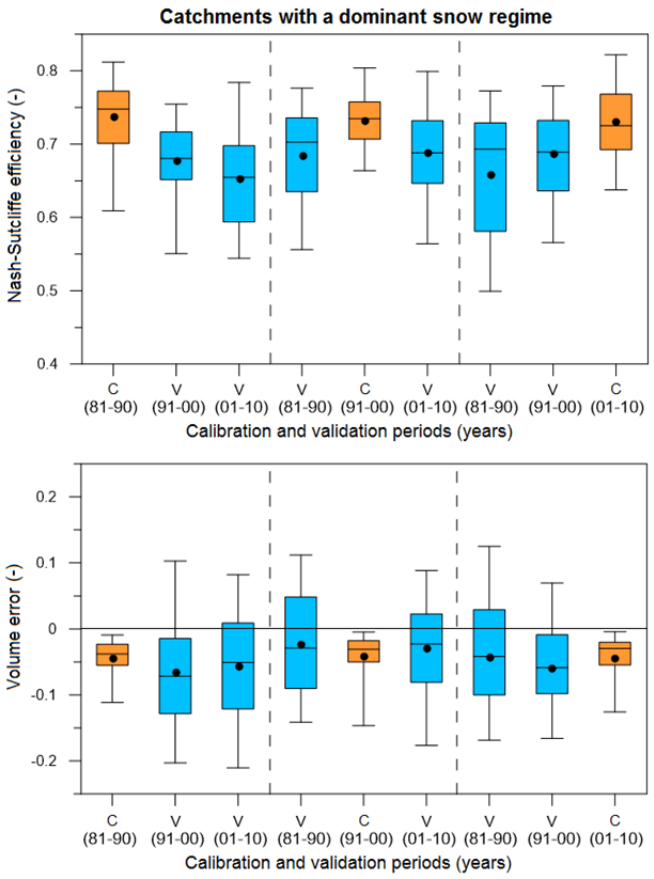

Fig. 3. Comparison of the variability of the Nash-Sutcliffe efficiency (NSE) and the volume error (VE) in the specified calibration and validation periods for catchments with a dominant snow regime. The horizontal line of box plots shows the median of the values, and the upper and lower whiskers show the 95 and 5 percentile values. The horizontal line inside the bottom graph shows a zero volume error. The orange box plots represent the calibration periods. The blue box plots represent the validation periods. The line inside the boxes shows the median of the NSE and VE. The black circles are the mean values of the NSE and VE. C are calibration periods and V are validation periods.

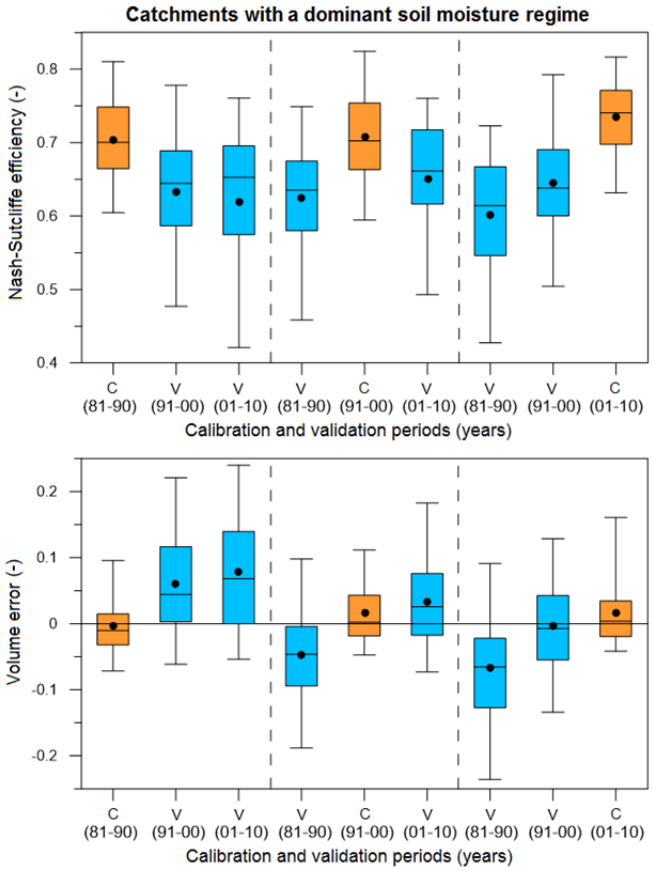

Fig. 4. Comparison of the variability of the Nash-Sutcliffe efficiency (NSE) and the volume error (VE) in the specified calibration and validation periods for catchments with a dominant soil moisture regime. The horizontal line of the box plots shows the median of the values, and the upper and lower whiskers show the 95 and 5 percentile values. The horizontal line inside the bottom graph shows a zero volume error. The orange box plots represent the calibration periods. The blue box plots represent the validation periods. The line inside the boxes shows the median of the NSE and VE. The black circles are the mean values of the NSE and VE. C are calibration periods, V are validation periods.

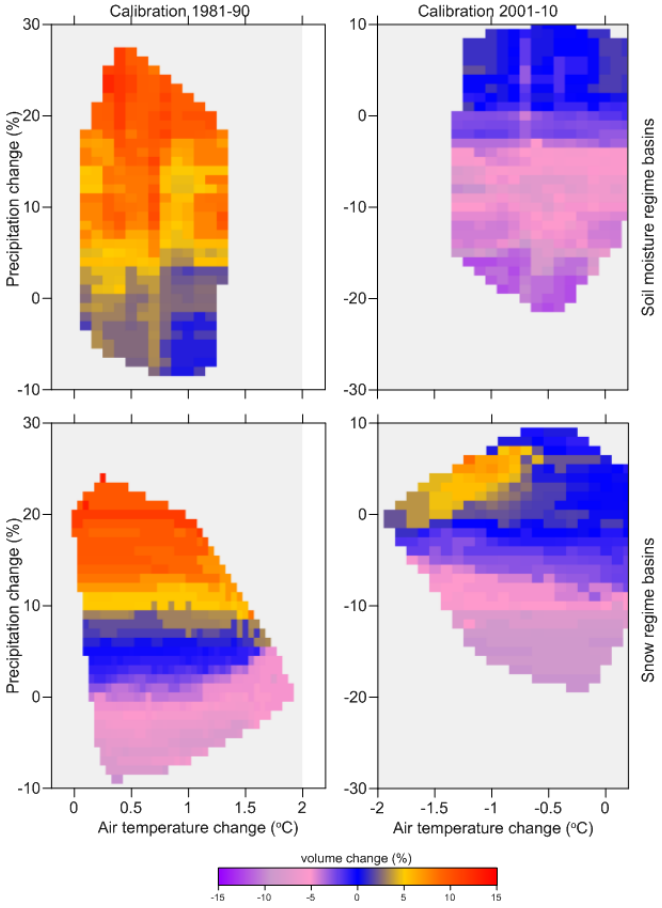

Fig. 5. Changes in the simulated runoff volume error when transferring model parameters calibrated in 1981–1990 (left panels) or 2001–2010 (right panels) to the remaining two decades. The changes in air temperature and precipitation indicate differences with respect to the calibration period. The change is estimated for basins with dominant snowmelt (bottom panels) and soil moisture (top panels) regimes.

The relationship between changes in the climatic characteristics and changes in the volume errors

Figure 5 shows changes in the simulated runoff volume errors between the calibration and the two validation periods as a function of changes in the mean annual precipitation and air temperature between those time periods. Thus, each catchment results in two data points. The data points were interpolated to obtain a smooth response surface. While the left panels in Figure 5 show the changes from a colder/drier calibration decade (i.e., 1981–1990) to warmer/wetter validation periods, the right panels show the changes from a warmer/wetter calibration period (i.e., 2001–2010) to colder/drier validation periods. The top and bottom panels show the changes in the snow and soil moisture-dominated catchments, respectively. The results indicate that transferring parameters to a colder/drier or warmer/wetter decade leads to runoff underestimation or overestimation, respectively. This trend is more pronounced in the catchments dominated by soil moisture processes. It can be seen that changes in simulated runoff volume are mainly related to changes in precipitation, but that this relationship tends not to be linear. An increase in mean annual precipitation of 10–20% leads to an increase in volume error of 5–15%. In contrast, when the change in precipitation is in a range of 0 to –20% and the air temperature decreases, the change in runoff volume errors is in a range of –5% to –10%. These results are in general agreement with the findings presented, e.g., by Oudin et al. (2006), Vaze et al. (2010), and Coron et al. (2012), who showed the significant effect of changing precipitation on a runoff model's efficiency. For example, Coron et al. (2012) compared the model efficiency of three commonly used lumped r-r models (GRJ4, MORDOR6, and SIMHYD) in relation to selected climatic characteristics (i.e., mean annual precipitation, air temperature). The results of their study indicated a 20% bias in total volumes when the mean rainfall differed by 10–20% between the calibration and validation periods. This study was performed in 216 catchments in southeast Australia. Along similar lines, Vaze et al. (2010) reported that simulations of runoff are acceptable when changes in precipitation are no more than 15% less or 20% greater than the precipitation during the calibration period.

Changes in the model parameters in different climatic periods

The changes in the selected model parameters (i.e., the degree-day melt parameter (DDF), the BETA parameter of runoff generation, the maximum soil moisture storage (FC), and the percolation rate (Cperc)) over three different decades are shown in Fig. 6. The selection of these parameters is based on the

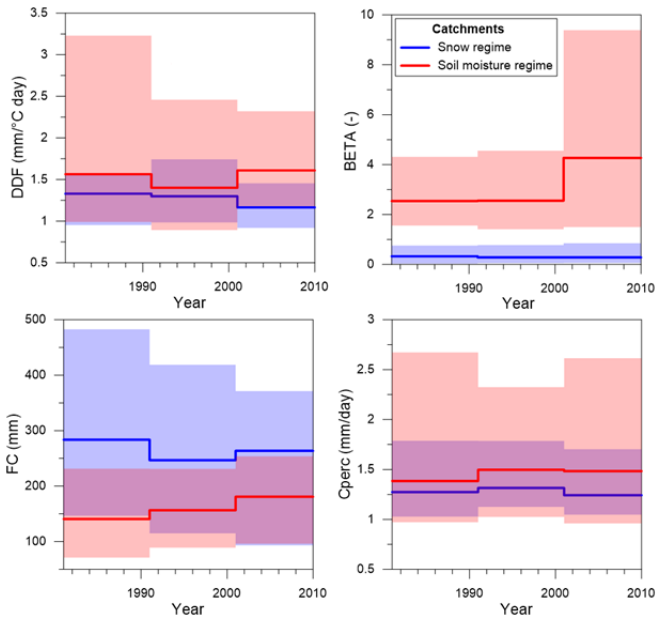

Fig. 6. Changes in the model parameters (the degree-day factor (DDF), the BETA parameter of runoff generation, the maximum soil moisture storage (FC) and the percolation rate (CPERC)) in three different climatic periods (1981–1990, 1991–2000, 2001–2010). The blue line indicates medians for the catchments with a snow regime (71 catchments), and the red line shows medians for catchments with a soil moisture regime (142 catchments). The shaded area represents 75% and 25% percentiles between the catchments.

results of the sensitivity analysis (see Section data, above). The changes in the parameters are described by selected percentiles (i.e., 25%, 50%, and 75%). The degree-day melt parameter (DDF) is one of the most sensitive parameters in catchments with a dominant snow regime. The results indicate that DDF tends to decrease in warmer/wetter decades. Such changes are likely to be associated with changes in snow melting in the spring, which tend to be greater in colder years (1981–1990) (see Merz et al., 2011). The DDF values in catchments with a soil moisture regime have a much larger scatter, but the median values are more stable over the decades. The BETA nonlinear runoff generation parameter and field capacity (FC) are the most sensitive parameters in catchments with a soil moisture regime. Both tended to increase over the decades analyzed (Fig. 6). This increase is likely associated with increasing evapotranspiration, mainly in flatland catchments. As was pointed out by Merz et al. (2011), an increasing trend in the BETA parameter is also connected with a more non-linear runoff generation in the last decade analyzed. The median values of FC in basins with a snow regime show a decreasing trend over decades; however, the scatter is large. Interestingly, the values of FC are higher in snow-dominated basins, which are largely in the mountainous region where one would expect shallow soils (generally, the small FC values imply shallow hydrologically active soil depths and vice versa, Merz et al., 2011). This is possibly due to (a) cross-correlation between the parameters BETA and FC, i.e., when FC is high, then BETA is small, (b) heterogeneous conditions (i.e., alpine vegetation, forests, bareland covers a substantial portion of the catchments areas, e.g., Merz and Blöschl, 2004). The findings also show that the median maximal available FC increased from 95 mm to approximately 150 mm within 20 years (Fig. 6). This can be related to increasing trend in air temperature (FC may vary in response to the variability of climatic conditions) between periods (see Fig. 2). The change in FC does not necessarily mean that the storage capacity of the soils has changed but can also be a sign of a compensation effect for the rather low potential evaporation (Nijzink et al., 2016). In this context, Wang-Erlandsson et al. (2016) pointed out that the root storage zone capacity (which determines the maximum soil moisture) is critical for correctly simulating surface runoff. Authors in their study present a method to estimate root zone storage capacity from satellite-based evaporation and observation-based precipitation data. The results showed that the method eliminated the need for poor resolution soil and rooting depth data and therefore can be useful for the modelling community.

The percolation rate (Cperc) is only sensitive in a few catchments, and the median values did not change much in both groups of catchments. Merz et al. (2011) found that changes in model parameters are related to changes in climate variables, such as increases in air temperature and potential evapotranspiration. Here, we show that the changes in model parameters are further related to whether the catchment belongs to a snow or soil processes-dominated group (i.e., different climatic conditions – catchments in mountainous part of regions vs. catchments in flatlands, see section Study region and data). In comparison to our study, Merz et al. (2011) analyzed changes in model parameters calibrated by a semidistributed version of the TUW model in different 5-year periods. Our results for DDF, the most sensitive snow model parameter, and the BETA nonlinear runoff generation parameter show similar trends in changes over time, but the tendency is different for the field capacity (FC) model parameter. While Merz et al. (2011) presented a clear increase in FC during 5-year calibration periods, our results indicate an increasing trend only in flatland catchments. The difference between the results is likely caused by the different spatial distribution of the model inputs and differences in the length of the calibration periods.

Factors controlling changes in runoff volume

In this section, we use regression trees to investigate which climatic and catchment characteristics controlled the differences in the simulated runoff volume error (VEdif) in two different decades.

The regression trees are identified separately for the two groups of catchments, and the results are presented in Figs. 7 and 8. Figure 7 shows a case of changing simulated flow volume (VEdif), when the model is calibrated in a colder/drier decade and applied (validated) in a warmer/wetter time decade. In both groups of catchments, the main controlling factor of the VEdif is the magnitude of the precipitation change (Pdif). In the snow-dominated catchments, an increase in the annual precipitation greater than 2.3% results in an average increase in the simulated runoff volume of 5%. In contrast, a decrease in the mean annual precipitation, particularly in catchments with a mean annual precipitation lower than 1834 mm and a size less than 124 km^2, results in an average 12% decrease in the simulated flow volume. In catchments with a dominant soil moisture regime (Fig. 7, right panels), a change in mean annual precipitation also affects the degree by which the simulated runoff volumes increase. In almost all the catchments the application of the model parameters from a colder/drier period to a warmer/wetter period leads to increased simulated runoff volumes. The largest increase was observed in catchments where the mean annual precipitation increased by at least 3.7% and the forest cover was greater than 45%.

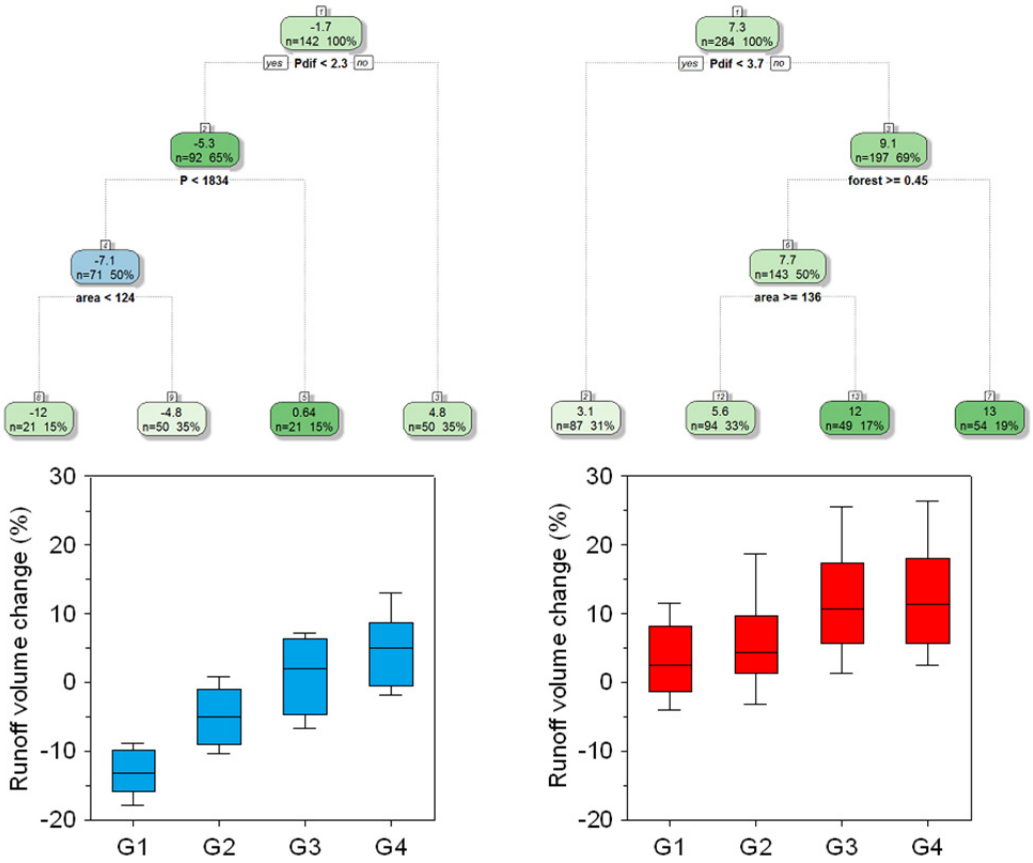

Fig. 7. Factors describing changes in runoff volume when simulating runoff in warmer and wetter decades (1991–2000 and 2001–2010) by using model parameters calibrated in a colder and drier period (1981–1990). The left side shows basins with a snow regime; the right side shows basins with a soil moisture regime. G1–G4 represent the final clusters (leaves) of the resulting trees.

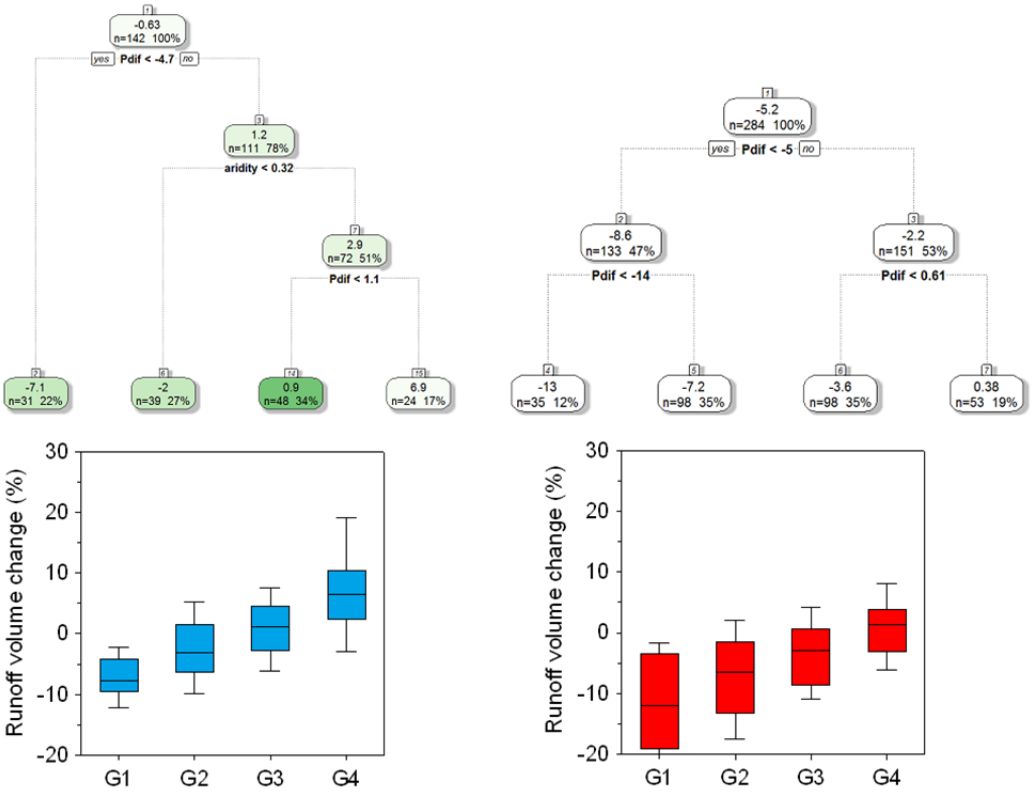

Fig. 8. Factors describing changes in runoff volume when simulating runoff in colder and drier decades (1981–1990 and 1991–2000) by using model parameters calibrated in a warmer and wetter period (2001–2010). The left side shows basins with a snow regime; the right side shows basins with soil moisture regime. G1–G4 represent the final clusters (leaves) of the resulting trees.

Fig. 8 shows the factors influencing the simulated runoff volume when applying model parameters calibrated in a warmer/wetter (2001–2010) decade and applied to colder/drier decade. The changes in the simulated runoff volume in different climate conditions are again mostly determined by changes in the mean annual precipitation (Pdif). The Pdif is the only differentiating factor in catchments with a dominant soil moisture regime (Fig. 8, right panels). Interestingly, in the snow-dominated catchments the second most influential factor is the aridity of the catchment. For drier catchments (aridity < 0.32) or catchments with a small Pdif, the difference in the changes in the simulated volume is the smallest (a range of –2% to 1%).

The results are in agreement with previous analyses (e.g., Coron et al., 2012; Oudin et al., 2006; Vaze et al., 2010), which showed that changes in model efficiency are mainly affected by changes in the mean annual precipitation. These results also correspond with the greatest correlations (not presented here) between the magnitude of changes in precipitation and changes in runoff volume. The size of the catchments and amount of aridity, which were determined to be important factors in previous studies (Nester et al., 2011; Poncelet et al., 2017), are only influential for smaller and snow-dominated catchments, respectively. In flatland catchments, (landcover) forest also has some impact on changes in the bias of simulated runoff volumes.

CONCLUSIONS

Hydrological models are simplified mathematical representations of complex rainfall-runoff processes. These models can be considered useful tools for the diagnosis of the impacts of climate change on water resources. The use of these models under conditions that may be significantly different to those used for their development still remains a challenging task.

In this study, we have evaluated the impact of changing climate conditions with differential split-sample testing. We found that changes in simulated runoff volume are clearly related to changes in precipitation, but the relationship is not always linear, particularly in flatland catchments. Our results indicate that a trustworthy simulation can be achieved if a change in mean precipitation is no more than ±10%.

The analysis of temporal changes in model parameters over three different decades showed that the parameters controlling snow processes (i.e., snow correction factor SCF and degree-day factor DDF), and soil moisture processes (i.e., parameter of runoff generation BETA and maximum soil moisture storage FC) have changed over time.

The evaluation of factors which control changes in simulated runoff volumes showed that the most influential factor is a change in mean annual precipitation. Additionally, the aridity or wetness of the catchments had some influence on catchments with a dominant snowmelt runoff regime.

From the results of our study we conclude that it is indeed important to re-calibrate conceptual r-r models (e.g., the HBV type and its derivatives) if the climatic conditions change. For practical applications of hydrological models, it would be suitable to consider various calibration periods and change the model parameters, depending on the hydroclimatic regime. The findings also revealed a need for regionalization of the methodology and a need to verify it in different climatic and physiographic conditions. More analysis needs to be done in the future, for example to apply similar testing approaches to different regions, to use HVB vs. physically based models, etc.

Acknowledgements. This work was supported by the Slovak Research and Development Agency under Contract Nos. APVV-15-0497 and APVV-15-0425; and VEGA 1/0710/15. We would like to thank the Austria Science Foundation (as part of the Vienna Doctoral Programme on Water Resource Systems (DK-plus W1219-N22) and the European Research Council under the ERC Advanced Grant “Flood Change”, Project No. 291152. We gratefully acknowledge support from the German Research Foundation (DFG) through a research scholarship to D.D. At the same time, we would also like to acknowledge the financial support from the National Scholarship Programme of the Slovak Republic. The contribution is also the result of the project implementation ITMS 26240120004 Centre of excellence for integrated flood protection of land supported by the Research & Development Operational Program funded by the ERDF. The authors are grateful to Peter Molnar and also two anonymous reviewers whose valuable comments and constructive suggestions helped improve and clarify the paper.

REFERENCES

Andréassian, V., Perrin, C., Michel, C., Usart-Sanchez, I., Lavarbe, J., 2001. Impact of imperfect knowledge on the efficiency and the parameters of watershed models. Journal of Hydrology, 205, 1–4, 206–223. http://dx.doi.org/10.1016/S0022-1694(01)00437-1.

Ardia, D., Mullen, K.M., Peterson, B.G., Ulrich, J., 2015. DEoptim: Diferential evolution in R. Version 2.2-3.

Bai, P., Liu, X., Liang, K., Liu, C., 2015. Comparison of performance of twelve monthly water balance models in different climatic catchments of China. Journal of Hydrology, 529, 1030–1040. DOI: 10.1016/j.jhydrol.2015.09.015.

Bergström, S., 1995. The HBV model. In: Sing, V.P. (Ed.): Computers Models of Watershed Hydrology. Water. Resour. Publ., pp. 443–476.

Beven, K.J., 2005. Rainfall-runoff modelling: Introduction. In: Anderson, M.G. (Ed): Encyclopedia of Hydrological Sciences, Wiley, Chichester, pp. 1857–1868.

Brath, A., Montanari, A., Toth, E., 2004. Analysis of the effects of different scenarios of historical data availability on the calibration of a spatially-distributed hydrological model. Journal of Hydrology, 291, 3–4, 232–253. http://dx.doi.org/10.1016/j.jhydrol.2003.12.044.

Breiman, L., Friedman, J., Stone, C.J., Olshen, R.A., 1984. Classification and Regression Trees. The Wadsworth and Brooks-Cole Statistics-Probability Series. Taylor & Francis, 368 p. ISBN: 0412048418, 9780412048418.

Brigode, P., Oudin, L., Perrin, C., 2013. Hydrological model parameter instability: A source of additional uncertainty in estimating the hydrological impacts of climate change? Journal of Hydrology, 476, 410–425. http://dx.doi.org/10.1016/j.jhydrol.2012.11.012.

Ceola, S., Arheimer, B., Baratti, E., Blöschl, G., Capell, R., Castellarin, A., Freer, J., Han, D., Hrachowitz, M., Hundecha, Y., Hutton, C., Lindström, G., Montanari, A., Nijzink, R., Parajka, J., Toth, E., Viglione, A., and Wagener, T., 2015. Virtual laboratories: new opportunities for collaborative water science. Hydrol. Earth Syst. Sci., 19, 2101–2117. DOI: 10.5194/hess-19- 2101-2015.

Chiew, F.H.S., Teng, J., Vaze, J., Post, D.A., Perraud, J.M., Kirono, D.G.C., Viney, N.R., 2009. Estimating climate change impact on runoff across southeast Australia: Method, results, and implications of the modeling method, Water Resour. Res., 45, W10414. DOI: 10.1029/2008WR007338.

Coron, L., Andréassian, V., Bourqui, M., Perrin, C., Hendrickx, F., 2011. Pathologies of hydrological model used in changing climatic conditions: a review. Hydro-climatology: Vari-

ability and change. In: Proceedings of IUGG2011 symposium J-H02, Melbourne, Australia.

Coron, L., Andréassian, V., Perrin, C., Lerat, J., Vaze, J., Bourqui, M., Hendrickx, F., 2012. Crash testing hydrological models in contrasted climate conditions: An experiment on 216 Australian catchments. Water Resour. Res., 48, W05552. DOI: 10.1029/ 2011WR011721.

Coron, L., Andréassan, V., Perrin, C., Bourqui, M., Hendrickx, F., 2014. On the lack of robustness of hydrologic models regarding water balance simulation: a diagnostic approach applied to three models of increasing complexity on 20 mountainous catchments. Hydrol. Earth Syst. Sci., 18, 727–746. DOI: 10.5194/hess-18-727-2014.

Das, T., Bárdossy, A., Zehe, E., He, Y., 2008. Comparison of conceptual model performance using different representations of spatial variability. J. Hydrol., 356, 106–118.

Farkas, C., Kværnø, S.H., Engebretsen, A., Barneveld, R., Deelstra, J., 2016. Applying profile and catchment-based mathematical models for evaluating the run-off from a Nordic catchment. J. Hydrol. Hydromech., 64, 3, 218–225. DOI: 10.1515/johh-2016-0022.

Fenicia, F., Kavetski, D., Savenije, H.H.G., 2011. Elements of a flexible approach for conceptual hydrological modeling: 1. Motivation and theoretical development. Water Resour. Res., 47, W11510. DOI: 10.1029/2010wr010174.

Finger, D., Heinrich, G., Gobiet, A., Bauder, A., 2012. Projections of future water resources and their uncertainty in a glacierized catchment in the Swiss Alps and the subsequent effects on hydropower production during the 21st century. Water Resour. Res., 48, 02521. DOI: 10.1029/2011WR010733, 2012.

Fowler, K.J.A., Peel, M.C., Western, A.W., Zhang, L., Peterson, T.J., 2016. Simulating runoff under changing climate conditions: Revising an apparent deficiency of conceptual rainfall-runoff models. Water. Resour. Res., 52, 1820–1846. DOI: 10.1002/2015WR018068.

Gaál, L., Szolgay, J., Kohnová, S., Parajka, J., Merz, R., Viglione, A., Blöschl, G., 2012. Flood timescales: Understanding the interplay of climate and catchment processes through comparative hydrology. Water Resour. Res., 48, W04511. DOI: 10.1029/ 2011WR011509.

Iorgulescu, I., Beven, K.J., 2004. Nonparametric direct mapping of rainfall-runoff relationships: An alternative approach to data analysis and modeling? Water Resour. Res., 40, W08403. DOI: 10.1029/2004WR003094.

Klemeš, V., 1986. Dilettantism in hydrology: Transition or destiny? Water Resour. Res., 22, 9, 177–188.

Kuentz, A., Arheimer, B., Hundecha, Y., Wagener, T., 2016. Understanding hydrologic variability across Europe through catchment classification. Hydrol. Earth Syst. Sci. Discuss., 21, 6, 1–28. DOI: 10.5194/hess-2016-428.

Magand, C., Ducharne, A., Le Moine, N., Brigode, P., 2015. Parameter transferability under changing climate: case study with a land surface model in the Durance watershed, France. Hydrological Sciences Journal, 60, 7–8, 1408–1423. DOI: 10.1080/02626667.2014.993643.

Merz, R., Blöschl, G., 2004. Regionalisation of catchment model parameters. Journal of Hydrology. 27, 95–123. DOI: 10.1002/hyp.6253.

Merz, R., Blöschl, G., Parajka, J., 2009. Scale effects in conceptual hydrological modelling. Water Resour. Res., 45, W09405. DOI: 10.1029/ 2009WR007872.

Merz, R., Parajka, J., Blöschl, G., 2011. Time stability of catchment model parameters: Implications for climate impact analyses. Water. Resour. Res., 47, 1015–1031. DOI: 10.1029/2010WR009505.

Nash, J.E. Sutcliffe, J.V., 1970. River flow forecasting through conceptual models part I-A discussion of principles, Journal of Hydrology, 10, 3, 282–290. DOI: 10.1016/0022-1694(70)90255-6.

Nester, T., Kirnbauer, R., Gutknecht, D., Blöschl, G., 2011. Climate and catchment controls on the performance of regional flood simulations. Journal of Hydrology, 340–356. http://dx.doi.org/10.1016/j.jhydrol.2011.03.028.

Nester, T., Komma, J., Blöschl, G., 2016. Real time forecasting in the Upper Danube basin. J. Hydrol. Hydromech., 64, 4, 404–414. DOI: 10.1515/johh-2016-0033.

Nijzink, R.C., Samaniego, L., Mai, J., Kumar, R., Thober, S., Zink, M., Schäfer, D., Savenije, H.H.G., Hrachowitz, M., 2016. The importance of topography-controlled sub-grid process heterogeneity and semi-quantitative prior constraints in distributed hydrological models. Hydrol. Earth Syst. Sci., 20, 1151–1176. DOI:10.5194/hess-20-1151-2016.

Osuch, M., Romanowicz, R.J., Booij, M.J., 2015. The influence of parametric uncertainty on the relationships between HBV model parameters and climatic characteristics. Hydrological Sciences Journal, 60, 7–8, 1299–1316. DOI: 10.1080/02626667.2014.967694.

Oudin, L., Perrin, C., Mathevet, T., Andréassian, V., and Michel, C., 2006. Impact of biased and randomly corrupted inputs on the efficiency and the parameters of watershed models. J. Hydrol., 320, 1–2, 62–83. DOI: 10.1016/j.jhydrol.2005.07.016.

Parajka, J., Blöschl, G., 2008. The value of MODIS snow cover data in validating and calibrating conceptual hydrologic models. Journal of Hydrology, 358, 3–4, 240–258. https://doi.org/10.1016/j.jhydrol.2008.06.006.

Parajka, J., Merz, R., Blöschl, G., 2005. A comparison of regionalisation methods for catchment model parameters. Hydrol. Earth Syst. Sci., 9, 157–171. DOI: 10.5194/hess-9-157-2005.

Parajka, J., Merz, R., Blöschl, G., 2007. Uncertainty and multiple calibration in regional water balance modelling case study in 320 Austrian catchments. Hydrol. Process, 21, 435–446. DOI: 10.1002/hyp.6253.

Pechlivanidis, I.G., Arheimer, B., 2015. Large-scale hydrological modelling by using modified PUB recommendations: the India-HYPE case. Hydrol. Earth Syst. Sci., 19, 4559–4579. DOI: 10.5194/hess-19-4559-2015.

Pebesma, E.J., 2001. Gstat User's Manual. Dep. of Phys. Geogr., Utrecht Univ., Utrecht, The Netherlands.

Perrin, C., Michel, C., Andréassian, V., 2001. Does a large number of parameters enhance model performance? Comparative assessment of common catchment model structures on 429 catchments. J. Hydrol., 242, 275–301. https://doi.org/10.1016/S0022-1694(00)00393-0.

Perrin, C., Michel, C., Andréassian, V., 2003. Improvement of a parsimonious model for streamflow simulation. J. Hydrol., 279, 275–289. DOI: 10.1016/s0022-1694(03)00225-7.

Perrin, C., Oudin, L., Andréassian, V., Rojas-Serna, C., Michel, C., Mathevet, T., 2007. Impact of limited streamflow data on the efficiency and the parameters of rainfall-runoff models. Hydrol. Sci. J., 52, 1, 131. http://dx.doi.org/10.1623/hysj.52.1.131.

Perrin, C., Andréassian, V., Rojas-Serna, C., Mathevet, T., Le Moine, N., 2008. Discrete parameterization of hydrological models: Evaluating the use of parameter sets libraries over 900 catchments. Water Resour. Res., 44, W08447. DOI: 10.1029/2007WR006579.

Poncelet, C., Merz, R., Parajka, J., Oudin, L., Andréassian, V., Perrin, C., 2017. Process-based interpretation of conceptual hydrological model performance using a multinational catchment set. Water Resource Research. DOI: 10.1002/2016WR019991.

R Development Core Team, 2011. R: A language and environment for statistical computing. R Foundation for Statistical Computing, Vienna, Austria. ISBN 3-900051-07-0, URL http://www.R-project.org/.

Saft, M., Western, A.W., Zhang, L., Peel, M.C., Potter, N.J., 2015. The influence of multiyear drought on the annual rainfall-runoff relationship: An Australian perspective. Water Resour. Res., 51, 2444–2463. DOI: 10.1002/2014WR015348.

Saft, M., Peel, M.C., Western, A.W., Zhang, L., 2016. Predicting shifts in rainfall-runoff partitioning during multiyear drought: Roles of dry period and catchment characteristics. Water Resour. Res., 52. DOI: 10.1002/ 2016WR019525.

Schaefli, B. Gupta, H.V., 2007. Do Nash values have value? Hydrol. Process., 21, 2075–2080. DOI: 10.1002/hyp.6825.

Seibert, J., 2003. Reliability of model predictions outside calibration conditions. Nordic Hydrology, 34, 477–492.

Seibert, M., Merz, B., Apel, H., 2016. Seasonal forecasting of hydrological drought in the Limpopo basin: A comparison of statistical methods. Hydrol. Earth Syst. Sci. Discuss. DOI: 10.5194/hess-2016-4, 2016.

Seifert, D., Sonnenborg, T.O., Refsgaard, J.C., Højberg, A.L., Troldborg, L., 2012. Assessment of hydrological model predictive ability given multiple conceptual geological models. Water Resour. Res., 48, W06503. DOI: 10.1029/2011WR011149.

Seiler, G., Anctil, F., Perrin, C., 2012. Multimodel evaluation of twenty lumped hydrological models under contrasted climate conditions. Hydrol. Earth Syst. Sci., 16, 4, 1171–1189. http://dx.doi.org/10.5194/hess-16-1171-2012.

Sleziak, P., Szolgay, J., Hlavčová, K., Parajka, J., 2016a. The impact of the variability of precipitation and temperatures on the efficiency of a conceptual rainfall-runoff model. Slovak Journal of Civil Engineering, 24, 4, 1–7. DOI: 10.1515/sjce-2016-0016.

Sleziak, P., Szolgay, J., Hlavčová, K., Parajka, J., 2016b. Assessment of the performance of a hydrological model in relation to selected climatic characteristics. In: Proc. 16th International Multidisciplinary Scientific GeoConference SGEM 2016, Book 3 Vol. 3, pp. 43–52. DOI: 10.5593/SGEM2016/HB33/S02.006.

Stauer, J.J., Stensvold, K.A., Gregory, M.B., 2010. Determination of biologically significant hydrologic condition metrics in urbanizing watersheds: an empirical analysis over a range of environmental settings. Hydrobiologia, 654, 1, 27–55. DOI: 10.1007/s10750-010-0362-0.

Sun, W., Wang, Y., Wang, G., Cui, X., Yu, J., Zuo, D., Xu, Z., 2017. Physically based distributed hydrological model calibration based on a short period of streamflow data: case studies in four Chinese basins. Hydrol. Earth Syst. Sci., 21, 251–265. DOI: 10.5194/hess-21-251-2017.

Therneau, T., Atkinson, B., Ripley, B., 2017. Recursive partitioning and regression trees. Version 4.1-11.

van Esse, W.R., Perrin, C., Booij, M.J., Augustijn, D.C.M., Fenicia, F., Kavetski, D., Lobligeois, F., 2013. The influence of conceptual model structure on model performance: a comparative study from 273 French catchments. Hydrol. Earth Syst. Sci., 17, 4227–4239. DOI: 10.5194/hess-17-4227-2013.

van Griensven, A., Meixner, T., Grunwald, S., Bishop, T., Diluzio, M., Srinivasan, R., 2006. A global sensitivity analysis tool for the parameters of multi-variable catchment models. Journal of Hydrology, 324, 10–23.

Valent, P., Szolgay, J., 2012. Assessment of the uncertainties of a conceptual hydrologic model by using artificially generated flows. Slovak Journal of Civil Engineering, 20, 4, 35–43. DOI: https://doi.org/10.2478/v10189-012-0020-9.

Vaze, J., Post, D.A., Chiew, F.H.S., Perraud, J.M., Viney, N.R., Teng, J., 2010. Climate nonstationarity – Validity of calibrated rainfall-runoff models for use in climatic changes studies. J. Hydrol., 394, 3–4, 447–457. DOI: 10.1016/j.jhydrol.2010.09.018.

Viglione, A., Parajka, J., Rogger, M., Salinas, J.L., Laaha, G., Sivapalan, M., Blöschl, G., 2013. Comparative assessment of predictions in ungauged basins – Part 3: Runoff signatures in Austria. Hydrol. Earth Syst. Sci., 17, 2263–2279. DOI: 10.5194/hess-17-2263-2013.

Viglione, A., Parajka, J., 2014. TUWmodel: Lumped hydrological model for educational purposes. Version 0.1-4. https://cran.r-project.org/web/packages/TUWmodel/index.html.

Viviroli, D., Zappa, M., Schwanbeck, J., Gurtz, J., Weingartner, R., 2009. Continuous simulation for flood estimation in ungauged mesoscale catchments of Switzerland – Part I: Modelling framework and calibration results. Journal of Hydrology, 377, 191–207. https://doi.org/10.1016/j.jhydrol. 2009. 08.023.

Wang-Erlandsson, L., Bastiaanssen, W.G.M., Gao, H., Jagermeyer, J., Senay, G.B., van Dijk, A.I.J.M., Guerschman, J.P., Keys, P.W., Gordon, L.J., Savenije, H.H.G., 2016. Global root zone sorage capacity from satellite-based evaporation. Hydrol. Earth Syst. Sci., 20, 1459–1481. www.hydrol-earth-syst-sci.net/20/1459/2016/.

Wilby, R.L., 2005. Uncertainty in water resource model parameters used for climate change impact assessment. Hydrol. Processes, 19, 16, 3201–3219.

Received 6 October 2017
Accepted 23 April 2018

J. Hydrol. Hydromech., 66, 2018, 4, 393–403
DOI: 10.2478/johh-2018-0026

Analysing 21st century meteorological and hydrological drought events in Slovakia

Miriam Fendeková[1*], Tobias Gauster[2], Lívia Labudová[3], Dana Vrablíková[1], Zuzana Danáčová[3], Marián Fendek[1], Pavla Pekárová[4]

[1] Department of Hydrogeology, Faculty of Natural Sciences of Comenius University in Bratislava, Mlynska dolina, Ilkovičova 6, 842 15 Bratislava 4, Slovakia.
[2] Institute of Applied Statistics and Computing, University of Natural Resources and Life Sciences, Gregor Mendel Str. 33, 1180 Vienna, Austria.
[3] Slovak Hydrometeorological Institute, Jeséniova 17, 833 15 Slovakia.
[4] Institute of Hydrology, Slovak Academy of Sciences, Dúbravská cesta 9, 841 04 Bratislava, Slovakia.
[*] Corresponding author. E-mail: miriam.fendekova@uniba.sk

Abstract: Several quite severe droughts occurred in Europe in the 21st century; three of them (2003, 2012 and 2015) hit also Slovakia. The Standardized Precipitation Index (SPI) and Standardized Precipitation and Evapotranspiration Index (SPEI) were used for assessment of meteorological drought occurrence. The research was established on discharge time series representing twelve river basins in Slovakia within the period 1981–2015. Sequent Peak Algorithm method based on fixed threshold, three parametric Weibull and generalized extreme values distribution GEV, factor and multiple regression analyses were employed to evaluate occurrence and parameters of hydrological drought in 2003, 2011–2012 and 2015, and the relationship among the water balance components. Results showed that drought parameters in evaluated river basins of Slovakia differed in respective years, most of the basins suffered more by 2003 and 2012 drought than by the 2015 one. Water balance components analysis for the entire period 1931–2016 showed that because of continuously increasing air temperature and balance evapotranspiration there is a decrease of runoff in the Slovak territory.

Keywords: Hydrological drought; Climatic conditions; River discharges; Probability distribution; Slovakia.

INTRODUCTION

The attention paid to drought periods occurrence is going to be more and more pronounced in both – scientific research community and governmental economy sector. Moreover, drought is much more perceived also by a general public. According to Andreu et al. (2015), over the last 25 years droughts covered more than 800,000 km^2 of EU territory (37%) and affected more than 100 million people (20%). The total cost of drought over the past 30 years amounts to more than 100 billion Euros.

Factors of drought development, quantification measures, and temporal and spatial propagation patterns are the most often studied aspects of drought in the research community. The attention paid to drought research is reflected also in the number of publications which could be found in scientific databases.

The economical consequences are also quite intense through rising prices of goods because of decreased agricultural production, increase of energy prices or decrease in employment. The perception of drought in the general public is more practically oriented on drought impacts, e.g. drinking water supply shortage, threat of wild fires, heat waves threatening human´s organism with over-heating and potential collapsing, degradation of aquatic ecosystems.

Several quite severe droughts occurred in Europe since the beginning of the 21st century, three of them: 2003, 2012 and 2015 hit also the territory of Slovakia.

The 2003 drought was widely studied by several authors because of its pan-European character. The climate synthesis of the 2003-year drought was done by Rebetez et al. (2006). They confirmed that the 2003 meteorological data showed over wide regions monthly mean temperatures more than 4°C above the long-term mean values. The affected areas were mainly in the South-West, from Eastern Spain to Southern Germany, including most of continental Italy, Sardinia, Corsica, Switzerland, and most of France. The heat lasted from May to September in large parts of the western and central Europe ranging from Spain to Hungary and from Iceland to Greece being pronounced also on the Slovak territory. The lack of precipitation was severest during the summer, but generally, precipitation was below normal from February 2003 until June 2004 (with exception of two months). Air humidity was below the normal, sunshine duration and potential evapotranspiration were clearly above normal in summer 2003.

A hydrological review of the 2003 drought describing the similar effect of the extremely high summer temperatures and low precipitation on streamflow discharges was done in many countries, e.g., in UK by Marsh (2004), for the Danube basin by Mikhailova et al. (2012), for Slovakia by Sekáčová et al. (2004) and by Melová and Lupták (2006). The review on Europe-wide reduction in primary productivity caused by the heat and drought in 2003 was done by Ciais et al. (2005).

Kendon et al. (2013) reported for the UK that for 2010–2012, the worst effects of an intense summer drought were avoided, because summer 2011 was cool and rather wetter than average overall. Most of the dry months occurred in the autumn, winter and spring seasons. Even though the 2010–2012 drought was not as severe as that of 1975–1976, it is comparable with several other major droughts in the past. According to Cindrić et al. (2016), the Croatian 2011–2012 drought was characterised by extremely long duration in the continental region and in the highlands, where it has had the highest magnitudes since the beginning of the twentieth century. In comparison with the extreme 2003 drought, which had the highest intensity mostly on short-time scales but was associated with a strong heat wave during the summer, the 2011–2012 drought

was a long-lasting one. The whole of 2003 was one of the 10 driest years since the beginning of the twentieth century due to extremely low spring precipitation amounts; whilst 2011 was one of the 2 driest years in the continental region and in the highlands. Corduneanu et al. (2016) analysed 2011–2012 drought, which was extremely severe in Prut River basin (Romania), beginning in late autumn in 2011 and lasted until autumn 2012. Zahradníček et al. (2015) noted that the weather conditions from August 2011 to May 2012 produced an extreme drought in the eastern Czech Republic (Moravia), whereas the patterns were nearly normal in its western region (Bohemia). According to the Palmer Drought Severity Index, the 2012 drought was classified as the worst in the past 130 years. The drought patterns were related to the prevailing high-pressure systems over Central Europe and the occurrence of weather types with different precipitation amounts in Bohemia and Moravia. The most substantial drought effects occurred in the agricultural sector. A decrease in cereal yields was observed in the analysed production areas in Moravia, which was unprecedented in the past 52 years. According to Zahradníček et al. (2015), Austria and Slovakia experienced a similar drought. Vido et al. (2016) documented the physiological response of tree species in the Central Slovakia on the driest months of the 2012; Šustek et al. (2017) documented the influence of the 2012 drought on decrease of beetle species number in the Tatra Mts. area.

The 2015 drought was studied from the point of view of precipitation and derived soil moisture by Orth et al. (2016). The performed analyses reveal that the 2015 event was drier than both the recent 2003 or 2012 extreme summers in Central Europe. In terms of precipitation and temperature anomalies, the 2015 summer in Central Europe is found to lie between historical climate in the region and that characteristic of the Mediterranean area. According to the authors, the 2015 drought event illustrates that potential future drying trends have severe implications and could be stronger than commonly assumed from the entire IPCC AR5 model ensemble. Ionita et al. (2017) confirmed that the summer 2015 was the hottest and climatologically driest one over the 1950–2015 study period for an area stretching from the eastern Czech Republic to Ukraine. Other detailed studies were done on the pan-European scale by van Lanen et al. (2016), and Laaha et al. (2017). According to Laaha et al. (2017), the 2015 drought, comparing to 2003 drought, had a different spatial extent and in terms of low flow magnitudes the drought was rather moderate in most parts of the Europe, but more severe with return period of 100 years in Czech Republic, South-Eastern Germany and Northern Austria. The occurrence of the 2015 drought for six stations in the middle Danube River basin was predicted using the stochastic modelling by Stojkovic et al. (2017).

Whereas the 2003 and 2012 droughts affected almost the whole territory of Slovakia, the 2015 drought in Slovakia can be characterized by spatial and temporal variability, affecting various regions with different strengths. The hydrological evaluation of the year 2015 was done by Škoda et al. (2016), drought development in groundwater was analysed by Slivová and Kullman (2016).

The paper is aiming to study five main items:

1. to characterize the meteorological situation in evaluated years 2003, 2012 and 2015 on the Slovak territory in context with the pan-European situation,
2. to assess meteorological drought in evaluated years based on Standardized Precipitation Index (SPI) and Standardized Precipitation and Evapotranspiration Index (SPEI),
3. to assess hydrological drought in evaluated years from the point of view of discharge absolute values, drought duration, deficit volumes, intensity and timing,
4. to analyse and discuss the hydrological drought with respect to long-term hydrological balance components changes
5. to accomplish the comparative analysis of the estimated drought parameters among the river basins and evaluated years.

MATERIAL AND METHODS

Study region

Slovakia is a landlocked central European country (16°–23° E, 47°–50° N), bordered by Poland, Ukraine, Hungary, Czech Republic and Austria (Fig. 1). The Slovak territory covers 49,035 km^2 with almost 80% over 720 m a.s.l. altitude. The Slovak middle and northern areas are mountainous with the Western Carpathian Arch, and lowlands are typical in the South and East. The highest point is the 2,655 m Gerlachovsky Peak in the northern High Tatra Mts. and the lowest is at 94 m near Streda nad Bodrogom village in the Eastern Slovak lowland. The climate varies between temperate and continental climate zones with relatively warm summers and cold, cloudy and humid winters. The average winter temperature is –2°C; with January the coldest month and the High Tatras the coldest area. The average summer temperature is 21°C, with July and August the warmest months and the Danubian Lowland the warmest area. Temperature and precipitation are altitude dependent, with annual precipitation ranging from 450 mm in the southern lowlands to over 2,000 mm in the northern High Tatras (Landscape Atlas of the Slovak Republic, 2002).

Slovakia has the Morava, Váh, Hron, Slaná, Ipeľ, Hornád, and Bodrog as main tributaries to the Danube River. Most Slovak territory (96%) is in the Danube River basin with the above rivers draining to the Black Sea. The remaining 4% drains to the Baltic Sea through the Poprad and Dunajec tributaries of the Vistula River. The main European divide between the Black Sea and Baltic Sea drainage areas follows the lower ridges and the flat landscape of the foothills of the High Tatras near Štrba and Šuňava villages. The long-term average water balance (period 1961–1990) can be described by the equation (Majerčáková in Landscape Atlas of the Slovak Republic, 2002):

P (734 mm) = ETP (494 mm including other minor losses) +
+ R (240 mm)

where: P = precipitation, ETP = evapotranspiration and R = runoff, considerably varying between years.

The mountainous character of the landscape and the position of mountain ranges, mostly stretching in the SW-NE direction, create conditions for orographic precipitation. The orographic division produces heavy rains in Slovak mountainous areas. The combination of the above factors ensures variable conditions with extreme hydrological phenomena occurrence in Slovakia.

Hydrological and meteorological data

Two types of the measured data were used for the analysis: (1) meteorological data on precipitation and air temperatures in a monthly step and (2) streamflow discharges from 12 gauging stations in a daily step.

The meteorological data used for Standardized Precipitation Index (SPI) calculation consisted in average monthly precipitation data over each of the evaluated river basins. The Standardized

Table 1. Basic data on river basins at discharge gauging stations.

Profile number and name	River	Area (km^2)	Gauge zero (m a.s.l.)	Coordinates WGS 84 - E	Coordinates WGS 84 - N
5020 Šaštín-Stráže	Myjava	32.02	324.34	17.15619	48.64055
5550 Liptovský Mikuláš	Váh	1107.21	567.68	19.60351	49.08637
5840 Trstená	Oravica	129.95	585.49	19.59491	49.35301
6200 Kysucké Nové Mesto	Kysuca	955.09	346.09	18.78494	49.29682
6730 Nitrianska Streda	Nitra	2093.71	158.27	18.17255	48.52395
6820 Vieska nad Žitavou	Žitava	295.46	154.27	18.35458	48.31590
7290 Brehy	Hron	3821.38	194.27	18.64623	48.40672
7440 Holiša	Ipeľ	685.67	172.40	19.74105	48.29752
7900 Vlkyňa	Rimava	1377.41	150.77	20.30173	48.28540
8320 Chmeľnica	Poprad	1262.41	507.41	20.73023	49.28918
8870 Košické Oľšany	Torysa	1298.30	185.70	21.33654	48.73260
9500 Hanušovce nad Topľou	Topľa	1050.05	160.40	21.51777	49.03310

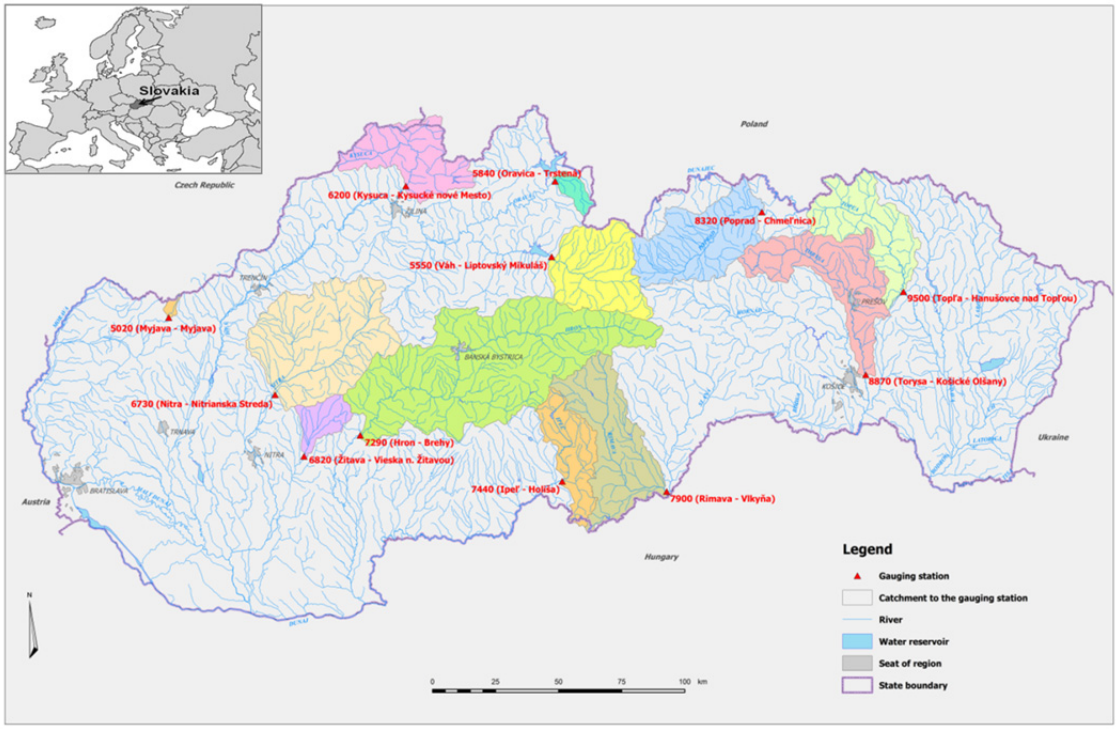

Fig. 1. Location of evaluated river basins.

Precipitation and Evapotranspiration Index (SPEI) values were calculated for meteorological stations located within or in the vicinity of the evaluated river basin, the value of potential evapotranspiration was estimated using the Penman-Monteith equation. The meteorological stations used for SPEI calculations were Senica, Oravská Lesná, Čadca, Prievidza, Mochovce, Žiar nad Hronom, Boľkovce, Rimavská Sobota, Podolínec, Prešov and Čaklov. Data representing the period 1.1.1981 to 30.6.2016 were used in both cases.

Moreover, air temperatures and areal precipitation data from the SHMI covering the Slovak territory were analyzed and compared with the meteorological conditions across the Europe (WMO, 2004; WMO, 2013; WMO, 2016).

Daily discharges at 12 gauging stations of Myjava, Váh, Oravica, Kysuca, Nitra, Žitava, Hron, Ipeľ, Rimava, Poprad, Topľa and Torysa River basins (Fig. 1) were processed, covering the period 1.1.1981 to 30.6.2016. The river basins were selected to cover the area of Slovakia; the majority of gauging profiles represent the near-natural runoff conditions. The basic data on river basins up to evaluated gauging stations are in Table 1. The evaluated time period included also the first half of the year 2016 in order to detect the multi-year hydrological drought occurrence if present in evaluated time series.

The homogeneity of the time series was assessed using the software package AnClim (Stepanek, 2003). The Alexandersson test (Alexandersson and Moberg, 1997; Alexandersson, 1986) was used to test the mean value change, as represented by the change in the mean value and the variance. Some statistical tests and procedures used within this study are based upon the normality requirement of the tested series. Therefore the X^2 and the Kolmogorov-Smirnov tests were used to test the distribution normality of the annual discharge series.

The spatial value of precipitation in each river basin was obtained using weighted average, in which the weights were estimated considering the area covered by the Thiessen polygons of rain-gauge stations, but also with consideration of annual precipitation regime at each station, which influence the contribution of particular station in total precipitation fallen in the river-basin.

The Standardized Precipitation Index (SPI) (McKee et al., 1993) was used to calculate values of indexes for 3-, 9- and 12-months. The SPI calculation for any location is based on the long-term precipitation record for a desired period (20–30 years of monthly values, optimally 60–70 years). This long-term record is fitted to a probability distribution (Gamma distribution

is recommended), which is then transformed into a normal distribution so that the mean SPI for the location and desired period is zero. Positive SPI values indicate greater than median precipitation and negative values indicate less than median precipitation. Because the SPI is normalized, wetter and drier climates can be represented in the same way; thus, wet periods can also be monitored using the SPI (Table 2). The n-month SPI (n could be equal to 3, 6, 9, 12 or 24 months) compares the precipitation for that period with the same n-month period over the historical record. The 6-month SPI (SPI6) indicates seasonal to medium-term trends in precipitation. SPIs of 9-, 12- and 24-months can be regarded as indicative for stream flows, reservoir levels, and even groundwater levels at longer timescales (WMO, 2013). The SPI12 values were used for detailed evaluation of the meteorological drought in the studied area; they were calculated based on monthly weighted average areal basin precipitation.

Table 2. Limit values of the standardized precipitation index SPI (according to McKee et al., 1993).

SPI value	Classification
2.00 and more	extremely wet
1.50 to 1.99	very wet
1.00 to 1.49	moderately wet
–0.99 to 0.99	near normal
–1.00 to –1.49	moderately dry
–1.50 to –1.99	very dry
–2.00 and less	extremely dry

The Standardized Precipitation and Evapotranspiration Index (SPEI) was also used to evaluate the meteorological drought occurrence and intensity. The SPEI index was designed to take into account both precipitation and potential evapotranspiration (PET) in determining drought (Vincente-Serrano et al., 2010). Thus, unlike the SPI, the SPEI captures the main impact of increased air temperature on water demand. The same classification scheme as for SPI (Table 2) was also used for the SPEI results analysis.

The runoff from the Slovak territory is calculated as the sum of the runoff depths from respective river basins, mostly based on the closing profiles data, recalculated into the total river basin area. In the case the river is the boundary river with another country, the runoff depths of the river tributaries are used for calculation.

Four basic drought parameters – the annual minimum 7 day-discharge ($m^3\ s^{-1}$), maximum drought duration (days), maximum deficit volume (m^3) and drought intensity ($m^3\ day^{-1}$) were calculated. The annual minimum 7-day index (AM7), representing the magnitude of the low flow event of a year, was obtained by using a central 7-day moving average (Laaha et al., 2017).

A constant threshold, given by the Q_{80} low flow quantile [$P(Q \geq Q_{80}) = 0.8$] computed for the entire reference period 1981–2010 was used to identify the largest absolute dry states of the system. The concept of Sequent Peak Algorithm (SPA), based on depletion and recovery of the storage required to sustain the threshold discharge (Tallaksen and Van Lanen, 2004), was used in the study. This concept often leads to detection of the multiyear drought in conditions with snowy winters when the discharges are naturally low because of very low recharge. After the drought event series have been identified, the event with the maximum volume per year was selected, described by drought duration and deficit volume. The last parameter - the drought intensity was calculated as the ratio between deficit volume and drought duration. All four drought parameters were compared with the values calculated for the reference period 1981–2010.

A three-parameter Weibull distribution was used to calculate the return period of the annual minimum value, and a generalized extreme values distribution (GEV) was used to calculate the return period of maximum drought duration, maximum deficit volume and drought intensity. The example of the drought parameters return periods estimation for Hron River basin is in Fig. 2. Timing of drought, based on the dates of drought beginning and termination, and its seasonality were also studied.

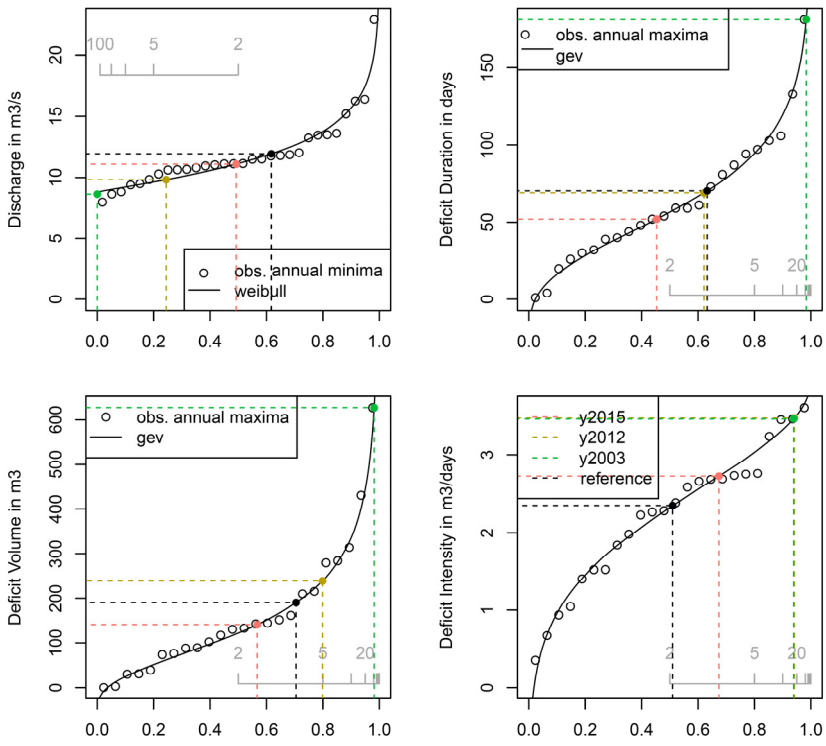

Fig. 2. Return periods estimation for drought parameters in Hron River basin at Brehy.

Classical factor analysis (method of principal factor, Varimax rotation) (Überla, 1971) was applied on all estimated drought parameters aiming to find relationships among the evaluated river basins. Multiple regression methods were applied to estimate relations among the water balance components. The area`s average precipitation and runoff were calculated from the measured data, the balance evapotranspiration was calculated as the difference between the precipitation and runoff values.

RESULTS AND DISCUSSION

Meteorological conditions

The study of meteorological data showed that the initial climatic conditions over the Europe were quite similar in all three dry years (2003, 2012, 2015). There was a positive 500-hPa geopotential height anomaly in the upper level atmospheric circulation over the continental Europe, especially over the central and Eastern Europe (Ionita et al., 2017; WMO, 2004; WMO, 2013; WMO, 2016).

The average summer temperatures for 2003 were higher than the long-term average of 1951–2015 across Slovakia. The anomaly reached up to 2.1°C in some places (South-Western part, the Hurbanovo station). Precipitation totals reached the area`s average value of 573 mm (74.5% of the long-term average, calendar year); the average precipitation deficit reached 189 mm (www.shmu.sk). According to area`s average precipitation, the year 2003 was very dry. However, two preceding years 2001 and 2002 were wet when comparing with the long-term average 1901–2000 (Melová and Lupták, 2006).

The temperature for 2012 was also higher than long-term average; the anomaly in Hurbanovo (SW Slovakia) reached 1.9°C. Summer months were the warmest. According to precipitation the year was classified as normal with the deficit of 49 mm, the highest deficit was reached in March and August with 23 and 26% of the long-term average (www.shmu.sk).

The temperature for 2015 was 2.0 (the Hurbanovo station, SW Slovakia) to 2.3°C (the Košice station, SE Slovakia) higher than the long-term average of 1961–1990. Annual precipitation reached 710 mm which makes 94.5% of the long-term average **(**www.shmu.sk**).** According to area`s average precipitation, the year was classified as normal with a deficit of 41 mm.

The temperature in summer and beginning of fall in Slovakia in all three years was higher (Table 3), but the precipitation totals were lower than the long-term average of 1961–1990 for water year.

Hydrological conditions

Table 3 shows the development of the hydrological balance components in Slovakia during the period 1991–2016 in comparison with the average values of reference periods 1931–1960 and 1961–1990. The precipitation amounts increased considerably by 41 mm when comparing to the 1931–1960 period and by 61 mm when comparing to the 1961–1990 period. Runoff decreased by 8.5/25.2 mm within the evaluated periods. However, the balance evapotranspiration (calculated as the difference between the precipitation and runoff value) increased by 69.4 mm comparing to the 1961–1990 period. Decrease in runoff and occurrence of drought despite increasing precipitation during 2001–2016 period is so pronounced that the deeper identification of such development would be necessary for each of evaluated basins.

Meteorological drought

The evaluation of meteorological drought in the Slovak territory was based on the SPI and the SPEI calculation and brought following results. The SPI12 divides the study period into two parts and this division is quite clear in the majority of selected river basins. Dry conditions prevailed in the 1980s and in the first half of 1990s in all regions of Slovakia. The most severe droughts at that time occurred in the northern river basins. For example, the long-lasting and quite intensive droughts in the Poprad River basin, representing the mountainous river basin were interrupted only with short normal periods (Fig. 3 top). River basins located in the southern Slovakia (Ipeľ, Rimava) having the lowland character in the major part of the basin, show very similar conditions in 1980s, but the period 1995–2010 was more heterogeneous than in the northern part of the country. Dry and wet periods had comparable duration and intensity and they alternated each other quite regularly (Fig. 3 bottom). The southern region has experienced two extreme events since 2010. The extreme wet event in 2010 was the most intensive there, which was caused by prevailing south western to south eastern cyclonic situations. On the other hand, the extreme drought occurred in 2011–2012. Recent years were rather wet, especially considering only precipitation.

Table 3. Development of the hydrological balance components in Slovakia, mean annual temperature in Hurbanovo, runoff coefficient (for water year, November–October).

Period	Average annual precipitation totals (mm)	Annual runoff (mm)	Balance Evapotranspiration (mm)	Average annual air temperature at Hurbanovo (°C)	Annual runoff coefficient (–)
2001	823	241	582	11.83	0.34
2002	829	219	610	10.89	0.29
2003	**554**	**143**	**411**	**11.19**	**0.26**
2004	804	206	598	10.66	0.26
2005	880	239	641	10.46	0.26
2006	681	304	377	10.47	0.27
2007	814	189	625	12.50	0.45
2008	770	208	562	11.33	0.23
2009	810	221	589	11.71	0.27
2010	1270	430	840	10.53	0.27
2011	769	172	597	11.49	0.34
2012	**710**	**143**	**567**	**11.65**	**0.22**
2013	854	289	565	11.05	0.20
2014	955	234	721	12.52	0.34
2015	**719**	**197**	**522**	**12.32**	**0.25**
2016	924	225	699	11.69	0.27
1931–1960	754.3	256.7	497.6	9.88	0.34
1961–1990	734.0	240.0	494.0	10.07	0.33
1951–2015	756.6	238.2	518.4	10.45	0.31
1991–2016	795.0	231.5	563.4	11.1	0.29

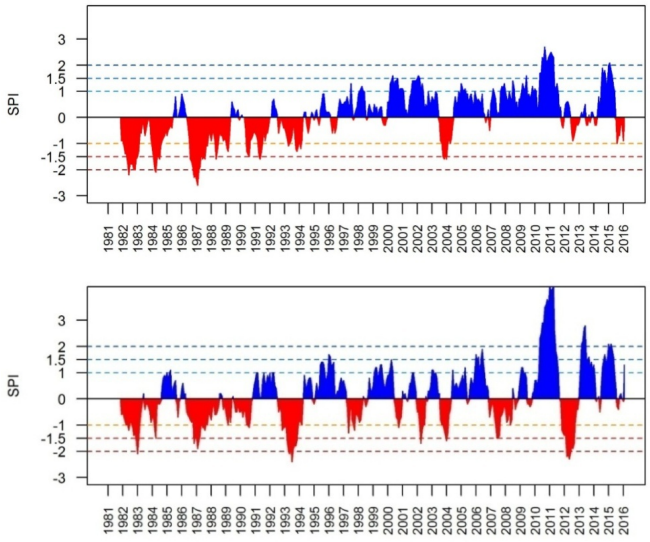

Fig. 3. The SPI12 in the Poprad River basin (top) and in the Ipeľ River Basin (bottom).

Involving the potential evapotranspiration into consideration, the wet events after 2010 were milder according to the SPEI12. If we compare the SPI12 and SPEI12, both indices reached more or less similar values until 2000. Since then the SPEI12 has got the tendency to lower values than the SPI12. The situation in the Poprad and Ipeľ River basins is in Fig. 4.

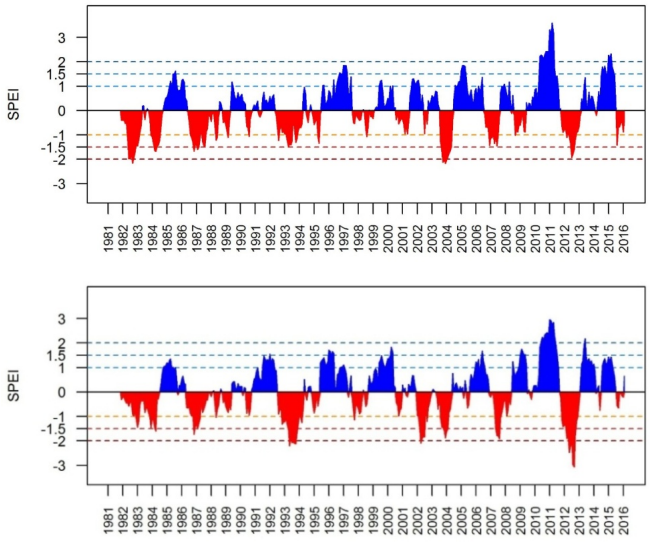

Fig. 4. The SPEI12 in the Poprad River basin (top) and in the Ipeľ River basin (bottom).

When comparing to the rest of the Slovakian territory, the Topľa River basin (eastern Slovakia) has shown considerably different conditions since the mid-1990s. Dry conditions from the early 1990s persisted in the region until the early 2000s on contrary to the rest of basins. Another difference is in the duration and intensity of following wet periods according to the SPI12. The difference between the SPI and the SPEI after 2000 is also higher than in other study areas.

Despite the fact that after 2000 three highly remarkable droughts occurred in the Eastern Slovakian area, the Torysa River basin shows similar water balance features during the whole period 1981–2015 with prevailing dry conditions according to both, SPI12 and SPEI12 values.

Completely opposite tendency in water balance was observed in the western river basin (Myjava), where the wet conditions have evidently prevailed since the mid-1990s.

Hydrological drought

The variability in physical-geographical conditions in Slovakia is reflected also in very different hydrological drought periods occurrence around the country in 2003, 2012 and 2015. The results of drought parameters for all three evaluated years and for the reference period 1981–2010 are given in Table 4.

Table 4. Comparison of drought event parameters in evaluated years 2003, 2012 and 2015.

River basin	Year	AM7 discharge ($m^3 s^{-1}$)	Drought event duration (days)	Deficit volume (m^3)	Intensity ($m^3 day^{-1}$)
Myjava	2003	0.319	222	77.2	0.348
	2012	0.482	98	23.4	0.239
	2015	0.519	79	6.12	0.125
	Ref. period	0.672	89.2	25.7	0.230
Váh	2003	5.71	176	335	1.9
	2012	4.97	125	302	2.41
	2015	7.96	10	6.36	0.636
	Ref. period	6.34	87.6	139	1.4
Oravica	2003	0.509	141	38.2	0.271
	2012	0.636	125	48.3	0.387
	2015	0.729	49	12.9	0.263
	Ref. period	0.728	62.4	17.6	0.273
Kysuca	2003	2.41	60.0	63.7	1.06
	2012	2.19	93.0	103.0	1.10
	2015	1.87	142.0	189.0	1.33
	Ref. period	2.51	39.7	46.0	1.11
Nitra	2003	2.6	188	281	1.49
	2012	2.73	122	177	1.45
	2015	3.34	107	54.7	0.512
	Ref. period	4.35	69.4	71.4	0.789
Žitava	2003	0.165	149	23	0.154
	2012	0.104	147	26.8	0.182
	2015	0.114	36	6.17	0.172
	Ref. period	0.341	72.3	9.55	0.104
Hron	2003	8.63	181	627	3.47
	2012	9.83	69	240	3.48
	2015	11.1	52	142	2.72
	Ref. period	11.9	70.3	190	2.35
Ipeľ	2003	0.220	82	23	0.28
	2012	0.153	170	50	0.294
	2015	0.613	4	0.227	0.0567
	Ref. period	0.403	76	15.1	0.175
Rimava	2003	0.83	232	71.2	0.307
	2012	0.721	143	48.1	0.336
	2015	1.01	50	20.3	0.406
	Ref. period	1.35	96.2	38.9	0.335
Poprad	2003	3.35	183	179	0.97
	2012	3.16	133	203	1.52
	2015	3.76	43	56.3	1.31
	Ref. period	4.07	76.3	107	1.18
Torysa	2003	1.10	266	210	0.79
	2012	0.99	77	61.5	0.799
	2015	1.12	88	66.7	0.758
	Ref. period	1.83	88.9	53.3	0.458
Topľa	2003	0.913	181	153	0.844
	2012	1.08	178	82.4	0.463
	2015	1.13	128	85	0.664
	Ref. period	1.6	60.9	42.6	0.591

The most extreme values of all four drought parameters (AM7, duration, deficit volume and intensity) were reached within the same year only in five out of twelve evaluated river basins. This situation occurred in Kysuca River basin in 2015, in Ipeľ in 2012, and in Myjava, Nitra and Topľa in 2003, as documented in Table 4. However, this was not the case in the rest of the basins, where either the lowest AM7 value, or the longest drought duration, or the highest deficit volume did not occur in the same year as the highest drought intensity. This is the case, e.g., of the Poprad River in 2012 (drought duration was in 50 days shorter than in 2003) or of Rimava River in 2015 (the value of AM7 was the highest among all three evaluated years).

The deficit volumes were the highest in most of evaluated basins in 2003 and 2012, being mostly also higher than the average highest deficit volumes in the reference period 1981–2010 (Table 4). This was the case of Váh, Oravica, Nitra, Žitava, Hron, Ipeľ, Rimava and Poprad River basins. Strongly different was the situation in Kysuca River basin, where the highest deficit volume was reached in 2015.

According to the highest value of the drought intensity, the year 2003 was the most extreme in Myjava and Topľa, the year 2012 in Váh, Oravica, Žitava and Poprad basins and 2015 in Kysuca and Rimava basins (Table 4). The drought intensity was almost the same in Nitra, Hron and Ipeľ River basins in 2003 and 2012, respectively. The specific drought conditions became evident in Torysa River basin where the drought intensity reached almost the same value in all three evaluated years 2003, 2012 and 2015.

The highest return periods of evaluated drought parameters were calculated as follows: (1) over 100 years for AM7 discharge minima in the Torysa River basin during the 2012 drought; (2) over 60 years for drought duration in the Hron in 2003; (3) over 50 years for maximum deficit volume in the Kysuca River in 2015 and almost 20 years for drought intensity in the Torysa River in 2012. Generally, the estimated return periods of evaluated drought parameters were higher for 2003 and 2012, reaching higher values than those, estimated for the reference period (Myjava, Žitava, Váh, Torysa) and for 2015. One exception was the situation in the Kysuca River basin, where the highest return periods were calculated for all drought parameters for the year 2015.

Hydrological drought timing

Timing of the drought periods with the highest deficit volume was different within evaluated years. The onset and ending timing of the assessed drought periods in 2003, 2011–2012, and 2015 are shown in Figs. 5, 6, and 7.

The drought in 2003 (Fig. 5) started in all basins during the summer period between 3 June and 12 August and ended between the 15 January and 28 March 2004. The only exception was the drought in the Kysuca River basin which lasted only for 60 days.

The starting day for 2012 drought was more variable comparing with the year 2003, dividing the evaluated river basins into two groups (Fig. 6). Drought in the first group which includes basins located in the western, northern and eastern Slovakia (Myjava, Váh, Oravica, Kysuca, Poprad and Topľa River basins) started already in the period between 31 August and 29 October 2011 and lasted until January to March 2012. The second group of basins, located in the central and southern Slovakia (Nitra, Žitava, Hron, Ipeľ, Rimava and Torysa River), had the starting day of the drought between 11 May and 12 August 2012 with the deficit volume ending in the same year.

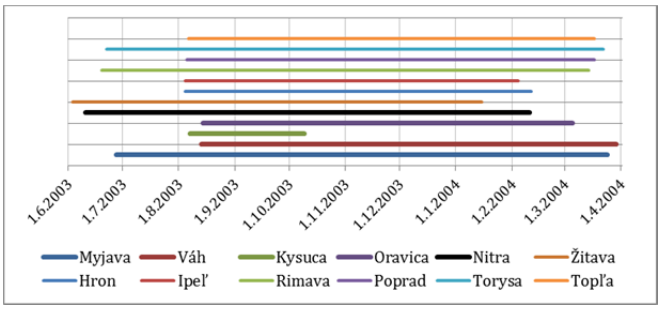

Fig. 5. Timing of 2003 droughts.

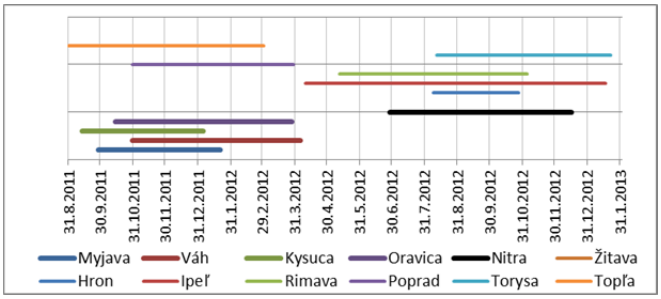

Fig. 6. Timing of 2011–2012 droughts.

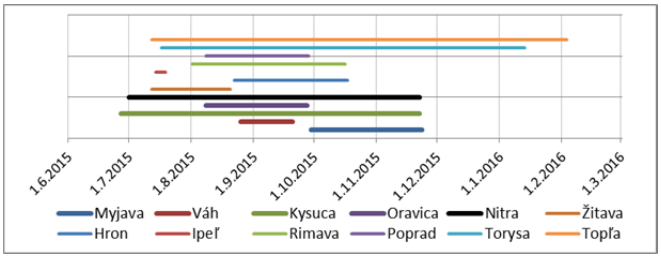

Fig. 7. Timing of 2015 droughts.

Moreover, drought in Žitava, Ipeľ and Torysa River basins lasted until January 2013.

In 2015 (Fig. 7), the starting day of the drought with the highest deficit volume was between the 26 June and 24 August except of the Myjava River basin, where the onset of drought was shifted to 28 September. The 2015 drought finished in the same year in all basins out of two - in Torysa and Topľa River basins the deficit volumes estimated by the SPA method lasted until 13 January 2016 in the Torysa and 3 February 2016 in the Topľa River basin.

The prolonged drought duration from the summer-autumn months over the winter is mostly connected to the low recharge of rivers during the winter period when the precipitation fall in the form of snow and the ground surface is frozen. Despite of the reasons, such drought is labelled as a multiyear drought (Tallaksen and Van Lanen, 2004).

Inter-relations among river basins according to drought parameters

The aim of the factor analysis utilization was to look after interrelationships among evaluated river basins according to estimated drought parameters in respective years. As it comes from the principles of the factor analysis method, the method is used either for reduction of variables in the model, or identification of groups of inter-related variables, or for finding the influence of some unobserved (underlying) variables.

The performed analysis enabled to identify three main groups of inter-related river basins with similar behaviour with respect to drought parameters. The principal method of factor analysis (PFA method, principal factors, VARIMAX rotation) was applied; four factors were extracted when evaluating the drought parameters (Table 4) in respective basins. Three of the factors were the common ones; the fourth factor was the unique one. Results of factor loadings calculated after VARIMAX rotation are in Table 5. Numbers in bold in Table 5 are the highest values in the respective factor. The initial communality estimates have been constructed from the squared multiple correlations of each variable with all of the other variables. The resulting communalities for all variables were very high, reaching the values 0.83 (Oravica) to 1.0 (Rimava and Poprad). The model of four extracted factors explained the 98.99% of the total variability of the original data.

The factor 1 is a common factor which implies all river basins located in the western, southern and eastern part of Slovakia (Myjava, Kysuca, Nitra, Žitava, Ipeľ, Rimava, Torysa and Topľa). Factor 2 is also a common factor implying river basins located in the central part of the country (Váh, Nitra and Hron) and factor 3 implies river basins in the northern part of Slovakia (Váh, Oravica and Poprad), all three representing the mountainous (alpine) type river basins. The factor 4 is a unique factor, implying only the Kysuca River basin. It can be seen, that high factor loading of the same river basin drought parameters could be found in two factors at the same time, as it is the case of the Kysuca River basin (factor 1 and 4), Nitra River basin (factor 1 and 2) and the Váh River basin (factor 2 and 3). The 3D plot of factor loadings for factors 1, 2 and 3 is in Fig. 8. The plot shows the distinct group of the mountainous basins located in the northern Slovakia (Poprad, Váh and Oravica), then the group of basins in the central Slovakia (Hron, Nitra) and the group of basins of the western, southern and eastern Slovakia (Myjava and Kysuca; Žitava, Ipeľ and Rimava; Topľa and Torysa).

The unobserved (underlying) variables which enabled the extraction of four factors can be identified as geographical location of the river basins, influencing the climatic conditions through the geomorphologic conditions, geological conditions, altitude, orientation towards the prevailing wet air masses movement, etc.

Table 5. Results of drought parameters factor analysis.

River basin	Factor 1	Factor 2	Factor 3	Factor 4
Myjava	**0.949**	0.212	0.116	0.049
Váh	0.026	**0.710**	**0.665**	–0.046
Oravica	0.378	0.021	**0.828**	0.078
Kysuca	**0.736**	0.194	0.157	**0.624**
Nitra	**0.668**	**0.668**	0.279	0.128
Žitava	**0.961**	0.0728	0.246	0.098
Hron	0.293	**0.919**	0.156	0.098
Ipeľ	**0.911**	0.109	0.160	0.147
Rimava	**0.944**	0.191	0.273	0.024
Poprad	0.181	0.481	**0.869**	0.069
Torysa	**0.822**	0.475	0.156	0.075
Topľa	**0.865**	0.351	0.211	0.225

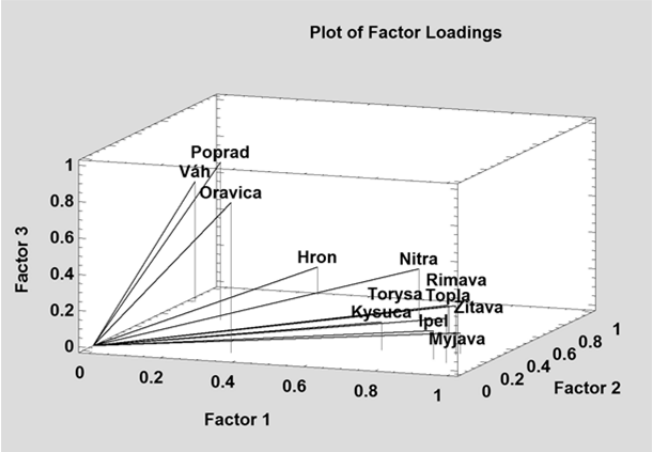

Fig. 8. Plot of factor loading after VARIMAX rotation.

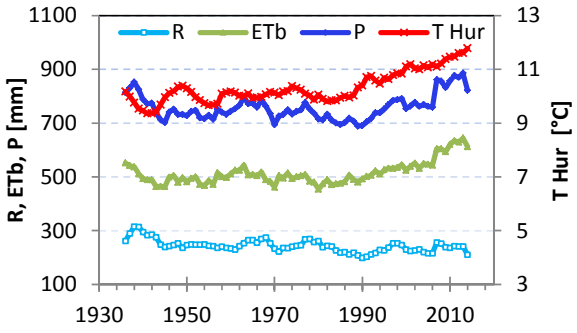

Fig. 9. Course of 7-years moving averages of the water balance components for areal values of: R – runoff, ETb – balance evapotranspiration, P – precipitation in Slovakia; local values of: T – 7-years moving averages of the air temperature at Hurbanovo station, Slovakia, 1931–2016 period.

Inter-relationships between water balance components

Considerable changes in the water balance are observed in Slovakia, especially during the last twenty to thirty years. After extremely low precipitation totals during normal period 1961–1990, next period 1991–2016 precipitation totals were extremely high (Table 3). Despite this, runoff from the Slovak territory decreases significantly. The course of 7-years moving averages of the water balance components is presented in Fig. 9; together with the course of the Hurbanovo 7-years moving averages air temperature.

The trend in precipitation is better visible in Fig. 10 where the period 1871–2016 is showed. It is obvious, that the trend in precipitation is not monotonic unlike the winter and summer temperature courses.

A multiple linear regression (Eq. 1) was used to determine the effect of air temperature and rainfall on the areal runoff depth:

$$R_{ar} = 167.60 + 0.3360\ P - 17.392\ T, \quad (1)$$

where:

R_{ar} – average runoff from the Slovak territory;
P – average precipitation annual totals on the Slovak territory;
T – average annual air temperature at meteorological Hurbanovo station.

The multiple correlation coefficient of 0.64 was reached, with the standard error of estimation amounting 46.9.

It follows from the long-term water balance analysis (Eq. 1) that a 100 mm drop in precipitation in Slovakia will cause the runoff drop of 33.6 mm. An increase of the mean annual temperature by 1°C brings decrease of runoff by 17.4 mm. Synchronously an increase of the mean annual air temperature by 1°C brings increase of balance evapotranspiration by 17.4 mm.

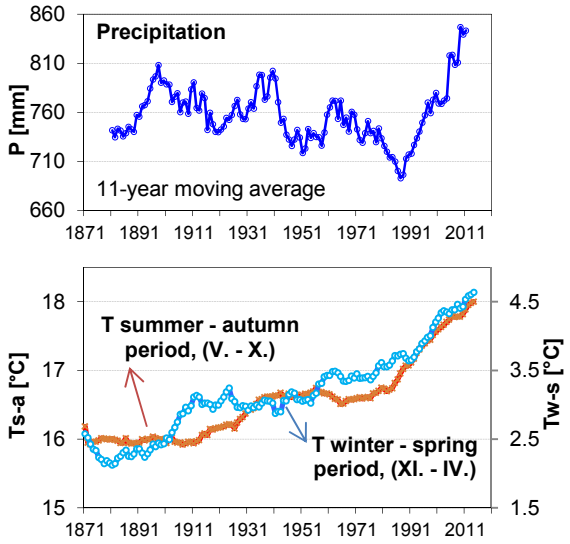

Fig. 10. Course of the 11-years moving averages of the (top) precipitation totals on the Slovak territory (P) and (bottom) air temperature (Ts-a summer-autumn, Tw-s winter-spring seasons) at Hurbanovo station (1881–2016).

DISCUSSION

Slovakia is located in the boundary zone between the southern Europe, where precipitation decrease is projected by climate change scenarios, and the northern Europe with expected precipitation increase (European Environmental Agency, 2012). Therefore, high inter-annual, as well as multiannual variability of precipitation is implied. Air temperature increase in winter and summer was proved by many studies not only in Slovakia, but on the global scale (e.g. Bindoff et al., 2013; Labudová et al., 2015).

Warmer air can hold more moisture, which is consequently transported over the continent. In summer, the continent can be very hot and intensive rainfalls occur more frequently also in Slovakia. But the intensive convective precipitation has only regional occurrence and the most of them is consumed by vegetation, or evaporates. The SPI and the SPEI cannot filter out such cases and often indicate normal conditions after heavy rainfalls occurring on only one day in month even thought the rest of month is without precipitation and high temperatures are recorded. Changing intensity and distribution of the precipitation in Slovakia is also noted by the values of the SPI and the SPEI, which reach extremer values on the both sides of the scale.

Increasing winter air temperature can cause higher precipitation in winter season due to potentially higher moisture content in air masses. This could be one possible explanation of the SPI results for the northern river basins. On the other hand, higher winter temperatures causes change of the precipitation state (snow – rain) and also duration of the snow cover. Increase in winter temperatures results in higher ratio of liquid precipitation on total winter precipitation and shorter snow cover duration (Pecho et al., 2010; Záhradníček et al., 2016). Consequently, higher discharges during the cold season could occur. Therefore, more attention should be paid also to snow conditions changes in further studies focused on the relationship between meteorological and hydrological drought occurrence.

The causes of increased evapotranspiration are several: especially higher air temperature and higher precipitation totals. There could be also other reasons, as increased forestation, or growing stock of wood (Pekárová et al., 2017).

The evaluation of the longest hydrological drought periods within the 2003, 2012 and 2015 years showed that there are some general similarities among the respective river basins. This was shown by the results of the factor analysis, where three main groups of river basin were estimated. The groups are regionally distributed, creating the group of the northern Slovakian river basins (Poprad, Váh and Oravica), group of the central Slovakian river basins (Hron, Nitra) and the group of the western, southern and eastern Slovakian river basins (Myjava and Kysuca; Žitava, Ipeľ and Rimava; Topľa and Torysa). This could point on differences in physical-geographical conditions in various parts of Slovakia causing differences in the wet/dry air masses movement, average annual/seasonal temperatures and consequently different values of evapotranspiration. All these factors are the important drought influencing conditions.

However, the situation seems more complicated when comparing adjacent river basins in detail, as published by Fendeková et al. (2017a). A detailed study of drought parameters in the Ipeľ and Rimava, and in the Topľa and Torysa River basins was done. Despite of the basins vicinity, there are differences in temporal and spatial manifestation of droughts in 2003, 2012 and 2015. The difference between the Ipeľ and the Rimava River basin consists in the basin area, and consequently in the average annual and minimum discharges. The Ipeľ River basin with the smallest area, lowest altitude and highest air temperature suffered from the 2012 drought which is in a good compliance with the meteorological drought occurrence expressed by the SPEI12 index calculated for the Boľkovce meteorological station. The situation in the Rimava basin was different despite of very similar meteorological drought parameters (Rimavská Sobota meteorological station) to those in the Ipeľ basin. The most pronounced drought period in the Rimava basin occurred in 2003, similarly to the Eastern Slovakian River basins of Torysa and Topľa. However, return periods of drought duration, deficit volume, and deficit volume intensity estimated for the Rimava basin were much lower than those calculated for the Torysa and Topľa basins. There, the basin area and river discharge could contribute to partial balancing the unfavourable climatic conditions.

Drought development in the Kysuca River basin gives another example of different conditions influencing the drought parameters. The Kysuca River basin was the only one basin with the most pronounced drought in all parameters in 2015. This was the most probably caused by the quite dry climatic conditions in the Kysuce region during the four preceding years 2011–2014 (Fendeková et al., 2017b). So, the degree of water saturation of the basin could also play the important role.

Quite good correlation between the meteorological and hydrological droughts occurrence in more than the half of the evaluated river basins was proven. The best results were obtained for the Myjava, Váh, Oravica, Kysuca, Nitra, Hron, Ipeľ and Topľa basins, where the meteorological drought was followed by the hydrological one. The lowest SPI values were obtained in the same year as the majority of the hydrological drought parameters in the respective basin. The drought in 2015 was exceptional in the Kysuca River basin, where the dry conditions since 2011 influenced the highest drought intensity in 2015.

On contrary, the hydrological drought parameters were in contradiction with the meteorological drought occurrence in Žitava, Rimava, Poprad and Torysa River basins. The hydrological drought intensity in the Žitava, Rimava and Poprad River basins in 2003 was the lowest one among the evaluated years, despite of the most pronounced low SPI values. The intensity of hydrological drought was better fitted by the values

of the SPEI index values in the case of the Žitava and Rimava River basins. The specific situation occurred in the Poprad River basin because of quite long, wet period since late 1990s. The situation in the Torysa River basin is also remarkable because the comparable SPI values in all three evaluated years resulted in the comparable drought intensities; however the 2012 drought intensity was a bit higher which was in coincidence with the lowest values of the SPEI in the same year.

The differences in methodology used for meteorological and hydrological drought evaluation within the presented study did not influence the results of the meteorological and hydrological droughts evaluation. However, the mutual comparison of the meteorological and hydrological droughts, as presented above, could be influenced by them. Whilst the SPI and SPEI compare the rainfall/potential evapotranspiration in a monthly step with the long-term value (1981–2010), the SPA method is based on the recovery of the daily discharges after their decrease below a certain threshold, similarly estimated as a long-term value of the same period. In both cases, there is a threshold limiting the drought occurrence – fixed value of the discharge Q_{80} in the case of hydrological drought and fixed limit value for meteorological drought occurrence – value of –1 of the SPI/SPEI. Despite of uncertainties connected to use of the two different methods, the obtained results of meteorological and hydrological droughts occurrence gave a simple picture on relations between the two types of drought in evaluated river basins.

The obtained results are in a good accordance with the results of Laaha et al. (2017). According to conclusions of Laaha et al. (2017), the hydrological drought of 2015 was characterised by a different spatial extent than the drought of 2003. In terms of low flow magnitude, a region around the Czech Republic was most affected with annual low flows in 2015 that exhibited return intervals of 100 years and more. This was also the case of the Kysuca River basin, neighbouring the Moravian part of the Czech Republic, where the highest return periods of all drought parameters were reached in 2015 (Table 4). Comparing the drought onset in 2003 and 2015 (Laaha et al., 2017), this was more dramatic in 2003, covering more quickly and more homogeneously a larger region of Europe. This was also the case of Slovakian river basins, as showed in Fig. 5. According to drought onset and duration, the 2003 drought was consistent over the whole territory of Slovakia. The only exception was the 2003 drought duration in the Kysuca River basin. Laaha et al. (2017) also stated, that the difference in spatio-temporal characteristics of the climatic and hydrological drought can best be explained by diverging conditions in the river basins. They found evidence that extreme droughts emerged as a consequence of dry preconditions in the preceding winter and spring months. Such a conclusion was fully confirmed in the case of the Kysuca River basin drought in 2015.

CONCLUSIONS

The evaluation of three drought periods in Slovakia showed that there is a significant difference between the drought parameters in respective years and evaluated river basins.

In general, considering meteorological drought, the increasing air temperature is resulting in the increasing potential evapotranspiration. The role of the potential evapotranspiration in the assessment of water balance has been evident since the mid-1990s, when the SPEI often reached lower values than the SPI. The most remarkable differences were noted in Poprad, Oravica, Torysa and Topľa River basins, located in the northern and eastern Slovakia.

Despite of generally similar weather conditions in all three evaluated years, the response of assessed river basins differed significantly. The deficit volume parameters during the most extreme drought period were the highest in the majority of evaluated basins in 2003 and 2012. The only exception was the Kysuca River basin, where the year 2015 was the most extreme one.

The summer droughts prevailed within the evaluated drought periods in the territory of Slovakia beginning in late May to June and peaking in July-August period. However, many of evaluated drought periods continued during the winter up to the next year, ending in early spring months. This was the case of the hydrological drought in the Myjava, Váh, Oravica, Kysuca, Poprad and Topľa River basins where the hydrological drought started already in the period between 31 August and 29 October 2011 and lasted until January to March 2012, or of the Topľa and Torysa River basins where the 2015 drought lasted until 13 January 2016 in Torysa and 3 February 2016 in the Topľa River basin.

The results of the study confirmed that according to evaluated drought parameters, the geographical location of the river basin, its climatic conditions, geological conditions, river basin area, discharge conditions and the climatic situation of the preceding years (influencing the water saturation of the basin) are the most important factors of drought occurrence and intensity.

Acknowledgement. The contribution was prepared and supported by the APVV-0089-12 (principal investigator Miriam Fendekova) and by the VEGA No. 2/0009/15 projects. The research also supports the work of the UNESCO-IHP VIII FRIEND-Water programme.

REFERENCES

Alexandersson, H., 1986. A homogeneity test applied to precipitation data. J. Climate, 16, 6, 661–675.

Alexandersson, H., Moberg, A., 1997. Homogenization of Swedish temperature data. Part I: Homogeneity test for linear trends. J. Climate, 17, 1, 25–34.

Andreu, J., Solera, A., Paredes-Arquiola, J., Haro-Monteagudo, D., van Lanen, H.A.J. (Eds.), 2015. Drought: Research and Science-Policy Interfacing. Taylor & Francis Group, London.

Bindoff, N.L., P.A. Stott, K.M. AchutaRao, M.R. Allen, N. Gillett, D. Gutzler, K. Hansingo, G. Hegerl, Y. Hu, S. Jain, I.I. Mokhov, J. Overland, J. Perlwitz, R. Sebbari, Zhang, X., 2013. Detection and Attribution of Climate Change: from Global to Regional. In: Stocker, T.F., Qin, D., Plattner, G.-K., Tignor, M., Allen, S.K., Boschung, J., Nauels, A., Xia, Y., Bex, V., Midgley, P.M. (Eds.): Climate Change 2013: The Physical Science Basis. Contribution of Working Group I to the Fifth Assessment Report of the Intergovernmental Panel on Climate Change Cambridge University Press, Cambridge, United Kingdom and New York, NY, USA.

Ciais, Ph., Reichstein, M., Viovy, N., Granier, A., Ogeé, J., Allard, V., Aubinet, M., Buchmann, N., Bernhofer, C., Carrara, A., Chevallier, F., De Noblet, N., Friend, A., Friedlingstein, P., Grünwald, T., Heinesch, B., Keronen, P., Knohl, A., Krinner, G., Loustau, D., Manca, G., Matteucci, G., Miglietta, F., Ourcival, J.M., Papale, D., Pilegaard, K., Rambal, S., Seufert, G., Soussana, J.F., Sanz, M.J., Schulze, E.D., Vesala, T., Valentini, R., 2005. Europe-wide reduction in primary productivity caused by the heat and drought in 2003. Nature, 437, 529–533. DOI: 10.1038/nature03972.

Cindrić, K., Telišman Prtenjak, M., Herceg-Bulić, I., Mihajlović, D., Pasarić, Z., 2016. Analysis of the extraordinary 2011/2012 drought in Croatia. Theor. Appl. Climatol., 123, 3–4, 503–522.

Corduneanu, F., Bucur, D., Cimpeanu, S.M., Apostol, I.C., Strugariu, A., 2016. Hazards resulting from hydrological extremes in the upstream catchment of the Prut River. Water Resources, 43, 1, 42–47.

European Environmental Agency, 2012. Climate Change, Impacts and Vulnerability in Europe 2012. An Indicator Based Report. EEA Report No. 12/2012. EEA, Copenhagen, 300 p.

Fendeková, M., Danáčová, Z., Gauster, T., Labudová, L., Fendek, M., Horvát, O., 2017a. Analysis of hydrological drought parameters in selected catchments of the southern and eastern Slovakia in the years 2003, 2012 and 2015. Acta Hydrologica Slovaca, 18, 2, 135–144.

Fendeková, M., Gauster, T., Slivová, V., Vrablíková, D., Fendek, M., Labudová, L., Danáčová, Z., 2017b. Surface and groundwater drought in the Kysuca river basin in the three dryiest years of the 21st century. Podzemná voda, 23, 1, 25–37.

Ionita, M., Tallaksen, L. M., Kingston, D. G., Stagge, J. H., Laaha, G., Van Lanen, H. A. J., Scholz, P., Chelcea, S. M., Haslinger, K., 2017. The European 2015 drought from a climatological perspective. Hydrology and Earth System Sciences, 21, 3, 1397–1419.

Kendon, M., Marsh, T., Parry, S., 2013. The 2010–2012 drought in England and Wales. Weather, 68, 88–95.

Laaha, G., Gauster, T., Tallaksen, L.M., Vidal J.-P., Stahl, K., Prudhomme, C., Heudorfer, B., Vlnas, R., Ionita, M., Van Lanen, H.A.J., Adler, M.-J., Caillouet, L., Delus, C., Fendekova, M., Gailliez, S., Hannaford, J., Kingston, D., Van Loon, A.F., Mediero, L., Osuch, M., Romanovicz, R., Sauquet, E., Stagge, J.H., Wong, W.K., 2017. The European drought from a hydrological perspective. Hydrol. Earth Syst. Sci., 21, 3001–3024.

Labudová, L., Faško, P., Ivaňáková, G., 2015. Changes in climate and changing climate regions in Slovakia. Morav. Geogr. Rep., 23, 71–82.

Landscape atlas of the Slovak Republic, 2002. Ministry of the Environment of the Slovak Republic, Bratislava, 344 p.

Marsh, T.J., 2004. The UK drought of 2003: A hydrological review. Weather, 59, 8, 224–230. DOI: 10.1256/wea.79.04.

McKee, T.B., Doesken, N.J., Kleist, J., 1993. The relationship of drought frequency and duration to time scales. In: Proceedings of the 8th Conference on Applied Climatology, 17.–22.1.1993. Anaheim, California, 1993, 179–183.

Melová, K., Lupták, L., 2006. Hydrological evaluation of surface streams in 2001 – 2005 period. Vodohospodársky spravodajca, 50, 1–2, 34–35. (In Slovak.)

Mikhailova, M.V., Mikhailov, V.N., Morozov, V.N., 2012. Extreme hydrological events in the Danube River basin over the last decades. Water Resources, 39, 2, 161–179.

Orth, R., Zscheischler, J., Seneviratne, S. I., 2016. Record dry summer in 2015 challenges precipitation projections in Central Europe. Scientific Reports, 6, 21, Article No. 28334.

Pecho, J., Faško, P., Mikulová, K., Šťastný, P., Nejedlík, P., Košťálová, J., 2010. Comparative analysis of selected snow cover characteristics in Slovakia within the 1950/1951-1979-1980 and 1980/1981–2009/2010 winters. Geophysical Research Abstracts, 12, EGU2010-11543.

Pekárová, P., Miklánek, P., Pekár, J., Pramuk, B., 2017. Identification of the Slovak rivers daily discharge regime changes. Part II Comparison of the two periods. Acta Hydrologica Slovaca, 18, 2, 183–192.

Rebetez, M., Mayer, H., Dupont, O., Schindler, D., Gartner, K., Kropp, J. P., Menzel, A., 2006. Heat and drought 2003 in Europe: a climate synthesis. Ann. For. Sci., 63, 569–577. DOI: 10.1051/forest: 2006043.

Sekáčová, Z., Šťastný, P., Faško, P., Lapin, M., 2004. Extremal manifestations of the weather in Slovakia in 2003. In: Rožnovský, J., Litschmann, T. (Eds): Extremes of weather and climate. Brno, pp. 1–6. ISBN 80-86690-12-1. (In Slovak.)

Slivová, V., Kullman, E., 2016. Evaluation of hydrological year 2015 from the point of view of groundwater. Vodohospodársky Spravodajca, 59, 3–4, 17–19. (In Slovak.)

Stepanek, P., 2003. AnClim - software for time series analysis and homogenization. http://www.climahom.eu/software-solution/anclim

Stojkovic, M., Plavšic, J., Prohaska, S., 2017. Annual and seasonal discharge prediction in the middle Danube River basin based on a modified TIPS (Tendency, Intermittency, Periodicity, Stochasticity) methodology. J. Hydrol. Hydromech., 65, 2, 165–174.

Škoda, P., Blaškovičová, L., Melová, K., 2016. Evaluation of the hydrological year 2015. Vodohospodársky Spravodajca, 59, 3–4, 14–16. (In Slovak.)

Šustek, Z., Vido, J., Škvareninová, J., Škvarenina J., Šurda, P., 2017. Drought impact on ground beetle assemblages (Coleoptera, Carabidae) in Norway spruce forests with different management after windstorm damage – a case study from Tatra Mts. (Slovakia). J. Hydrol. Hydromech., 65, 4, 333–342.

Tallaksen, L.M., Van Lanen, H.A.J. (Eds.), 2004. Hydrological drought: processes and estimation methods for streamflow and groundwater. Developments in Water Science, 48, The Netherlands, Amsterdam, Elsevier Science, 579 p.

Überla, K., 1971. Faktorenanalyse. Eine systematische Einführung für Psychologen, Mediziner, Wirtschafts- und Sozialwissenschaftler. 2 Auflage. Springer, Berlin, 399 p.

Van Lanen, H.A.J., Laaha, G., Kigstnon, D.G., Gauster, T., Ionita, M., Vidal, J.-P., Vlnas, R., Tallaksen, L.M., Stahl, K., Hannaford, J., Delus, C., Fendekova, M., Mediero, L., Prudhomme, C., Rets, E., Romanowicz, R.J., Gailliez, S., Wong, W.K., Adler, M.-J., Blauhut, V., Caillouet, L., Chelcea, S., Frolova, N., Gudmundsson, L., Hanel, M., Haslinger, K., Kireeva, M., Osuch, M., Sauquet, E., Stagge, J.H., Van Loon, A.F., 2016. Hydrology needed to manage droughts: The 2015 European case. Hydrological Processes, 30, 17, 3097–3104.

Vido, J., Střelcová, K., Nalevanková, P., Leštianska, A., Kandrík, R., Pástorová, A., Škvarenina, J., Tadesse, T., 2016. Identifying the relationships of climate and physiological responses of a beech forest using the Standardised Precipitation Index: a case study for Slovakia. J. Hydrol. Hydromech., 64, 3, 246–251.

Vincente-Serrano, S. M., Beguería, S., López-Moreno, J. I., 2010. A Multi-scalar drought index sensitive to global warming: The Standardized Precipitation Evapotranspiration Index – SPEI. Journal of Climate, 23, 1696–1718.

WMO, 2004. WMO Statement on the Status of the Global Climate in 2003. World Meteorological Organization, WMO-No. 966, Geneva, Switzerland, 2004, 11 p., ISBN 92-63-10966-4.

WMO, 2013. WMO Statement on the Status of the Global Climate in 2012. World Meteorological Organization, WMO-No. 1108, Geneva, Switzerland, 2013, 33 p., ISBN 978-92-63-11108-1.

WMO, 2016. WMO Statement on the Status of the Global Climate in 2015. World Meteorological Organization, WMO-No. 1167, Geneva, Switzerland, 2016, 23 p., ISBN 978-92-63-11189-0. www.shmu.sk

Zahradníček, P., Trnka, M., Brázdil, R., Možný, M., Štěpánek, P., Hlavinka, P., Žalud, Z., Malý, A., Semerádová, D., Dobrovolný, P., Dubrovský, M., Řezníčková, L., 2015. The extreme drought episode of August 2011–May 2012 in the Czech Republic. International Journal of Climatology, 35, 11, 3335–3352.

Zahradníček, P., Štepánek, P., Trnka, M., Farda, A., 2016. Projevy změny klimatu na území České republiky. In: Rožnovský, J., Vopravil, J. (Eds.): Půdní a zemědelské sucho (28.–29.4.2016 Kutná Hora, ČR). Výskumný ústav meliorací a ochrany půdy, Praha.

Received 21 July 2017
Accepted 2 January 2018

J. Hydrol. Hydromech., 66, 2018, 4, 404–415
DOI: 10.2478/johh-2018-0032

Comparison of two concepts for assessment of sediment transport in small agricultural catchments

Kamila Hlavčová[1*], Silvia Kohnová[1], Yvetta Velísková[2], Zuzana Studvová[1], Valentin Sočuvka[2], Peter Ivan[1, 3]

[1] Slovak University of Technology, Faculty of Civil Engineering, Department of Land and Water Resources Management, Radlinského 11, SK 810 05 Bratislava, Slovakia. E-mail: silvia.kohnova@stuba.sk
[2] Institute of Hydrology, SAS, Dúbravská cesta 9, 841 04 Bratislava, Slovakia. E-mail: veliskova@uh.sav.sk
[3] Slovak Water Management Enterprise, Koháryho 44, 934 80 Levice, Slovakia.
[*] Corresponding author. E-mail: kamila.hlavcova@stuba.sk

Abstract: The erosion, transport and deposition of sediments in small valley reservoirs represent a significant impact on their operations, mainly with regard to reducing the volume of their accumulation. The aim of this study is a comparison and uncertainty analysis of two modelling concepts for assessment of soil loss and sediment transport in a small agricultural catchment, with an emphasis on estimating the off-site effects of soil erosion resulted in sedimentation of a small water reservoir. The small water reservoir (polder) of Svacenicky Creek which was built in 2012, is a part of the flood protection measures in Turá Lúka and is located in the western part of Slovakia, close to the town of Myjava. The town of Myjava in recent years has been threatened by frequent floods, which have caused heavy material losses and significantly limited the quality of life of the local residents. To estimate the amount of soil loss and sediments transported from the basin, we applied two modelling concepts based on the USLE/SDR and WaTEM/SEDEM erosion models and validated the results with the actual bathymetry of the polder. The measurements were provided by a modern Autonomous Underwater Vehicle (AUV) hydrographic instrument. From the sediment data measured and the original geodetic survey of the terrain conducted at the time of the construction of the polder, we calculated changes in the storage volume of the polder during its four years of operation. The results show that in the given area, there has been a gradual clogging of the bottom of the polder caused by water erosion. We estimate that within the four years of the acceptance run, 10,494 m^3 of bottom sediments on the Svacenicky Creek polder have accumulated. It therefore follows that repeated surveying of the sedimentation is very important for the management of the water reservoir.

Keywords: Soil erosion; Reservoir storage volume; Sediment; Bathymetry, Svacenicky Creek.

INTRODUCTION

Erosion and sediment transport and deposition are major environmental issues that affect society through soil loss, reduction of the capacity of reservoirs, and intensification of both water pollution and floods (Abril and Knight, 2004; Fasching and Bauder, 2001; Lane et al., 1997; Nelson and Booth, 2002; van Rompaey et al., 2001; Walling, 1983). The problem of soil erosion is closely related to flash floods and muddy floods which generally occur in small to medium-sized basins (Hlavčová et al., 2016).

Soil erosion by water causes the greatest loss of soil in Europe compared to other soil degradation processes. It is one of the most widespread forms of soil degradation (Boardman and Poesen, 2006; Bosco et al., 2015) and can lead not only to soil loss but also to other soil threats, such as the breakdown of soil structure, reduction of water-holding capacity (Hlaváčiková et al., 2018), and declines in organic matter and nutrient contents. During the past decade, the problem of soil erosion has become part of the environmental agenda in the European Union (EU) due to its impacts on food production, drinking water quality, ecosystem services, mud floods, eutrophication and biodiversity (Boardman and Poesen, 2006). It is listed in the Soil Thematic Strategy of the European Commission (EC, 2006) as one of the eight threats to soil. Recent policy developments formulated by the European Commission (the Soil Thematic Strategy, the Common Agricultural Policy, Europe 2020, and the 7th Environmental Action Programme) have called for quantitative assessments of soil loss intensity at the European level (Panagos et al., 2015a).

The processes of soil erosion by water consist of the detachment of soil particles by the kinetic energy of raindrops or overland flow, the transport of the detached soil particles by overland flow, and sediment deposition. The main kinds of water erosion are sheet, rill, gully and in-stream erosion. Sheet erosion induces a uniform detachment of soil, so that soil particles from the surface are evenly distributed across a slope (Hairsine and Rose, 1992). Rill erosion occurs when water flowing over a soil surface flows along preferential pathways and forms easily recognisable channels (Rose, 1993). Rills are small erosion channels which can be eliminated by tillage. The flow in rills is a transporting agent for the removal of sediment downslope from rill and interill sources, although if the shear stress in the rill is high enough, the rill flow may also detach significant amounts of soil (Nearing et al., 1994). Sheet and rill erosion can be considered as overland flow erosion; both processes are often analysed together in the modelling of erosion (Merritt et al., 2003). Gully erosion forms channels of concentrated flow that are too deep to be obliterated by cultivation (Rose, 1993).

The analysis and quantification of soil erosion processes and the assessment of their impact on soil loss and the quality of water on slope, catchment or regional scales are required by water managers and catchment stakeholders. Various erosion models have been developed to predict soil erosion intensities by water. These models differ greatly in terms of their complexity, inputs, and spatial and temporal scales, so that different modelling approaches can lead to significantly different soil erosion rates even when the same model is applied within the

same region (Shen et al., 2009). The heterogeneity of the models also affects the processes they represent, the manner in which these processes are represented, and the types of output information they provide (de Vente et al., 2013). Therefore, research is needed to improve methods for estimating soil erosion rates using modelling approaches upon which mitigation strategies can be assessed and implemented (Bosco et al., 2015). Models for estimating the soil erosion of large areas, e.g., PESERA (Kirkby et al., 2008), that require input data with a sufficient degree of accuracy may not always be available for large spatial extents (Jones et al., 2003). A comprehensive review of erosion and sediment transport models was done by Merritt et al. (2003). He characterised various existing erosion models based on empirical, conceptual, and physical bases. Empirical models are usually based on an analysis of observations, and data requirements for such models are less than for conceptual and physically-based models. The parameters used in empirical models may be obtained by calibration, and they are often transferred from calibrations at experimental sites (Merritt et al., 2003). The most widely-used empirical erosion models for estimating long-term mean annual soil loss by sheet and rill erosion are the Universal Soil Loss Equation USLE (Wischmeier and Smith, 1978) and its revised versions, e.g., RUSLE (Renard et al., 1997).

Conceptual models (e.g., AGNPS, WaTEM/SEDEM) describe general catchment processes; because of the simplification of interactions between them, they do not require detailed catchment data. Various developed conceptual models have provided outputs in a spatially distributed way. Physically-based models (e.g., LISEM, TOPOG, WEPP) are based on the solution of fundamental physical equations describing runoff and sediment transport processes. The parameters used in physically-based models are measurable, but the large number of parameters means that these parameters must often be calibrated against observed data (Beck et al., 1995).

The rate of erosion and sediment transport from a catchment can also be determined by estimating sediment yields, which can be quantified in various ways, i.e., from reconnaissance methods through the use of catch pits for measurements of the flow and sediment loads or from the quantities of sediment trapped in water reservoirs. Many of the problems associated with sampling river sediments can be avoided when data derived from reservoir surveys are used to estimate sediment yields (Lawrence, 1996). Reservoir surveys are usually carried out to determine the rate at which storage is being lost due to sedimentation and to provide information on changes in the storage volume curve. But the data derived from surveys can also be used to estimate catchment sediment yields. This kind of survey can be performed by "dry survey techniques" (when a reservoir is dry) or "wet survey techniques" (hydrographical survey). Autonomous Underwater Vehicles (AUVs) have recently become available as an effective tool or device for hydrographical surveys which investigate the bathymetry of a reservoir in high resolution (Wynn et al., 2014).

The objective of this study is a comparison and uncertainty analysis of two modelling concepts for assessment of soil loss and sediment transport in a small agricultural catchment, with an emphasis on estimating the off-site effects of soil erosion resulted in sedimentation of a small water reservoir. The methodology for validation of both modelling approaches by comparing sediment transport from a catchment with sediment yields in a small water reservoir is developed. The possibilities for reducing erosion processes by land and crop management are discussed.

The paper is structured in the following way: A brief introduction of the problems studied is presented in Chapter 1. In Chapter 2 the methodology used is described. We characterise the USLE, SDR and WaTEM/SEDEM models for estimating the soil erosion and sediment transport on a catchment scale and the methodology for measurement of bed sediment loads in a small water reservoir using the AUV EcoMapper device. Chapter 3 describes the study area of the Svacenicky Creek catchment and the Svacenicky Creek polder and the input data for modelling the soil erosion and sediment transport and for modelling the bathymetry of the polder (mission planning). Chapter 4 contains the results of modelling the soil erosion and sediment transport by the USLE/SDR and WaTEM/SEDEM models and the results of the polder bathymetry. A comparison of the modelled sediment transport to the polder with the measured bed sediment loads is provided. Chapter 5 discusses the results and states our conclusions.

METHODS

Modelling of soil loss and sediment transport

Two modelling approaches were applied for quantifying the soil erosion by water on a catchment scale. First, the mean annual soil loss and sediment transport from the catchment were estimated by the Universal Soil Loss Equation (USLE) and the Sediment Delivery Ratio (SDR) model. The second approach was presented by the WaTEM/SEDEM spatially-distributed soil erosion and sediment delivery model.

The Universal Soil Loss Equation (USLE) is an empirical model which can be used to estimate soil loss with an emphasis on sheet and rill erosion, without taking into account the sediment transport and deposition. In the modified version of USLE with the LS topographical factor, the mean annual soil loss is calculated according to the equation:

$$E = R \cdot K \cdot LS \cdot C \cdot P \tag{1}$$

where E is the mean annual soil loss (t ha^{-1} year^{-1}); K is the soil erodibility factor (t ha^{-1} year^{-1} on one unit of R); R is the rainfall erosivity factor (MJ ha^{-1} cm h^{-1}); LS is the topographical factor (–); C is the vegetation cover factor (–); and P is the erosion control measure factor (–). The R factor represents the long-term value of rain erosivity on a yearly basis. The K factor depends on soil properties such as soil texture and structure, the content of organic matter, and soil permeability. The LS factor is a representation of the spatial variability of soil erosion caused by the topography. The L factor is a measure of slope length, and the S factor is proportional to the local slope.

The USLE2D methodology was applied to calculate the LS topographical factor. In the USLE2D the LS factor is derived for closed eroded units (parcels) based on a raster digital elevation model. The raster structure of the digital elevation model allows for taking into account a slope's variability in the separate cells of a square grid area, together with increasing the slope's length in the direction of the surface runoff. Increasing the slope length in the model is expressed by a unit contributing area, which is defined by several algorithms.

The basic expression of the relationship between the length and steepness of a slope was defined by Foster and Wischmeier (1974). The formula for the topographic factor of an irregular slope has the shape:

$$LS = \sum_{j=1}^{N} \frac{S_j \cdot \lambda_j^{m+1} - S_j \cdot \lambda_{j-1}^{m+1}}{\left(\lambda_j - \lambda_{j-1}\right) \cdot (22.13)^m} \tag{2}$$

where S_j – factor of the slope's steepness for the j-th element (m m^{-1}),
λ_j – the length between the lower boundary of the j-th element and the upslope field boundary (m),
m – the slope length exponent.

The equation can be expanded to a three-dimensional topography:

$$LS = \sum_{i,j} \frac{S(i,j)\cdot\lambda(i,j)_{outlet}^{m+1} - S(i,j)\cdot\lambda(i,j)_{inlet}^{m+1}}{\left(\lambda(i,j)_{outlet}^{m+1} - \lambda(i,j)_{inlet}^{m+1}\right)\cdot(22.13)^{m}} \quad (3)$$

where LS – the topographical factor for one parcel or a whole river basin,
$\lambda(i,j)$ – the slope length at the input for the i-, j-th grid cell (m),
$\lambda(i,j)$ – the slope length at the output for the i-, j-th grid cell (m),
$S(i,j)$ – the slope factor for the i-, j-th grid cell,
m – the slope length exponent.

The factor of the slope's steepness for individual cells is expressed by several algorithms:

Wischmeier and Smith`s relationship (1978):

$$S(i,j) = 65.41 \cdot \sin^2 \theta_{i,j} + 4.56 \cdot \sin \theta_{i,j} + 0.065 \quad (4)$$

McCool`s relationship (McCool et al., 1989), which was used in RUSLE:

$$S(i,j) = 10.8 \cdot \sin \theta_{i,j} + 0.03 \text{ where } \theta_{i,j} \leq 9\% \quad (5)$$

$$S(i,j) = 16.8 \cdot \sin \theta_{i,j} - 0.5 \text{ where } \theta_{i,j} > 9\% \quad (6)$$

Gowers`s expression (Desmed and Govers, 1996):

$$S(i,j) = (\tan \theta_{i,j} / 0.09)^{1.45} \quad (7)$$

Nearing`s formula for a slope`s steepness is expressed in the form:

$$S = -1.5 + \frac{17}{\left(1 + e^{\left[2.3 - 6.1\cdot\sin(\theta)\right]}\right)} \quad (8)$$

The USLE model does not take into account the sediment transport and deposition. Therefore, the sediment transport was estimated using the Sediment Delivery Ratio (SDR) model by Wiliams (1977). The SDR calculates the percentage of total soil loss that is delivered to a catchment outlet by the equation:

$$SDR = 1.366\cdot10^{-11} \cdot A^{-0.0998} \cdot S_r^{0.3629} \cdot CN^{5.444} \quad (9)$$

where A – the catchment area (km^2),
Sr – the relief ratio (m km^{-1}), it is the ratio between the difference in elevations in a catchment divide and outlet, and the longest route of the flow path,
CN – the average SCS curve number of the catchment.

The mean annual sediment transport is then estimated by multiplication of the mean annual catchment's soil loss and the catchment's SDR value (Janeček, 2007).

The second modelling approach is represented by the WaTEM/SEDEM spatially distributed soil erosion and sediment delivery model developed at the Physical and Regional Geography Research Group of KU Leuven (Van Oost et al., 2000; Van Rompaey et al., 2001; Verstraeten et al., 2002). The model consists of two submodels that calculate water and tillage erosion, including sediment delivery to rivers, using proportional, multiple-flow calculations of transport capacity. In the first submodel the soil loss is estimated by the RUSLE equation (Renard et al., 1991, 1994). Unlike RUSLE, WaTEM/SEDEM works with a 2D approach to the topographical factor. The algorithm (Desmet and Govers, 1996) uses a digital elevation model and a parcel map and was adjusted by Takken et al. (2001) so that the direction of the tillage is taken into account. The location of roads is also included, i.e., water on a road will always follow that road to the lowest point. Both topographical parameters are derived from a DEM (Verstraeten and Poesen, 2001).

The second submodel of WaTEM/SEDEM is the calculation of the sediment transport and sedimentation. It calculates the amount of sediments that is exported towards surface water. This is done by routing the sediments towards the surface water and taking into account the possible deposition of sediments. This deposition is controlled by the transport capacity (Tc), which is calculated for each pixel. The transport capacity is the maximal amount of sediments that can pass through one pixel. WaTEM/SEDEM has two ways of calculating the Tc, i.e., proportional and non-proportional. All the versions of the model except for WaTEM/SEDEM 2005 assume that the transport capacity is proportional to the volume of the potential gully erosion (Van Rompay et al., 2001):

$$Tc = ktc \cdot Eprg = ktc \cdot R \cdot K \cdot \left(LS - 4.12 \cdot Sg^{0.8}\right) \quad (10)$$

where ktc – transport capacity coefficient,
$Eprg$ – potential gully erosion,
Sg – local slope (m m^{-1}),
R, K and LS are the factors from the RUSLE equation.

The values of ktc should be calibrated and validated to use the model. Several sets of calibrated parameters are available. For each land use type, transport capacity can be different. Using sediment yield data for 26 catchments in the Belgian Loess Belt, Van Rompaey et al. (2001) calibrated a transport capacity coefficient for arable land and for non-erodible land surfaces such as pastures or forests. These values are respectively 75 and 42. However, since the first calibration phase of WaTEM/SEDEM, some changes have been made to the model, and a new calibration points out that the values are 200 and 100 respectively for the following PTEF and parcel connectivity values (PTEF arable land: 0; forest & pasture: 75; parcel connectivity arable land: 10; forest & pasture 75). For other areas, new values of ktc need to be calibrated first. In WaTEM/SEDEM, a threshold C-factor value needs to be given to indicate for which areas the high ktc needs to be used. This threshold is set at 0.1. A transport capacity map will then be created using the C-factor map. Roads are given a very high ktc such that no sediment deposition is modelled on road surfaces.

Measurement of the sediment yields in the water reservoir

The bathymetry measurement of the polder

For the hydrographic research and data mapping of the Svacenicky polder, the Autonomous Underwater Vehicle (AUV) EcoMapper device was used. AUVs represent devices which are currently used in a wide range of hydrographic research, marine geoscience, and the military, commercial, and policy sectors. In general, they have the shape of a torpedo and were originally developed for military purposes. The first AUV was developed at the Applied Physics Laboratory at the University of Washington as early as 1957. The vehicle was used to study

diffusion, acoustic transmissions and submarine wakes (Vijay, 2011). During the 1980s, AUVs were also used for water exploration and hydrographic surveys. One of the most significant instruments is IFREMER L'Epaulard, which was built by ECA Group in association with the French Oceanology Research Institute in the 1980s. IFREMER L'Epaulard was used for oceanographic surveys with a depth range of up to 6000 m. In subsequent years the research and development of new AUV devices have allowed for their use in inland conditions and have also increased the range of the measurements of biological and geochemical parameters.

EcoMapper represents a device which is capable of moving on surface and subsurface water levels independently and performing data logging. This device is ideal for coastal and shallow water applications such as hydrographic surveys and spatial environmental monitoring. A survey mission by EcoMapper can be performed in water with a depth of more than one meter, and it is fully capable of subsurface operations down to 100 m. EcoMapper was developed by YSI Company (USA) and is designed for the quick and easy collection of bathymetric, sonar, and water quality data.

The EcoMapper device consists of a hardware part (Fig. 1) and the Vector Maps software program, which is designed for mission planning and for the partial analysis of measured data. Physically, the vehicle can be divided into 3 distinct parts. The bow section contains water quality sensors that interact with the aquatic environment and a Dopler Velocity Log (DVL) for navigation under water. The middle section includes an onboard computer, electronic components, batteries, and weights to balance the vehicle. The tail section contains a propulsion system and GPS antennas for navigating on the water's surface (YSI, 2009).

While it is measuring (its mission), the Ecomapper collects predetermined parameters every second; they are automatically associated with geographic coordinates (latitude, longitude). Water quality measurements include information such as the water temperature, dissolved oxygen, turbidity, pH, chlorophyll, salinity, etc. Measuring the depth of the bottom (bathymetry) is carried out by an integrated single beam echo-sounder. The device uses a frequency of 500 kHz and has a range of measurement depth from 1 to 100 m and a measurement accuracy ± 0.003 m.

Mission planning

The EcoMapper follows a predefined mission plan created by the user. This mission plan is created in the graphic user environment of the Vector Map Software. Mission planning starts by downloading available geo-referenced charts, maps or satellite images into the Vector Maps planning software and then clicking the position of waypoints for the vehicle's navigation (Fig. 4).

The mission planning includes set points for each leg to a waypoint, speed, depth or undulate for data collection. Additionally, operators can click and drag any waypoints to edit a mission. This simple but powerful tool lets you program the vehicle and sensor parameters for each leg or for a complete survey.

The programme output is an ASCII mission file that is uploaded to the EcoMapper via a wireless interface prior to the mission's start. Once the vehicle has started its mission, it operates independently and uses GPS waypoints and DVL navigation to complete its programmed course. Throughout the course, the vehicle constantly steers toward the line drawn in the mission planning software (VectorMap) and essentially follows a more accurate course of coordinates instead of transversing waypoint-to-waypoint. Upon completing its mission, the vehicle uses Windows® Remote Desktop to relay the collected data via a WiFi connection, which is facilitated by the Communications Box, to the user's computer (YSI, 2009).

DESCRIPTION OF THE CATCHMENT AND INPUT DATA

The catchment of the Svacenicky Creek with its area of 8.61 km^2 is located in the Myjava River basin (Korbeľová and Kohnová, 2017; Valent et al., 2016) in Western Slovakia (Fig. 2a). The creek has a length of 5.4 km and is a right-hand tributary of the Myjava River, which it joins near the Turá Lúka site at an altitude of 308 m a.s.l. The spring of the creek lies on the boundary between the White Carpathian Mountains and the Myjava Hill Land, eastward to a ground elevation of 507.9 m a.s.l. and northward to the Zimovci settlement at an altitude of 460 m a.s.l. The Svacenicky Creek flows into the Myjava River at 69.0 river km, close to Turá Lúka.

For modelling the erosion and sediment transport, the catchment's outlet at the Svacenicky Creek polder was considered. The area of the catchment to the polder is 626.32 ha, with 513.32 ha of arable land (81.96% of the area), 46.45 ha of forest (7.42%), 46.78 ha of urban areas (7.47%), 9.01 ha of roads (1.44%) and 10.76 ha of water bodies/rivers (1.72%).

The Svacenicky Creek polder is a part of the flood protection measures in Turá Lúka and is located near the outlet of the Svacenicky Creek (Fig. 2b). The Svacenicky Creek polder, which was built in 2012, can reduce a 100-year maximum design flood of 16.00 m^3 s^{-1} to 0.21 m^3 s^{-1}. The volume of the polder according to the project is 215,808 m^3, and it is able to retain a flood wave of 207,330 m^3. The levee of the polder has been constructed as a homogenous embankment dam built from impervious clay soils. The embankment dam is 147 m long and has a width of 4.5 m. The shape of the dam has an upstream slope inclination of 1:2.5 and a slope gradient of 1:3.0 on the downstream slope. The close vicinity of the polder is covered with oak-beech woods, beech-oak woods and alder woods.

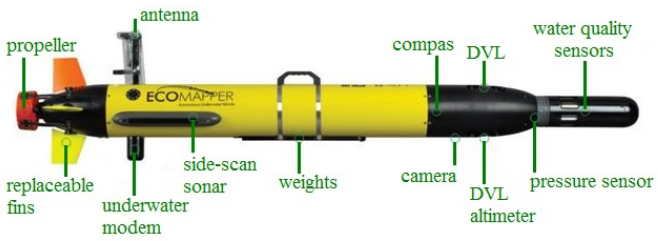

Fig. 1. YSI EcoMapper side view (YSI, 2009).

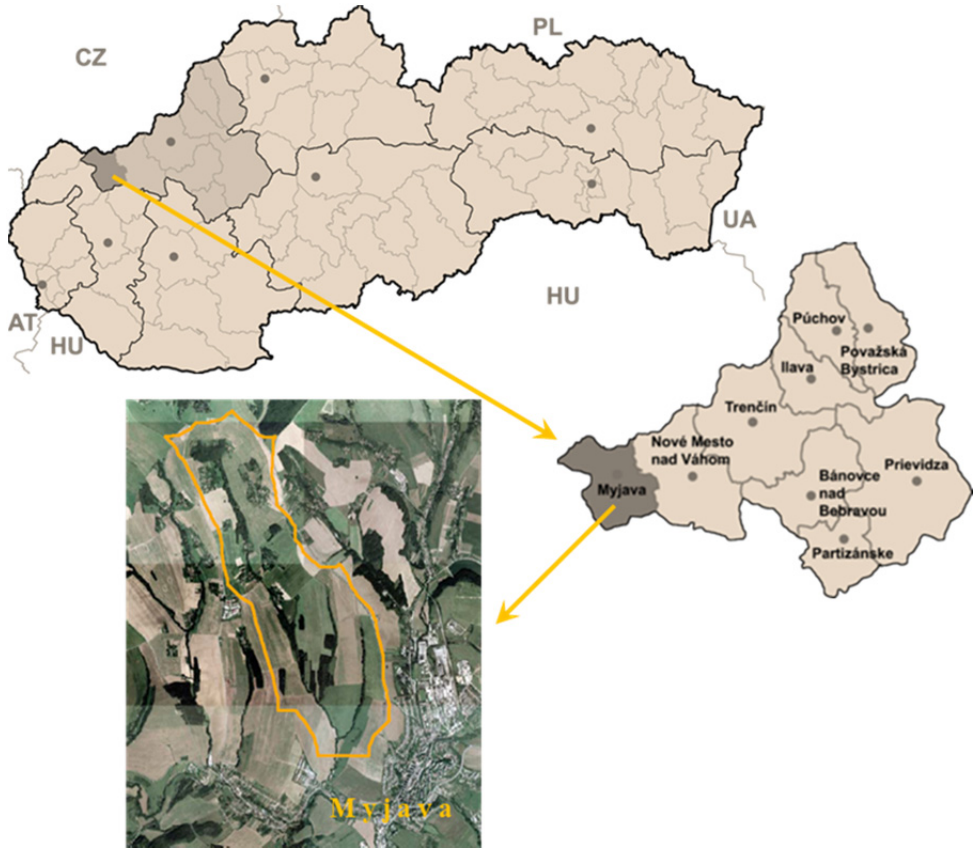

Fig. 2a. Locations of the the Svacenicky Creek basin.

Fig. 2b. The Svacenicky Creek polder and flooded area.

Input data for modelling the soil erosion and sediment transport

For modelling the soil erosion and sediment transport, the morphological, hydrological, land use and soil data were prepared. The morphological data were represented by a digital elevation model with a raster size of 10 m x 10 m (Fig. 3a). The precipitation data were represented by the rainfall erosivity factor R (MJ ha^{-1} cm h^{-1}) = 30 (Malíšek, 1990). The soil data were represented by a map of the soil erodibility factor, which was developed from a soil texture map with values of K (t ha^{-1} year^{-1} on one unit of R) = 0.45 for loamy soils and K = 0.60 for clay-loamy soils (Alena, 1991). The land use data was entered into the modelling in the form of vegetation factor C (–) with values of C = 0 for forested areas and grasslands and different C values for the various crops considered: C = 1 for bare soil, C = 0.72 for maize for silage, C = 0.61 for maize for grain, C = 0.12 for winter wheat and C = 0.22 for winter rapeseed (Alena, 1991). For modelling the soil erosion using the WaTEM/SEDEM model, a map of parcels with arable lands, roads and a generated river network was created from the land use map (Fig. 3b).

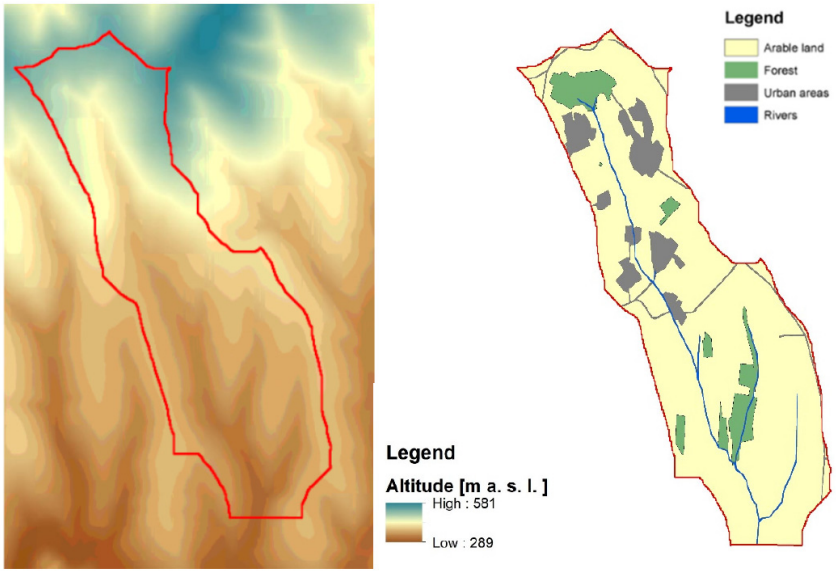

a) b)

Fig. 3. The Svacenicky Creek catchment a) Digital elevation model b) Land use map.

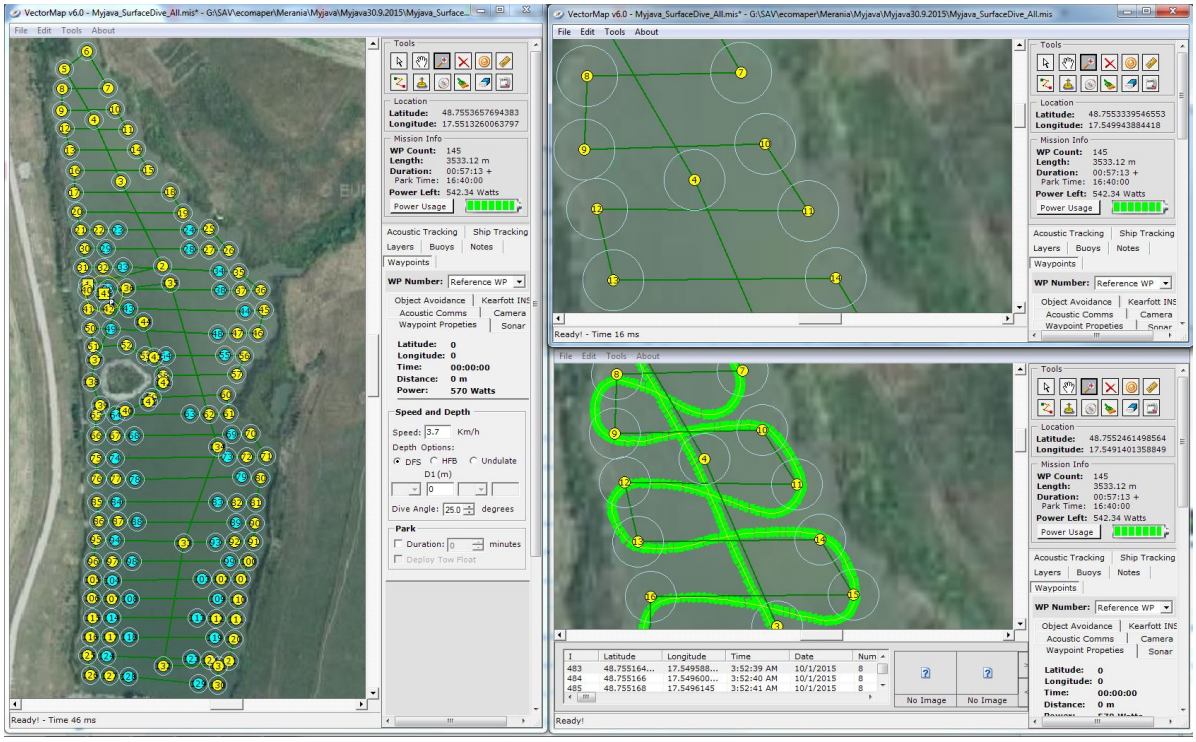

Fig. 4. Mission planning using the VectorMap software program.

Data for the polder bathymetry – mission planning

The hydrographic survey of the Svacenicky Creek polder was carried out in two stages. In the first stage, on 22.09.2015, a preliminary survey of the polder using the EcoMapper device was conducted; the measurements were only taken on the water surface of the polder. In the second stage (30.9.2015) more detailed research was carried out by where the measurements took place alternately from the water surface and from a depth of 0.5 meters below the surface. The aim was to obtain in-depth data, water quality parameters, and images of the polder's bottom to create a database of this information. Water level during measurement was of 316.45 m. a.s.l.

The mission represents 84 navigation points (Fig. 4). During the first measurement a certain distance had to be kept from the polder's shore, due to the dense vegetation and shallow depth, especially in the northern part of the polder. After entering the navigation points, cross sections at distances of 10–12 meters were created. The total length of the measurement was 2878.97 m. The EcoMapper velocity was set at 3.7 km h^{-1}, wherein one measurement took about 47 minutes. The collecting intervals of the qualitative and depth data were set at 1 second. The total amount of data collected during the measurement of the water level was 3004 values for each parameter. Based on the evaluation of the first phase of the measurement, the navigation points in the second mission were extended to a

total of 145. This amount includes the points used during the underwater measurements. The total length measured during the second stage was 3533.12 m; the velocity remained at 3.7 km h^{-1}. The mission lasted 57 minutes, and the total amount of data collected was 3413 values for all the parameters measured.

RESULTS

Modelling the soil erosion and sediment transport from the Svacenicky Creek basin

The results of modelling the erosion and sediment transport from the Svacenicky Creek catchment (to the outlet of the polder) are presented in the form of erosion/sediment deposition maps (WaTEM/SEDEM) and in tables with the total mean annual soil loss in (t ha^{-1} $year^{-1}$) and (t $year^{-1}$) and the total mean annual sediment transport to the catchment outlet (polder) in (t $year^{-1}$). The erosion/sediment deposition maps for the bare soil and the winter wheat are shown in Figs. 5 and 6. The maps illustrate the spatial distribution of the erosion (soil loss) and sediment deposition in (t ha^{-1} $year^{-1}$) calculated by the WaTEM/SEDEM model and the various algorithms for estimating the LS factor.

Tables 1 and 2 present the results of the mean annual soil loss for the selected crops and the bare soil in (t ha^{-1} $year^{-1}$) and (t $years^{-1}$), respectively. The comparison shows that the greatest intensities of soil loss were achieved by the bare soil without vegetation and from the planting of maize for silage. The lowest values were achieved from the planting of winter wheat.

In both tables "WS" is the LS algorithm developed by Wischmeier-Smith; "Mc Cool-l", "Mc Cool-m" and "Mc Cool-h" are algorithms developed by Mc Cool low, Mc Cool moderate, and Mc Cool high; "Nearing-WS" is the LS algorithm developed by Nearing and Wischmeier Smith; and "Nearing-Mc" is the LS algorithm developed by Nearing and Mc Cool.

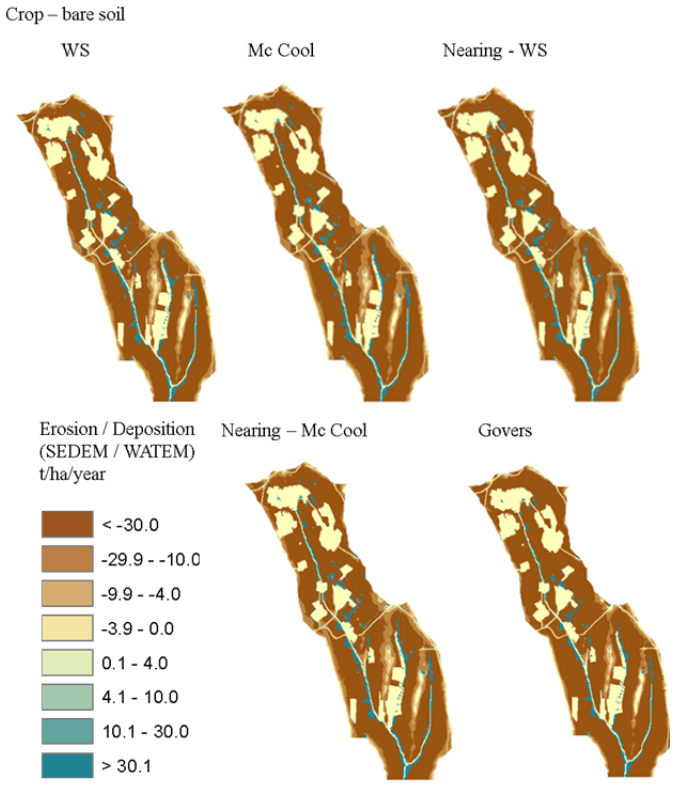

Fig. 5. The erosion/sediment deposition maps for the bare soil (t ha^{-1} $year^{-1}$).

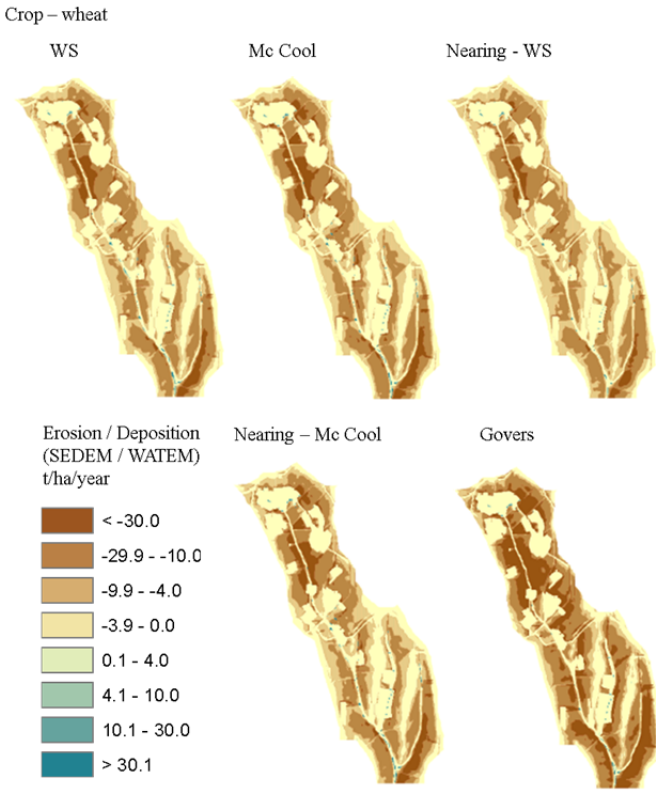

Fig. 6. The erosion/sediment deposition maps for the winter wheat (t ha^{-1} $year^{-1}$).

Table 1. Comparison of the mean annual soil loss (t ha^{-1} $year^{-1}$) according to the USLE and WaTEM/SEDEM models and various LS algorithms.

Model	LS algorithm	Soil loss (t ha^{-1} $year^{-1}$)				
		Winter wheat	Winter rapeseed	Maize for corn	Maize for silage	Bare soil
USLE	WS	8.93	16.38	45.41	53.60	74.45
USLE	Mc Cool-l	6.17	11.32	31.37	37.03	51.43
USLE	Mc Cool-m	9.74	17.85	49.49	58.41	81.13
USLE	Mc Cool-h	14.79	27.11	75.18	88.74	123.24
USLE	Nearing-WS	7.86	14.41	39.97	47.18	65.52
USLE	Nearing-Mc	9.43	17.29	47.95	56.60	78.61
WaTEM/SEDEM	WS	11.15	20.35	54.77	63.70	84.95
WaTEM/SEDEM	Mc Cool	12 .44	22.73	61.35	71.53	95.66
WaTEM/SEDEM	Nearing-WS	9.78	17.87	48.03	55.82	74.05
WaTEM/SEDEM	Nearing-Mc	12.06	22.03	59.44	69.30	92.64
	Mean value	**10.29**	**18.76**	**51.30**	**60.19**	**82.17**

Table 2. Comparison of the total mean annual soil loss (t year^{-1}) according to the USLE and WaTEM/SEDEM models and various LS algorithms.

Model	LS algorithm	Total soil loss (t year^{-1})				
		Winter wheat	Winter rapeseed	Maize for corn	Maize for silage	Bare soil
USLE	WS	5998.18	10996.66	30490.75	35989.08	49984.84
USLE	Mc Cool-l	4143.78	7596.93	21064.22	24862.68	34531.50
USLE	Mc Cool-m	6535.93	11982.54	33224.31	39215.58	54466.08
USLE	Mc Cool-h	9929.27	18203.66	50473.78	59575.61	82743.89
USLE	Nearing-WS	5278.79	9677.79	26833.87	31672.76	43989.95
USLE	Nearing-MC	6333.40	11611.23	32194.79	38000.40	52778.34
WaTEM/SEDEM	WS	6980.55	12747.10	34300.43	39896.88	53206.72
WaTEM/SEDEM	Mc Cool	7793.53	14234.29	38425.35	44798.68	59911.48
WaTEM/SEDEM	Nearing-WS	6128.32	11193.59	30084.17	34963.18	46379.28
WaTEM/SEDEM	Nearing-Mc	7552.26	13794.84	37231.19	43406.48	58020.42
	Mean value	**6667.40**	**12203.86**	**33432.29**	**39238.13**	**53601.25**

The mean annual amount of sediments transported from the catchment of the Svacenicky Creek to the catchment's outlet (polder) was estimated by the USLE and the "Sediment Delivery Ratio" (SDR) models (USLE/SDR) and by the WaTEM/SEDEM model.

The SDR was calculated as a function of the CN values, the catchment area, and the relief ratio (Table 3). It presents the ratio of the total soil loss from the catchment area which can be transported to the outlet of the catchment.

Table 3. Values for estimation of SDR.

	RP	CN	SDR (–)
Winter wheat	16.76	72.94	0.45
Maize	16.76	77.04	0.60
Bare soil	16.76	82.78	0.89

The values of the mean annual amount of the sediments transported to the catchment outlet estimated by the USLE/SDR and WaTEM/SEDEM models and various algorithms for the estimation of the LS factor are presented in Table 4.

Table 4. Total sediment transport to the catchment outlet (polder) in (t year^{-1}).

Mean annual sediment transport (t year^{-1})				
Model	Algorithm	Winter wheat	Maize	Bare soil
USLE/SDR	WS	2684.36	18374.76	44536.2
USLE/SDR	Mc Cool-l	1854.46	12694.01	30767.36
USLE/SDR	Mc Cool_m	2925.02	20022.09	48528.96
USLE/SDR	Mc Cool-h	4443.64	30417.21	73724.32
USLE/SDR	Nearing-WS	2362.42	16171.00	39194.79
USLE/SDR	Nearing-Mc	2834.38	19401.67	47025.19
WaTEM/SEDEM	WS	3771.95	11269.06	12834.55
WaTEM/SEDEM	Mc Cool	4173.95	12122.90	13897.52
WaTEM/SEDEM	Nearing-WS	3425.74	11150.58	13003.83
WaTEM/SEDEM	Nearing-Mc	4031.43	11676.03	13326.17
	Mean value	**3250.74**	**16329.93**	**33683.89**

From the results of estimation of mean annual and total soil loss presented in the Tables 1 and 2 we can conclude, that the results by Mc Cool-h provide always the highest values compared to other methods which have comparable results. The lowest values were achieved using the Mc Cool-l algorithm. The greatest intensities of soil loss were achieved by the bare soil without vegetation (from 51.43 to 123.24 t ha^{-1} year^{-1}) and from the planting of maize for silage (from 37.03 to 88.74 t ha^{-1} year^{-1}). The lowest values were achieved from the planting of winter wheat (from 6.17 to 14.79 ha^{-1} year^{-1}).

The total mean annual sediment transport to the polder for the soil without vegetation varied from 12,834 to 73,724 t year^{-1} and for the winter wheat from 1,854 t year^{-1} to 4,443 t year$^{-1,}$ (Table 4).

Measurement of the sediment yields in the polder

The geodetic points measured during the polder´s construction were first used for the creation of a digital terrain model to characterize the original morphology of the polder bed. The geodetic points of the dike and regulated river above and below the dike were then measured in December 2010. The geodetic points of the road and the polder's bed were measured in May 2011.

The polder's bed was only modelled in the flooded area during the bathymetry measurement on September 22, 2015, when a water level height of 316.45 m. a.s.l. was estimated. A resolution of 1 square meter per cell of the digital terrain model was chosen. The digital terrain model created is shown in Fig. 7.

The network of points determing the current bed with sediments is the output that came from the bathymetry measurements (Fig. 8). This network was used for creating the actual morphology of the polder bed after the process of sedimentation. During the creation of the digital terrain model of the sediments, it was nevertheless difficult to define the morphology in the areas without any measured points. Those areas had a water depth lower than 20 cm, but measuring equipment cannot be used when the water level is so low. In this case, the same resolution of the raster was chosen. The final version of the digital terrain model of the sediments is shown in Fig. 9.

The final analysis was based on calculating the differences in height between the digital terrain model of the polder bed and the digital terrain model of the sediments. The results of this analysis are shown in Fig. 10. In the flooded area, a maximal height of the sediments of 1.74 m was identified. This maximal height of the sediments was localized near the dike. The maximal depth of the terrain decreased by erosion was identified to be around 0.54 m. It is evident from Fig. 10 that sedimentation areas clearly dominate over the areas of polder bed erosion.

The results confirmed our theories about the on-going sedimentation processes in the Svacenicky Creek polder. According to the analysis with the ArcGis 10.1 software – the function Surface Volume, it was determined that during the last 4 years, over 10,474 m^3 of sediments were deposited on an area above 32,444 m^2 at a water level of 316.45 m. a.s.l.

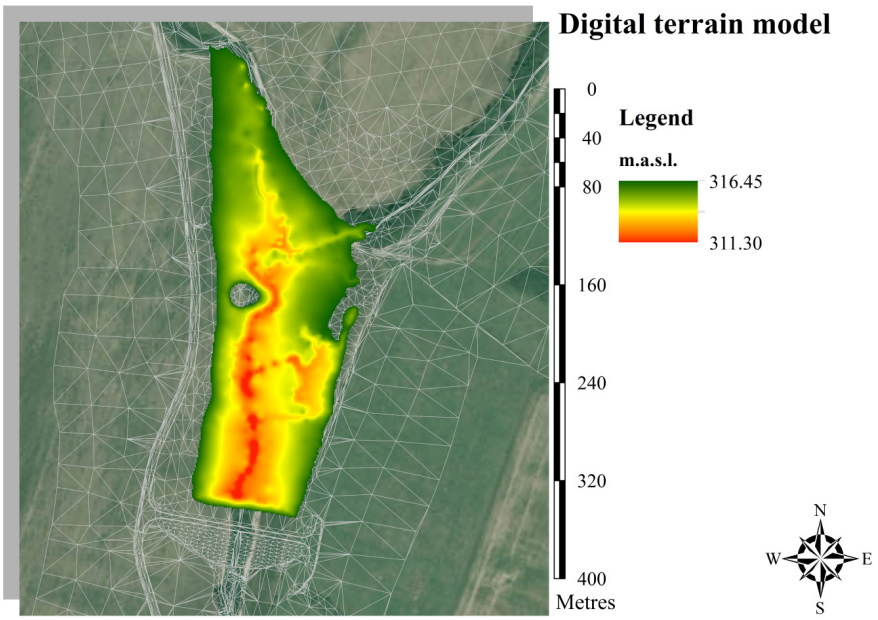

Fig. 7. Digital terrain model of Svacenicky Creek (ArcMap 10.1).

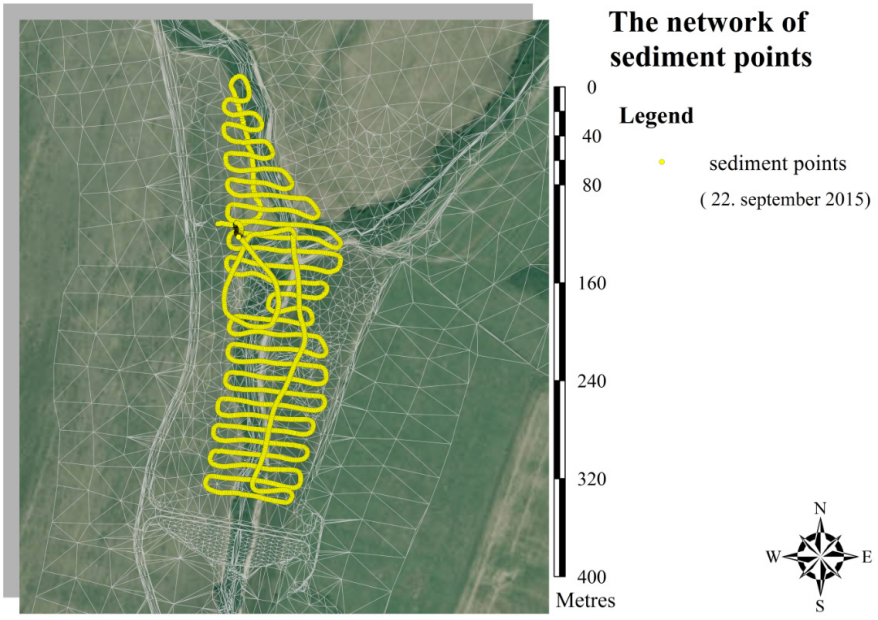

Fig. 8. The network of sediment points using the ArcMap 10.1. software program.

Subsequently, we compared the values of the mean annual sediment transport calculated using the USLE/SDR and WaTEM/SEDEM models with measurements of the sediment yields in the polder using the AUV EcoMapper for the period of four years after the polder´s construction. The estimation of the mean annual value of the measured sediment yields in tons is presented in Table 5. We assumed the bulk density of the bed sediments to be 1.9 t m^{-3}.The results presented confirmed our theories about the on-going sedimentation processes in the Svacenicky Creek polder. According to the analysis presented, we determined that during the last four years, over 10,474 m^3 of bed sediments on the area of the Svacenicky Creek polder have accumulated, i.e., a mean annual value of 2,618 m^3 or 4,975 t.

Table 5. The mean annual measured sediment yields in the polder of Svacenicky Creek.

Measurement	Method	
Sediment yield in 2015	AUV EcoMapper	10,474 m^3
Annual average of sediment yield in tons		4,975.15 t

The modelling results for the winter wheat are comparable with the measurements, i.e., the estimated mean annual sediment transport is 4,174 t according to the WaTEM/SEDEM model and Mc Cool LS algorithm, and 4,444 t according to the USLE/SDR model and the Mc Cool high LS algorithm.

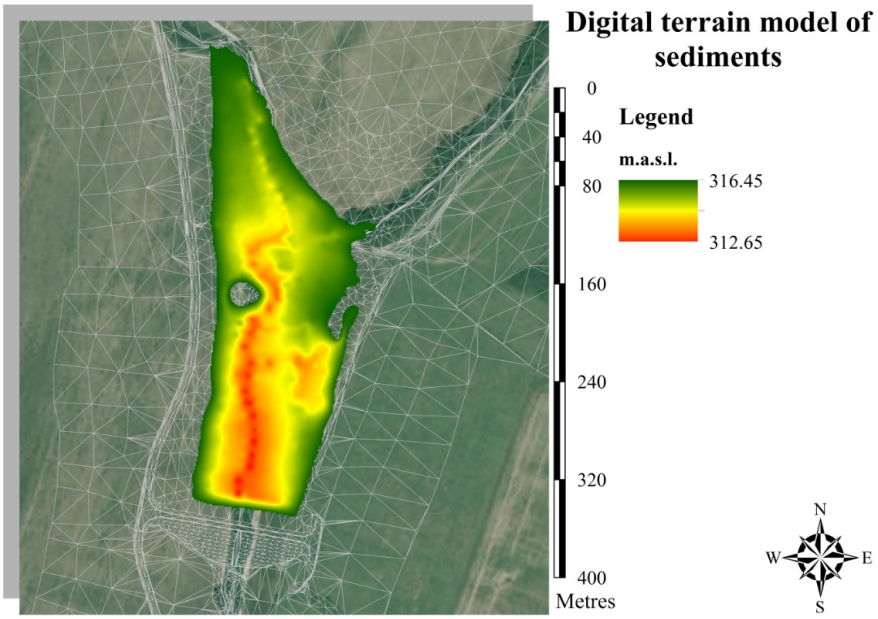

Fig. 9. Digital terrain model of sediments using the ArcMap 10.1. software program.

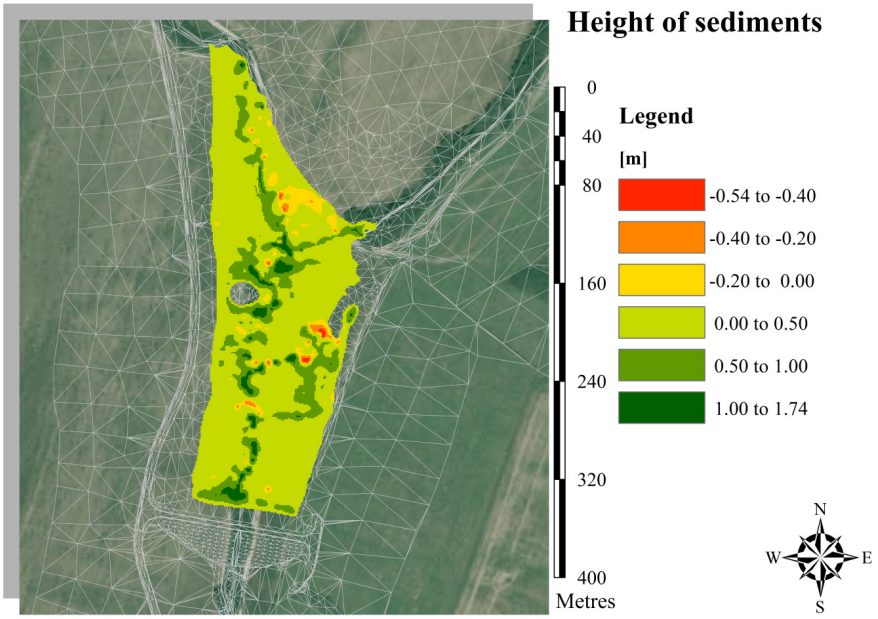

Fig. 10. Height of sediments using the ArcMap 10.1.software program.

DISCUSSION AND CONCLUSIONS

The main objective of this study was to quantify both the soil loss from agriculturally arable lands and the transport of sediments to the dry water reservoir (polder) of the Svacenicky Creek. The estimation was mainly focused on the off-site effect of soil erosion processes that result in the sedimentation of a small, flood protection water reservoir in the catchment outlet. In contrast to the on-site effect of soil erosion, which directly affects the people who control the source of the erosion, off-site impacts affect neighbouring areas where the people affected have little or no influence on source of the erosion (Renschler and Harbor, 2002). The import of sediments and nutrients causes changes in nutrient budgets, sediment loading, and the eutrophication of surface water bodies with impacts on the protective function of water reservoirs and water quality.

For estimating the mean annual soil loss and sediment transport from the catchment, empirical (USLE/SDR) and conceptual (WaTEM/SEDEM) approaches were applied. The USLE and SDR represent empirical models which are often criticised for employing simplified assumptions about the physics of the catchment system, i.e., they ignore the heterogeneity of catchment inputs and characteristics such as rainfall and soil types, as well as ignore the inherent non-linearities in the catchment system (Merritt, 2003). However, empirical models are frequently used in preference to more complex models as they can be applied in catchments with limited data and parameter inputs and are particularly useful as a first step in identifying sources of sediment and nutrient generation. The USLE belongs among the widely-used prediction equations in the world (Kinnell, 2010). Although it was designed to predict long-term average annual soil loss, it

has the capacity to predict event-based soil losses reasonably well at some geographic locations. Its lack of capacity to predict event-based erosion is highly influenced by the fact the event-based rainfall–runoff factor used in the USLE and its revisions (RUSLE, RUSLE2) do not explicitly consider runoff.

Most of the empirical parameters of the models applied in this study originate from the original or modified members of the USLE equation; only the rainfall erosivity factor R is a physically based parameter, which is estimated from measured rainfall data. There have been many efforts to estimate and develop these parameters at the European level (e.g., Panagos, 2015a, b). Therefore, in the paper we did not focus on the calibration of the parameters but rather on their validation by comparing results of the modelled and measured sediment yields at the river basin outlet. We are aware of many uncertainties in this approach but on the base of the models validation we tried to recommend the most applicable model for engineering practice in our conditions. The best results, in terms of comparing the sediment yields, were achieved by the combination of USLE/SDR model and LS factor calculated by Mc Cool-h and Watem/SEDEM with McCool algorithm of LS.

The impact of land use and management was parameterised by the vegetation (cover-management) factor C. The C-factor is among the five factors that are used to estimate the risk of soil erosion within the Universal Soil Loss Equation (USLE) and its revised versions. The C-factor is perhaps the most important factor with regard to policy and land use decisions, as it represents conditions that can be most easily managed to reduce erosion (Panagos, et al., 2015b). The vegetation factor was parametrized with values of $C = 0$ for forested areas and grasslands and different C values for the various crops considered: $C = 1$ for bare soil, $C = 0.72$ for maize used for silage, $C = 0.61$ for maize used for grain, $C = 0.12$ for winter wheat, and $C = 0.22$ for winter rapeseed.

From the results of the estimated the mean annual soil losses in Table 1, the effect of various crops on reducing soil erosion is evident despite some differences in the modelling approaches used. The greatest intensities of soil loss were achieved by the bare soil without vegetation (from 51.43 to 123.24 t ha^{-1} $year^{-1}$) and from the planting of maize for silage (from 37.03 to 88.74 t ha^{-1} $year^{-1}$). The lowest values were achieved from the planting of winter wheat (from 6.17 to 14.79 ha^{-1} $year^{-1}$). The total mean annual sediment transport to the polder for the soil without vegetation varied from 12,834 to 73,724 t $year^{-1}$ and for the winter wheat from 1,854 t $year^{-1}$ to 4,443 t $year^{-1}$.

Next, the results of the sediment transport were compared with the results of the actual bathymetry of the polder. The AUV EcoMapper was used to gather the data on the Svacenicky Creek polder in September 2015. Based on the field measurements of the polder bottom's bathymetry, the current status of the clogging of the reservoir was evaluated. The results confirmed our theories about the on-going sedimentation processes in the Svacenicky Creek polder. According to the analysis with the ArcGis 10.1 software, it was determined that during the last 4 years, over 10,474 m^3 of sediments were deposited on an area of more 32,444 m^2 at a water level of 316.45 m. a.s.l. The sediment transport modelled from the Svacenicky Creek catchment to the polder for winter wheat is comparable with the measurements, i.e., the estimated mean annual sediment transport is 4,174 t according to the WaTEM/SEDEM model and Mc Cool LS algorithm, and 4,444 t according to the USLE/SDR model and the Mc Cool high LS algorithm.

Finally, it can be stated that public awareness of the problem of reservoir sedimentation and its relation to the sustainability of reservoirs should be increased by a more appropriate transfer of knowledge from researchers to the entities responsible and to the general public. It is necessary to pay more attention to soil conservation and erosion control on agricultural land. Approaches to soil conservation on cultivated lands are based on agronomic measures, soil management or mechanical methods. Agricultural and management practices play an important role in controlling soil erosion. For instance, soil loss rates decrease exponentially as vegetation cover increases (Gyssels et al., 2005). Besides vegetation cover, several other land use and management factors affect soil loss, such as the type of crop, tillage practice, etc. In this paper agronomic measures for soil conservation based on the protective effect of plant covers to reduce soil erosion were tested. The simplest way to combine different crops is to grow them consecutively in rotation or in strips. With strip-cropping, row crops and protection-effective crops are grown in alternating strips aligned on the contour. Erosion is limited to the row-crop strips and soil removed from these strips is trapped within and behind the next strip downslope.

Acknowledgements. This work was supported by the EU-FP7 RECARE project under the 603498 project ID, by the Slovak Research and Development Agency under Contract No. APVV-15-0497 and APVV-15-0425, and the VEGA Grant Agency No 1/0710/15 and No 2/0058/15.

REFERENCES

Abril, B., Knight, D.W., 2004. Stabilising the Paute River in Ecuador. Proceedings of the ICE, Civil Engineering, 156, 1, 32–38.

Alena, F., 1991. Erosion Control on Arable Land. Handbook. ŠMS in Bratislava, Bratislava, 191 p.

Beck, M.B., Jakeman, A.J., McAleer, M.J., 1995. Construction and evaluation of models of environmental systems. In: Beck, M.B., McAleer, M.J. (Eds.): Modelling Change in Environmental Systems. John Wiley and Sons, pp. 3–35.

Boardman, J., Poesen, J., 2006. Soil Erosion in Europe. John Wiley & Sons Ltd, 855 p. ISBN: 978 0-470-85910-0.

Bosco, C., de Rigo, D., Dewitte, O., Poesen, J., Panagos, P., 2015. Modelling soil erosion at European scale: towards harmonization and reproducibility. Nat. Hazards Earth Syst. Sci., 15, 225–245. www.nat-hazards-earth-syst-sci.net/15/225/2015/. DOI: 10.5194/nhess-15-225-2015.

Desmet, P.J.J., Govers, G., 1996. A GIS procedure for automatically calculating the USLE LS factor on topographically complex landscape units. Journal of Soil and Water Conservation, 51, 5, 427–433.

De Vente, J., Poesen, J., Verstraeten, G., Govers, G., Vanmaercke, M., Van Rompaey, A., Arabkhedri, M., Boix-Fayos, C., 2013. Predicting soil erosion and sediment yield at regional scales: where do we stand? Earth-Sci. Rev., 127, 16–29.

EC, 2006. European Commission, Thematic Strategy for Soil Protection (Communication). Brussels, 22-9-2006. COM (2006) 231 p.

Fasching, R.A., Bauder, J.W., 2001. Evaluation of agricultural sediment load reductions using vegetative filter strips of cool season grasses. Water Environ. Res., 73, 5, 590–596.

Foster, G.R., Wischmeier, W.H., 1974. Evaluating irregular slopes for soil loss prediction. Trans. ASAE, 17, pp. 305–309.

Gyssels, G., Poesen, J., Bochet, E., Li, Y., 2005. Impact of plant roots on the resistance of soils to erosion by water: a review. Prog. Phys. Geog., 2, 189–217.

Hairsine, P., Rose, C., 1992. Modelling water erosion due to

overland flow using physical principles: 2. Rill flow. Water Resources Research, 28, 1, 245–250.

Hlaváčiková, H., Novák, V., Kostka, Z., Danko, M., Hlavčo, J., 2018. The influence of stony soil properties on water dynamics modeled by the HYDRUS model. J. Hydrol. Hydromech., 66, 2, 181–188.

Hlavčová, K., Kohnová, S., Borga, M., Horvát, O., Šťastný, P., Pekárová, P., Majerčáková, O., Danáčová, Z., 2016.Post-event analysis and flash flood hydrology in Slovakia, J. Hydrol. Hydromech., 64, 4, 304–315.

Janeček, M. et al., 2007. Protection of agricultural soils against erosion. Methodic. VÚMOP, Prague. (In Czech.)

Jones, J.W., Hoogenboom, G., Porter, C.H., Boote, K.J., Batchelor, W.D., Hunt, L.A., Wilkens, P.W., Singh, U., Gijsman, A.J., Ritchie, J.T., 2003.The DSSAT cropping system model. European Journal of Agronomy, 18, 3–4, 235–265.

Kinnell, P.I.A., 2010. Event soil loss, runoff and the Universal Soil Loss Equation family of models: A review. Journal of Hydrology, 385, 384–397.

Kirkby, M.J., Irvine, B.J., Jones, R.J.A., Govers, G., and the PESERA Team, 2008. The PESERA coarse scale erosion model for Europe. I.-Model rationale and implementation. Eur. J. Soil Sci., 59, 1293–1306.

Korbeľová, L., Kohnová, S., 2017. Methods for improvement of the ecosystem services of soil by sustainable land management in the Myjava River Basin. Slovak Journal of Civil Engineering, 25, 1, 29–36. DOI: 10.1515/sjce-2017-0005.

Lane, L.J., Hernandez, M., Nichols, M., 1997. Processes controlling sediment yield from watersheds as functions of spatial scales. Environmental Modelling and Software, 12, 4, 355–369.

Lawrence, P., 1996. Guidelines on field measurement procedures for quantifying catchment sediment yields. TDR project R5836, Report OD/TN77, HR Wallingford, (http://eprints.hrwallingford.co.uk/177/1/ODTN77.pdf, the last view on 20th of March 2017.)

Malíšek, A., 1990. Calculation and application of R-factor in the soil loss equation in conditions of Slovakia. PhD Thesis. Agricultural University in Nitra, Nitra, 119 p.

McCool, D.K, Foster, G.R., Mutchler, C.K., Meyer, L.D., 1989. Revised slope length factor for the Universal Soil Loss Equation. Transactions of the ASAE, 32, 5, 1571–1576.

Merritt, W.S., Letcher, R.A., Jakeman, A.J., 2003. A review of erosion and sediment transport models. Environmental Modelling & Software, 18, 761–799.

Nearing, M.A., Lane, L.J., Lopes, V.L., 1994. Modelling soil erosion. In: Lal, R. (Ed.): Soil Erosion: Research Methods. St. Lucie Press, pp. 127–156.

Nelson E.J., Booth, D.B., 2002. Sediment sources in an urbanizing, mixed land-use watershed. J. Hydrology, 264, 51–68.

Panagos, P., Borrelli, P., Poesen, J., Ballabio, C., Lugato, E., Meusburger, K., Montanarella, L., Alewell, C., 2105a. The new assessment of soil loss by water erosion in Europe. Environmental Science & Policy, 54, 438–447.

Panagos, P., Borrelli, P., Meusburger, K., Alewell, Ch., Lugato, E., Montanarella, L., 2015b. Estimating the soil erosion cover-management factor at the European scale. Land Use Policy, 48, 38–50.

Renschler, C.S., Harbor, J., 2002. Soil erosion assessment tools from point to regional scales – the role of geomorphologists in land management research and implementation. Geomorphology, 47, 189–209.

Rose, C.W., 1993. Erosion and sedimentation. In: Bonell, M., Hufschmidt, M.M., Gladwell, J.S. (Eds.): Hydrology and Water Management in the Humid Tropics: Hydrological Research Issues and Strategies for Water Management. Cambridge University Press, pp. 301–343.

Renard, K.G., Foster, G.R., Weesies, G.A., Porter, J.P., 1991. RUSLE – revised universal soil loss equation. J. Soil Water Conserv., 46, 1, 30– 33.

Renard, K.G., Foster, G.R., Yoder, D.C., McCool, D.K., 1994. RUSLE revisited: status, questions, answers, and the future. J. Soil Water Conserv., 49, 3, 213–220.

Renard, K.G., Foster, G.R., Weesies, G.A., McCool, D.K., Yoder, D.C., 1997. Predicting Soil Erosion by Water: A Guide to Conservation Planning with the Revised Universal Soil Loss Equation (RUSLE). Agric. Handbook No. 703. US Department of Agriculture, Washington, DC, 251 p.

Shen, Z.Y., Gong, Y.W., Li, Y.H., Hong, Q., Xu, L., Liu, R.M., 2009. A comparison of WEPP and SWAT for modeling soil erosion of the Zhangjiachong watershed in the Three Gorges reservoir area. Agr. Water Manage., 96, 1435–1442. DOI: 10.1016/j.agwat.2009.04.017.

Takken., I., Govers, G., Jetten, V., Nachtergaele, J., Steegen, A., Poesen, J., 2001. Effects of tillage on runoff and erosion pattrens. Soil and Tillage Research, 61, 1–2, 55–60.

Valent, P., Rončák, P., Maliariková, M., Behan, Š., 2016. Utilization of historical maps in the land use change impact studies: A case study from Myjava River basin. Slovak Journal of Civil Engineering, 24, 4, 15–26. DOI: 10.1515/sjce-2016-0018.

Van Oost, K., Govers, G., Desmet, P.J.J., 2000. Evaluating the effects of changes in landscape structure on soil erosion by water and tillage. Landscape Ecology, 15, 577–589.

Van Rompaey, A.J.J., Verstraeten, G., Van Oost, K., Govers, G., Poesen, J., 2001. Modelling means annual sediment yield using a distributed approach. Earth Surfaces Proc. Landforms, 26, 1221–1236.

Verstraeten, G., Poesen, J., 2001. Factors controlling sediment yield for small intensively cultivated catchments in a temperate humid climate. Geomorphology, 40, 123–144.

Verstraeten, G., Van Oost, K., Van Rompaey, A., Poesen, J., Govers, G., 2002. Evaluating an integrated approach to catchment management to reduce soil loss and sediment pollution through modelling. Soil Use and Management, 18, 386–394.

Vijay, S., 2011. Autonomous underwater vehicles. Seminar on Autonomous Underwater Vehicles, PESCE Mandya, http://www.scribd.com/doc/55826714/Autonomous-Under water-Vehicles.

Williams, J.R., 1977. Sediment delivery ratios determined with sediment and runoff models. In: Erosion and Solid Matter Transport in Inland Waters. IAHS-AISH Publication No. 122, pp. 168–179.

Wischmeier, W.C., Smith, D.D., 1978. Predicting Rainfall Erosion Losses – A Guide to Conservation Planning. Agricultural Handbook No. 537. US Dept Agric., Washington, DC.

Walling, D.E., 1983. The sediment delivery problem. J. Hydrology, 65, 209–237.

Wynn, R.B., Huvenne, V.A.I., Le Bas, T.P., Murton, B.J., Connelly, D.P., Bett, B.J., Ruhl, H.A., Morris, K.J., Peakall, J., Parsons, D.R., Sumner, E.J., Darby, S.E., Dorrell, R.M., Hunt, J.E., 2014. Autonomous Underwater Vehicles (AUVs): Their past, present and future contributions to the advancement of marine geoscience. Marine Geology, 352, 451–468. http://dx.doi.org/10.1016/j.margeo.2014.03.012.

YSI, 2009. Ecomapper Operation Manual. Yellow Springs Instruments, Yellow Springs, Ohio.

Received 18 December 2017
Accepted 30 May 2018

J. Hydrol. Hydromech., 66, 2018, 4, 416–420
DOI: 10.2478/johh-2018-0036

Impact of soil compaction on water content in sandy loam soil under sunflower

Viliam Nagy[1], Peter Šurda[1*], Ľubomír Lichner[1], Attila J. Kovács[2], Gábor Milics[2]

[1] Institute of Hydrology, Slovak Academy of Sciences, Dúbravská cesta 9, 841 04 Bratislava, Slovakia.
[2] University of West Hungary, Institute of Biosystems and Food Engineering, 9200 Mosonmagyaróvár, Hungary.
[*] Corresponding author. E-mail: surda@uh.savba.sk

Abstract: Soil compaction causes important physical modifications at the subsurface soil, especially from 10 to 30 cm depths. Compaction leads to a decrease in infiltration rates, in saturated hydraulic conductivity, and in porosity, as well as causes an increase in soil bulk density. However, compaction is considered to be a frequent negative consequence of applied agricultural management practices in Slovakia.

Detailed determination of soil compaction and the investigation of a compaction impact on water content, water penetration depth and potential change in water storage in sandy loam soil under sunflower (*Helianthus annuus* L.) was carried out at 3 plots (K1, K2 and K3) within an experimental site (field) K near Kalinkovo village (southwest Slovakia). Plot K1 was situated on the edge of the field, where heavy agricultural equipment was turning. Plot K2 represented the ridge (the crop row), and plot K3 the furrow (the inter–row area of the field). Soil penetration resistance and bulk density of undisturbed soil samples was determined together with the infiltration experiments taken at all defined plots.

The vertical bulk density distribution was similar to the vertical soil penetration resistance distribution, i.e., the highest values of bulk density and soil penetration resistance were estimated at the plot K1 in 15–20 cm depths, and the lowest values at the plot K2. Application of 50 mm of water resulted in the penetration depth of 30 cm only at all 3 plots. Soil water storage measured at the plot K2 (in the ridge) was higher than the soil water storage measured at the plot K3 (in the furrow), and 4.2 times higher than the soil water storage measured at the most compacted plot K1 on the edge of the field. Results of the experiments indicate the sequence in the thickness of compacted soil layers at studied plots in order (from the least to highest compacted ones): K2–K3–K1.

Keywords: Soil compaction; Soil penetration resistance; Bulk density; Water flow.

INTRODUCTION

The negative consequences of intensively exploited agricultural systems include also soil compaction from wheel traffic by heavy agricultural equipment. Compaction rearranges soil particles changing pore-size distribution and pore connectivity. The effect of soil compaction on saturated water flow is largely controlled by larger pores (i.e., preferential flow) (Ehlers, 1975; Lin et al., 1996; Lipiec et al., 1998) that are negatively related to soil compaction (Carter, 1990). It has been shown that increased soil compactness induced by vehicular traffic reduced the volume of stained macropores contributing to water flow (Håkansson and Lipiec, 2000) and their continuity (Lipiec and Stepniewski, 1995). It leads to a decrease in infiltration rates, saturated hydraulic conductivity and porosity, to an increase in soil bulk density, and to negative consequences for crop production (reduced growth, lower yield, increased fungi diseases, more weeds) (Horn, 2015; Martínez et al., 2008). There are many studies describing the effects of soil compaction on the soil water flow regime. Warkentin (1971) reviewed empirical evidence suggesting that macropores are the most significantly reduced in size following compaction, which can have a profound effect on both saturated and unsaturated water transmission. Recently an image analysis has been used to examine the differences in soil water flow associated with vehicle compaction (Kulli et al., 2003). Depending on soil texture and on the degree of soil compaction, preferential flow can also be favoured (Mooney and Nipattasuk, 2003). Kooistra (1994) studied the porosity of tilled sandy loam soils by optical microscopy of thin sections and distinguished macropores (mean diameter>100 μm) and smaller pores which were considered as micropores. It was shown that total porosity was often less decreased by compaction than the macroporosity, because the microporosity increased. Richard et al. (2001) demonstrated that compaction did not affect the textural porosity (i.e. matrix porosity), but it created relict structural pores that are accessible only through the micropores of the matrix. It showed the effect of soil compaction on the hydraulic properties, which can be used as an indicator of the consequences of compaction. In summary, according to Alaoui and Helbling (2006) the studies related to soil compaction show the necessity: a) to take into account matrix pores and macropores; b) to consider the field scale of soil profiles rather than the laboratory scale of cores to also assess the heterogeneity induced by compaction, and c) to consider directly the hydrodynamic functionality of the pores in conducting water and air rather than dwelling on the morphology of soil structure.

The degree of soil compaction depends not only on the applied load but also on soil characteristics and landscape position (Bertolino et al., 2010). However, some soils are inherently resilient to compaction, whereby they may recover following removal of the stress (Gregory et al., 2007). Bathke et al. (1992) found that the root elongation stopped where soil penetration resistance values ranged from 2 to 5 MPa.

The objectives of this study were (i) to estimate the soil compaction using the soil penetration resistance and bulk density distribution along the sandy loam soil profile and (ii) to assess the impact of soil compaction on water content, water penetration depth and potential increase in water storage in individual layers of sandy loam soil.

MATERIAL AND METHODS

Study area

Experimental site Kalinkovo (48°3’53’’ N, 17°12’12’’ E) at the Danubian Lowland, southwestern Slovakia, represents

Table 1. Particle-size distribution of the sandy-loam soil from Kalinkovo.

Depth (m)	Sand (%) ≥0.05 mm	Silt (%) 0.05–0.001 mm	Clay (%) ≤0.002 mm	Clay particles (%) ≤0.01 mm
0.10–0.20	61.81	32.70	5.49	15.71
0.25–0.35	62.47	32.23	5.30	17.09
0.45–0.55	66.60	29.56	3.84	14.31
0.75–0.85	67.93	28.91	3.16	11.45
1.10–1.20	10.88	79.52	11.60	45.19

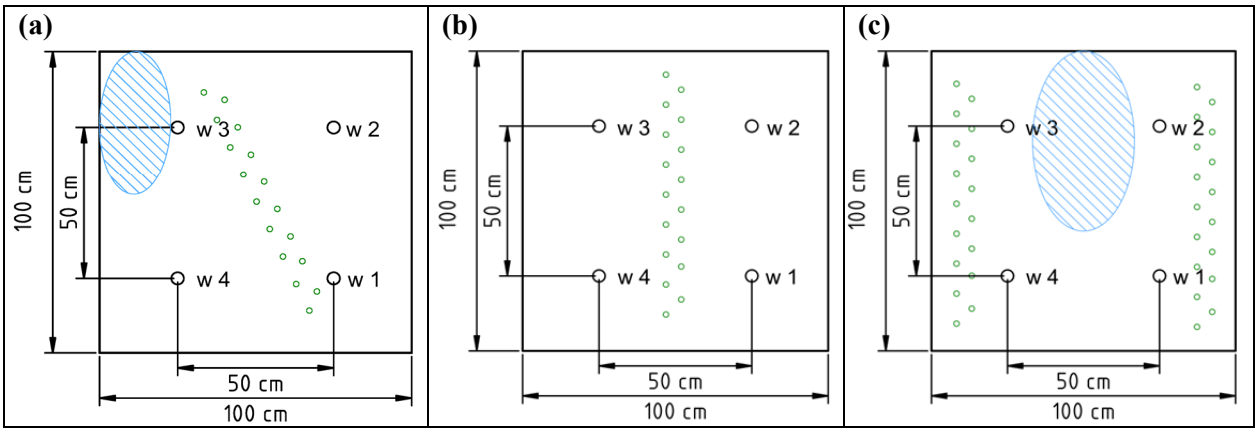

Fig. 1. Scheme of the field experiment with indication of ponding water (hatched ellipsoid), rows of sunflower (small circles) and location of the access tubes (w1–w4) for (a) K1 (the edge of the field), (b) K2 (ridge, crop row), and (c) K3 (furrow, inter-row area).

agricultural land, where sunflower (*Helianthus annuus* L.) was grown during the field campaign.

Soil at the experimental site, evolved on fluvial deposits of Danube River, is classified as Calcaric Fluvisol (IUSS Working Group WRB, 2015) and has a sandy loam texture (Soil Survey Division Staff, 1993). The top soil (0–5 cm) layer contained 52.67, 39.70 and 7.63% of sand, silt and clay respectively, 7.00% of $CaCO_3$, 1.27% of C_{org} with pH values 8.15 (H_2O) and 8.11 (KCl).

Particle-size distribution for whole soil profile is stated in Table 1.

According to MKSPS (Morphogenetic soil classification system of Slovakia–2000) the soil-type at Kalinkovo site is light sandy–loam fluvial anthrosol carbonate - FMac. The substrate is a carbonate sandy–loam alluvium; groundwater is located at the depth of 300 cm.

Pedon description:

Akpc 0–28 cm: colour 10YR 4/4, dry, loose, sandy-loam, weakly polyhedral, strong rooting, presence of carbonates,

A/Cc 28–38 cm: colour 10YR 5/4, slightly humid, crumbly, sandy-loam, weakly structural, medium rooting, presence of carbonates,

C1c 38–72 cm: colour 10YR 6/4, slightly humid, crumbly, sandy-loam, granular, rarely rooting, presence of carbonates (CaCO3 powders), carbonate alluvium,

C2c 72–138 cm: colour 10YR 6/3, slightly humid, crumbly, sandy-loam, granular, presence of carbonates (CaCO3 powders), carbonate alluvium,

C3c > 138 cm: colour 10YR 6/4, slightly humid, crumbly, sandy-loam, granular, presence of carbonates (CaCO3 powders), carbonate alluvium.

Three plots were studied at this site. Plot K1 (Fig. 1a) was situated on the edge of the field, where heavy agricultural equipment was turning. Plot K2 (Fig. 1b) was situated in the ridge (in the row), and plot K3 (Fig. 1c) in the furrow (in the bare soil inter-row area).

The BBCH-scale (Lancashire et al., 1991) identifies the phenological development stages of the sunflower (*Helianthus annuus* L.). At the time of field measurements from July 28 to July 31, the sunflower was in principal growth stage 6: Flowering (65 – Full flowering: disc florets in middle third of inflorescence in bloom – stamens and stigmata visible).

Agrotechnical operations at the field site

After the pre-crop was harvested, stubble tillage at a depth of 0.10–0.12 m was performed. The furrows were treated with rollers and then PK-fertilizers were applied through the medium-deep plowing (0.25 m). Dragging was the first agrotechnical operation in the spring followed by preparing the seed bed by the compactor. Sunflowers were sown with a seed drill to a depth of 40 mm on the April 21, 2015.

Field measurements

Soil penetration resistance was measured in 1 cm interval up to the depth of 50 cm with the Penetrologger (Eijkelkamp – Soil and Water), using the Cone with 1.0-cm^2 surface. Five sets of measurements were taken in the ridges (in the rows), five sets in the furrows (in the inter-row area), and five sets on the edge of the field. In this study, readings of ≥5 MPa serve as an indicator of soil compaction, which is in accordance with Carrara et al. (2007). Measured values of penetration resistance over 5 MPa in our study indicate compacted soil layer with serious consequences for the growth of plants and the transport of water and chemicals.

Bulk density ρ_d of undisturbed soil samples was determined according to the Soil Survey Manual (Soil Survey Division Staff, 1993). Kopecký steel cylinders (100-cm^3) were used to collect soil samples every 5 cm along the soil profile (0–100 cm). The field moist samples were weighed in the laboratory, oven dried at 105°C and weighed once more. Soil bulk density (g cm^{-3}) was calculated as the ratio of the mass of the oven-dried soil from the Kopecký cylinder and 100-cm^3 volume of the cylinder.

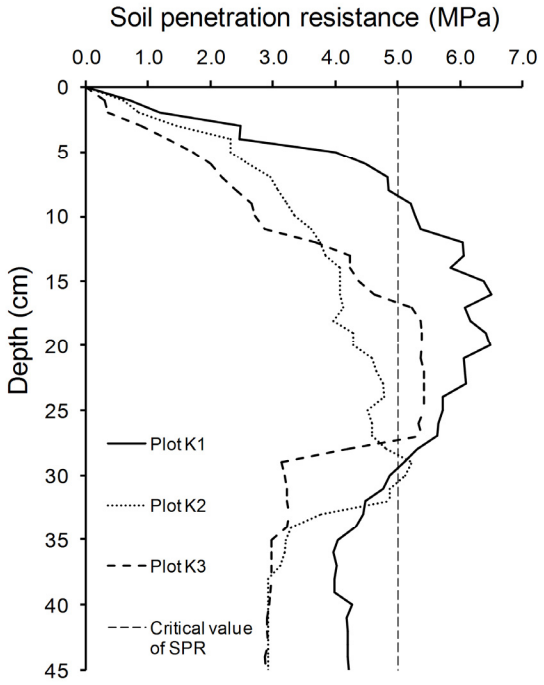

Fig. 2. Soil penetration resistance – SPR (average from 5 measurements) for the three experimental plots in Kalinkovo. Plot K1 – on the edge of the field, plot K2 – on the ridge (in the crop row), and plot K3 – in the furrow (in the inter-row position).

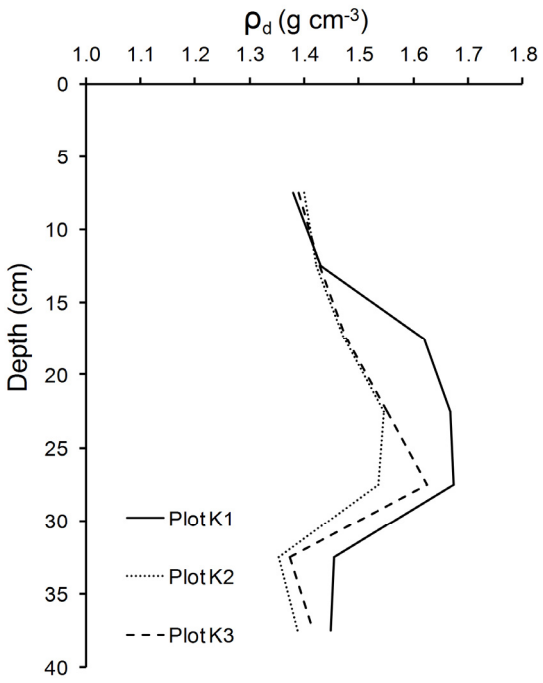

Fig. 3. Soil bulk density ρ_d (1 measurement per plot) for the three experimental plots in Kalinkovo. Plot K1 – on the edge of the field, plot K2 – on the ridge (in the crop row) and plot K3 – in the furrow (in the inter-row position).

Infiltration experiments were undertaken at three 100 cm × 100 cm plots (Fig. 1a, b, and c) from July 28 to July 31, 2015. At each of these plots four steel access tubes w1–w4 (with inner diameter of 4.3 cm and length of 200 cm) were inserted vertically into holes made with an auger. The volumetric soil water content ($m^3\ m^{-3}$) before and after irrigation was measured every 10 cm between 0 and 100 cm using the neutron moisture meter with Am-Be probe (Holdsworth, 1970).

Fifty mm of water was applied manually with a watering pot at a rate of about 2 mm min^{-1}, and the application and redistribution lasted 50 minutes. Two hours after water application, soil moisture was measured and the neutron counting rates, *CR*, were transformed to the volumetric water content, θ ($m^3\ m^{-3}$), using Equation (1) obtained from our former calibration using gravimetric method:

$$\theta = 0.001145\ CR + 0.001722\ c \quad (1)$$

where c is clay content (%).

The above-mentioned calibration equation was developed for the upper 1.5 m of four soil profiles (one sandy soil and three sandy loam soils) using the multiple linear regression analysis of the dataset of simultaneously collecting *CR*, θ and soil texture.

The water penetration depth z_{max} was estimated as maximal depth of soil (soil layer) where the difference in volumetric water content measured prior and after irrigation was registered, i.e., where ($\theta_{170\ min}$ − SD) > ($\theta_{0\ min}$ + SD). The radius of influence r (cm) (equal to the radius of the spherical cloud containing 95% of neutrons retarded by the soil) as a function of volumetric water content θ ($m^3\ m^{-3}$) was calculated from equation (Sumner, 1999):

$$r = 15\ (1/\theta)^{1/3} \quad (2)$$

RESULTS AND DISCUSSION

The depths, in which the soil penetration resistance was ≥5 MPa (indicated the soil compaction in this study) ranged from 9 to 31 cm below soil surface (Fig. 2). The thickest compacted soil layer (with a thickness of 21 cm) was measured at the plot K1. It occurred at depth from 9 to 30 cm. The thinnest compacted soil layer (with a thickness of 2 cm) was measured at plot K2. It occurred at the depth from 29 to 31 cm. The compacted soil layer at plot K3 was 10-cm thick and occurred at the depth from 17 to 27 cm. These findings are similar to the findings of Jabro et al. (2015), who found that less compaction was observed in crop rows compared to inter-rows. Maximum value (average from 5 measurements) of the soil penetration resistance was 6.38 MPa at the depth of 15 cm at the site K1, 5.22 MPa at the depth of 29 cm at the site K2, and 5.42 MPa at the depth from 22 to 25 cm at the site K3. These results are in line with the findings of Sağlam and Dengiz (2017), who claimed that the soils with high sand content have penetration resistance greater than 3.0 MPa (except for 0–5 cm).

The bulk density distribution along the soil profile (1 measurement per plot) for the three experimental plots in Kalinkovo is shown on Fig. 3. The results were similar with the results of vertical penetration resistance measurements, i.e., the highest values of bulk density and soil penetration resistance were measured at the plot K1, and the lowest values (with the exception of 28–33 cm depths, where the soil penetration resistance values culminated) at the plot K2. These findings are in line with the findings of Cassel (1983), who found that soil bulk density was significantly greater for trafficked inter-row position compared with row and non-trafficked inter-row positions.

The highest values of the soil bulk density at the plot K1 were measured at the depths of 15–20 cm, 20–25 cm, and 25–30 cm, which is in agreement with the results of soil penetration resistance measurements.

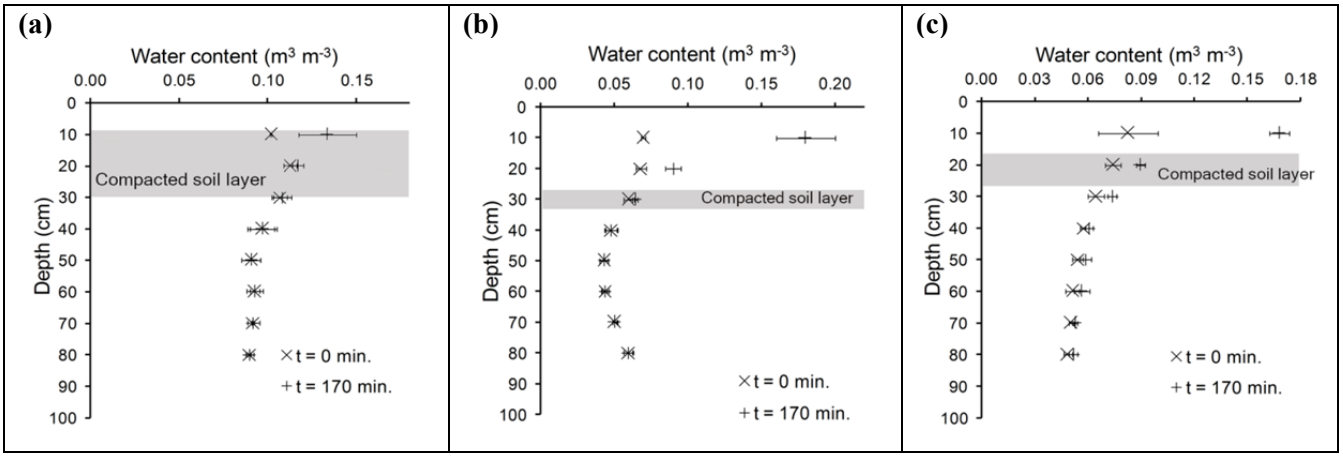

Fig. 4. Soil water content (mean values with standard deviations) at the plot K1 (edge of the field) before (×, t = 0 min) and after (+, t = 170 min) irrigation. Grey area represents compacted soil layer.

Comparison of the values taken at the plot K2 revealed that the highest values of the soil bulk density were measured at the depths of 20–25 cm and 25–30 cm, while the compacted soil layer occurred at the depth from 29 to 31 cm according to the soil penetration resistance measurements.

Comparison of the values taken at the plot K3 revealed that the highest values of bulk density were measured at the depths of 25–30 cm, while the compacted soil layer occurred at depth from 17 to 27 cm according to the soil penetration resistance measurements.

Mean values with standard deviations of the soil water content (m^3 m^{-3}) measured along the soil profiles of experimental plots are presented in Fig. 4. The impact of the compacted soil layer on the water flow was evident at all three plots. While the water penetration depth z_{max} was 30 cm at all three plots, increase in the soil water content was measured at the plot K1 to the depth of 20 cm only, and at the plots K2 and K3 to the depth of 30 cm.

The maximum increase in the soil water storage was estimated at the plot K2 and it was 12.82 mm, which means that the upper (0–30 cm) part of soil profile with sunflower roots retained 25.63% of applied water. Remaining water flowed out (drained) through the horizontal subsurface flow. At the plot K3, the increase in the soil water storage was 10.97 mm, which means that the upper (0–30 cm) part of soil profile retained 21.9% of applied water. Remaining water flowed out as in the previous case. At the extremely compacted plot K1, the increase in soil water storage was 3.73 mm only, which means that the upper (0–20 cm) part of soil profile retained 7.46% of applied water. Remaining water flowed out (drained) through the horizontal subsurface flow and/or along the access tube w3, where the ponded surface water infiltrated and flowed preferentially. For this reason, the vertical soil water content distribution and increase in soil water storage taken at the plot K1 in the access tube w3 had to be discarded and the average values of soil water content and increase in soil water storage were calculated from three values only.

The soil water content measured during this study is different from the soil water content measured after application of 50 mm of water at the three sites with uncultivated sandy soil covered with vegetation representing different stages of primary succession in Sekule, in the Borská nížina lowland of southwestern Slovakia (Šurda et al., 2015), at the two sites with non-tilled sandy loam soil covered with grassland in Zábrod (in mountainous area of the Šumava, Czech Republic) after an application of 62 and 112 mm of water (Lichner et al., 2014), and at the site with cultivated clay loam soil sown with spring barley in Most pri Bratislave (in the Danubian lowland in southwestern Slovakia) after an application of 100 mm of water (Lichner et al., 2013), where the increase in soil water content was registered up to the depth of 60–90 cm.

CONCLUSIONS

The soil bulk density distribution along the soil profiles was similar to vertical penetration resistance distribution, i.e., the highest values of bulk density and soil penetration resistance were measured at the plot K1, and the smallest values at the plot K2. The impact of compacted soil layers on water flow was evident at all three plots. Application of 50 mm of water resulted in the penetration depth of 30 cm only at all experimental plots. Increase in the soil water storage estimated after irrigation at the plot K2 on the ridge (in the crop row) was 1.17 times higher than the soil water storage estimated at the plot K3 in the furrow (in the inter-row position), and 3.43 times higher than the soil water storage estimated at the plot K1 on the edge of the field. Results of the experiment indicate the sequence in the thickness of compacted soil layers at studied plots in order (from the least to the most compacted ones): K2–K3–K1.

Acknowledgement. The authors thank Dr. Csilla Farkas, the JHH Associate editor handling this paper, and two anonymous reviewers for their wise comments and suggestions, which helped to improve the paper. This contribution was supported by the Scientific Grant Agency VEGA Project No. 2/0054/14, VEGA Project No. 2/0189/17, and Project APVV-15-0160. This publication is the result of the project implementation ITMS 26240120004 Centre of excellence for integrated flood protection of land supported by the Research & Development Operational Programme funded by the ERDF.

REFERENCES

Alaoui, A., Helbling, A., 2006. Evaluation of soil compaction using hydrodynamic water content variation: Comparison between compacted and non-compacted soil. Geoderma, 134, 1–2, 97–108.

Bathke, G.R., Cassel, D.K., Hargrove, W.L., Porter, P.M., 1992. Modification of soil physical properties and root growth response. Soil Science, 154, 316–329.

Bertolino, A.V.F.A., Fernandes, N.F., Miranda, J.P.L., Souza, A.P., Lopes, M.R.S., Palmieri, F., 2010. Effects of plough pan development on surface hydrology and on soil physical properties in Southeastern Brazilian plateau. Journal of Hydrology, 393, 94–104.

Carrara, M., Castrignanò, A., Comparetti, A., Febo, P., Orlando, S., 2007. Mapping of penetrometer resistance in relation to tractor trafficusing multivariate geostatistics. Geoderma, 142, 294–307.

Carter, M.R., 1990. Relative measures of soil bulk density to characterize compaction in tillage studies on fine sandy loams. Can. J. Soil Sci., 70, 425–433.

Cassel, D.K., 1983. Spatial and temporal variability of soil physical properties following tillage of Norfolk loamy sand. Soil Science Society of America Journal, 47, 2, 196–201.

Ehlers, W., 1975. Observations on earthworm channels and infiltration on tilled and untilled loess soil. Soil Science, 119, 242–249.

Gregory, A.S., Watts, C.W., Whalley, W.R., Kuan, H.L., Griffiths, B.S., Hallett, P.D., Whitmore, A.P., 2007. Physical resilience of soil to field compaction and the interactions with plant growth and microbial community structure. European Journal of Soil Science, 58, 1221–1232.

Håkansson, I., Lipiec, J., 2000. A review of the usefulness of relative bulk density values in studies of soil structure and compaction. Soil and Tillage Research, 53, 71–85.

Holdsworth, P.M., 1970. User's Schedule for the Wallingford Probe System. Institute of Hydrology Wallingford Report, Wallingford, 10 p.

Horn, R., 2015. Soil compaction and consequences of soil deformation on changes in soil functions. In: Northcliff, S. (Ed.): Task Force – Solutions under Foot. Catena Verlag, Reiskirchen, pp. 28–32.

IUSS Working Group WRB, 2015. World Reference Base for Soil Resources 2014, update 2015. International soil classification system for naming soils and creating legends for soil maps.World Soil Resources Reports No. 106. FAO, Rome.

Jabro, J.D., Iversen, W.M., Stevens, W.B., Evans, R.G., 2015. Spatial and temporal variability of soil penetration resistance transecting sugarbeet rows and inter-rows in tillage systems. Applied Engineering in Agriculture, 31, 2, 237–246.

Kooistra, M.J., 1994. Effects of compaction on soil microstructure. In: Soane, B.D., van Ouwerkerk, C. (Eds.): Soil Compaction in Crop Production. Elsevier, Amsterdam, pp. 91–111.

Kulli, B., Gysi, M., Fluhler, H., 2003. Visualizing soil compaction based on flow pattern analysis. Soil and Tillage Research, 70, 29–40.

Lancashire, P.D., Bleiholder, H., Langeluddecke, P., Stauss, R., van den Boom T., Weber E.,Witzen-Berger A., 1991. A uniform decimal code for growth stages of crops and weeds. Ann. Appl. Biol., 119, 3, 561–601.

Lichner, Ľ., Dušek, J., Dekker, L.W., Zhukova, N., Faško, P., Holko, L., Šír, M., 2013. Comparison of two methods to assess heterogeneity of water flow in soils. Journal of Hydrology and Hydromechanics, 61, 4, 299–304.

Lichner, Ľ., Dušek, J., Tesař, M., Czachor, H., Mészáros, I., 2014. Heterogeneity of water flow in grassland soil during irrigation experiment. Biologia, 69, 11, 1555–1561.

Lin, H.S., McInnes, K.J., Wilding, L.P., Hallmark, C.T., 1996. Effective porosity and flow rate with infiltration at low tensions in a well-structured subsoil. Trans. ASAE, 39, 131–133.

Lipiec, J., Stepniewski, W., 1995. Effects of soil compaction and tillage systems on uptake and losses of nutrients. Soil and Tillage Research, 35, 37–52.

Lipiec, J., Hatano, R., Słowińska-Jurkiewicz, A., 1998. The fractal dimension of pore distribution patterns in variously compacted soil. Soil and Tillage Research, 47, 61–66.

Martínez, E., Fuentes, J.-P., Silva, P., Valle, S., Acevedo, E., 2008. Soil physical properties and wheat root growth as affected by no-tillage and conventional tillage systems in a Mediterranean environment of Chile. Soil and Tillage Research, 99, 232–244.

MKSPS, 2000. Morfogenetický klasifikačný system pôd Slovenska. Bazálna referenčná taxonómia. (Morphogenetic soil classification system of Slovakia. Basal reference taxonomy). VÚPOP, Bratislava, 76 p. (In Slovak.)

Mooney, S., Nipattasuk, W., 2003. Quantification of the effects of soil compaction on water flow using dye tracers and image analysis. Soil Use and Management, 19, 356–363.

Richard, G., Cousin, I., Sillon, J.F., Bruand, A., Guérif, J., 2001. Effect of compaction on the porosity of a silty soil: influence on unsaturated hydraulic properties. Eur. J. Soil Sci., 52, 49–58.

Sağlam, M., Dengiz, O., 2017. Spatial variability of soil penetration resistance in an alluvial delta plain under different land uses in middle Black Sea Region of Turkey. Archives of Agronomy and Soil Science, 63, 60–73.

Soil Survey Division Staff, 1993. Soil Survey Manual.Soil Conservation Service. U.S. Department of Agriculture Handbook 18, 437 p.

Sumner, M.E., 1999. Handbook of Soil Science. CRC Press, Boca Raton, 2148 p.

Šurda, P., Lichner, Ľ., Nagy, V., Kollár, J., Iovino, M., Horel, Á., 2015. Effects of vegetation at different succession stages on soil properties and water flow in sandy soil. Biologia, 70, 11, 1474–1479.

Warkentin, B.P., 1971. Effects of compaction on content and transmission of water in soils. In: Barnes, K.K. (Ed): Compaction in Agricultural Soils. American Society of Agricultural Engineers, St. Joseph, Michigan, pp. 126–154.

Received 25 May 2018
Accepted 17 September 2018

J. Hydrol. Hydromech., 66, 2018, 4, 421–428
DOI: 10.2478/johh-2018-0034

Can a single dose of biochar affect selected soil physical and chemical characteristics?

Dušan Igaz[1*], Vladimír Šimanský[2], Ján Horák[1], Elena Kondrlová[1], Jana Domanová[1], Marek Rodný[3], Natalya P. Buchkina[4]

[1] Department of Biometeorology and Hydrology, Faculty of Horticulture and Landscape Engineering, Slovak University of Agriculture, Tr. A. Hlinku 2, 94 901 Nitra, Slovakia.
[2] Department of Soil Science, Faculty of Agrobiology and Food Resources, Slovak University of Agriculture, Tr. A. Hlinku 2, 949 76 Nitra, Slovakia.
[3] Institute of Hydrology, Slovak Academy of Sciences, Dúbravská cesta 9, 841 04 Bratislava, Slovakia.
[4] Agrophysical Research Institute, 14 Grazhdansky prospect, 195220 St. Petersburg, Russian Federation.
[*] Corresponding author. Tel.: +421 37641 5245. E-mail: dusan.igaz@uniag.sk

Abstract: During the last decade, biochar has captured the attention of agriculturalists worldwide due to its positive effect on the environment. To verify the biochar effects on organic carbon content, soil sorption, and soil physical properties under the mild climate of Central Europe, we established a field experiment. This was carried out on a silty loam Haplic Luvisol at the Malanta experimental site of the Slovak Agricultural University in Nitra with five treatments: Control (biochar 0 t ha^{-1}, nitrogen 0 kg ha^{-1}); B10 (biochar 10 t ha^{-1}, nitrogen 0 kg ha^{-1}); B20 (biochar 20 t ha^{-1}, nitrogen 0 kg ha^{-1}); B10+N (biochar 10 t ha^{-1}, nitrogen 160 kg ha^{-1}) and B20+N (biochar 20 t ha^{-1}, nitrogen 160 kg ha^{-1}). Applied biochar increased total and available soil water content in all fertilized treatments. Based on the results from the spring soil sampling (porosity and water retention curves), we found a statistically significant increase in the soil water content for all fertilized treatments. Furthermore, biochar (with or without N fertilization) significantly decreased hydrolytic acidity and increased total organic carbon. After biochar amendment, the soil sorption complex became fully saturated mainly by the basic cations. Statistically significant linear relationships were observed between the porosity and (A) sum of base cations, (B) cation exchange capacity, (C) base saturation.

Keywords: Biochar; Soil physical characteristics; Soil sorption characteristics; Soil organic carbon; *Zea mays*.

INTRODUCTION

The potential benefits of biochar application to agricultural soils have been extensively analyzed in several environmental studies. Biochar was primarily discussed from the point of view of carbon sequestration, and its potential to reduce greenhouse gas emissions to the atmosphere (Lehmann et al., 2011). Biochar, as a product of thermal modification of organic matter by pyrolysis, is a solid porous material with a high carbon content.

The scientific community is interested in biochar application to soil in the terms of its impact on the agro-environmental parameters such as soil chemistry, pH, and soil organic carbon (Jien and Wang, 2013; Peng et al., 2011), as well as absorption, movement of nutrients in the plant root zone and their leaching. Also of interest is the impact on soil organic matter content (Brodowski et al., 2007), soil aggregate stability and soil crust formation (Ajayi and Horn, 2016; Sun and Lu, 2014; Šimanský et al., 2016). Various studies have shown that biochar has the potential to influence the physical characteristics of soil (Buchkina et al., 2017; Castellini et al., 2015; Herath et al., 2013) and thus change the rootzone water balance of ecosystems. Observations have included soil properties such as bulk density (Ajayi and Horn, 2016) soil porosity (Obia et al., 2016), soil water content (Novak et al., 2012, Vitkova et al., 2017), the available water capacity of the soil (Abel et al., 2013; Brockhoff et al., 2010), the water holding capacity of the soil and field capacity (Busscher et al., 2010; Jones et al. 2010; Novak et al., 2012) and the soil-water retention curve (Liu et al., 2011).

Several studies have indicated that the addition of about 1–2% (w/w) of the biochar to soil influences the water holding capacity of the soil and increases the soil's water content. Depending on the amount applied, biochar can modify the soil structure (Ajayi and Horn, 2016). These physical properties can affect the various processes that impact the formation, structure, and stability of aggregates, as well as the, shapes and the size of soil pores (Lin et al., 2012). However, there are very few studies that have focused on the processes and mechanisms of the biochar's interactions with the soil environment. Despite the clear connection between biochar porosity and the soil porosity after its application, very few studies have reported a direct effect of biochar pore size on subsequent changes in the soil properties. Ajayi and Horn (2016) reported that after repeated wetting and draining of biochar-amended sandy soil, the formation of finer soil pores comprised of finer biochar particles in the vicinity of the coarser sandy particles. Similar results were also found in the study of Rizhiya et al. (2015).

Several authors have investigated with the impact of the biochar application on soil water content and more specifically on the available water content which is defined as the amount of plant available water in the root zone being the range from permanent wilting point up to field capacity. According to Jones et al. (2010), the field capacity of sandy soil increased from 0.11 (cm^3 cm^{-3}) up to 0.16 and 0.20 (cm^3 cm^{-3}) after biochar application at rates of 2.6 and 5.2% (g g^{-1}), respectively. Similar observations were reported by the other authors at different rates of biochar application (Karhu et al., 2011; Novak et al., 2012). In contrast, a study of Busscher et al. (2010) showed a decrease of the field capacity of a loam sandy soil after biochar application at 0.5; 1.0 and 2.0% (g g^{-1}).

As yet, the interaction between biochar and biochar with nitrogen fertilizer, in commercial field setting has not been explored in field conditions of Slovakia. Therefore, the aim of this

study was to determine the impact of different rates of biochar application with, and without inorganic nitrogen, on selected soil chemical and physical characteristics. This was carried out via field experiments conducted in Malanta, Slovakia. We hypothesized that the application of biochar to the soil would (i) increase the soil's water content, (ii) increase the total organic carbon content, (iii) increase the saturation of the soil's sorption complexes.

MATERIAL AND METHODS

Field site

Field experiment was established in the spring of 2014 at the experimental site of the Slovak University of Agriculture located in Malanta municipality, in the Danubian Upland (48°19´00´´ N; 18°09´00´´ E). The altitude of the site is 175 m, the soil is classified as Haplic Luvisol and the topsoil contains 249 g kg^{-1} of clay, 599 g kg^{-1} of silt and 152 g kg^{-1} of sand, giving it a silt loam texture. The soil is slightly acidic (pH 5.71) and low in organic carbon content (9.13 g kg^{-1}). The locality is characterized by a warm lowland climate with long, warm and dry summers, and short dry winters and only a very short duration of snow cover (14–30 days). For the first year of the project in 2015, the average annual air temperature at the Malanta site was 9.6°C and the annual rainfall was 532 mm. The average annual temperature varied in the range of 9 to 10°C and the average annual precipitation varied from 500 up to 600 mm.

In March 2014, a single dose of biochar at 0, 10, and 20 t ha^{-1} was applied on trial plots by hand and incorporated into the soil to a depth of 0–0.1 m with a tractor cultivator. Subsequently, the influence of biochar on selected soil characteristics under corn crop *(Zea mays* L.) was analyzed in 2015.

Five treatments of the experiment were established in 3 replicates on plots of 4 m x 6 m with a protection zone of 0.5 m (Fig. 1).The treatments were as follows: Control (biochar 0 t ha^{-1}, nitrogen 0 kg ha^{-1}); B10 (biochar 10 t ha^{-1}, nitrogen 0 kg ha^{-1}); B20 (biochar 20 t ha^{-1}, nitrogen 0 kg ha^{-1}); B10+N (biochar 10 t ha^{-1}, nitrogen 160 kg ha^{-1}) and B20+N (biochar 20 t ha^{-1}, nitrogen 160 kg ha^{-1}). The N-fertilizer was manually applied at two times: 80 kg N ha^{-1} on 24 April, 2015 and 80 kg N ha^{-1} on 5 August, 2015, and was in the form of calcium-ammonium nitrate. The rate of N applied was calculated according a nutrient balance method, which reflects the crop's nitrogen requirements. The same form of N-fertilizer had been applied at rate of 40 kg ha^{-1} to the spring barley crop in the previous year on the same day as the biochar (10 March, 2014).

Properties of the used biochar

The biochar used for the experiment was made from the mixture of paper fiber sludge and cereal husks in a weight ratio 1:1 and was produced by Sonnenerde, in Austria using pyrolysis at 550°C for 30 min in a Pyreg reactor (Pyreg GmbH, Dörhe, Germany). On average the biochar contained 57 g kg^{-1} of Ca, 3.9 g kg^{-1} of Mg, 15 g kg^{-1} of K and 0.77 g kg^{-1} of Na (DIN EN ISO 11 885). Total C content of biochar was 53.1%, while total N content was 1.4% (DIN 51732), so the C:N ratio was 37.9. The specific surface area (SSA) was 21.7 m^2 g^{-1} (DIN 66132/ISO 9277) and the ash content was 38.3% (DIN 51719). On average, the pH($CaCl_2$) of the biochar was 8.8 (DIN ISO 10390).

Soil sampling and subsequent analyzes

The soil moisture was determined from disturbed soil samples by the gravimetric method (g g^{-1}) every week during the growing season (March 2015–October 2015). The gravimetric water content (w/w) was determined according to the weight of soil sample before and after drying as the ratio of the weight of water (m_w) in the sample to the weight of the dried soil (m_s) after drying at 105°C in the oven until reaching a constant weight. Subsequently, the mass water content (w/w) was multiplied by the soil bulk density (ρ_d) to calculate the volumetric water content (θ, v/v).

To determine the selected physical and hydro-physical characteristics, two sampling events were conducted, one in the spring of 2015 and again in the autumn of 2015. Three undisturbed soil samples were taken from each plot (a total of 45 samples) of all treatments (n = 5) across the 3 replicates. This means that each soil property was determined from 9 representative undisturbed soil samples that were collected from a depth of 5–10 cm using stainless steel cylinders with a volume of 100 cm^3 and the height of 5.1 cm. The cylinders were gently pushed into the soil using the soil sampler. To maintain the soil water content close to field capacity, the soil sampling was conducted 2 days after intensive rainfall.

The relationship of the soil water potential and the water content (the water retention curve) was determined using a pressure-plate apparatus. The drainage retention curve was derived from pre-saturated soil samples placed on ceramic plates at the pressure potentials of 0, –1, –5.5, –20, –55, –100 and –300 kPa. Prior every increase of pressure potential, the undisturbed soil samples were weighed and the water content corresponding to each pressure potential was calculated. At the end, the soil samples were dried for 24 h at 105°C and weighed.

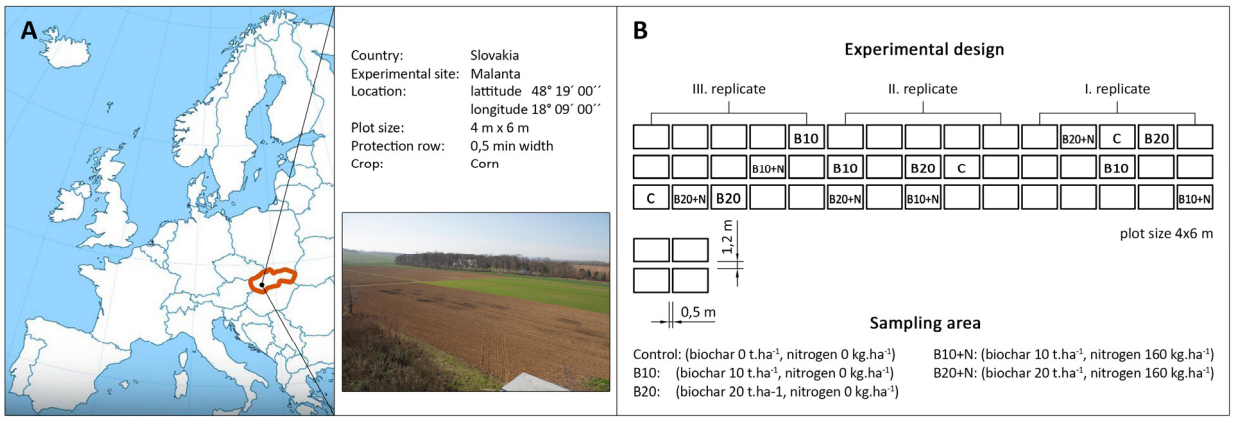

Fig. 1. The location (A) and experimental design of the field experiment (B).

The readily available water content (RAWC) is that water in the soil that is easily extracted by the plant. The RAWC was calculated as a difference between measured values of field capacity (FC, at a pressure potential of –20 kPa) and the refill point (RP, at pressure potential of –300 kPa). The refill point is the water content when the plant has used all readily available water. Beyond refill point, as the soil dries out, the plant needs to work harder to extract water via its roots and crop becomes under stress.

According to convention, the available water content (AWC) corresponds to the moisture interval between the limit of the field capacity (FC) and the wilting point (WP). The value of the FC was determined from the measured values. Wilting point (-1500 kPa) was calculated using the RETC software (Leij et al., 1992) with a van Genuchten soil-moisture retention model (VG) (van Genuchten, 1980). The unknown parameters of the VG model, namely the shape parameters (α, n), and the saturated water content (θ_s) were found via the optimization process and used to calculate the WP. The RETC code minimizes the sum of squared residuals (RMSE) between model-predicted and the observed water retention data by means of a weighted least-squares approach based on Marquardt's maximum likelihood method (Marquardt, 1963). Following Mualem (1976), the shape parameter m was set equal to $1 - 1/n$. To reduce the number of parameters being estimated, the residual soil water content θ_r was handled as a constant and its value was estimated with the means of a pedotransfer function to be $\theta_r = 0.040$ (Skalová et al., 2015).

The soil porosity was estimated as the volumetric water content found after saturating the undisturbed soil samples for 24 h at the free-water potential of 0 kPa, and was calculated as the volumetric proportion of water in the sample. The undisturbed soil samples were also used for calculating the bulk density as the ratio of dried soil mass (for 24 h at 105°C) to the total soil sample volume (100 cm^3).

Soil samples for determination of the soil organic carbon content (SOC) and sorption parameters were collected at the same time from the same depths and plots as the samples for the purposes of the physical characteristics. The SOC was determined by wet combustion method of Tyurin (Dziadowiec and Gonet, 1999), by oxidizing the organic matter using a mixture of 0.07 M H_2SO_4 and $K_2Cr_2O_7$ with titration using 0.01 M Mohr's salt ($(NH_4)_2SO_4$. $FeSO_4$. $6H_2O$). The sorption parameters such as hydrolytic acidity (Ha) and the sum of exchangeable base cations (SBC) were determined by the Kappen method (Hanes, 1999). Cation exchange capacity (CEC) was calculated as the sum of Ha and SBC, while the base saturation (Bs) was calculated as the ratio of SBC to CEC (Hrivňáková et al., 2011).

Statistical analysis

The impact of biochar amendment on chemical and physical soil characteristics, organic carbon, and soil sorption parameters was assessed by a statistical one-way analysis of variance (ANOVA) using the Statgraphics Centurion software by LSD test (p <0.05). The statistical analysis was performed on the treated value set excluding the highest and lowest values for all treatments of the experiment (n = 7). Further, regression analysis was used to determine the interrelationships between the soil organic matter, sorption complex parameters and physical characteristics.

RESULTS AND DISCUSSION

Effect of biochar on water content dynamics

The impact of the single application of biochar at 0, 10 and 20 t ha^{-1} in March 2014 on the water content dynamics in 2015 under the corn crop (*Zea mays* L.) is presented in Fig. 2. The water content trends are influenced by precipitation and the subsequent dry down due to transpiration, soil evaporation and drainage runoff. Prior to, and during the spring, the highest average soil water content was in B10+N and B20+N treatments and the lowest in the control treatment. From early May 2015, soil water contents started to diverge, with higher values across all treatments compared to control. This difference in this trend was subsequently observed throughout the whole growing season.

An interesting effect of biochar application on the water content was recorded in the relation to the crop *(Zea mays* L.) and its growth phases. Corn is a water demanding plant, particularly during crop emergence and then subsequently from silking until the beginning of kernel milk stage. During germination (15th May 2015) soil water contents were ranked in the following order: Control < B10 < B20+N < B10+N < B20 at 13.2 < 21.6 < 22.2 < 23.5 < 23.8 % vol., respectively. Next, at the beginning of silking stage (8th July 2015) the soil water contents increased in the order: Control < B10 < B10+N < B20 < B20+N and 5.1 < 6.7 < 7.2 < 9.6 < 10.1 % vol., respectively. At the beginning of the kernel milk stage (31st July 2015) the soil water contents increased as follows: Control < B20 < B10 < B20+N < B10+N and 5.8 < 9.0 < 9.1 < 9.7 < 9.9 % vol., respectively. At this growth stage, the corn root system had

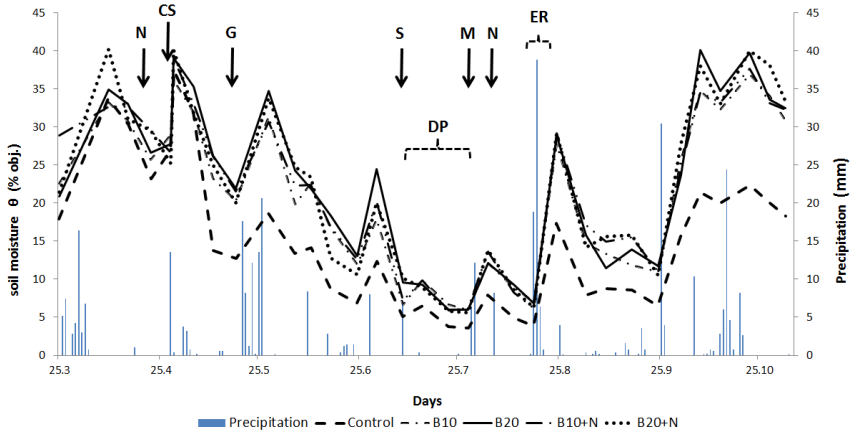

Fig. 2. The trend in the soil water content (% vol.) at the depth from 0.05–0.1 m under the corn crop in 2015 and the daily total precipitation (mm). N – nitrogen fertilizer application, CS – sowing of corn, G – corn germination, S – beginning of silking, M – beginning of the kernel milk stage, DP – dry period, ER – extreme rainfall.

reached a depth of 0.4–0.5 m, while our soil water contents were determined just at the depth of 0.05–0.1 m. So the water contents here represent only the water content of biochar-enriched surface layer of soil and not the available water storage needed for transpiration.

In the period from 17th up to 18th August 2015 an intense rainfall event occurred (57.6 mm). After subsequent soil sampling (24th August 2015) the water contents increased in the order: Control < B10 < B20 < B10+N = B20+N and 17.3 < 27.8 < 28.9 < 29.1 = 29.1% vol., respectively. We conclude that the biochar-enriched soil is capable of retaining more water after such rainfall events compared to the soil without biochar. This has a positive effect on the rainfall-runoff processes and presumably the storage of available water in the root zone.

The soil water content in 2015 reached its minimum during the dry period lasting for 20 days (7th July up to 28th July 2015). That was interrupted only by two episodes with little rainfall of 0.4 mm (13th July 2015) and 0.05 mm (25th July 2015). The soil moistures ranged in the order: Control < B20+N+< B10 = B20 < B10+N and 3.6 < 5.6 < 6.0 = 6.0 < 6.2% vol., respectively. The ability of biochar to maintain higher water contents during the dry period of 20 days agrees with the results of several authors (Jones et al., 2010; Karhu et al., 2011).

Biochar effect on soil water retention characteristics

From the spring sampling collected 12 months after the biochar application, we found that the applied biochar significantly increased the water content in the soil at the pressure potentials of –1 kPa and –5.5 kPa in all treatments (Table 1). An increase in the water content was recorded also at the pressure potentials of –20 kPa and –55kPa for treatments B20, B10+N and B20+N. At the pressure potentials of –100 kPa and –300 kPa, water contents significantly higher than control were found only in B10+N and B20+N treatments. Similar results have been presented by Brockhoff et al. (2010) and Abel et al. (2013), who observed the increase of water content after biochar application in their laboratory experiment. However, for the autumn sampling, some 20 months after biochar application, there were no significant differences between control and the biochar-amended treatments (Table 1). With decreasing moisture content there is a trend of decreasing differences in soil water content (compare Table 1 at –300 kPa), while at moister conditions (especially at the pressure potentials of –5.5, –20 and –55kPa) all amended treatments displayed higher water contents than the control.

Impact of biochar on available water content of soil

The trends of the soil water retention curves influenced by biochar application are shown in Fig. 3. The figure shows the measured soil water content at different pressure potentials and trends of retention curves modeled by RETC. A noticeable effect of biochar on the water retention curves can be seen for the spring sampling. In autumn, such noticeable changes were not recorded. Table 2 presents RAWC values. Biochar has increased RAWC for all treatments in the spring and autumn samples. A statistically significant increase was observed in the treatment of B20 + N. Table 2 also presents the individual retention-curve shape parameters of α, and *n* as well as the individual limits. When evaluating the impact of biochar on plant available water content (AWC), sometimes also referred to as plant available water (PAW), the AWC was considered as the difference between FC and permanent wilting point (WP, at pressure potential of –1500 kPa).

One year after biochar application, in the spring soil samples a trend of an AWC increase was found in all treatments. In the case of the B20+N treatment the increase was statistically significant (Table 2). Based on the results from autumn sampling, a positive influence of biochar on AWC still remained, since the AWC was higher across all treatments as compared to control. A statistically significant increase was found in the B20+N treatment (Table 2). These findings are consistent with the study of Abel et al. (2013).

Effect of biochar on soil porosity

A statistically significant increase in soil porosity was observed during spring for all treatments (B10, B20, B10+N, B10+N) (Table 1). Similar observations were presented by Masulili (2010), who recorded an increase in the porosity after biochar application at the rates of 10 t ha^{-1} and 15 t ha^{-1}. The increase of soil porosity has also been pointed out by several other authors (Ajayi and Horn, 2016; Jones et al., 2010; Lin et al., 2012). This might be due to the high porosity and therefore higher water-retention capacity of biochar (Hlaváčiková et al., 2016; Obia et al., 2016). In addition, the process of incorporation, or certain sorption with the multivalent cations as the

Table 1. Effect of the biochar application on the bulk density, porosity and water content in the soil at pressure potentials of –1, –5.5, –20, –55, –100 and –300 kPa (means ± standard deviations).

Treatments	BD	P	WC–1.0kPa	WC–5.5kPa	WC–20kPa	WC–55kPa	WC–100kPa	WC–300kPa
	($g.cm^{-3}$)	(%vol.)						
Spring								
Control	1.6±0.06ab	35.4±0.84a	32.7±1.08a	31.8±1.29a	30.8±1.17a	28.6±2.15a	27.2±1.71a	26.1±1.31a
B10	1.6±0.08ab	37.7±1.58b	35.3±2.20b	33.7±2.30b	32.1±1.84ab	30.3±2.34ab	28.4±2.17ab	27.3±2.17ab
B20	1.6±0.03b	37.5±1.68b	35.2±1.50b	34.2±1.61bc	33.4±1.52bc	30.7±1.73b	29.0±1.35ab	27.8±1.31ab
B10+N	1.7±0.04b	37.1±1.02b	35.0±0.91b	33.8±1.01b	32.7±0.99bc	31.0±1.01b	29.3±1.10b	28.2±0.96b
B20+N	1.6±0.05a	39.8±1.45c	37.4±1.40c	35.7±1.65c	34.3±1.83c	31.6±1.51b	29.4±1.64b	28.4±1.14b
Autumn								
Control	1.7±0.07ab	38.4±1.23b	35.3±0.92b	33.2±0.45a	31.1±0.89a	29.5±0.91a	28.7±0.97a	27.2±1.37a
B10	1.7±0.39ab	37.7±1.54ab	34.9±1.31ab	33.6±1.36a	32.1±0.79a	30.5±0.83a	28.6±0.86a	27.2±1.37a
B20	1.7±0.06b	36.7±1.29a	34.0±1.24a	33.3±1.09a	31.8±0.68a	30.5±0.56a	29.5±0.93a	26.9±1.79a
B10+N	1.6±0.03ab	38.6±0.97b	36.7±1.08c	34.1±1.14a	32.1±1.24a	30.0±1.44a	29.2±1.93a	26.4±1.49a
B20+N	1.6±0.05a	38.2±1.98ab	35.9±1.19ab	33.8±1.09a	31.6±1.13a	30.2±0.82a	29.2±1.03a	27.2±2.34a

BD – bulk density, P – porosity, WC – water content by different pressure potential.
Different letters (a, b, c) indicate that treatment means are significantly different at $p < 0.05$ according to LSD test.

Table 2. Effect of the biochar application on the basic limits and water retention curve shape parameters α and *n* determined according van Genuchten model (means ± standard deviations).

Treatments	FC	RP	RAWC	*α*	*n*	WP	AWC
	(%vol.)			(cm^{-1})	–	(%vol.)	
Spring							
Control	30.8±1.17a	26.1±1.31a	4.5±1.38a	0.08±0.06a	1.06±0.02a	25.0±2.51a	5.5±1.71a
B10	32.1±1.84ab	27.3±2.17ab	4.9±1.44a	0.06±0.08a	1.07±0.02a	26.1±1.99a	6.5±1.56a
B20	33.4±1.52bc	27.8±1.31ab	5.2±1.63ab	0.06±0.09a	1.07±0.03a	26.3±2.19ab	6.7±2.05ab
B10+N	32.7±0.99bc	28.2±0.96b	4.7±1.22ab	0.04±0.03a	1.06±0.02a	27.0±1.91ab	5.9±1.83ab
B20+N	34.3±1.83c	28.4±1.14b	6.5±0.65b	0.44±1.13a	1.08±0.01a	28.2±2.27b	8.2±1.10b
Autumn							
Control	31.1±0.89a	27.2±1.37a	3.8±1.46a	0.31±0.56a	1.06±0.02a	25.0±1.75a	5.4±1.29a
B10	32.1±0.79a	27.2±1.37a	4.7±1.04ab	0.07±0.09a	1.08±0.02ab	24.2±2.00a	6.7±1.81ab
B20	31.8±0.68a	26.9±1.79a	5.1±1.46ab	0.02±0.02a	1.09±0.03ab	23.8±2.43a	7.5±2.02ab
B10+N	32.1±1.24a	26.4±1.49a	5.2±2.20ab	0.05±0.08a	1.1±0.04ab	23.5±2.08a	7.7±2.30ab
B20+N	31.6±1.13a	27.2±2.34a	4.8±1.67b	0.23±0.05a	1.08±0.02b	24.1±1.79a	6.7±1.66b

FC- field capacity (measured), RP – refill point (measured), RAWC – readily available water content,
α, *n* – shape parameters, WP – wilting point (modelled), AWC – available water content.
Different letters (a, b, c) indicate that treatment means are significantly different at $p < 0.05$ according to LSD test.

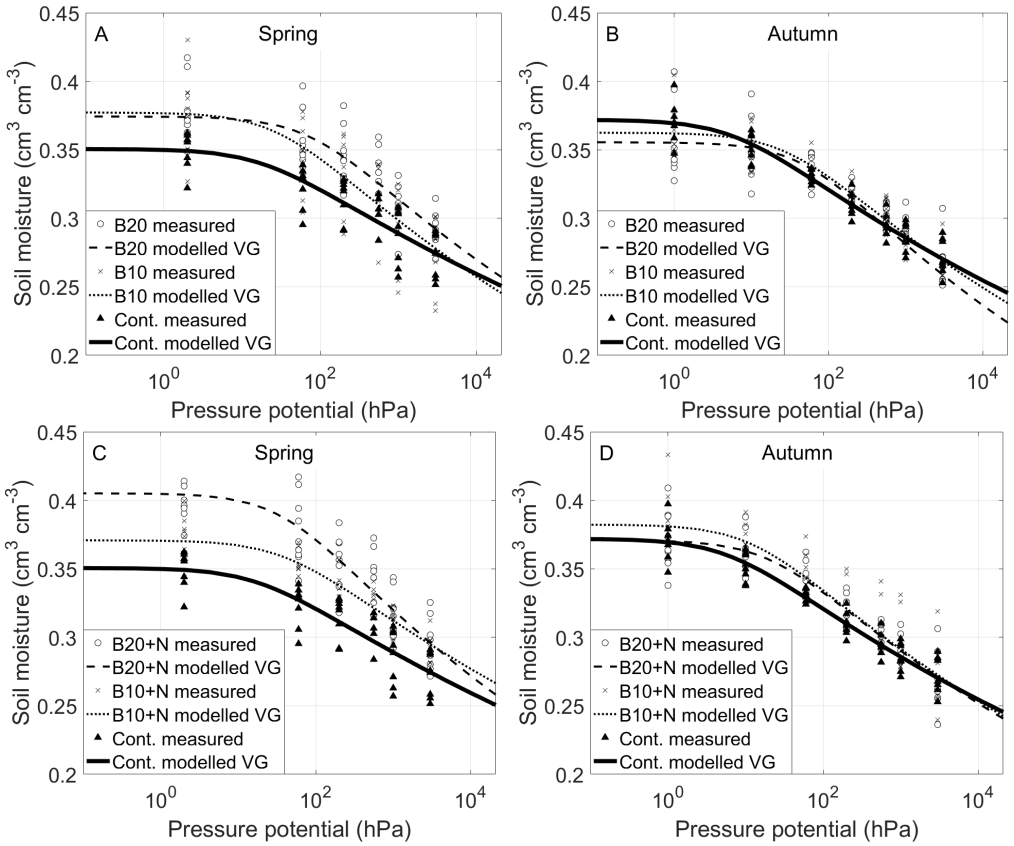

Fig. 3. The effect of biochar (A, B) and biochar with N fertilizer application (C, D) on the water retention curves found by the RETC software using the measured water contents. Soil samples were sampled from 0.05–0.10 m during spring (A, C) and autumn (B, D).

bonding material has been observed between the biochar and the mineral particles of the soil (Joseph et al., 2013, Lin et al., 2012). It has been pointed out that the bonding to the mineral particles of the soil occurs around the biochar particles, which in turn physically prevents draining of biochar-amended soil. As biochar particles bond with soil minerals, soil aggregates are formed, and this contributes to the formation of the more favorable soil structure (Sohi et al., 2009). After the autumn sampling, some 20 months after the biochar application, no significant increase in the soil porosity was recorded (Table 1).

Effect of biochar on soil sorption parameters and organic carbon content

The parameters characterizing the soil sorption capacity in relation to application of the biochar with, or without nitrogen, are shown in Table 3. For the hydrolytic acidity (Ha), a decreasing trend was observed with biochar with, or without, fertilizer. A significant decrease of Ha was observed after the autumn sampling, except for the B10 treatment. A reason for the complex acid-basic equilibrium following biochar applica-

tion to the soil could lie in the mixture of the organic and inorganic functional groups of alkali present in the biochar (DeLuca et al. 2009; Yuan et al. 2011). The acidic effect of the N fertilizer itself was eliminated by the addition of Ca and Mg in fertilizer (LAV 27), but also by relatively high buffering capacity of the soil (Hanes, 1999) and the organic matter content (Šimanský and Poláková, 2014; Stevenson, 1982). In the spring soil samples a significant increase of the sum of exchange base cations (SBC) and cation exchange capacity (CEC) was observed in the B20, B10+N and B20+N treatments, while in autumn the differences were no longer significant. Neff et al. (2002) reported that fertilization may cause change in soil pH and the electrolyte concentrations, which is then reflected in the sorption parameters of soil (Thomas et al., 2007). The base saturation (Bs) significantly increased in spring after the application of biochar at the rates of 10 and 20 t ha^{-1} with N fertilizer. It means that the sorption complex was fully saturated by basic cations. For the autumn sampling, no significant differences between treatments were observed. In our case, the biochar is a significant source of basic cations, as on average it contained 57 g kg^{-1} of Ca, 3.9 g kg^{-1} of Mg, 15 g kg^{-1} of K and 0.77 g kg^{-1} of Na. Rajkovich et al. (2012) noted that biochar ash contains nutrients, including base cations such as Ca and Mg, which cause a positive effect on the values of Bs, but that the effectiveness will decrease with time after its application (Šimanský et. al., 2018).

Incorporation of biochar in the soil has had a favorable effect on the retention of soil carbon (Agegnehu et al., 2016; Mekuria et al., 2014). Our study showed that biochar significantly contributed to an increase in the SOC in all treatments as compared to control, except for the B10 treatment at the autumn sampling. The highest SOC contents were determined in the following order B20+N > B20 > B10 = B10+N as compared to the control at spring sampling. In autumn, the content of SOC decreased in the following order: B20+N > B20 > B10+N > B10. The results show that the higher the application of biochar and N fertilizer resulted in higher SOC values (Table 3). These findings correspond with the other data from this experiment (Šimanský et al., 2016), that have already been published.

Relationships between organic carbon content, soil sorption parameters, porosity and water content at different negative pressure potentials

We have found significant linear relationships between the SBC, CEC and the Bs with total porosity (Fig. 4A, 4B and 4C). With increasing base saturation due to the application of biochar, the total porosity of the soil increased (Fig. 4C). Biochar contains base cations (Rajkovich et al., 2012), which can be joined by the means of cationic bridges with clay and organic particles (Bronick and Lal, 2005) thereby creating a favorable soil structure condition. But, the general increase in SOC content did not have any significant effect on total porosity (data not shown). The same applies to the water contents at different pressure potentials. Thus, it can be concluded that increasing SOC content did not show a direct impact on the soil water retention characteristics. Several studies have been published where authors report that the addition of biochar increases porosity (Ajayi and Horn, 2016; Lin et al., 2012; Masulili, 2010). However, our findings indicate that the total SOC content is not the only driver for increasing the soil porosity. Biochar is a material characterized by a high content of stable organic matter (Fischer and Glaser, 2012). The biochar used in our experiment was produced from the paper fiber sludge and grain husks by pyrolysis at 550°C for 30 minutes in a Pyreg reactor. Our biochar could be more stable. The reaction of stable C with soil particles is more complicated and thus the direct effect of C on the porosity was not statistically significant. The effects of biochar on soil properties largely depend on the properties of the biochars properties, which can vary widely

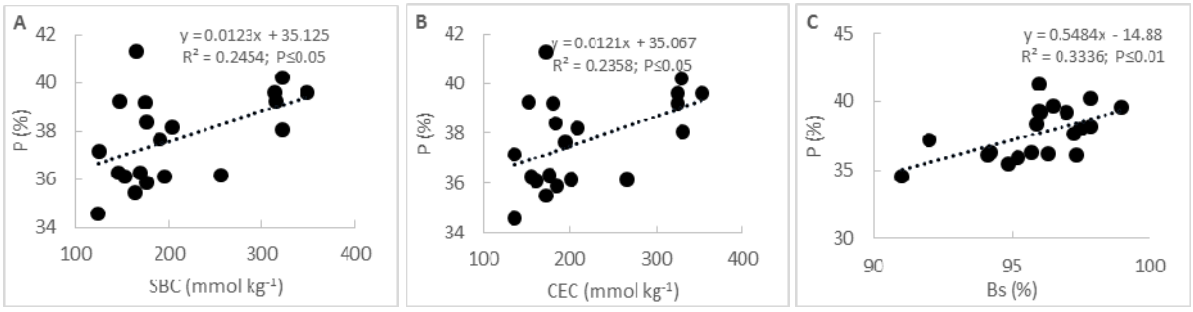

Fig. 4. The linear relationship between the porosity (P) and sum of base cations (SBC) (A), cation exchange capacity (CEC) (B) and base saturation (Bs) (C) at both (spring and autumn) samplings.

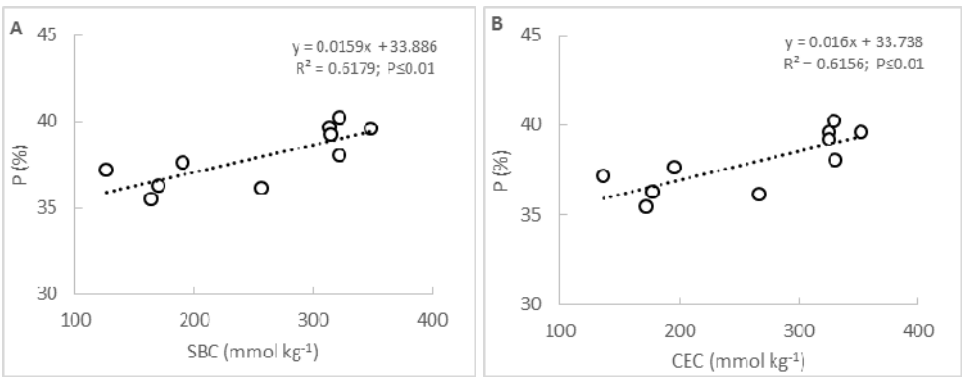

Fig. 5. The linear relationship between porosity (P) and sum of base cations (SBC) (A), cation exchange capacity (CEC) (B) at the autumn sampling.

Table 3. Statistical evaluation of soil sorption parameters and soil organic carbon (means ± standard deviations).

Treatments	Spring					Autumn				
	Ha	SBC	CEC	Bs	SOC	Ha	SBC	CEC	Bs	SOC
	(mmol kg^{-1})			(%)	(g kg^{-1})	(mmol kg^{-1})			(%)	(g kg^{-1})
Control	10.6±2.27^{b}	135.4±16.1^{a}	146.1±13.9^{a}	92.6±2.25^{a}	11.5±1.22^{a}	11.1±0.31^{d}	220.3±23.3^{a}	231.4±23.6^{a}	94.3±3.17^{a}	12.6±1.28^{a}
B10	7.84±2.39^{ab}	150.3±3.50^{ab}	158.2±5.90^{ab}	95.1±1.33^{ab}	14.2±0.12^{b}	9.83±0.06^{cd}	286.2±41.4^{a}	296.1±41.3^{a}	96.7±0.49^{a}	14.1±0.26^{ab}
B20	8.01±1.16^{ab}	175.6±1.40^{c}	183.6±2.57^{c}	95.7±0.57^{ab}	15.7±0.57^{b}	8.58±0.37^{bc}	243.1±58.2^{a}	251.7±58.9^{a}	96.3±1.85^{a}	16.8±0.14^{c}
B10+N	4.94±0.61^{a}	200.4±5.61^{d}	205.4±5.00^{d}	97.6±0.35^{b}	14.2±1.08^{b}	4.51±1.23^{a}	269.9±60.2^{a}	274.4±60.0^{a}	98.1±1.21^{a}	14.8±0.25^{b}
B20+N	7.23±0.43^{ab}	171.2±7.70^{bc}	178.4±8.14^{c}	96.0±0.06^{b}	16.2±1.05^{b}	7.28±0.37^{b}	246.1±38.1^{a}	253.3±37.6^{a}	96.8±1.50^{a}	17.5±0.55^{c}

Ha - hydrolytic acidity, SBC - sum of basic cations, CEC - cation exchange capacity, Bs - base saturation, SOC – soil organic carbon content.
Different letters between lines (a, b, c, d) indicate that treatment means are significantly different at $p < 0.05$ according to LSD multiple-range test.

between different biochars, mainly due to the variation in feedstock materials (Heitkötter, 2015; Purakayastha et al., 2015) and also due to the pyrolysis conditions (Wang et al., 2013). For example, with increasing temperature of pyrolysis the biochar is more stable. On the other hand with pyrolysis at low temperatures the biochar might have more reactive groups and be available for decomposition processes in the soil (Dickinson et al., 2016). We observed significant and positive linear relationships between SCB, CEC and the porosity at the autumn sampling (Fig. 5A and 5B). These relationships were not observed at spring sampling. We assume that a longer duration of soil processes might be necessary to change the porosity and retention characteristics. As mentioned above, biochar contains base cations (Rajkovich et al., 2012), which can act as a bond between the mineral particles of the soil, and the biochar particles (Joseph et al., 2013; Lin et al., 2012). This process could favorably influence soil sorption parameters.

CONCLUSIONS

Biochar application with, and without N fertilizer, positively influenced the soil water content in our silty loam soil during the corn growing season of 2015. Due to the biochar application, the soil moisture was higher in all treatments during dry summer period, as well as wet season later in the year. Biochar, as well as its combination with nitrogen, substantially increased porosity, RAWC, AWC and the soil water contents at the pressure potentials of –1; –5.5; –20; –55, –100 and –300 kPa as measured after the spring sampling. The higher the rate of biochar applied, the more intense neutralizing effect on the soil was observed. Generally, the most favorable changes in the soil sorption parameters were observed after biochar application at the rate of 10 t ha^{-1} in combination with N fertilizer. In such a case the soil sorption complex became fully saturated and the soil organic carbon content has significantly increased. The most favorable effect on SOC was observed after application of 20 t ha^{-1} of biochar in combination with N fertilizer.

Acknowledgement. This study was partially supported by the Slovak Research and Development Agency under the project No. APVV-15-0160, Cultural and Educational Grant Agency (KEGA) – project No. 019SPU-4/2017 and 026SPU-4/2017 and the Scientific Grant Agency (VEGA) – project No. 1/0604/16 and 1/0136/17. We also acknowledge Deniz Aydın and Brent Clothier for proof checking and valuable comments on the paper.

REFERENCES

Abel, S., Peters, A., Trinks, S., Schonsky, H., Facklam, M., Wessolek, G., 2013. Impact of biochar and hydrochar addition on water retention and water repellency of sandy soil. Geoderma, 202–203, 183–191.

Agegnehu, G., Bass, A.M., Nelson, P.N., Bird, M.I., 2016. Benefits of biochar, compost and biochar–compost for soil quality, corn yield and greenhouse gas emissions in a tropical agricultural soil. Sci. Tot. Environ., 543, 295–306.

Ajayi, A.E., Horn, R., 2016. Modification of chemical and hydrophysical properties of two texturally differentiated soils due to varying magnitudes of added biochar. Soil Tillage Res., 164, 34–44.

Brockhoff, S.R., Christians, N.E., Killorn, R.J., Horton, R., Davis, D.D., 2010. Physical and mineral-nutrition properties of sand-based turfgrass root zones amended with biochar. Agronomy Journal, 102, 6, 1627–1631.

Brodowski, S., Amelung, W., Haumaier, L., Zech, W., 2007. Black carbon contribution to stable humus in German arable soils. Geoderma, 139, 220–228.

Bronick, C.J., Lal R., 2005. The soil structure and land management: a review. Geoderma, 124, 3–22.

Buchkina, N.P., Balashov, E.V., Šimanský, V., Igaz, D., Horák, J., 2017. Changes in biological and physical parameters of soils with different texture after biochar application. Selskokhozyaistvennaya Biologiya (Agricultural Biology), 52, 3, 471–477.

Busscher, W.J., Novak, J.M., Evans, D.E., Watts, D.W., Niandou, M.A.S., Ahmedna, M., 2010. Influence of pecan biochar on physical properties of a norfolk loamy sand. Soil Sci., 175, 10–14.

Castellini, M., Giglio, L., Niedda, M., Palumbo, A.D., Ventrella, D., 2015. Impact of biochar addition on the physical and hydraulic properties of a clay soil. Soil Till. Res., 154, 1–13.

DeLuca, T.H., MacKenzie, M.D., Gundale, M.J., 2009. Biochar effects on soil nutrient transformations. In: Lehmann, J., Joseph, S. (Eds.): Biochar for Environmental Management. Science and Technology. Earthscan, London, Sterling, VA, 251–270.

Dickinson, D., Ronsse, F., Mašek, O., 2016. Biochar production and feedstock. In: Shackley, S., Ruysschaert, G., Zwart, K., Glaser, B. (Eds.): Biochar in European Soils and Agriculture, Routledge, London, 40–64.

Dziadowiec, H., Gonet, S.S., 1999. Methodical Guide-Book for Soil Organic Matter Studies. Polish Society of Soil Science, Warszawa, 65 p. (In Polish.)

Fischer, D., Glaser, B., 2012. Synergisms between compost and biochar for sustainable soil amelioration. In: Kumar, S. (Ed.): Management of Organic Waste. Earthscan, Rijeka, pp. 167–198.

Hanes, J., 1999. Analyzes of sorptive characteristics. SSCRI, Bratislava. (In Slovak.)

Heitkötter, J., Marschner, B., 2015. Interactive effects of biochar ageing in soils related to feedstock, pyrolysis temperature, and historic charcoal production. Geoderma, 245–246, 56–64.

Herath, H.M.S.K., Camps-Arbestain, M., Hedle, M., 2013. Effect of biochar on soil physical properties in two contrasting soils: an Alfisol and an Andisol. Geoderma, 209–210, 188–197.

Hlaváčiková, H., Brezianská, K., Novák, V., 2016. Influence of a biochar application on a sandy-loam soil water retention properties. Acta Hydrologica Slovaca, 17, 2, 279–286.

Hrivňáková, K., Makovníková, J., Barančíková, G., Bezák, P., Bezáková, Z., Dodok, R., Grečo, V., Chlpík, J., Kobza, J., Lištjak, M., Mališ, J., Píš, V., Schlosserová, J., Slávik, O., Styk, J., Širáň, M., 2011. Uniform methods of soil analyses. VÚPOP, Bratislava. (In Slovak.)

Jien, S.H., Wang, C.S., 2013. Effects of biochar on soil properties and erosion potential in a highly weathered soil. Catena, 110, 225–233.

Jones, B.E.H., Haynes, R.J., Phillips, I.R., 2010. Effect of amendment of bauxite processing sand with organic materials on its chemical, physical and microbial properties. J. Environ. Manage., 91, 2281–2288.

Joseph, S., Graber, E.R., Chia, C., Munroe, P., Donne, S., Thomas, T., Nielsen, S., Marjo, C., Rutlidge, H., Pan, G.X., Li, L., Taylor, P., Rawal, A., Hook, J., 2013. Shifting paradigms: development of high-efficiency biochar fertilizers based on nano-structures and soluble components. Carbon Manage., 4, 3, 323–343.

Karhu, K., Mattila, T., Bergström, I., Regina, K., 2011. Biochar addition to agricultural soil increased CH_4 uptake and water holding capacity – Results from a short-term pilot field study. Agric. Ecosyst. Environ., 140, 309–313.

Lehmann, J., Rillig, M.C., Thies, J., Masiello, C.A., Hockaday, W.C., Crowley, D., 2011. Biochar effects on soil biota - a review. Soil Biol. Biochem., 43, 9, 1812–1836.

Leij, F.J., van Genuchten, M.Th., Yates, S.R., Russell, W.B., Kaveh, F., 1992. RETC: A computer program for analyzing soil water retention and hydraulic conductivity data. In: van Genuchten, M.Th., Leij, F.J., Lund, L.J. (Ed.): Proc. Int. Workshop on Indirect Methods for Estimating the Hydraulic Properties of Unsaturated Soils. University of California, Riverside, CA, pp. 263–272.

Lin, Y., Munroe, P., Joseph, S., Henderson, R., Lin, Y., Munroe, P., Joseph, S., Henderson, R., Ziolkowski, A., 2012. Water extractable organic carbon in untreated and chemical treated biochars. Chemosphere, 87, 2, 151–157.

Liu, X., Xiao, X., Yang, G., Ren, T., 2011. Water retention curves of soil aggregates as affected by long-term fertilizer management. Soil Sci., 176, 10, 537–542.

Marquardt, D.W., 1963. An algorithm for least-squares estimation of nonlinear parameters. J. Soc. Ind. Appl. Math., 11, 431–441.

Masulili, A., 2010. Rice husk biochar for rice based cropping system in acid soil. 1. The characteristics of rice husk biochar and its influence on the properties of acid sulfate soils and rice growth in West Kalimantan, Indonesia. Journal of Agricultural Science, 2, 1.

Mekuria, W., Noble, A., Sengtaheuanghoung, O., Hoanh, Ch., T., Bossio, D., Sipaseuth, N., McCartney, M., Langan, S., 2014. Organic and clay-based soil amendments increase corn yield, total nutrient uptake, and soil properties in Lao PDR. Agroecol. Sustain. Food Syst., 38, 936–961.

Mualem, Y., 1976. A new model for predicting the hydraulic conductivity of unsaturated porous media. Wafer Resour. Res., 12, 3, 513–522.

Neff, J.C., Townsend, A.R., Gleixner, G., Lehman, S.J., Turnbull, J., Bowman, W.D., 2002. Variable effects of nitrogen additions on the stability and turnover of soil carbon. Nature, 419, 915–917.

Novak, J.M., Busscher, W.J., Watts, D.W., Amonette, J.E., Ippolito, J.A., Lima, I.M., Gaskin, J., Das, K.C., Steiner, C., Ahmedna, M. et al., 2012. Biochars impact on soil-moisture storage in an Ultisol and two Aridisols. Soil Sci., 177, 310–320.

Obia, A., Mulder, J., Martinsen, V., Cornelissen, G., Børresen, T., 2016. In situ effects of biochar on aggregation, water retention and porosity in light-textured tropical soils. Soil Till. Res., 155, 35–44.

Peng, X., Ye, L.L., Wang, C.H., Zhou, H., Sun, B., 2011. Temperature-and duration-dependent rice straw-derived biochar: characteristics and its effects on soil properties of an Ultisol in southern China. Soil Till. Res., 112, 2, 159–166.

Purakayastha,T.J., Kumari, S., Pathak, H., 2015. Characterisation, stability, and microbial effects of four biochars produced from crop residues. Geoderma, 239–240, 293–303.

Rajkovich, S., Enders, A., Hanley, K., Hyland, C., Zimmerman, A.R., Lehmann, J., 2012. Corn growth and nitrogen nutrition after additions of biochars with varying properties to a temperate soil. Biol. Fertil. Soils, 48, 271–284.

Rizhiya, E.Y., Buchkina, N.P., Mukhina, I.M., Belinets, A.S., Balashov, E.V., 2015. Effect of biochar on the properties of loamy sand spodosol soil samples with different fertility levels: a laboratory experiment. Eurasian Soil Science, 48, 2, 192–200.

Skalová, J., Kotorová, D., Igaz, D., Gomboš, M., Nováková, K., 2015. Regionalization of pedotransfer functions of moisture retention curves in Slovak soils. STU, Bratislava. (In Slovak.)

Stevenson, F.J., 1982. Humus chemistry, genesis, composition, reactions. John Wiley & Sons, New York.

Sun, F., Lu, S., 2014. Biochars improve aggregate stability, water retention, and pore-space properties of clayey soil. J. Plant Nutrit. Soil Sci., 177, 1, 26–33.

Šimanský, V., Polláková, N., 2014. Soil organic matter and sorption capacity under different soil management practices in a productive vineyard. Archives of Agronomy and Soil Science, 60, 8, 1145–1154.

Šimanský, V., Horák, J., Igaz, D., Jonczak, J., Markiewicz, M., Felber, R., Rizhiya, E.Y., Lukac, M., 2016. How dose of biochar and biochar with nitrogen can improve the parameters of soil organic matter and soil structure? Biologia, 71, 989–995.

Šimanský, V., Horák, J., Igaz, D., Balashov, E., Jonczak, J., 2018. Biochar and biochar with N fertilizer as a potential tool for improving soil sorption of nutrients. Journal of Soil and Sediments, 18, 4, 1432–1440.

Sohi, S.P., Lopez-Capel, E., Krull, E., Bol, R., 2009. Biochar, climate change and soil: A review to guide future research. CSIRO Land and Water Science Report, 5, 9, 64.

Thomas, G.A., Dalal, R.C., Standley, J., 2007. No-till effects on organic matter, pH, cation exchange capacity and nutrient distribution in a Luvisol in the semi-arid subtropics. Soil Till. Res., 94, 295–304.

Van Genuchten, M.Th., 1980. A closed-form equation for predicting the hydraulic conductivity of unsaturated soils. Soil Sci. Soc. Am. J., 44, 892–898.

Vitkova, J., Kondrlova, E., Rodny, M., Surda, P., Horak, J., 2017. Analysis of soil water content and crop yield after biochar application in field conditions. Plant, Soil and Environment, 63, 12, 569–573.

Wang, Y., Hu, Y., Zhao, X, Wang, S., Xing, G., 2013. Comparisons of biochar properties from wood material and crop residues at different temperatures and residence times. Energ. Fuel, 27, 5890–5899.

Yuan, J.H., Xu, R.K., Zhang, H., 2011. The forms of alkalis in the biochar produced from crop residues at different temperatures. Bioresour. Technol., 102, 3488–3497.

Received 7 August 2017
Accepted 12 June 2018

Note: Colour version of Figures can be found in the web version of this article.

J. Hydrol. Hydromech., 66, 2018, 4, 429–436
DOI: 10.2478/johh-2018-0033

Response of soil organic carbon and water-stable aggregates to different biochar treatments including nitrogen fertilization

Vladimír Šimanský[1*], Dušan Igaz[2], Ján Horák[2], Peter Šurda[3], Marek Kolenčík[1], Natalya P. Buchkina[4], Łukasz Uzarowicz[5], Martin Juriga[1], Dušan Šrank[1], Žaneta Pauková[6]

[1] Department of Soil Science, Faculty of Agrobiology and Food Resources, Slovak University of Agriculture, Tr. A. Hlinku 2, 949 76 Nitra, Slovakia.
[2] Department of Biometeorology and Hydrology, Faculty of Horticulture and Landscape Engineering, Slovak University of Agriculture, Tr. A. Hlinku 2, 94901 Nitra, Slovakia.
[3] Institute of Hydrology, Slovak Academy of Sciences, Dúbravská cesta 9, 841 04 Bratislava, Slovakia.
[4] Agrophysical Research Institute, 14 Grazhdansky prospect, 195220 St. Petersburg, Russian Federation.
[5] Warsaw University of Life Sciences SGGW, Faculty of Agriculture and Biology, Department of Soil Environment Sciences, Nowoursynowska Str. 159, building no. 37, 02-776 Warsaw, Poland.
[6] Department of Ecology, Faculty of European Studies and Regional Development, Slovak University of Agriculture, Tr. A. Hlinku 2, 949 76 Nitra, Slovakia.
[*] Corresponding author. Tel.: +421 37641 4398. E-mail: Vladimir.Simansky@uniag.sk

Abstract: Recent studies show that biochar improves physical properties of soils and contributes to the carbon sequestration. In contrast to most other studies on biochar, the present study comprise a long-term field experiment with a special focus on the simultaneous impact of N-fertilizer to soil structure parameters and content of soil organic carbon (SOC) since SOC has been linked to improved aggregate stability. However, the question remains: how does the content of water-stable aggregates change with the content of organic matter? In this paper we investigate the effects of biochar alone and in a combination with N-fertilizer (i) on the content of water-stable macro- (WSA_{ma}) and micro-aggregates (WSA_{mi}) as well as soil structure parameters; and (ii) on the contents of SOC and labile carbon (C_L) in water-stable aggregates (WSA).

A field experiment was conducted with different biochar application rates: B0 control (0 t ha^{-1}), B10 (10 t ha^{-1}) and B20 (20 t ha^{-1}) and 0 (no N), 1st and 2nd level of nitrogen fertilization. The doses of level 1 were calculated on required average crop production using the balance method. The level 2 included an application of additional 100% of N in 2014 and additional 50% of N in the years 2015–2016 on silty loam Haplic Luvisol at the study site located at Dolná Malanta (Slovakia). The effects were investigated after the growing season of spring barley, maize and spring wheat in 2014, 2015 and 2016, respectively.

The results indicate that the B10N0 treatment significantly decreased the structure vulnerability by 25% compared to B0N0. Overall, the lower level of N combined with lower doses of biochar and the higher level of N showed positive effects on the average contents of higher classes of WSA_{ma} and other soil structure parameters. The content of SOC in WSA in all size classes and the content of C_L in WSA_{ma} 3–1 mm significantly increased after applying 20 t ha^{-1} of biochar compared to B0N0. In the case of the B20N1 treatment, the content of SOC in WSA_{ma} within the size classes >5 mm (8%), 5–3 mm (19%), 3–2 mm (12%), 2–1 mm (16%), 1–0.5 mm (14%), 0.5–0.25 mm (9%) and WSA_{mi} (12%) was higher than in B0N1. We also observed a considerably higher content of SOC in WSA_{ma} 5–0.5 mm and WSA_{mi} with the B10N1 treatment as compared to B0N1. Doses of 20 t biochar ha^{-1} combined with second level of N fertilization had significant effect on the increase of WSA_{ma} and WSA_{mi} compared to the B0N2 treatment. A significant increase of C_L in WSA was determined for size classes of 2–0.25 mm and WSA_{mi} in the B20N2 treatment. Our findings showed that biochar might have beneficial effects on soil structure parameters, SOC, C_L in WSA and carbon sequestration, depending on the applied amounts of biochar and nitrogen.

Keywords: Soil structure; Soil organic carbon; Labile carbon; Aggregate stability; Biochar; N fertilizer.

INTRODUCTION

Refining our understanding of how soil structure develops is important because soil structure has a major influence on plant growth (Millar et al., 1962). SOC is one of the most important factors affecting soil structure (Kodešová et al., 2015; Saha et al., 2011; Šimanský and Jonczak, 2016), since SOC acts as a significant binding agent for soil particles (Bronic and Lal, 2005). Organic manure is one of the most important secondary sources of SOC in arable soils. A decline in livestock population in Slovakia over the last years has been reported, which leads to a reduced organic fertilizer production. At present, a deficit of organic matter on agricultural soils between 30 up to 50% is observed. The annual production of organic fertilizers is now around 10 mil. t y^{-1}, which is less than 5 t ha^{-1} of agricultural soil (Green Report, 2014). With respect to sustainable land management, it is essential to look for new resources in order to achieve a sufficient balance of organic substances. The application of biochar could serve as a plausible and innovative solution to this problem. Biochar is a stable source of organic carbon (Fischer and Glaser, 2012). Recent results showed that biochar incorporated to soils increases organic carbon content what contributed to its sequestration (Agegnehu et al., 2016; Cross et al., 2016). Over the last decade, biochar research focused on the agricultural sector also due to its positive effects on improvement of soil physical properties such as retention

water capacity, total porosity, soil structure and soil water content (Atkinson et al., 2010; Barrow, 2012; Jones et al., 2010; Obia et al., 2016; Vitkova et al., 2017). Biochar particles associate with soil particles resulting in stable soil aggregates with favourable structure (Brodowski et al., 2006; Jien and Wang, 2013). Potential benefits of biochar applications needs to be carefully discussed with farmers, particularly when compared in relation to soil organic matter. Application of farmyard manure, compost or crop residues are classical methods used to improve soil fertility. Although biochar addition might be accompanied with an elevated content of organic matter, improved structure of soil and soil fertility, the residual effects might be very different (Cross et al., 2016).

The application of biochar to the soil could increase the immobilization of macro- (especially nitrogen) and micronutrients and decrease their uptake by plants (Šimanský et al., 2018). The effects of biochar on soil properties largely depends on biochars' properties, which vary widely between different biochars, mainly due to variations in feedstock materials (Butnan et al., 2015) and also pyrolysis conditions (Wang et al., 2013). The different effects might be a result of differences in the biochar reactivity (i.e., amount of reactive functional groups) that strongly depends on production conditions and feedstock (Keluweit et al., 2010). Combining biochar with a nitrogen fertilizer appears to be a promising practice for sustainable agriculture. Since the interactions between biochar, mineral fertilizer and soil are complex processes, additional research is needed.

In this context, we hypothesised that: (i) a higher application rate of biochar combined with N-fertilizer will improve soil structure since nitrogen may intensify the mineralization processes of biochar and enhance the association of biochar particles with soil particles, (ii) higher doses of biochar are responsible for more water-stable macro-aggregates compared to micro-aggregates and for a higher content of SOC inside of individual size classes of the water-stable aggregates. Since labile carbon is a very sensitive soil parameter (Szombathová, 1999), we suppose that (iii) adding biochar combined with N fertilizer will lead to intensive changes in labile carbon content.

The objective of this study were to quantify the effects of biochar and biochar in combination with N fertilizer (i) on the content of water-stable aggregates and soil structure parameters, and (ii) on the content of soil organic and labile carbon in water-stable aggregates.

MATERIAL AND METHODS

Description of study site

The field experiment was conducted at the experimental site of the Slovak University of Agriculture in Nitra, Dolná Malanta (48°19′00″ N; 18°09′00″ E). The site has a temperate climate, with a mean annual air temperature of 9.8°C, and with mean maximum and minimum temperatures of 17°C (July) and –3°C (January). The mean annual precipitation at this site is 540 mm (150–200 mm between June and August). The parent material consists of little previous rocks with high quantities of fine particles. Young Neogene deposits consist of various clays, loams, sand gravels on which loess were deposited in the Pleistocene Epoch. The soil is classified as Haplic Luvisol according to the Soil Taxonomy (IUSS WRB, 2014) with 9.13 g kg^{-1} of soil organic carbon, 5.71 pH and a silty loam texture (content of sand 15.2%, silt 59.9% and clay 24.9%).

Experimental design and field management

Prior to the experiment, the soil at the experimental site were cultivated for over 100 years using conventional agriculture techniques. Our experiment started in March 2014. The experimental field is shown in Fig. 1a. Fig. 1b shows a schematic layout of the experimental design. The investigated treatments are presented in Table 1. The study was carried out on 27 plots. Each plot had an area of 24 m^2 (4 m x 6 m). Three groups consisting of nine plots was arranged in a row and treated as replications. The spacing between the neighbouring replications was 0.5 m. The field was ploughed, harrowed and biochar was evenly applied to the soil surface and immediately incorporated into the 0–10 cm soil layer combined with or without N fertilizer.

Table 1. The investigated treatments.

Treatment	Description
B0N0	no biochar, no N fertilization
B10N0	biochar at rate of 10 t ha^{-1}
B20N0	biochar at rate of 20 t ha^{-1}
B0N1	no biochar combined with first level of N fertilization: dose of N were 40, 160 and 100 kg N ha^{-1} in 2014, 2015 and 2016, respectively.
B10N1	biochar at rate of 10 t ha^{-1} with N: dose of N were 40, 160 and 100 kg N ha^{-1} in 2014, 2015 and 2016, respectively.
B20N1	biochar at rate of 20 t ha^{-1} with N: dose of N were 40, 160 and 100 kg N ha^{-1} in 2014, 2015 and 2016, respectively.
B0N2	no biochar combined with second level of N fertilization: dose of N were 80, 240 and 150 kg N ha^{-1} in 2014, 2015 and 2016, respectively.
B10N2	biochar at rate of 10 t ha^{-1} with N: dose of N were 80, 240 and 150 kg N ha^{-1} in 2014, 2015 and 2016, respectively.
B20N2	biochar at rate of 20 t ha^{-1} with N: dose of N were 80, 240 and 150 kg N ha^{-1} in 2014, 2015 and 2016, respectively.

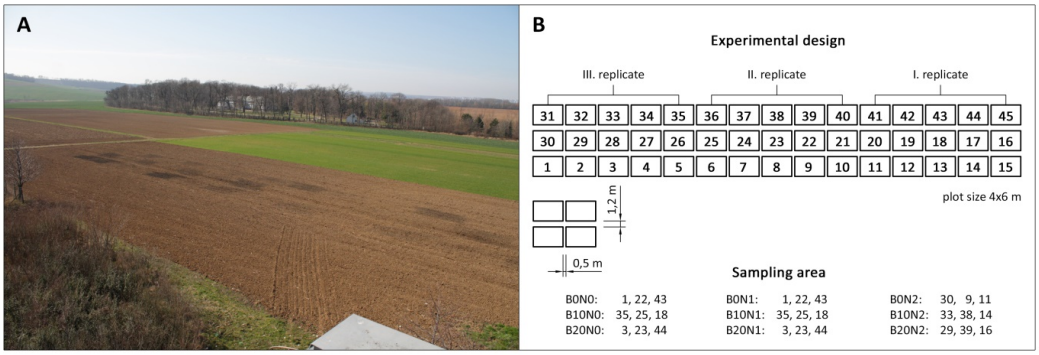

Fig. 1. Schematic layout of the experimental field.

A standard N fertilizer (Calc-Ammonium nitrate with dolomite, LAD 27) was used in this experiment. The biochar used in this study was provided from commercial producer (Sonnenerde, Austria). The biochar was produced from paper fiber sludge and grain husks (1:1 w/w). As declared by the manufacturer, the biochar was produced at a pyrolysis temperature of 550°C applied for 30 minutes in a Pyreg reactor. The pyrolysis product (biochar) has particle sizes between 1 to 5 mm. On average, the product contains 57 g kg^{-1} of Ca, 3.9 g kg^{-1} of Mg, 15 g kg^{-1} of K and 0.77 g kg^{-1} of Na. The total C content of the biochar is 53.1%, while the total N content is 1.4%, with the C:N ratio of 37.9. The specific surface area (SSA) is 21.7 m^2 g^{-1} and the content of ash is 38.3%. On average, the pH of the biochar is 8.8. The field experiment had the following annual crop rotation starting with spring barley (*Hordeum vulgare* L.) in 2014, followed by maize (*Zea mays* L.) in 2015 and spring wheat (*Triticum aestivum* L.) in 2016.

Sampling and measurements

Soil samples (depths 0–20 cm) were collected from all treatments. Sampling of soil was conducted monthly to cover the whole growing season of spring barley (from 17 April to 13 July in 2014), maize (from 15 April to 28 September in 2015) with sampling extended to 2016 to cover the whole spring growing season of wheat (sampling dates: on 20 April, 17 May, 22 June, and 18 July). The sampling campaign was conducted one, two, three and four months after biochar application in 2014. In 2015, sampling was conducted 13, 14, 15, 16, 17 and 18 months after biochar application. In 2016, sampling was conducted 26, 27, 28 and 29 months after the biochar was applied.

The soil samples were carefully taken using a spade to avoid disruption of the soil aggregates. The samples were mixed to produce an average representative sample from each plot. Roots and large pieces of crop residues were removed. Large clods were gently disrupted along natural fracture lines in the laboratory, and air-dried at the laboratory temperature. The dry soil samples were sieved (dry sieving) to the following seven size fractions: >7, 7–5, 5–3, 3–2, 2–1, 1–0.5, 0.5–0.25 mm. The percentage of water-stable aggregates (*WSA*) was determined by the Baksheev method (Vadjunina and Korchagina, 1986). The analysis started with a 30g sample of aggregates. The aggregates were first rinsed with distilled water. After two hours, each sample was transferred to the top sieve (>5 mm) with a cylindrical container (Baksheev device) filled with distilled water. Six sieves with mesh sizes of 5, 3, 2, 1, 0.5 and 0.25 mm were used. The cylinder was hermetically sealed and the samples were sieved for 12 minutes (soaked in water). The obtained fractions of water-stable aggregates were transferred from the individual sieves to a filter paper and dried in an oven at 45 °C. The residual material was quantified on each sieve except for micro-aggregates, i.e., water-stable aggregates < 0.25 mm (WSA_{mi}), for which the content was calculated as the difference between the total weight of the soil sample and the sum of the macro-aggregates (WSA_{ma}). The soil organic carbon (Dziadowiec and Gonet, 1999) and the labile carbon (Loginow et al., 1987) were analyzed for all fraction sizes of the WSA. Briefly, the content of soil organic carbon (SOC) in the water-stable aggregates (WSA) was determined using the wet combustion method - oxidizing organic matter in a mixture of 0.07 M H_2SO_4 and $K_2Cr_2O_7$ with titration using 0.01 M Mohr's salt. The labile carbon content (C_L) in the WSA was extracted from the samples containing 1 g of individual particle-size fractions of WSA by shaking in 50 mL of 0.005 M $KMnO_4$ for 2 hours. After centrifugation, the C_L was determined by oxidation of 0.07 M H_2SO_4 and $K_2Cr_2O_7$ with titration using 0.05 M Mohr's salt.

The dried and wet-sieved samples were used to calculate the mean dry and wet weight diameters (MWD_d and MWD_w) of water-stable aggregates, vulnerability coefficient (K_v) by Valla et al. (2000) as well as the stability index of water-stable aggregates (*Sw*) by Henin (Lal and Shukla, 2004). The above-mentioned soil structure parameters (MWD_d, MWD_w, K_v and *Sw*) were calculated according to the following equations (1–4):

$$Sw = \frac{WSA - 0.09sand}{silt + clay} \quad (1)$$

where: *Sw* is the index of aggregate stability and *WSA* is the content of water-stable aggregates (%).

$$MWD_d = \sum_{i=1}^{n} x_i w_i \quad (2)$$

where: MWD_d is the mean weight diameter of aggregates for dry sieving (mm), x_i is the mean diameter of each size fraction (mm) and w_i is the portion of the total sample weight within the corresponding size fraction, and *n* is the number of size fractions.

$$MWD_w = \sum_{i=1}^{n} x_i WSA \quad (3)$$

where: MWD_w is mean weight diameter of water stable aggregates (mm), x_i is mean diameter of each size fraction (mm), and *WSA* is portion of the total sample weight within the corresponding size fraction, and *n* is the number of size fractions.

$$K_v = \frac{MWD_d}{MWD_w} \quad (4)$$

where: K_v is the vulnerability coefficient, MWD_d is the mean weight diameter of aggregates for dry sieving (mm), and MWD_w is the mean weight diameter of water stable aggregates (mm).

The Philips scanning electron microscope (SEM) with energy dispersive X-ray microanalysis (EDX) was used to characterize the biochar in the analyzed soil aggregates. The measurements were performed at VŠB – Technical University of Ostrava (Nanotechnology Centre), Czech Republic. SEM images were recorded using secondary electrons in the mode of back scattering electrons at an operating voltage of 20 kV.

The mineral components in the soil aggregates were identified by X-ray powder diffraction (XRD) analysis on the diffractometer PW1710 (Philips, The Netherlands) under the following conditions: Bragg-Brentano geometry (Theta-2Theta), Cu anticathode (λa_1 = 1.54060 Å), beam current 40 mÅ, and accelerating voltage of 40 kV. The step size was 0.01°2 Θ, the settled step time 1 s per one step at measurement range from 4 to 65° 2Θ. X-ray powder diffraction analysis was conducted at the Slovak Academy of Sciences.

Statistics

The data were analyzed by ANOVA tests implemented in the software package Statgraphics Centurion XV.I (Statpoint Technologies, Inc., USA). Comparisons between samples were conducted using least significant differences (LSD) at the probability level of $P = 0.05$.

RESULTS AND DISCUSSION

Content of water-stable aggregates and soil structure parameters

The average parameters of soil structure such as: MWD_w, K_v, Sw, WSA_{ma} and WSA_{mi} as a result of biochar amendment are shown in Table 2. The results of Atkinson et al. (2010) and Barrow (2012) show that biochar has positive effects on soil structure. In our case, the effects of biochar and biochar combined with N fertilization on soil structure parameters were different. The one-way ANOVA test did not show any significant differences between the biochar treatments without N in terms of WSA_{ma}, WSA_{mi}, Sw and both values of MWD. Our results suggest that biochar without N fertilization did not enhance the soil structure parameters except the K_v values. When no nitrogen was applied, a significant effect on K_v was observed in the treatment with 10 t biochar ha^{-1}, and no significant effect was determined after application 20 t biochar ha^{-1} compared to B0N0. The lower soil structure vulnerability can be explained also by the lower dose of biochar, an effect already observed after one year after the incorporation of biochar to the soil (Šimanský et al., 2016). High levels of labile C fraction in biochar explain this effect (Cross et al., 2016). Adding less biochar with no N fertilizers may thus be more beneficial for soil aggregation that higher doses of biochar. On the other hand, biochar with both levels of N fertilization improved the soil structure (Table 2). The average contents of WSA_{ma} in the B0N1, B10N1, B20N1, B0N2, B10N2 and B20N2 treatments were 69.9, 75.0 and 77.5% or 67.3, 73.1 and 78.7%, respectively. These figures indicates a significant increase in the WSA_{ma} contents due to higher doses of biochar in combination with N fertilization. The same trends (significant increase/decrease) were observed in the case of Sw, K_v, MWD_w and contents of WSA_{mi}. Combinations 10 t biochar ha^{-1} with the first level of N fertilization (N1) and biochar at a rate of 20 t ha^{-1} with a second level of N fertilization (N2) significantly increased MWD_w compared to the B0N1 and B0N2 treatments. An apparent increase of MWD_w, as reported by Jien and Wang (2013), might indicate that a biochar might more facilitate the formation of macro-aggregates. This explains the decreasing of WSA_{mi}. This effect is enhanced with addition of N (Table 2). As reported by Ma et al. (2016), applications of biochar and N-fertilizer contributes to a significant increase of SOC, which could be related to a higher absorption of cations (Liang et al., 2006), intensive cation exchange capacity (Yuan and Xu, 2012) and finally higher soil structure stability (Obia et al., 2016). In our case, a higher dose of biochar with both N fertilization levels resulted in a better structure state of the soil. Contradictory findings have been published as to how biochar affects soil structure. It is still unclear how combining biochar with N fertilization affects soil structure, but the major responsible factors include particle-size distribution of studied soils (Liu and Zhou, 2012), application rate of biochar, time after biochar application (Ruysschaert et al., 2016) its combination with other fertilizers (Ma et al., 2016) and biochar properties (Alburquerque et al., 2014). The surface of biochar particles after oxidation may contain hydroxyl and carboxylic groups which are able to absorb soil particles and clays and form macro-aggregates (Jien and Wang, 2013), however, this process requires a substantially longer times to take place. As reported by Herath et al. (2013), the formation of soil aggregates is a function of biological activity and time, and it is unlikely to occur immediately upon biochar application. In our study, applying biochar at rates of 10 and 20t ha^{-1} with no N fertilization did not affect the average contents of individual size classes of WSA_{ma} during studied period (2014–2016). On the other hand, a combination of both rates of biochar applied with both levels of nitrogen fertilizer showed a significant effect on the individual size classes of WSA_{ma} compared to the B0N1 and B0N2 treatments (Table 3).

Table 2. Parameters of soil structure (means and standard deviation).

Treatments	WSA_{ma}	WSA_{mi}	Sw	K_v	MWD_d	MWD_W
B0N0	73.4±6.89^{a}	26.6±6.89^{a}	0.85±1.10^{a}	4.28±1.10^{b}	2.98±0.18^{a}	0.73±0.25^{a}
B10N0	77.9±8.51^{a}	22.1±8.51^{a}	0.90±0.10^{a}	3.22±0.56^{a}	2.83±0.61^{a}	0.89±0.21^{a}
B20N0	75.2±8.38^{a}	24.8±8.38^{a}	0.87±0.10^{a}	4.12±1.70^{b}	2.82±0.44^{a}	0.80±0.33^{a}
B0N1	69.9±9.11^{a}	30.1±9.11^{b}	0.81±0.11^{a}	4.66±1.44^{b}	2.91±0.58^{a}	0.68±0.23^{a}
B10N1	75.0±8.81^{ab}	25.0±8.81^{ab}	0.87±0.10^{ab}	3.60±1.45^{a}	2.98±0.50^{a}	0.93±0.32^{b}
B20N1	77.5±8.43^{b}	22.5±8.43^{a}	0.90±0.10^{b}	3.45±1.33^{a}	2.78±0.48^{a}	0.88±0.28^{ab}
B0N2	67.3±7.01^{a}	32.7±7.01^{c}	0.78±0.08^{a}	4.25±1.22^{b}	2.58±0.69^{a}	0.59±0.13^{a}
B10N2	73.1±8.15^{b}	26.9±8.15^{b}	0.85±0.10^{b}	4.12±1.58^{ab}	2.60±0.56^{a}	0.69±0.19^{a}
B20N2	78.7±6.65^{c}	21.3±6.65^{a}	0.91±0.08^{c}	3.26±0.91^{a}	2.82±0.51^{a}	0.91±0.23^{b}

WSA_{ma} – content of water-stable macro-aggregates, WSA_{mi} – content of water-stable micro-aggregates, Sw – stability index of water-stable aggregates, K_v – vulnerability coefficient, MWD_d – mean weight diameter of aggregates for dry sieving, MWD_W – mean weight diameter of water stable aggregates.
Different letters (a, b, c) between lines indicate that treatment means are significantly different at $P<0.05$ according to LSD multiple-range test.

Table 3. Contents of individual size fraction of water-stable macro-aggregates in % (means and standard deviation).

	Individual size fractions of water-stable macro-aggregates in mm					
Treatments	>5	5–3	3–2	2–1	1–0.5	0.5–0.25
B0N0	2.21±1.34^{a}	3.90±1.88^{a}	8.49±3.25^{a}	15.8±7.92^{a}	25.6±4.22^{a}	17.4±4.69^{a}
B10N0	3.26±1.08^{a}	5.41±2.96^{a}	10.7±3.40^{a}	20.1±7.91^{a}	23.1±3.45^{a}	15.3±4.24^{a}
B20N0	2.47±1.43^{a}	4.94±2.21^{a}	9.51±3.67^{a}	16.3±6.68^{a}	25.5±5.87^{a}	16.5±4.54^{a}
B0N1	2.26±1.58^{a}	3.75±2.91^{a}	7.30±3.61^{a}	13.9±4.68^{a}	24.4±4.01^{a}	18.4±3.90^{b}
B10N1	4.22±2.26^{b}	6.60±2.11^{b}	10.6±4.82^{b}	15.6±6.27^{a}	21.2±3.46^{a}	16.8±5.13^{ab}
B20N1	3.40±2.74^{ab}	5.26±3.12^{ab}	10.0±3.80^{ab}	19.3±7.54^{a}	24.5±5.62^{a}	15.0±3.41^{a}
B0N2	1.94±1.07^{a}	3.06±1.57^{a}	5.78±2.14^{a}	10.5±4.52^{a}	27.2±4.88^{a}	18.9±3.64^{b}
B10N2	2.19±0.98^{a}	3.45±1.70^{a}	7.65±3.67^{a}	14.4±6.12^{a}	26.0±5.24^{a}	18.6±4.22^{b}
B20N2	2.81±1.75^{a}	5.86±2.37^{b}	11.5±3.56^{b}	20.3±6.70^{b}	24.2±5.85^{a}	14.8±4.91^{a}

Different letters (a, b, c) between lines indicate that treatment means are significantly different at $P<0.05$ according to LSD multiple-range test.

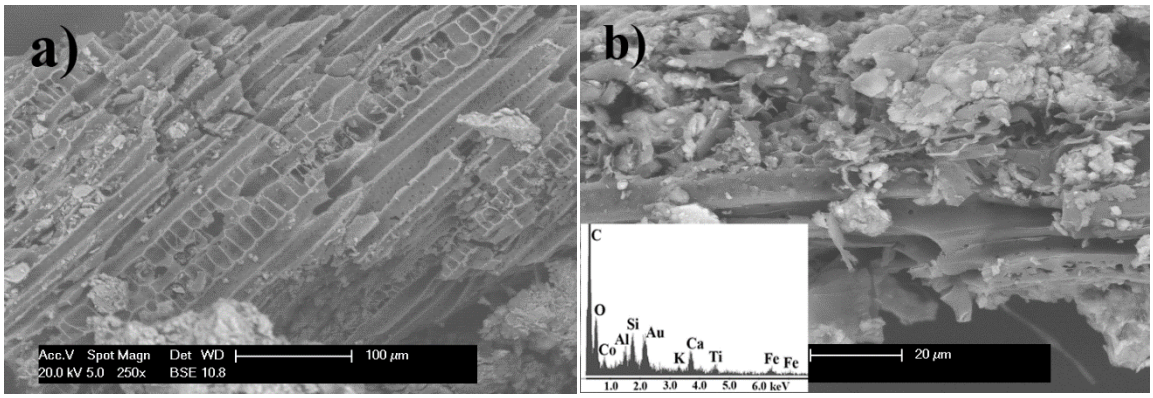

Fig. 2. a) Visualised high surface area and presence of micropores in biochar-related structure, b) Soil aggregate consists of biochar (in the center) with original surface lamellae texture and structure associated with various minerals. Incorporate minerals pose particular size, morphology, and sticking coefficients with biochar (Scanning electron microscopy); inset: chemical analysis of aggregate contained dominant element C (come from biochar), and elements O, Al, Si, Ti, Ca, K, Fe, Co which related to others soil minerals. Gold dispersed over the sample provided better conduction properties (Energy Dispersive Spectrum). This is one possible composition of elements to take the heterogeneity of soils into account.

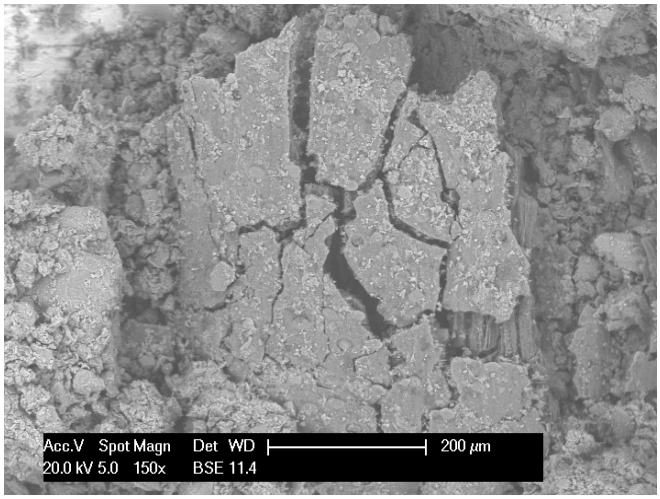

Fig. 3. Biochar incorporated into soil. Surface disruptions are visible. Large pore sizes increase the surface-to-volume ratio (Scanning Electron Microscopy).

In the case of the B10N1 treatment, the contents of WSA_{ma} in the size classes >5 mm (87%), 5–3 mm (76%), 3–2 mm (45%) were higher than in B0N1. We observed a considerably higher content of WSA_{ma} 2–1 mm and lower content of WSA_{ma} 0.5–0.25 mm, probably due to application of biochar at a rate of 20 t ha^{-1} together with first level of N fertilization as compared B0N1. Both doses of biochar as well as N fertilization levels did not have a noticeable effect on WSA_{ma} 1–0.5 mm as compared to the B0N1 and B0N2 treatments. The dosage of 20 t biochar ha^{-1} combined with second level of N fertilization had an significant positive effect on WSA_{ma} in size classes 5–3 mm (92%), 3–2 mm (99%) and 2–1 mm (93%) compared to the B0N2 treatment. The lower level of N combined with lower dose of biochar as well as the higher level of N with higher dose of biochar resulted in positive effects on average contents of higher classes of WSA_{ma}. Biochar as a soil amendment has a large specific surface area (Chintala et al., 2014) with the presence of micropores (Jones et al., 2010; Mukherjee et al., 2011). Fig. 2a shows the original texture and structure of the source material. Fig. 2b shows soil aggregate with biochar being in the center. This biochar is in connection with mineral particles which are present in the soil. Apparently, the surface of biochar (Fig. 3) gradually degraded, as indicated by the visually detected disruptions, large pores size distribution, and the increased biochar surface-to-volume ratio with high specific surface area. On the other hand, the portion of extractable biochar could support soil aggregate creation and physical aggregate stability as several authors reported (Chan et al., 2007; Lehmann et al., 2011; Spokas, 2010). Minerals constitute the main components in the formation of aggregates. The X-ray diffraction analysis (Fig. 4) revealed that the dominant mineral components were α-quartz (SiO_2), anorthite $Ca(Al_2Si_2O_8)$, and muscovite $(KAl_2(AlSi_3O_{10})(OH)_2)$. The chemical analysis of aggregates (Fig. 2b) showed the presence of O, Al, Si, Ti, Ca, K, Fe, Co and C. The stability of aggregates can be influenced by the presence, content and the type of clay minerals (Bai et al. 2013). As presented by Lehmann (2007), adding nitrogen to soil in combination with biochar may improve microbial activity, increase the intensity of biochar mineralization processes (Cross et al., 2016) and increase the cation exchange capacity (Yeboah et al., 2009; Yuan and Xu, 2012) and active surface area (Liang et al., 2006; Mukherjee et al., 2011) with positive effects on soil aggregation (Bronick and Lal, 2005).

Contents of soil organic carbon and labile carbon in water-stable aggregates

The results indicate that the biochar became part of the soil aggregates (Fig. 2b, Fig. 3) after its incorporation to the soil, since the soil particles tend to form aggregates with occluded biochar (Brodowski et al., 2006). This explains the elevated carbon content in the aggregates (Blanco-Canqui and Lal, 2004) and the mechanism of carbon sequestration (Six et al., 2002). On the other hand, biochar is very stable compared to other organic matter amendments (Fischer and Glaser, 2012; Kuzyakov et al., 2009; Lehmann et al., 2008; Lopez-Capel et al., 2016) with insignificant increase of SOC levels even though the biochar had a high TOC content (Jien and Wang, 2013).

Our study showed that different application rates of biochar alone, and biochar combined with N fertilizer affected the distribution of SOC and C_L concentration in the analysed WSA (Table 4). The largest fractions of WSA_{ma} contained higher SOC and C_L in all treatments. The smaller fractions of WSA_{ma} and WSA_{mi} contained lower SOC and C_L. These findings are consistent with Tisdall and Oades (1980) and Six et al. (2004) who found higher concentrations of organic C in macro-

Table 4. Contents of soil organic carbon and labile carbon in the individual size fractions of water-stable aggregates (means and standard deviation).

Treatments	Individual size fractions of water-stable aggregates in mm						
	>5	5–3	3–2	2–1	1–0.5	0.5–0.25	<0.25
	Content of soil organic carbon in water-stable aggregates in %						
B0N0	1.46±0.25^{a}	1.35±0.12^{a}	1.29±0.10^{a}	1.35±0.12^{a}	1.23±0.09^{a}	1.15±0.09^{a}	1.03±0.07^{ab}
B10N0	1.41±0.24^{a}	1.28±0.17^{a}	1.26±0.15^{a}	1.30±0.22^{a}	1.21±0.15^{a}	1.15±0.13^{a}	0.97±0.15^{a}
B20N0	1.55±0.22^{a}	1.57±0.34^{b}	1.49±0.17^{b}	1.58±0.26^{b}	1.36±0.14^{b}	1.28±0.15^{b}	1.09±0.11^{b}
B0N1	1.33±0.18^{a}	1.22±0.10^{a}	1.21±0.10^{a}	1.28±0.13^{a}	1.18±0.09^{a}	1.13±0.06^{a}	0.97±0.06^{a}
B10N1	1.34±0.16^{a}	1.39±0.16^{b}	1.32±^{b}	1.44±0.17^{b}	1.28±0.09^{b}	1.20±0.11^{ab}	1.01±0.11^{b}
B20N1	1.43±0.13^{b}	1.45±0.19^{b}	1.36±0.13^{b}	1.48±0.18^{b}	1.35±0.14^{b}	1.23±0.11^{b}	1.09±0.10^{b}
B0N2	1.37±0.15^{a}	1.34±0.12^{a}	1.27±0.09^{a}	1.39±0.13^{a}	1.25±0.09^{a}	1.18±0.05^{a}	1.01±0.08^{a}
B10N2	1.52±0.24^{ab}	1.50±0.23^{b}	1.42±0.16^{b}	1.47±0.26^{a}	1.30±0.12^{ab}	1.17±0.09^{a}	1.04±0.13^{ab}
B20N2	1.57±0.26^{b}	1.44±0.18^{ab}	1.41±0.11^{b}	1.48±0.21^{a}	1.34±0.09^{b}	1.27±0.07^{b}	1.11±0.10^{b}
	Content of labile carbon in water-stable aggregates in g kg^{-1}						
B0N0	1.47±0.32^{a}	1.39±0.27^{a}	1.24±0.26^{a}	1.19±0.19^{a}	1.19±0.19^{a}	1.28±0.20^{a}	1.12±0.10^{a}
B10N0	1.65±0.30^{a}	1.40±0.14^{a}	1.29±0.15^{ab}	1.30±0.20^{a}	1.32±0.21^{a}	1.28±0.20^{a}	1.12±0.19^{a}
B20N0	1.72±0.44^{a}	1.55±0.35^{a}	1.40±0.20^{b}	1.48±0.23^{b}	1.28±0.19^{a}	1.30±0.16^{a}	1.16±0.18^{a}
B0N1	1.62±0.41^{a}	1.51±0.38^{a}	1.37±0.28^{a}	1.35±0.26^{a}	1.28±0.23^{a}	1.21±0.20^{a}	1.10±0.18^{a}
B10N1	1.68±0.33^{a}	1.32±0.31^{a}	1.43±0.20^{a}	1.46±0.25^{a}	1.38±0.26^{a}	1.31±0.26^{a}	1.20±0.17^{a}
B20N1	1.67±0.39^{a}	0.15±0.33^{a}	1.39±0.23^{a}	1.42±0.24^{a}	1.37±0.23^{a}	1.34±0.20^{a}	1.25±0.26^{a}
B0N2	1.63±0.33^{a}	1.44±0.23^{a}	1.33±0.27^{a}	1.24±0.14^{a}	1.19±0.17^{a}	1.13±0.25^{a}	1.04±0.14^{a}
B10N2	1.60±0.39^{a}	1.57±0.32^{a}	1.40±0.16^{a}	1.45±0.18^{b}	1.30±0.22^{ab}	1.20±0.15^{a}	1.10±0.18^{a}
B20N2	1.82±0.43^{b}	1.52±0.30^{a}	1.46±0.28^{a}	1.47±0.29^{b}	1.38±0.22^{b}	1.38±0.26^{b}	1.24±0.23^{b}

Different letters (a, b, c, d) between lines indicate that treatment means are significantly different at $P<0.05$ according to LSD multiple-range test.

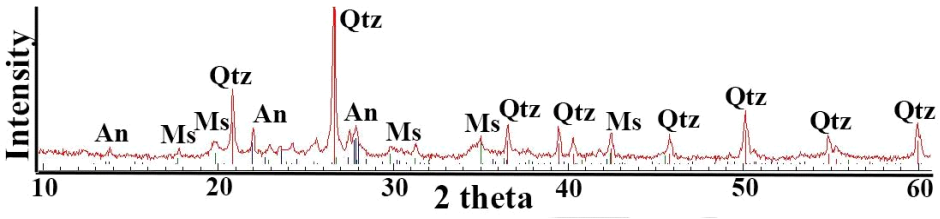

Fig. 4. X-ray powder diffraction analysis reveals the presence of soil aggregate minerals with dominant content of α-quartz (Qtz), anorthite (An), and muscovite (Ms).

aggregates than in micro-aggregates. Elliott (1986) suggested that macro-aggregates show elevated C concentrations because of the organic matter binding micro-aggregates into macro-aggregates, and because this organic matter is "qualitatively more labile and less highly processed" than the organics stabilizing micro-aggregates. In our study, the SOC in WSA significantly increased in all size classes (except >5 mm) after applying biochar at a rate of 20 t ha^{-1} compared to the B0N0 as well as B10N0 treatments. C_L in WSA significantly increased only in WSA_{ma} 3–1 mm and in B20N0 (Table 4). The application of 10 and 20 t ha^{-1} of biochar combined with both N fertilization levels significantly affected the re-distribution of SOC and C_L in WSA during the investigated period. The highest increase of SOC in WSA_{mi} and WSA_{ma} were determined in the B20N1 treatment compared to B0N1 (Table 4). A significant increase of SOC in WSA_{mi} and WSA_{ma} 5–0.5 mm in the B10N1 treatment as compared to B0N1 was observed. The same trends (increase of SOC in WSA) were observed in both application rates of biochar combined with the second N fertilization level. The significant effects were found in B20N2 for size classes of WSA_{ma} 1–0.25 and >2 mm as well as WSA_{mi}; however, in the B10N2 treatment the trend was observed only within size classes of WSA_{ma} 5–2 mm. Adding N to biochar might be responsible for intensive mineralization processes of biochar resulting in a higher increase of microbial activity in the soils (Cross et al., 2016; Jien and Wang, 2013; Liang et al., 2006) which might be related to higher contents of labile C in WSA and with enhancement aggregation (Bronick and Lal, 2005). The contents of C_L in WSA_{mi}, WSA_{ma} 0.5–0.25 mm, 1–0.5, 2–1 mm and >5 mm in the B20N2 treatment were higher by 19, 21, 16, 18 and 11%, respectively compared to the same size classes of WSA in the B0N2 treatment.

CONCLUSIONS

The results lead us to a conclusion that adding lower amounts of biochar with no N fertilizers might be more beneficial for soil structure vulnerability than higher rates of biochar. On the other hand, biochar combined with both N fertilization levels improved soil structure. Biochar facilitates the formation of macro-aggregates from micro-aggregates. This process is consequently accompanied with a lower content of water-stable micro-aggregates upon adding nitrogen. The higher content of soil organic and labile carbon in the aggregates is a result of biochar its combination with N fertilization. It can be concluded that the higher content of soil organic carbon and labile carbon delivered to the soils through biochar led to more water-stable aggregates.

The results of this study confirmed the effectiveness of biochar alone or combined with N in improving the soil structure and carbon sequestration in water-stable aggregates. In terms of sustainable agriculture, applying biochar with a nitrogen fertilizer appears to be a promising practice offering a chance to increase carbon sequestration rates.

Acknowledgement. This study was partially supported by the Slovak Research and Development Agency under the project No. APVV-15-0160, and the Scientific Grant Agency (VEGA) – project No. 1/0604/16 and 1/0136/17. Many thanks to Dr. Ľubica Puškelová from Earth Science Institute of the SAS, Slovak Academy of Sciences, Slovak republic for minerals identification using XRD analysis, and Dr. Gabriela Kratošová from VŠB- Technical University of Ostrava, Nanotechnology Centre, Czech republic for aggregate and biochar SEM and EDX analysis.

REFERENCES

Agegnehu, G., Bass, A.M., Nelson, P.N., Bird, M.I., 2016. Benefits of biochar, compost and biochar–compost for soil quality, maize yield and greenhouse gas emissions in a tropical agricultural soil. Sci. Tot. Environ., 543, 295–306.

Alburquerque, J.A., Calero, J.M., Barrón, V., Torrent, J., del Campillo, M.C., Gallardo, A., Villar, R., 2014. Effects of biochars produced from different feedstocks on soil properties and sunflower growth. J. Plant Nutr. Soil Sci., 177, 16–25.

Atkinson, C.J., Fitzgerald, J.D., Hipps, N.A., 2010. Potential mechanisms for achieving agricultural benefits from biochar application to temperate soils: a review. Plant Soil, 337, 1–18.

Bai, M., Wilske, B., Buegger, F., Esperschütz, J., Kammann, C.I., Eckhardt, C., Koestler, M., Kraft, P., Bach, M., Frede, H.G., Breuer, L., 2013. Degradation kinetics of biochar from pyrolysis and hydrothermal carbonization in temperate soils. Plant Soil, 372, 1–2, 375–387.

Barrow, C.J., 2012. Biochar: potential for countering land degradation and for improving agriculture. Appl. Geogr., 34, 21–28.

Blanco-Canqui, H., Lal, L., 2004. Mechanisms of carbon sequestration in soil aggregates. Crit. Rev. Plant Sci., 23, 481–504.

Brodowski, S., John, B., Flessa, H., Amelung, W., 2006. Aggregate-occluded black carbon in soil. Eur. J. Soil Sci., 57, 539–546.

Bronick, C.J., Lal, R., 2005. The soil structure and land management: a review. Geoderma, 124, 3–22.

Butnan, S., Deenik, J.L., Toomsan, B., Antal, M.J., Vityakon, P., 2015. Biochar characteristics and application rates affecting corn growth and properties of soils contrasting in texture and mineralogy. Geoderma, 237–238, 105–116.

Cross, A., Zwart, K., Shackley, S., Ruysschaert, G., 2016. The role of biochar in agricultural soils. In: Shackley, S., Ruysschaert, G., Zwart, K., Glaser, B. (Eds.): Biochar in European Soils and Agriculture. Routledge, London, New York, pp. 73–98.

Dziadowiec, H., Gonet, S.S., 1999. Methodical Guide-Book for Soil Organic Matter Studies. Polish Society of Soil Science, Warszawa, 65 p. (In Polish.)

Elliott, E.T., 1986. Aggregate structure and carbon, nitrogen, and phosphorus in native and cultivated soils. Soil Sci. Soc. Am. J., 50, 627–633.

Fischer, D., Glaser, B., 2012. Synergisms between compost and biochar for sustainable soil amelioration. In: Kumar, S. (Ed.): Management of Organic Waste. In Tech Europe, Rijeka, pp. 167–198.

Green Report, 2014. Green Report for 2013. Bratislava, Národné poľnohospodárske a potravinárke centrum, 2014, 65 p., ISBN 978.80-8058-597-6.

Herath, H.M.S.K., Camps-Arbestain, M., Hedley, M., 2013. Effect of biochar on soil physical properties in two contrasting soils: an Alfisol and an Andisol. Geoderma, 209–210, 188–197.

Chan, K.Y., Van Zwieten, L., Meszaros, I., Downie, A., Joseph, S., 2007. Agronomic values of greenwaste biochar as a soil amendment. Aust. J. Soil Res., 45, 8, 629–634.

Chintala, R., Owen, R., Kumar, S., Schumacher, T.E., Malo, D., 2014. Biochar impacts on denitrification under different soil water contents. World Cong. Soil Sci., 6, 157–157.

IUSS WRB, 2014. World reference base for soil resources 2014. International soil classification system for naming soils and creating legends for soil maps. World Soil Resources Reports No. 106, FAO, Rome, 112 p.

Jien, S.H., Wang, C.S., 2013. Effects of biochar on soil properties and erosion potential in a highly weathered soil. Catena, 110, 225–233.

Jones, B.E.H., Haynes, R.J., Phillips, I.R., 2010. Effect of amendment of bauxite processing sand with organic materials on its chemical, physical and microbial properties. J. Environ. Manag., 91, 2281–2288.

Keluweit, M., Nico, P.S., Johmon, N.G., Kleber, M., 2010. Dynamic molecular structure of plant biomass dried black carbon (biochar). Environ. Sci. Technol., 44, 1247–1253.

Kodešová, R., Němeček, K., Žigová, A., Nikodem, A., Fér, M., 2015. Using dye tracer for visualizing roots impact on soil structure and soil porous system. Biologia, 70, 1439–1443.

Kuzyakov, Y., Subbotina, I., Chen, H., Bogomolova I., Xu, X., 2009. Black carbon decomposition and incorporation into microbial biomass estimated by ^{14}C labeling. Soil Biol. Biochem., 41, 210–219.

Lal, R., Shukla, M.K., 2004. Principles of Soil Physics. Marcel Dekker, New York, 345 p.

Lehmann, J., 2007. Bio-energy in the black. Front. Ecol. Environ., 5, 381–387.

Lehmann, J., Skjemstad, J., Sohi, S., 2008. Australian climate-carbon cycle feedback reduced by soil black carbon. Nat. Geosci., 1, 832–835.

Lehmann, J., Rillig, M.C., Thies, J., Masiello, C.A., Hockaday, W.C., Crowley, D., 2011. Biochar effects on soil biota - A review. Soil Biol. Biochem., 43, 9, 1812–1836.

Liang, B., Lehmann, J., Solomon, D., Kinyang, J., Grossman, J., O'Neill, B., Skjemstard, J.O., Thies, J., Luiza, F.J., Peterson, J., Neves, E.G., 2006. Black carbon increases CEC in soils. Soil Sci. Soc. Am. J., 70, 1719–1730.

Liu, C.A., Zhou, L.M., 2012. Soil organic carbon sequestration and fertility response to newly-built terraces with organic manure and mineral fertilizer in a semi-arid environment, Soil Till. Res., 172, 39–47.

Loginow, W., Wisniewski, W., Gonet, S.S., Ciescinska, B., 1987. Fractionation of organic carbon based on susceptibility to oxidation. Pol. J. Soil Sci., 20, 47–52.

Lopez-Capel, E., Zwart, K., Shackley, S., Postma, R., Stenstrom, J., Rasse, D.P., Budai, A., Glaser, B., 2016. Biochar properties. In: Shackley, S., Ruysschaert, G., Zwart, K., Glaser, B. (Eds.): Biochar in European Soils and Agriculture. Routledge, London, New York, pp. 41–72.

Ma, N., Zhang, L., Zhang, Y., Yang, L., Yu, Ch., Yin, G., Doane, T.A., Wu, Z., Zhu, P., Ma, X., 2016. Biochar improves soil aggregate stability and water availability in a Mollisol after three years of field application. PLoS ONE, 11, 1–10.

Millar, C.E., Turk, L.M., Foth, H.D., 1962. Fundamentals of Soil Science. John Wiley and Sons, New York, 526 p.

Mukherjee, A., Lal, R., 2013. Biochar impacts on soil physical properties and greenhouse gas emission. Agronomy, 3, 2, 313–339.

Ruysschaert, G., Nelissen, V., Postma, R., Bruun, E., O´Toole, A., Hammond, J., Rödger, J.M., Hylander, L., Kihlberg, T., Zwart, K., Hauggaard-Nielsen, H., Shackley, S., 2016. Field application of pure biochar in the North Sea region and across Europe. In: Shackley, S., Ruysschaert, G., Zwart, K., Glaser, B. (Eds.): Biochar in European Soils and Agriculture. Routledge, London, New York, pp. 99–135.

Obia, A., Mulder, J., Martinsen, V., Cornelissen, G., Børresen, T., 2016. In situ effects of biochar on aggregation, water retention and porosity in light-textured tropical soils. Soil Till. Res., 155, 35–44.

Saha, D., Kukal, S.S., Sharma, S., 2011. Land use impacts on SOC fractions and aggregate stability in typic Ustochrepts of Northwest India. Plant Soil, 339, 457–470.

Six, J., Bossuyt, H., Degryze, S., Denef, K., 2004. A history of research on the link between (micro)aggregates, soil biota, and soil organic matter dynamics. Soil Till. Res., 79, 7–31.

Six, J., Conant, R.T., Paul, E.A., Paustian, K., 2002. Stabilization mechanisms of soil organic matter: Implications for Csaturation of soils. Plant Soil, 241, 155–176.

Spokas, K.A., 2010. Review of the stability of biochar in soils: Predictability of O:C molar ratios. Carbon Manag., 1, 2, 289–303.

Szombathová, N., 1999. The comparison of soil carbon susceptibility to oxidation by $KMnO_4$ solutions in different farming systems. Hum. Subst. Environ., 1, 35–39.

Šimanský, V., Jonczak, J., 2016. Water-stable aggregates as a key element in the stabilization of soil organic matter in the Chernozems. Carp. J. Earth Environ. Sci., 11, 511–517.

Šimanský, V., Horák, J., Igaz, D., Jonczak, J., Markiewicz, M., Felber, R., Rizhiya, E.Y., Lukac, M., 2016. How dose of biochar and biochar with nitrogen can improve the parameters of soil organic matter and soil structure? Biologia, 71, 989–995.

Šimanský, V., Jonczak, J., Parzych, A., Horák, J., 2018. Contents and bioaccumulation of nutrients from soil to corn organs after application of different biochar doses. Carp. J. Earth Environ. Sci., 13, 315–324.

Tisdall, J.M., Oades, J.M., 1980. The effect of crop rotation on aggregation in a red-brown earth. Austr. J. Soil Res., 18, 423–433.

Vadjunina, A.F., Korchagina, Z.A., 1986. Methods of Study of Soil Physical Properties. Agropromizdat, Moscow, 415 p.

Valla, M., Kozák, J., Ondráček, V., 2000. Vulnerability of aggregates separated from selected Anthrosols developed on reclaimed dumpsites. Rostl. Vyr., 46, 563–568.

Vitkova, J., Kondrlova, E., Rodny, M., Surda, P., Horak, J., 2017. Analysis of soil water content and crop yield after biochar application in field conditions. Plant, Soil and Environment, 63, 12, 569–573.

Wang, S., Zhao, X., Xing, G., Yang, L., 2013. Large-scale biochar production from crop residues: a new idea and the biogas-energy pyrolysis. Bioresources, 8, 8–11.

Yeboah, E., Ofori, P., Quansah, G.W., Dugan, E., Sohi, S.P., 2009. Improving soil productivity through biochar amendments to soils. Afr. J. Environ. Sci. Technol., 3, 34–41.

Yuan, J.H., Xu, R.K., 2012. Effects of biochars generated from crop residues on chemical properties of acid soils from tropical and subtropical China. Soil Res., 50, 570–578.

Received 16 August 2017
Accepted 20 June 2018

Note: Colour version of Figures can be found in the web version of this article.

J. Hydrol. Hydromech., 66, 2018, 4, 437–447
DOI: 10.2478/johh-2018-0035

An approximate method for 1-D simulation of pollution transport in streams with dead zones

Marek Sokáč[1*], Yvetta Velísková[2], Carlo Gualtieri[3]

[1] Department of Sanitary and Environmental Engineering, Faculty of Civil Engineering, Slovak University of Technology in Bratislava, Radlinského 11, 810 05 Bratislava, Slovakia.
[2] Institute of Hydrology of the Slovak Academy of Sciences, Dúbravská cesta 9, 841 04 Bratislava, Slovakia.
[3] Department of Civil, Architectural and Environmental Engineering, University of Naples Federico II, Via Claudio 21, 80125 Naples, Italy.
[*] Corresponding author. E-mail: marek.sokac@stuba.sk

Abstract: Analytical solutions describing the 1D substance transport in streams have many limitations and factors, which determine their accuracy. One of the very important factors is the presence of the transient storage (dead zones), that deform the concentration distribution of the transported substance. For better adaptation to such real conditions, a simple 1D approximation method is presented in this paper. The proposed approximate method is based on the asymmetric probability distribution (Gumbel's distribution) and was verified on three streams in southern Slovakia. Tracer experiments on these streams confirmed the presence of dead zones to various extents, depending mainly on the vegetation extent in each stream. Statistical evaluation confirms that the proposed method approximates the measured concentrations significantly better than methods based upon the Gaussian distribution. The results achieved by this novel method are also comparable with the solution of the 1D advection-diffusion equation (ADE), whereas the proposed method is faster and easier to apply and thus suitable for iterative (inverse) tasks.

Keywords: Environmental hydraulics; River pollution; Hydrodynamic dispersion; Longitudinal dispersion; Dead zones.

INTRODUCTION

The transport of a solute in a stream is usually driven by a combination of advection and dispersion. Both phenomena are related to the characteristics of the streamflow and help to reduce the maximum concentration values in the stream. The main parameter of dispersion is the dispersion coefficient, whose determination plays therefore a key role in studies about the transport of pollutants in streams and water quality modelling (Baek and Seo, 2016; Toprak and Cigizoglu, 2008; van Mazijk, 1996).

Furthermore, solute transport in streams and rivers is strongly related to river characteristics, such as mean flow velocity, velocity distribution, secondary currents and turbulence features. These parameters are mainly determined by the river morphology and the discharge conditions. Most natural channels are characterized by relevant diversity of morphological conditions. In natural channels, changing river width, curvature, bed form, bed material and vegetation are the reason for this diversity. In rivers, which are regulated by man-made constructions, such as spur dikes, groins, stabilized bed and so on, the morphological diversity is often less pronounced and, thus, flow velocities across the stream are more homogeneous.

In natural channels, some of these morphological irregularities, such as small cavities existing in sand or gravel beds, side arms and embayments, bigger obstacles, bank vegetation, uprooted trees can produce recirculating flows which occur on different scales on both the riverbanks and the riverbed. These irregularities act as dead zones for the current flowing in the main stream direction. In regulated rivers, groyne fields are the most important sort of dead zones. Groyne fields can cover large parts of the river significantly affecting its flow field. Dead-water zones or dead zones can be defined as geometrical irregularities existing at the river periphery, within which the mean flow velocity in the main stream direction is approximately equal to zero (or even negative) (Weitbrecht, 2004).

Dead zones significantly modify velocity profiles in the main channel as well as they are affecting dispersive mass transport within the river. They collect and separate part of the solute from the main current. Subsequently the solute is being slowly released and incorporated back to the main current in the stream. Even the hyporheic exchanges between the surface waters and the adjacent/underlying groundwater may affect the transport of solutes with the long-time tailing behaviour in the time-concentration curves (Tonina, 2012).

Thus, in recent years exchange processes between the main stream and its dead zones were increasingly studied, mostly using experimental laboratory and field works (Brevis et al., 2006; Engelhardt et al., 2004; Jamieson and Gaskin, 2007; Kimura and Hosoda, 1997; Kurzke et al., 2002; Muto et al., 2000; Sukhodolov, 2014; Uijttewaal, 1999, 2005; Uijttewaal et al., 2001; Weitbrecht and Jirka, 2001; Weitbrecht et al., 2008; Yossef and de Vriend, 2011). Also, computational methods were widely carried out to investigate hydrodynamics in channels with dead zones of different type and shape (Gualtieri, 2008, 2010; McCoy, 2008; McCoy et al., 2006; Weitbrecht, 2004).

Mathematical solution of the dispersion in streams with dead zones has been extensively described (De Smedt, 2006, 2007; De Smedt et al., 2005; Runkel, 1998) as well as the effect of the vegetation in stream (Shucksmith et al., 2010) (Shucksmith et al., 2011), (Murphy et al., 2007). However, the majority of these solutions are complicated, regarding the mathematical apparatus and their numerical application (Czernuszenko et al., 1998; Davis and Atkinson, 2000; De Smedt, 2006; De Smedt et al., 2005). Code programming is quite difficult and longer computing time is required, especially in cases where many simulations are needed. On the other hand, based on the nature of analytical solutions, the superposition principle can be applied. Based on this, the analytical solutions can be widely applied in engineering practice including their ability to simulate various types of pollution inputs (continuous, discontinu-

ous, steady, unsteady etc.) as well as other specific pollution types, e.g. turbidity (Wang et al., 2017).

The goal of this paper is to provide a simple mathematical method, which would allow quick and easy one-dimensional modelling of the dispersion process in streams with influence of dead zones. Our effort was oriented to find a mathematical approximation formula of the dispersion process with focus on instantaneous injection. This formula was verified on tracer experiments data measured on three streams (channels) in southern Slovakia, where a significant presence of the dead zones was found (Malá Nitra, Šúrsky and Malina streams).

DEAD ZONES EFFECT ON MASS TRANSPORT IN RIVERS

The classical Dead-Zone-Model

Following a tracer cloud from the source until it is spread over the entire river cross-section, three stages of mixing can be distinguished (Rutherford, 1994). In the *near-field* mixing is dominated by buoyancy and momentum forces that are determined by the effluent, so transport phenomena must be considered as 3D problems. In the *mid-field* the tracer mass is already mixed over the river depth, so transport phenomena can be treated as depth-averaged 2D problems. The sum of the above mixing zone is also termed as *advective length*. In the *far-field*, the tracer mass is well-mixed over the entire river cross-section, so transport phenomena are often studied as cross-sectional 1D problem. Also, in the far-field the skewness of the tracer distribution in the longitudinal direction slowly vanishes. Therefore, in the far-field, solute transport is usually analyzed by using the classical 1D advection-dispersion equation (ADE), where the main problem is to apply a reasonable value of the longitudinal dispersion coefficient. The general form of the ADE is (Socolofsky and Jirka, 2005)

$$\frac{\partial C}{\partial t} + v_x \frac{\partial C}{\partial x} = D_x \left(\frac{\partial^2 C}{\partial x^2} \right) + M_s \qquad (1)$$

where t is the time (s), C is the concentration of a substance (kg m^{-3}), D_x is the dispersion coefficient in the longitudinal direction (m^2 s^{-1}), v_x is the velocity of water flow in x (longitudinal) direction of flow (m s^{-1}), M_s is a function representing the sources of pollution (kg m^{-3} s^{-1}), x is the spatial coordinate – distance (m).

However, many field studies demonstrated that the ADE predictions often do not fit well with the observed tracer concentrations from instantaneous spills. Two discrepancies were observed (Weitbrecht, 2004). First, the tracer concentration curve shows a sharp front and a long tailing. Second, in natural channels, the average velocity of the solute is always somewhat lower than the average water velocity of the river. This can be explained by the exchange processes between the main flow in the channel and the dead-water zones existing at its periphery – the solute cloud is retarded by boundary trapping. Due to momentum exchange across the interface with the main channel, flow patterns inside the dead zones are characterized by recirculating flows which occur on different scales and exhibit flow velocity in the main stream direction close to zero. Therefore, the most important effect of dead zones on mass transport in rivers is the storage of some amount of the contaminants or nutrients being transported by the main stream inside the dead zones, i.e. some mass of solutes is trapped in the dead zones and later, after an average storage time T_{DZ}, is released back into the main flow. The storage time depends on the strength of the exchange processes occurring between the main stream and the dead zones, which are mostly due to turbulent mixing in the lateral or in the vertical direction, if the dead zone is at the riverbanks or at the riverbed, respectively (Muto et al., 2000; Weitbrecht, 2004).

In a channel without dead zones, the average transport velocity of a tracer cloud that is completely mixed over the river cross-section equals the mean flow velocity. If dead zones are present, the part of the tracer cloud trapped in the dead zones is retarded in comparison with the part of tracer cloud travelling in the main stream with the mean flow velocity. In this case, the transport velocity of the tracer cloud is lower than the average flow velocity. Also, dead zones produce an increased stretching of a passing tracer cloud, which means that the longitudinal dispersion is enhanced. These results in a tail of the contaminants cloud longer than that predicted by the ADE (Czernuszenko et al., 1998) and the length of the tail depends on the exchange between the main flow and the dead zones. This could be explained by two processes (Weitbrecht, 2004). First, dead zones modify the transverse profile of flow velocity in the main channel and increase lateral turbulent mixing, which are the determining parameters for longitudinal dispersion. It is well known that transverse mixing is important in determining the rate of longitudinal mixing because it tends to control the exchange between regions of different longitudinal velocity. Particularly, transverse mixing and longitudinal mixing are inversely proportional. A strong transverse mixing tends to erase the effect of differential longitudinal advection and pollutants particles migrate across the velocity profile so fast that they essentially all move at the mean speed of the flow, causing only a weak longitudinal spreading. On the other hand, a weak transverse mixing implies a long time for differential advection to take effect, so the pollutants patch is highly distorted while it diffuses moderately in the transverse direction and longitudinal mixing is large (Cushman-Roisin, 2012). Second, the tracer cloud is stretched because solute parcels are trapped within the dead zones and only later released back into the main channel. The temporary accumulation of the transported substance commonly causes deformation of the concentration distribution curve (van Mazijk and Veling, 2005). The substance is released later and more slowly, giving rise to the steep front of the concentration distribution curve, followed by "long tail" (Fig. 1). Both processes result in longitudinal dispersion process character, which leads to lower peak levels of tracer concentration, but also to a longer period of time. Finally, these processes are strongly related to the geomorphological conditions of the dead zones. Obviously, if the stream cross-section is not regular, Fick's law cannot be applied even after a long period, since the concentration distribution due to large irregularities of the stream bed will never be a Gaussian (Davis et al., 2000; Nordin and Troutman, 1980).

Therefore, models accounting for the dead zones effects were proposed to be applied in rivers where there is a relevant presence of dead zones. The basic idea of the dead-zone model (DZM) is to distinguish two zones within the cross-section of a river, the main stream and the dead-zone. In the main stream the mass transport is governed by advection in the longitudinal direction, longitudinal shear due to the velocity distribution and transverse turbulent diffusion. Thus, the transport processes in the main stream can be modeled under well mixed conditions using the 1D ADE. In the dead zone, since velocity in the main stream direction is close to zero, transverse turbulent diffusion across the interface between the dead zone and the main stream is the dominant mechanism, which leads to momentum and mass exchange processes. Assuming that in the dead zone the

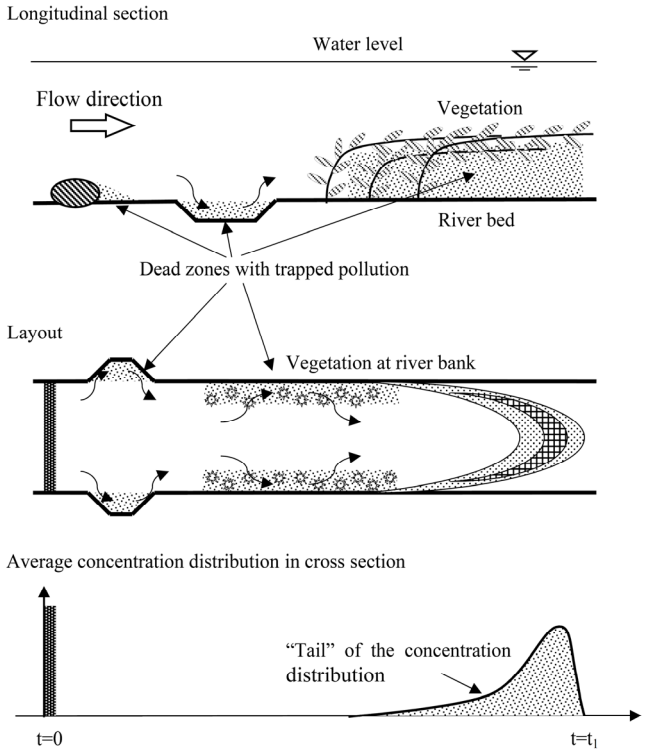

Fig. 1. Scheme of the "dead zones" effects on pollution transport in a stream.

solute concentration is uniform, mass exchange between the dead zone and the main stream is proportional to the difference of the averaged concentration in the dead zone and in the main channel (Chanson, 2004; De Smedt et al., 2005; Jirka, 2004; Jirka et al., 2004; Rowiński et al., 2004; Valentine and Wood 1979). To set up the DZM, conservation of mass for the main stream and the dead-zone should be considered (Czernuszenko and Rowinski, 1997; De Smedt et al., 2005; Nordin and Troutman, 1980):

$$\frac{\partial C}{\partial t} = D_x\left(\frac{\partial^2 C}{\partial x^2}\right) - v_x\frac{\partial C}{\partial x} - m\left(C - C_s\right) + M_s \tag{2}$$

$$n\frac{\partial C_s}{\partial t} = m\left(C - C_s\right) \tag{3}$$

where C_s is the concentration of the substance in the storage zone (kg m^{-3}), m is the mass exchange coefficient between the main stream and the storage zone (s^{-1}), n is the ratio between the storage zone and the main stream cross-sectional area (–). If m or n becomes zero, Eq. (2) reduces to Eq. (1). The set of Eq. (2) and Eq. (3) was also used for developing the OTIS software (Runkel, 1998).

Hypothetically, the DZM problem can be also solved using two-dimensional approach, where the transversal movement of pollution will reflect the effect of dead zones. However, two-dimensional analytic solutions are also complicated and their numerical application is difficult (Djordjevich et al., 2017; Skublics et al., 2016).

In general, besides the basic parameters (stream hydraulic parameters, e.g. discharge, dimensions, flow velocity) and the dispersion coefficient, it is necessary to determine also the size of the dead zone (ratio between the active and dead zone) and the coefficient of the solute transfer between the dead and active zones. These parameters should be determined by model calibration, based on the field tracer experiments. Application of values estimated by analogy with other tracer studies, is problematic and can lead to misleading results.

The solution of Eq. (1) for simplified conditions (instantaneous point source, prismatic streambed, steady and uniform flow) by Socolofsky and Jirka (2005), eventually by Fischer et al. (1979) and Martin and McCutcheon (1998), has the following general mathematical expression:

$$C = \frac{M}{A\sqrt{D_x t}}\, f\left(\frac{x}{\sqrt{D_x t}}\right) = \frac{M}{A}\, p\left(\frac{1}{\sqrt{D_x t}}\,;\frac{x}{\sqrt{D_x t}}\right) \tag{4}$$

where A is a cross- sectional area of the stream (m^2), M is a pollutant mass (kg), and p are the unknown functions („similarity solution“). The unknown function f (or p) can be determined in two different ways (Socolofsky and Jirka, 2005):

1. Based on experiment derive a curve fit to real data.
2. Solve the Eq. (4) analytically.

Solving analytically the Eq. (4), the one-dimensional analytical solution of the ADE for above mentioned simplified initial and boundary conditions, immediate pollution input implies that the solute particles will be spatially symmetrically spread, following the Gaussian normal distribution, whereas the standard deviation σ is temporally depending. The mathematical solution can be obtained in the form (Fischer et al., 1979)

$$C(x,t) = \frac{M}{2A\sqrt{\pi D_x t}}\, \exp\left(-\frac{\left(x - \overline{v}_x t\right)^2}{4\, D_x\, t}\right) \tag{5}$$

where $\overline{v}_x$ is the mean flow velocity in a stream.

The proposed approximate model

By comparing Eq. (4) and Eq. (5), it could be seen that the analytical solution of the function p has spatially the form of a Gaussian normal distribution with parameters of normal distribution (e.g. standard deviation σ, etc.). In the often-applied temporal expression form (Eq. (5)), this curve does not have the exact shape of a Gaussian normal distribution, but it has asymmetric form. It is caused by substitution of the standard deviation σ (which is constant in Gaussian distribution) by the time-dependent term $\sqrt{2D_x t}$. Another interpretation could be that the asymmetry is caused by the fixed position of the observer on the stream bank. If the observer moves with the same speed as the water flows, the concentrations distribution from the observer's point of view (spatial distribution) will have symmetrical shape of the Gaussian normal distribution.

Analytical solution of advection – dispersion equation in form of (Eq. (5)) is currently considered as the standard solution, but the validity of this solution is limited to flow without barriers, with the assumption of a symmetrical movement of particles at the front and rear of the cloud in downstream and upstream direction. In real streams, however, this assumption is not always valid: movement of particles is slowed down (retarded) by the accumulation of particles in dead zones of streams.

For this reason, in the case of flow in real conditions with occurrence of dead zones in a stream, it is appropriate to approximate the function p from Eq. (4) not in the form of the Gaussian normal distribution as in (Eq. (5)), but to use different statistical distribution form with asymmetric shape.

Based on our field experiments, we propose as an appropriate approximation of the function p from the Eq. (4) the Gumbel's distribution. This distribution was selected based on our field experiments among other distributions because of its simplicity, asymmetry and ability to good fit with the measured data in streams with dead zones. Of course, other distributions may also be used, but this study examines suitability of this one.

The general equation of the Gumbel's distribution is

$$g = \frac{1}{\xi}\, e^{-\left(z+e^{-z}\right)} \tag{6}$$

$$z = \frac{x-\mu}{\xi} \tag{7}$$

where g is the distribution probability (density), the parameter μ is the location parameter and the parameter ξ is the scale parameter.

The parameters from the Eq. (6) (considering the Eq. (4)) can be defined as follows:

$$\xi = \sqrt{D_{x,G}t} \tag{8}$$

$$z = \frac{\overline{v}_x t - x}{\sqrt{D_{x,G}t}} \tag{9}$$

where the $D_{x,G}$ is the dispersion coefficient in the longitudinal direction (m^2 s^{-1}), used in the proposed model. To be dimensionally consistent, z is a dimensionless parameter and ξ has the dimension of a length (m).

By substituting parameters from Eq. (8) and Eq. (9) into Eq. (6), the one-dimensional analytical solution has the unitary form:

$$g(x,t) = \frac{1}{\sqrt{D_{x,G}t}} \exp\left[-\frac{\overline{v}_x t - x}{\sqrt{D_{x,G}t}} - \exp\left(-\frac{\overline{v}_x t - x}{\sqrt{D_{x,G}t}}\right)\right] \tag{10}$$

By substituting Eq. (10) to Eq. (4) we get the proposed solution, results are in concentration units (kg m^{-3})

$$c(x,t) = \frac{M}{A\sqrt{D_{x,G}t}} \exp\left[\frac{x-\overline{v}_x t}{\sqrt{D_{x,G}t}} - \exp\left(\frac{x-\overline{v}_x t}{\sqrt{D_{x,G}t}}\right)\right] \tag{11}$$

FIELD MEASUREMENTS

Derived Eq. (11) was verified using the experimental data from three tracer studies in Malá Nitra, Šúrsky and the Malina streams. Tracer experiments were conducted in years 2012–2016.

Test A was performed on a reach of the Malá Nitra stream, located within the village Veľký Kýr (N48.181799°, E18.155373°). The experiments described in this paper were performed in two reaches with lengths of 785 and 1340 metres, respectively. The first reach of the stream was straight, the second was slightly curved in both directions (left & right bend). In these reaches, the channel was at the bed about 4 m wide with a banks height of 2.5 m and a bank slope of approximately 1:2. It should be mentioned that the original prismatic cross section was not fully preserved and its form was modified because of ongoing morphological processes. The discharge in the whole measurements period ranged from 0.138 to 0.553 m^3 s^{-1}, but for the model tests a stable discharge, from 0.230 up to 0.235 m^3 s^{-1} was used. The hydraulic roughness was determined from field measurements and hydraulic calculations (Limerinos, 1970), leading to a Manning coefficient n = 0.035. Water level slope, determined by geodetic levelling, was found constant and approximately equal to 1.5‰. The shape of the stream can be considered in the examined reach of the stream as a prismatic one. The stream had a width of 5.5 m and a water depth in the range from 0.4 up to 0.6 m. The range of determined longitudinal dispersion coefficient was from 0.5 to 2.5 m^2 s^{-1}.

Test B was performed on straight stream reach of the Šúrsky stream, located close to the village Svätý Jur (Slovakia, N48.232957°, E17.202934°). The field measurements were made in 300 up to 500 m long straight reach with relatively prismatic cross section profile. The stream width was from 4 to 5.5 m, depth was in the range from 0.4 to 0.8 m, flow velocity from 0.21 to 0.36 m s^{-1} and discharge was from 0.38 to 0.43 m^3 s^{-1}. The range of determined longitudinal dispersion coefficient was from 0.63 to 0.98 m^2 s^{-1}.

Test C was performed at the Malina stream, located in the cadastral areas of Lab and Zohor municipalities (N48.334771°, E16.967445°). The experiments were carried out on selected stream reach with a length of 1415 m. It was a straight section of the Malina stream, without significant directional changes.

Originally constructed cross section shape was significantly influenced by vegetation. The measured discharge during the experiments was 0.408 m^3 s^{-1}. The water level slope, specified

Fig. 2. Map of the field tracer experiments.

by levelling measurements, was about 0.45‰. The stream shape in the examined stream section can be considered prismatic, the width was around 5 m, the average depth was 0.88 m, the determined dispersion coefficient was 0.95 $m^2 s^{-1}$.

In the first two locations, common salt was used as a tracer. Conductivity was measured at the end of examined stream reach and converted to the salt concentration using local specific calibration curve. However, in both cases a linear dependency between conductivity and salt concentration was determined within the ranges of observed concentrations. Because of this it is possible to show graphs in this paper also with conductivity units.

In the test C (Malina stream) the colouring agent – E133 (brilliant blue, food colour) was used and the tracer concentration was measured and determined using field spectrophotometry device.

In all field experiments an instantaneous tracer injection in the centre of the stream width was used. The tracer (common salt, colouring agent) was thoroughly mixed in a barrel with some amount of the water (typically 30–50 litres) and such homogenous mixture was injected to the centre of the stream.

The experiments on the sites A and C (Malá Nitra and Malina stream) were performed in high summer and the vegetation was present in large extent (emergent as well as submerged vegetation). The tracer experiment B (Šúrsky channel) was performed on early spring and the vegetation presence was minimal. The covering of the cross-sectional area of the streams was not exactly determined, just estimated as follows: experiment B – 10%, exp. A – 30%, exp. C – 40% of the cross - stream sectional area was influenced by vegetation (see also Table 4).

RESULTS

During the field measurements, deformations of the concentration distribution at all streams were found. It shows significant presence of dead zones. These zones were formed by the stream beds irregularities as well as by the vegetation along the stream banks and on bed.

Some results from measured data and concentration distribution approximated by Eq. (5) and Eq. (11) are shown for illustration in Figs. 3–7. From the Figures, it is visually clear that the proposed method (Eq. (11)) approximates the measured very well, particularly in the increasing part of the curve.

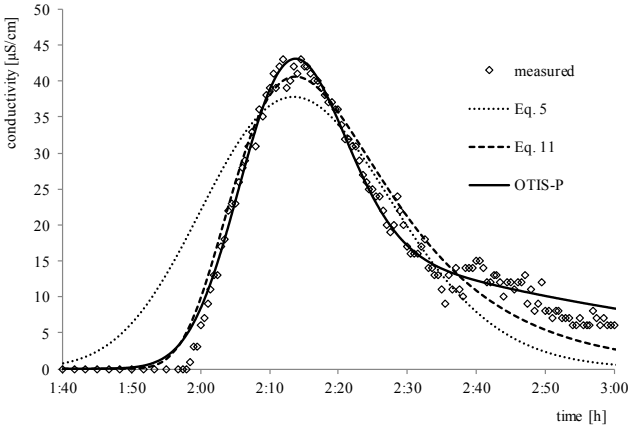

Fig. 3. Comparison of measured and simulated conductivity distribution in the test A - Malá Nitra stream, experiment Nr. 5-V (1340 m).

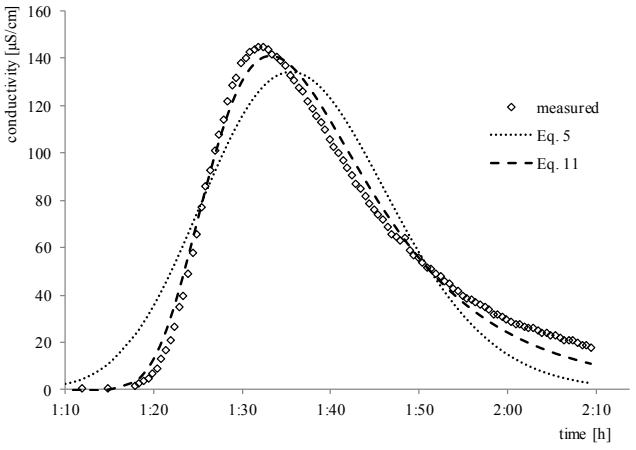

Fig. 4. Comparison of measured and simulated conductivity distribution in the test A - Malá Nitra stream, exp. Nr. 12-III (785 m).

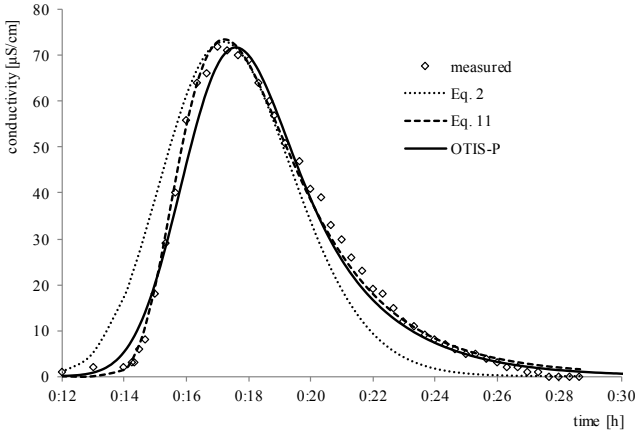

Fig. 5. Comparison of measured and simulated conductivity distribution in the selected profiles on the test B - Šúrsky stream, exp. Nr. 7-II (300 m).

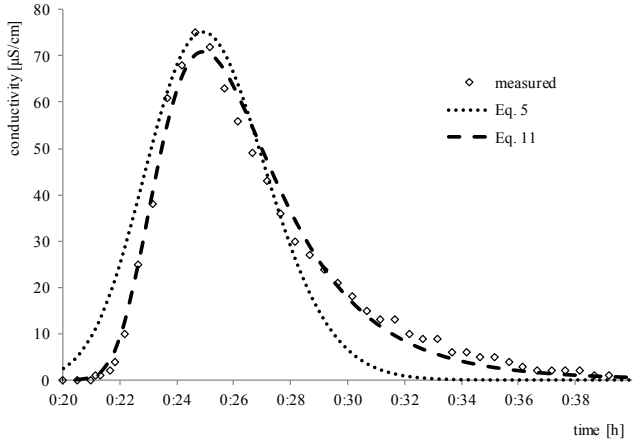

Fig. 6. Comparison of measured and simulated conductivity distribution in the selected profiles on the test B - Šúrsky stream, exp. Nr. 11-II (406 m).

The field tracer experiments performed within the case C (the Malina stream), in addition to standard evaluation of tracer experiments mentioned above, were also evaluated by the OTIS-P software (Runkel, 1998) with optimization of parameters, used in Eq. (2). The optimised parameters were set-up by

the OTIS-P software as the following: D_x = 0.0213 m^2 s^{-1}, the storage zone cross-sectional area was A_s = 1.53 m^2, the storage rate exchange coefficient m = 4.08 x 10^{-4} s^{-1}. A graphical comparison of the results of measured data and approximations (Eq. (5), Eq. (11) and OTIS-P) is presented on Fig. 3, Fig. 5 and Fig. 7.

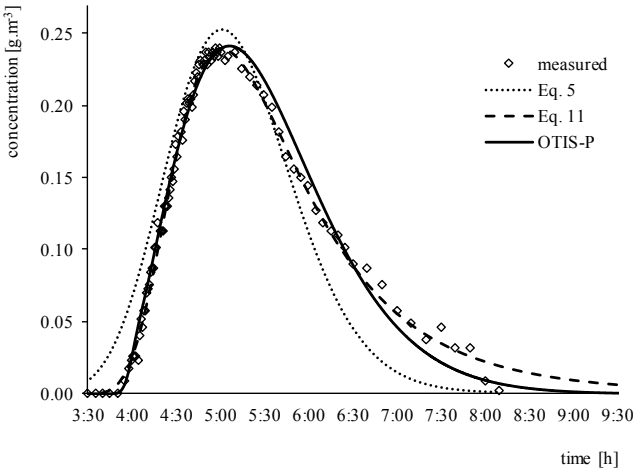

Fig. 7. Comparison of approximation results – test C, the Malina stream (approximation using Eq. (5) and Eq. (11) and the OTIS software).

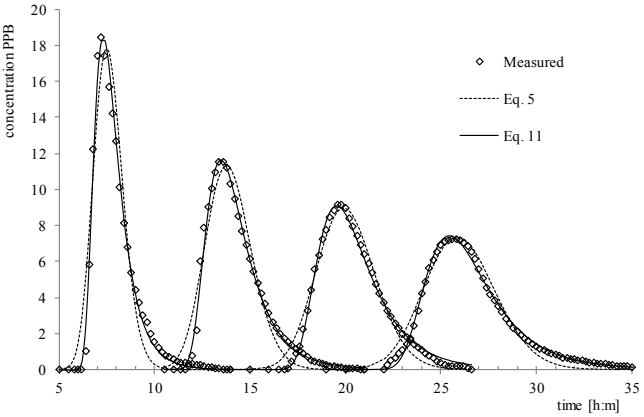

Fig. 8. Comparison between the results of the approximate method and the experimental data – Monocacy River.

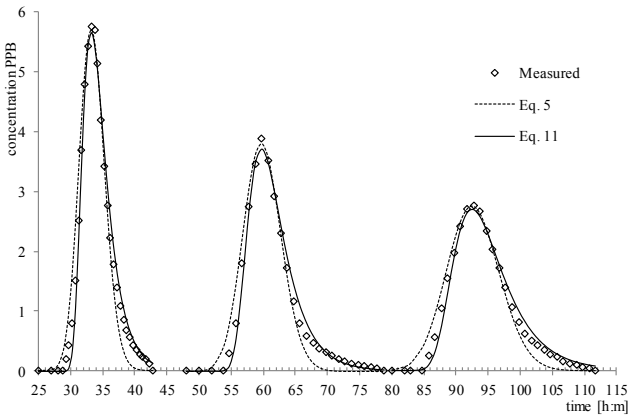

Fig. 9. Comparison between the results of the approximate method and the experimental data – Red River.

As it can be seen on these figures, the approximation with the proposed method according Eq. (11) and OTIS software are quite similar, whereas the approximation with Eq. (5) is less accurate.

The proposed approximate method should be also verified for different ranges of the stream characteristics (longitudinal dispersion coefficient, lengths, travelling times etc.) Such field tracer experiments were not conducted in Slovakia, so the experimental data from (Nordin and Sabol, 1974) collected in the Monocacy and Red Rivers were applied. These data were also used by (Deng and Jung, 2009).

The first tracer dispersion experiment was conducted on June 7, 1968 in the Monocacy River. The four sampling sites were located at 10.30 km, 18.34 km, 26.80 km, and 34.28 km downstream of the tracer injection site. The second field tracer experiment was performed on April 7, 1971 in the Red River. The three sampling sites on the Red River were located at 5.74 km, 75.64 km, and 132.77 km downstream of the tracer injection site. The optimal set of parameters was achieved by the best fit of simulated concentration by the Eq. (5) and Eq. (11), respectively, to the observed concentrations. The input parameters applied in both numerical experiments, as well as those used by (Deng and Jung, 2009), are listed in Table 1.

Table 1. Parameters used in numerical experiments.

Parameter	Unit	River	
		Monocacy River	Red River
$\bar{v}_x$ (Eq. (11))	m s^{-1}	0.381	0.609
U (Deng, 2009)		0.37	0.62
K_s (Deng, 2009)	m^2 s^{-1}	16	40
D_x (average, Eq. (5))	m^2 s^{-1}	27.74	86.20
$D_{x,G}$ (average, Eq. (11))	m^2 s^{-1}	45.44	143.28

Note: K_s is the Fickian dispersion coefficient, calculated by semi empirical method for determination of the Fickian dispersion coefficient, see (Deng and Jung, 2009).

Statistical evaluation

The goodness of fit between measured values and the results from Eq. (5) and Eq. (11) was evaluated by comparing the sum of differences square between the measured and approximated values, i.e.

$$Dif = \sum_{t=t_1}^{t=t_2} \left(\Delta y_t\right)^2 = \sum_{t=t_1}^{t=t_2} \left(y_{m,t} - y_{a,t}\right)^2 \qquad (12)$$

where Dif is the sum of differences square, $y_{m,t}$ is the measured value in the time t, $y_{a,t}$ is the approximated value in the time t, t_1 is the measurement start time and t_2 is the measurement end time. The sum of differences square for each measurement and their basic statistical evaluation are presented in Table 2. The model fit shown on Figs. 3–7 was obtained using the built-in nonlinear regression in the standard Excel worksheet (the Solver add-in, using the non-linear GRG algorithm). For the optimization, all physical parameters were taken from the field measurements (velocity, cross-sectional area, the same values of these parameters were used for the OTIS optimization model), the optimized variables were the dispersion coefficient (Eq. (5) and Eq. (11)) as well as the coefficient for the reduction of tracer mass to keep the mass balance. Unfortunately, the optimal parameters dataset for the Eq. (5) (Gaussian) specifies very often the peak time out of the "reasonable" similarity. This means in fact two different values of flow velocity for one field

tracer experiment. This can be considered as a non-comparable case and because of this the peak time for each field tracer experiment was fixed.

Suitability of the use of the Gumbel distribution can be assessed by analogy with the goodness of fit test, which is used to verify the conformity of the measured data with the corresponding theoretical distribution. In our case, it was used a procedure analogous to Kolmogorov-Smirnov test (for continuous distributions), using supremum values, defined as it follows:

$$S_n = sup\left|F_n(t) - F(t)\right| \tag{13}$$

where S_n is the supremum, $F_n(t)$ is the normalised value of the cumulative measured concentration, $F(t)$ is the normalised value of the theoretical cumulative (distribution) function. Normalised values in this case means that the values are in the interval <0;1>. The supreme value can be also interpreted as the percentage difference of the measured and modelled distribution value.

The hypothesis H_0 - the measured distribution function is a distribution of the theoretical distribution was tested. In our case the theoretical distributions were according the Eq. (5) and Eq. (11). Hypothesis H_0 is rejected, if $S_n > S_n(\alpha)$, where the $S_n(\alpha)$ is the critical value of the Kolmogorov distribution on the level α.

The critical value of the $S_n(\alpha)$ was defined as it follows:

$$S_{j(\alpha)} \cong \sqrt{\frac{1}{2j}\ln\left(\frac{2}{\alpha}\right)} \tag{14}$$

where j is the number of the measurement points (values), α is the significance level. Results of the statistical evaluation of the results are presented in the Table 2.

DISCUSSION

The above statistical analysis demonstrated that the proposed approximate method (Eq. (11)), if compared with the results from Eq. (5), is much more accurate to reproduce the distribution of the tracer concentration over the time in streams with dead zones. The statistical test of the hypothesis H_0 (the measured distribution function is a distribution of the theoretical distribution), using a high confidence level (α = 0.95), has been confirmed for the Eq. (5) only 4 times (19% of performed measurements), whereas for the Eq. (11) the hypothesis H_0 was confirmed 16 times (76.2%) from total 21 measurements. Other facts that support this statement, are significantly lower supremum values for the proposed method (in average 2.8 times lower) as well as the sum of the squared differences (7.2 times lower).

All the own field experiments were performed with relatively short distances, so the question arises whether it has been achieved the stage of complete transversal and vertical mixing (pollution concentration homogeneity) to meet the assumption of one-dimensional (1D) mixing conditions. Tracer concentrations along the stream width (transversal direction) were measured only in the field experiments in the Malá Nitra stream. A good tracer homogenisation was observed in the distance of 150 m (Velísková et al., 2013). In this experiment the tracer source was placed at the river bank, so for the experiments, presented in this paper (all with stream centre injection) we can assume even smaller mixing length.

Table 2. Comparison of the longitudinal dispersion coefficients values from Eq. (5) and Eq. (11). (α = 0.95).

Site	Experiment Nr.	X distance	D_x Eq. (5)	$D_{x,G}$ Eq. (11)	crit. value $S_n(\alpha)$	S_n Eq. (5)	S_n Eq. (11)	*Dif* Eq. (5) $\sum(\Delta y)^2$	*Dif* Eq. (11) $\sum(\Delta y)^2$
Unit		(m)	($m^2\ s^{-1}$)	($m^2\ s^{-1}$)	(–)	(–)	(–)	(–)	(–)
Test A Malá Nitra stream	5-V	1340	1.17	1.56	0.0517	0.1268	0.0622	6288.3	1226.8
	8-IV	785	0.5	0.73	0.0643	0.1024	0.0396	24867.5	2695.6
	8-V	1340	0.6	1.18	0.0533	0.0956	0.0358	5826.0	32.5
	11-III	785	0.67	1.02	0.0623	0.1756	0.0775	31544.1	4524.9
	11-IV	1340	2.5	6.8	0.0374	0.2379	0.0626	998.4	53.3
	12-III	785	0.75	0.86	0.0590	0.1495	0.0557	67609.5	9690.8
	12-IV	1340	0.95	1.96	0.0456	0.0728	0.0219	16150.8	1817.0
Test B Šúrsky stream	1-III	300	0.82	1.10	0.1062	0.0666	0.0402	274.0	46.8
	2-III	300	0.63	0.8	0.1245	0.1092	0.0219	506.4	48.0
	7-II	300	0.64	1.05	0.0872	0.1412	0.0138	4152.3	162.1
	7-III	397	0.74	1.01	0.1114	0.0953	0.0308	1550.7	143.8
	8-II	300	0.7	0.89	0.0930	0.1326	0.0280	3430.3	457.4
	8-III	397	0.74	1.11	0.1046	0.0784	0.0436	933.5	220.1
	9-III	306	0.6	0.74	0.1062	0.1304	0.0465	5445.9	799.8
	10-II	406	0.64	0.77	0.1003	0.1735	0.0629	4486.9	747.2
	10-III	506	0.8	1.15	0.0815	0.1545	0.0575	3845.1	528.7
	11-II	406	0.39	0.77	0.0830	0.1794	0.0350	2826.5	289.9
	11-III	506	0.82	1.11	0.0815	0.1958	0.1035	5973.0	1533.9
	12-II	406	0.45	0.71	0.0900	0.1636	0.0526	3626.5	602.5
	12-III	506	0.98	1.2	0.0788	0.1770	0.0939	4953.3	1331.2
Test C Malina stream	III	1415	0.95	2.41	0.0562	0.0656	0.0305	592.5	69.7
Minimum						0.0656	0.0138	274.0	32.5
Maximum						0.2379	0.1035	67609.5	9690.8
Average						0.1345	0.0484	9327.7	1286.8

Notice: the grey fields in the Table mean that the hypothesis H_0 can be accepted, i.e. the measured values have the assumed theoretical distribution (Eq. (5) or Eq. (11)). Similar comparison of the sum of squared differences between the measured and approximated values *Dif* (see Eq. (12)) was made also in the cases of Monocacy and Red Rivers. In all examined cases the sum of the differences squared using the Eq. (11) was smaller than sum of the differences using Eq. (5). The value of the sum of the differences using Eq. (11) was in the range of 4–40%, compared to the difference sum using Eq. (5).

Table 3. Examples of formulas for mixing length calculation.

Author	Formula	Mixing length for average parameter (m)
(Socolofsky and Jirka, 2005)	$L_{mix} \approx B^2/3h$	13.9
(Fischer et al., 1979)	$L_{mix} \approx 0.1\left(B^2 u/D_T\right)$	75
Yotsukura, N., 1968 – as referred in (Kilpatrick et al., 1970)	$L_{mix} \approx 8.52\left(B^2 u/h\right)$	106.5
(Ruthven, 1971)	$L_{mix} \approx 0.075\left(B^2 u/D_T\right)$	56.25
(Kilpatrick et al., 1970)	$L_{mix} \approx 1.3\left(B^2 u/h\right)$	16.25

Table 4. Dead zones and vegetation parameters in examined streams.

Experimental stream	Estimated vegetation presence	D_x average value	$D_{x,G}$ average value	$D_x / D_{x,G}$ ratio
	(% of the cross-sectional area of the stream, influenced by vegetation)	($m^2 s^{-1}$)	($m^2 s^{-1}$)	(–)
A – Malá Nitra	30	1.02	2.02	1.98
B – Šúrsky channel	10	0.69	0.95	1.39
C- Malina	40	0.95	2.41	2.54

Examples of various formulas for estimation of mixing length can be found in Table 3. In this table we also present the mixing lengths for the average parameters of examined streams $B = 5$ m, $u = 0.3$ m s^{-1}, $D_T = 0.01$ m^2 s^{-1}, $h = 0.6$ m.

As can be seen from the Table 3, the mixing length for complete transversal and vertical mixing for the examined streams ranges - with realistic estimation - from 50 up to 100 m. Comparing this length with the lengths of experimental sections, stated in Table 2, the mixing length was about to 7–14% (Malá Nitra stream), 20–30% (Šúrsky stream) and 7% for the Malina stream. This can be considered as an acceptable percentage of the stream section length, in which the measurements were performed.

Similar situation is also in the numerical experiment, described above – the Monocacy and Red Rivers. The experimental reaches in this case have the length of 34.28 km (Monocacy River) and 132.77 km (Red River), so it can be assumed that the mixing length in these cases is really a very small proportion (less than 1–2%) of the total experimental reach length.

An interesting question is, if there is a relationship between the dispersion coefficients, determined by Eq. (5) and Eq. (11) (D_x and $D_{x,G}$). Theoretically, there is no relationship between the both coefficients, but regarding the determined coefficient values of field experiments in Table 2, some relation between both coefficients can be observed. Statistical analysis confirmed significant degree of the correlation between these values, the correlation coefficient was in the range $R^2 = 0.6$ up to $R^2 = 0.9$ (depending of the method used). Assuming a dependency between both coefficients, the value of $D_{x,G}$ could be defined as

$$D_{x,G} = p_{DG}(D_x) \tag{15}$$

where p_{DG} is a function determining the dependency between the values of D_x and $D_{x,G}$.

Using statistical approach, focused to find the best theoretical fit between the values given by Eq. (5) and Eq. (11), a simple linear relationship can be obtained

$$D_{x,G} \approx 1.588 D_x + 0.22 \tag{16}$$

which is valid in the values range of the longitudinal dispersion coefficient D_x from 0.25 up to 2.5 m^2 s^{-1}. Such a relationship was also confirmed by the above mentioned statistical evaluation of the tracer experiments. In our case, both equations were used for approximation of specific measured data and the compliance rate with these data varies, depending on a stream flow character, the dead zone extent and its influence on the dispersion process. The correlation degree between both dispersion coefficients depends on the site conditions (hydraulic conditions, extent and the influence degree of the dead zones) and due the local conditions the multiplication and addition factors in Eq. (16) were slightly different.

As shown in the Table 4, field tracer experiments clearly confirm the dependency between the dead zone parameters and the vegetation extent – increase of the percentage of the stream cross-sectional area, influenced by vegetation caused increase of the longitudinal dispersion coefficients (Gaussian, Eq. (5), as well as Gumbel's - Eq. (11)) and causes increase of the ratio between the longitudinal coefficients. This can be the future base for the expression of the dead zone parameters in proposed solution (Eq. (11)).

It seems that a problem occurs in relation to the analytical solution (Eq. (5)) of the advection dispersion equation (Eq. (1)) and the presented solution (Eq. (11)). Both Eq. (5) and Eq. (11) are solutions of Eq. (1), and this means that this equation can have two (or even more) different solutions.

For this case, it is necessary to point out the reference (Socolofsky and Jirka, 2005). The idea of this study is to provide a theoretical basis and replace the Gaussian form of the function f (or p) in the general similarity solution (Eq. (4)) with a different and asymmetric one that would better correspond with data measured in natural stream. Such function substitution cannot be considered as a solution of the advection – dispersion equation (Eq. (1)) for simplified boundary and initial conditions, but just as a simple approximation, based on the similarity. It is quite clear that such approximation does not explain the dispersion processes in the dead zones and has no specific parameters to characterize the size, residence time or other parameters of the transient storage zones in rivers. The

presented approach assumes constant parameters - this is not suitable for the complex simulations of long river reaches. But there is still a possibility to divide the modelled river reach to several branches or sub-reaches with different parameters. The breakthrough curve (output) at the end of previous branch could be used as an input to the next branch, etc.

Results of this study show that proposed approximate method in form of Eq. (11) has better accuracy of concentration distribution in a natural stream with dead zones than the approximation by Eq. (5).

Although nearly all literature sources are based on the application of the Eq. (5) (theory, experiments, coefficients), it can be assumed that proposed approximation by Gumbel distribution will bring significant increase of the accuracy of the dispersion processes simulation in natural stream with dead zones, eventually in case of some special applications with extensive consumption of computer time (e.g. iterative tasks – pollution source localisation).

It is clear that the proposed method requires for practical use careful calibration of the applied dispersion coefficient ($D_{x,G}$), in the ideal case based on in-situ measurements (tracer experiments). On the other hand, each simulation of pollution transport in a stream, based on hydrodynamic approach, needs for correct processing the set of hydraulic parameters, and again in an ideal case this set is based on in-situ measurements.

Simulation without the knowledge of the real conditions and without calibration and verification based on real field experiments, can lead to misleading results. The most frequent cause of this is an inaccurate dispersion coefficient determination, but also neglecting the presence of dead zones, eventually incorrect determination of the dead zones influence. Application of the proposed approximation reduces these inaccuracies in some extent. Furthermore, in some cases it could be hard to detect the presence of dead zones and their extent, even the determination of their parameters can be very difficult. Consequently, the proposed approximation could be useful and helpful for the simulation of pollution spreading in a stream with dead zones without arduous determination of these dead zones parameters. However, it is necessary to mention again that every simulation should be accompanied by the calibration and verification at least in form of one simple tracer experiment.

The use of 1D model approach has its limitations, but we believe that it is still advantageous to use it in the practice also for short reaches. 2D, eventually 3D approach requires much more data – physical dimensions and model boundaries, velocities and dispersion parameters for 2 (or 3) dimensions. Such data are not always available and it can be very difficult, time and money consuming task to collect necessary data.

CONCLUSIONS

In this paper a simple numerical approximate method for one-dimensional simulation of the dispersion of a solute in a stream is introduced. The presented method is suitable especially for streams with significant influence of dead zones, which cause a strong asymmetry in the shape of the concentration distribution curves over the time. Eq. (5) is not fully applicable in such conditions and the differences from measured values are considerable. Similar analytical solutions for streams with occurrence of dead zones, described in literature sources up to now (De Smedt et al., 2005) are clearly mathematically correct and accurate, but these methods are difficult for code programming and computational time, especially in case of inverse tasks solving (iterative tasks, brute force methods).

The proposed method was verified using the experimental data from three tracer field studies. The field experiments were performed at three streams in south Slovakia – Šúrsky channel, Malá Nitra and Malina streams. Evaluation of the field tracer experiments from all streams has shown considerable asymmetry of the concentration distribution, which clearly indicates extensive presence of dead zones in all the streams. The statistical evaluation of the proposed method shows that the (Eq. (11)) is much more accurate for simple approximation of the concentration distribution in streams with dead zones than Eq. (5).

Another verification was performed for rivers with different hydraulic parameters and longer distances, using previously published data (Nordin and Sabol, 1974) for the Monocacy and Red river field tracer experiments. The proposed approximation method (Eq. (11)) was significantly more accurate than the standard method (Eq. (5)) even in this case. The sum of squared difference was in case of the approximate method smaller by 60, up to 96%.

Results of the study confirmed that proposed one-dimensional analytical method approximates the solute concentration distribution very well and is fully applicable in the practice for simple tasks (simulations) of the pollution dispersion in streams. Its advantage is simple programming and computational speed (less computational time is needed). This could be very advantageous for iterative tasks solving, e.g. the inverse task (pollution source localisation). For full application, a simple verification and calibration is sufficient, but it is not necessary to determine the parameters of dead zones, used in Eq. (2). Besides, the estimation of these parameters is quite difficult in practice. Finally, major advantage of the proposed method is the possibility to apply on it the superposition principle (a common feature of all analytical solutions). This allows simulation of various arbitrarily defined pollution inputs into the stream.

Acknowledgement. This paper was prepared with the financial support of the Scientific Grant Agency VEGA within the scientific project Nr. VEGA 1/0805/16 “Localisation of accidental point sources of pollution in watercourses based on-line monitoring data”. It was also supported by the Ministry of Education, Science, Research and Sport of the Slovak Republic within the Research and Development Operational Programme for the project "University Science Park of STU Bratislava", ITMS 26240220084, and the project "Centre of excellence for integrated flood protection of land", ITMS 26240120004, both co-funded by the European Regional Development Fund.

REFERENCES

Baek, K.O., Seo, I.W., 2016. On the methods for determining the transverse dispersion coefficient in river mixing. Advances in Water Resources, 90, 1–9.

Brevis, W., Niño, Y., Vargas, J., 2006. Experimental characterization and visualization of mass exchange process in dead zones in rivers. In: Proceedings of 3rd International Conference on Fluvial Hydraulics (RiverFlow 2006), pp. 235–242.

Cushman-Roisin, B., 2012. Turbulent Dispersion. In: Fernando, H.J.S. (Ed.): Handbook of Environmental Fluid Dynamics, Volume One: Overview and Fundamentals. CRC Press, Taylor & Francis Group, pp. 263–271.

Czernuszenko, W., Rowinski, P.M., 1997. Properties of the dead-zone model of longitudinal dispersion in rivers. Journal of Hydraulic Research, 35, 4, 491–504.

Czernuszenko, W., Rowinski, P.M., Sukhodolov, A., 1998. Experimental and numerical validation of the dead-zone model for longitudinal dispersion in rivers. Journal of Hydraulic Research, 36, 2, 269–280.

Davis, P.M., Atkinson, T.C., 2000. Longitudinal dispersion in natural channels: 3. An aggregated dead zone model applied to the River Severn, U.K. Hydrology and Earth System Sciences, 4, 3, 373–381.

Davis, P.M., Atkinson, T.C., Wigley, T.M.L., 2000. Longitudinal dispersion in natural channels: 2. The roles of shear flow dispersion and dead zones in the River Severn, U.K. Hydrology Earth System Sciences, 4, 355–371.

De Smedt, F., 2006. Analytical solutions for transport of decaying solutes in rivers with transient storage. Journal of Hydrology, 330, 3–4, 672–680.

De Smedt, F., 2007. Analytical solution and analysis of solute transport in rivers affected by diffusive transfer in the hyporheic zone. Journal of Hydrology, 339, 29–38. DOI: 10.1016/j.jhydrol.2007.02.002.

De Smedt, F., Brevis, W., Debels, P., 2005. Analytical solution for solute transport resulting from instantaneous injection in streams with transient storage. J. Hydrol., 315, 25–39.

Deng, Z.Q., Jung, H.S., 2009. Scaling dispersion model for pollutant transport in rivers. Environmental Modelling & Software, 24, 627–631.

Djordjevich, A., Savović, S., Janićijević, A., 2017. Explicit finite-difference solution of two-dimensional solute transport with periodic flow in homogenous porous media. J. Hydrol. Hydromech., 65, 4, 426–432 .

Engelhardt, C., Kruger, A., Sukhodolov A., Nicklisch, A., 2004. A study of phytoplankton spatial distributions, flow structure and characteristics of mixing in a river reach with groynes. Journal of Plankton Research, 26, 11, 1351–1366.

Fischer, H.B., List, E., Koh, R.C.Y., Imberger, J., Brooks, N.H., 1979. Mixing in Inland and Coastal Waters. Academic Press, New York.

Gualtieri, C., 2008. Numerical simulation of flow patterns and mass exchange processes in dead zones. In: Proceedings of the iEMSs Fourth Biennial Meeting: International Congress on Environmental Modelling and Software (iEMSs 2008), Barcelona, Spain.

Gualtieri, C., 2010. Numerical simulation of mass exchange processes in a dead zone of a river. In: Mihalovic, D.T., Gualtieri, C. (Eds.): Advances in Environmental Fluid Mechanics. World Scientific, Singapore, pp. 249–274.

Chanson, H., 2004. Environmental Hydraulics of Open Channel Flows. Elsevier, 430 p.

Jamieson, E., Gaskin, S.J., 2007. Laboratory study of 3 dimensional characteristics of recirculating flow in a river embayment. In: Proceedings of the XXXII IAHR Congress, Venice, Italy.

Jirka, G.H., 2004. Mixing and dispersion in rivers. In: Greco, M., Carravetta, A., Della Morte, R. (Eds.): Proceedings of the Second International Conference on Fluvial Hydraulics, Vol. 1, pp. 13–28.

Jirka, G.H., Bleninger, T., Burrows, R., Larsen, T., 2004. Environmental Quality Standards in the EC-Water Framework. European Water Management Online.

Kilpatrick, F.A., Wilson, J.F. Jr., 1970. Measurement of time of travel and dispersion by dye tracing. In: Techniques of Water-Resources Investigations 3-A9 [version 2]. US Geological Survey, Washington D.C.

Kimura, I., Hosoda, T., 1997. Fundamental properties of flows in open channels with dead zone. Journal of Hydraulic Engineering, 123, 2, 322–347.

Kurzke, M., Weitbrecht, V., Jirka, G.H.J., 2002. Laboratory concentration measurements for determination of mass exchange between groin fields and main stream. In: Proceedings of 1st International Conference on Fluvial Hydraulics (River Flow 2002), 1, pp. 369–376.

Limerinos, J.T., 1970. Determination of the Manning coefficient for measured bed roughness in natural channels. Water Supply Paper 1898-B, 47 p.

Martin, J.L., McCutcheon, S.C., 1998. Hydrodynamics and Transport for Water Quality Modeling. CRC Press, 816 p. ISBN 0-87371-612-4.

McCoy, A., 2008. Numerical investigation of flow hydrodynamics in a channel with a series of groynes. Journal of Hydraulic Engineering, 134, 2, 157–172.

McCoy, A., Constantinescu, G., Weber, L., 2006. Exchange processes in a channel with two vertical emerged obstructions. Flow, Turbulence and Combustion, 77, 1–4, 97–126.

Murphy, E., Ghisalberti, M., Nepf , H., 2007. Model and laboratory study of dispersion in flows with submerged vegetation. Water Resources Research, 43, 5.

Muto, Y., Imamoto, H., Ishigaki, T., 2000. Turbulence characteristics of a shear flow in an embayment attached to a straight open channel. In: Proceedings of the 4th International Conference on HydroScience & Engineering (ICHE 2000), Seoul, Korea. 2000.

Nordin, C.F., Sabol, G.V., 1974. Empirical data on longitudinal dispersion. Water-Resources Investigations Report 74-20. U.S. Geological Survey, 332 p.

Nordin, C.F., Troutman, B.M., 1980. Longitudinal dispersion in rivers: The persistence of skewness in observed data. Water Resour. Res., 16, 1, 123–128.

Rowiński, P.M., Dysarz, T., Napiórkowski, J.J., 2004. Estimation of longitudinal dispersion and storage zone parameters. In: Greco, M., Carravetta, A., Della Morte, R. (Eds.): Proceedings of the Second International Conference on Fluvial Hydraulics, Vol. 1, pp. 1201–1210.

Runkel, R.L., 1998. One-dimensional transport with inflow and storage (OTIS): a solute transport model for streams and rivers. Water-Resources Investigations Report 98–4018. U.S. Geological Survey, Denver, Colorado.

Rutherford, J.C., 1994. River Mixing. John Wiley & Sons, Chichester, U.K. 348 p.

Ruthven, P.M., 1971. The dispersion of a decaying effluent discharged continiously into a uniformly flowing stream. Water Research, 5, 6, 343–352.

Shucksmith, J.D., Boxall, J.B., Guymer, I., 2010. Effects of emergent and submerged natural vegetation on longitudinal mixing in open channel flow. Water Resources Research, 46, W04504.

Shucksmith, J.D., Boxall, J.B., Guymer, I., 2011. Determining longitudinal dispersion coefficients for submerged vegetated flow. Water Resources Research, 47, 10.

Socolofsky, S.A., Jirka, G.H., 2005. Special Topics in Mixing and Transport Processes in the Environment. Texas A&M University, College Station.

Skublics, D., Blöschl, G., Rutschmann, P., 2016. Effect of river training on flood retention of the Bavarian Danube. J. Hydrol. Hydromech., 64, 4, 349–356. DOI: 10.1515/johh-2016-0035.

Sukhodolov, A., 2014. Hydrodynamics of groyne fields in a straight river reach: Insight from field experiments. Journal of Hydraulic Research, 52, 1.

Tonina, D., 2012. Surface water and streambed sediment interaction: The hyporheic exchange. In: Gualtieri, C., Mihalo-

vic, D.T. (Eds.): Fluid Mechanics of Environmental Interfaces. CRC Press, Boca Raton, pp. 255–294.

Toprak, Z.F., Cigizoglu, H.K., 2008. Predicting longitudinal dispersion coefficient in natural streams by artificial intelligence methods. Hydrological Processes, 22, 4106–4129.

Uijttewaal, W.S.J., 1999. Groyne field velocity patterns determined with particle tracking velocimetry. In: Proceedings of the XXVIII IAHR Congress. Graz, Austria.

Uijttewaal, W.S.J., 2005. Effects of groyne layout on the flow in groyne fields: laboratory experiments. Journal of Hydraulic Engineering, 131, 9, 782–791.

Uijttewaal, W.S.J., Lehmann, D., van Mazijk, A., 2001. Exchange processes between a river and its groyne fields: model experiments. Journal of Hydraulic Engineering, 127, 11, 928–936.

Valentine, E.M., Wood, I.R., 1979. Experiments in Longitudinal Dispersion with Dead Zones. Journal of the Hydraulics Division, 105, HY9, 999–1016.

van Mazijk, A., 1996. One-dimensional approach of transport phenomena of dissolved matter in rivers. (PhD Thesis 2796). Technische Universiteit Delft, Delft.

van Mazijk, A., Veling, E.J.M., 2005. Tracer experiments in the Rhine Basin: evaluation of the skewness of observed concentration distributions. Journal of Hydrology, 307, 1–4, 60–78.

Velísková, Y., Sokáč, M., Koczka Bara, M., Dulovičová, R., 2013. Hydrodynamický prístup k modelovaniu kvality povrchových vôd. (Hydrodynamic approach to modeling of surface water quality. Acta Hydrologica Slovaca, 14, 1, 145–153. (In Slovak.)

Wang, Z., Xia, J., Deng, S., Zhang, J., Li, T., 2017. One-dimensional morphodynamic model coupling open-channel flow and turbidity current in reservoir. J. Hydrol. Hydromech., 65, 1, 68–79.

Weitbrecht, V., 2004. Influence of dead-water zones on the dispersive mass-transport in rivers. Dissertationsreihe am Institut fuer Hydromechanik der Universitat Karlsruhe, Vol. 2004/1. Universitätsverlag Karlsruhe, Karlsruhe.

Weitbrecht, V., Jirka, G.H.J., 2001. Flow patterns and exchange processes in dead zones of rivers. In: Proceedings of the XXIX IAHR Congress, Seoul, Korea.

Weitbrecht, V., Socolofsky, S.A., Jirka, G.H., 2008. Experiments on mass exchange between groin fields and the main stream in rivers. Journal of Hydraulic Engineering, 134, 2, 173–183.

Yossef, M.F.M., de Vriend, H.J., 2011. Flow Details near River Groynes: Experimental Investigation. J. Hydraul. Eng., 137, 5, 504–516.

Received 5 September 2017
Accepted 25 June 2018

J. Hydrol. Hydromech., 66, 2018, 4, 448–456
DOI: 10.2478/johh-2018-0028

CFD simulation of flow behind overflooded obstacle

Yvetta Velísková[1*], Zdeněk Chára[2], Radoslav Schügerl[1], Renáta Dulovičová[1]

[1] Institute of Hydrology of the Slovak Academy of Sciences, Dúbravská cesta 9, 841 04 Bratislava, Slovakia.
[2] Institute of Hydrodynamics of the Czech Academy of Sciences, v. v. i., Pod Patankou 30/5, 166 12 Prague 6, Czech Republic.
[*] Corresponding author. E-mail: veliskova@uh.savba.sk

Abstract: This paper deals with studying of two topics – measuring of velocity profile deformation behind a over-flooded construction and modelling of this velocity profile deformation by computational fluid dynamics (CFD). Numerical simulations with an unsteady RANS models - Standard k-ε, Realizable k-ε, Standard k-ω and Reynolds stress models (ANSYS Fluent v.18) and experimental measurements in a laboratory flume (using ADV) were performed. Results of both approaches showed and affirmed presence of velocity profile deformation behind the obstacle, but some discrepancies between the measured and simulated values were also observed. With increasing distance from the obstacle, the differences between the simulation and the measured data increase and the results of the numerical models are no longer usable.

Keywords: Velocity profile; Computational fluid dynamics (CFD); Free surface flow; Bridge; ADV; Laboratory flume; Numerical simulation; RANS models.

INTRODUCTION

Researchers typically address problems in science and engineering through two complementary approaches: experimental and analytical (or numerical). In many applications the governing equations are nonlinear and analytical solutions are very often not available. In addition, fluid mechanics applications are often multidimensional in nature and time-dependent. Accurate modelling of velocity profile is essential for estimating discharge capacity, flow conditions in a stream or the impact of various constructions to morphological stability of stream bed, etc. The measurement of instantaneous velocities in water flows has long been a challenging issue. Observing a velocity distribution inside flowing water streams is not easy in natural conditions. Existing flow velocity will not be uniform in the stream neither without nor with obstacles.

In practice of civil engineering numerical models are accepted as a means of predicting water flow (Kerenyi et al., 2008; Versteegh, 1990). While for the final design of some important projects or hydraulic problems the physical model scale are being built (Evangelista et al., 2017; Kocaman and Ozmen-Cagatay, 2012), the preliminary designs are more and more tested by numerical models (Kerenyi et al., 2008; Nagata et al., 2005; Schmidt and Thiele, 2002). But each numerical model should be verified, so the objective of this work was to verify the numerical simulation by measurement in laboratory condition.

Flows may be considerably affected by the presence of natural or artificial obstacles. In the case of severe floods, for example due to dam- or dike-break, the influence of such obstacles is even amplified. Neglecting this influence in numerical simulations of such flows could lead to heavy misinterpretation. The presence of obstacles is common in river as well in minor bed (bridge piers) as in floodplains (abutments, dikes, trees and vegetation, debris from former floods, etc.). Moreover, if the river embankments are overtopped or the flood dikes breached, flow will occur in areas that are normally not subject to inundation, not prepared to support such a hazard, and thus presenting a series of obstacles, for example roads, railways, dwellings, industrial and commercial structures, etc. (Frazao et al., 2004; Laks et al., 2017).

The impact of obstacles in the riverbed on changing the velocity profile can be studied through a variety of experimental and numerical approaches. In this paper, we focused on a simple model of a bridge structure located in a rectangular laboratory flume and to determine the effect of this model on the velocity field behind the obstacle.

Identification of computational fluid dynamics (CFD) is one of the aspects that must be taken into account when we make or pick out the numerical model for application. Numerical modelling of the flow structures surrounding these obstructions is challenging, yet it represents an important tool for velocity profile assessment. Several three-dimensional CFD models have been already applied to typical hydraulic engineering cases, as through bridge piers and dam breaks. For instance, Shen and Diplas (2008) conducted numerical simulations using CFD models to assess their ability to produce complex flow patterns triggered by the presence of obstacles at various discharges. It is concluded that numerical models can provide an accurate description of the heterogeneous velocity patterns favored by many aquatic species over a broad range of flows, especially under deep flow conditions when the various obstructions are submerged. A comprehensive study of the CFD was provided by Olsen (1999). Numerical modelling of flow around a submerged obstacle is described for example by Janssen et al. (2012), Keylock et al. (2012), Baranya et al. (2012), Stoesser et al. (2015), and Zhang et al. (2009).

The finite volume method was used to perform numerical simulations and in the physical model the velocity field was measured using the ADV (Acoustic Doppler Velocimetry) method. ADV method has become the tool of choice for mapping velocity fields that are used to assess aquatic habitat and validate numerical models (Mueller et al., 2007). Takashi et al. (2004) present velocity profiles and accurate flow rate measurements in open channel flow using ultrasonic Doppler method.

DESCRIPTION OF MODEL SITUATION

As a model situation the flow condition in rectangular cross section shape channel was chosen. It is well-known that during a flood on a creek or a small river, a bridge opening may run completely full or even the entire bridge may be submerged by

the flow (Kerenyi et al., 2008; Picek et al., 2007). Additionally, presence of aquatic vegetation is typical and frequent in lowland channels (Fig. 1). So, the shape of the used obstacle expresses the reduction of cross-section profile flow area as a result of dense vegetation and a bridge construction during a flood event. It is very difficult to obtain any information of flow characteristics on bridge constructions during flood events. Therefore a physical modelling or CFD simulations are used to obtain reasonable data. In this paper we focused on the use of CFD simulations with verification on a physical model.

Fig. 1. Lowland channel part with vegetation and a bridge construction (Chotárny channel, Žitný Ostrov).

NUMERICAL SIMULATIONS

As it was mentioned above, the objective of this study was to perform a comparison of the CFD simulations with an experimental observation. We tested four turbulence models - Standard k-ε, Realizable k-ε, Standard k-ω and Reynolds stress models which all are implemented in the CFD software ANSYS-Fluent 18.0.

The k-ε models have become one of the most widely used turbulence models as it provides robustness, economy and reasonable accuracy for a wide range of turbulent flows. The Standard k-ε model calculates the turbulent viscosity from the equation

$$\mu_t = \rho C_\mu \frac{k^2}{\varepsilon} \tag{1}$$

where k is the turbulent kinetic energy, ε is the rate of dissipation of the turbulent kinetic energy and C_μ is a constant. To obtain the turbulent kinetic energy and its rate of dissipation additional two equations have to be solved. For the incompressible flow condition the equations can be written as

$$\frac{\partial}{\partial t}(\rho k) + \frac{\partial}{\partial x_i}(\rho k u_i) = \frac{\partial}{\partial x_j}\left[\left(\mu + \frac{\mu_t}{\sigma_k}\right)\frac{\partial k}{\partial x_j}\right] + \mu_t S^2 - \rho\varepsilon \tag{2a}$$

$$\frac{\partial}{\partial t}(\rho\varepsilon) + \frac{\partial}{\partial x_i}(\rho\varepsilon u_i) = \frac{\partial}{\partial x_j}\left[\left(\mu + \frac{\mu_t}{\sigma_\varepsilon}\right)\frac{\partial \varepsilon}{\partial x_j}\right] + C_{1\varepsilon}\frac{\varepsilon}{k}\mu_t S^2 - C_{2\varepsilon}\rho\frac{\varepsilon^2}{k} \tag{2b}$$

The Prandtl numbers σ_k and σ_ε have values of 1.0 and 1.3, respectively. The model constants C_μ, $C_{1\varepsilon}$ and $C_{2\varepsilon}$ of 0.09, 1.44 and 1.92 were used.

The Realizable k-ε model features two main differences from the Standard k-ε model. It uses a new equation for the turbulent viscosity and the dissipation rate transport equation has been derived from the equation for the transport of the mean-square vorticity fluctuation. The equation for the turbulent kinetic energy is the same as for the Standard k-ε model. Although the equation for the turbulent viscosity is formally identical with the equation (1) the term C_μ is no more constant

$$C_\mu = \frac{1}{A_0 + A_s \frac{k}{\varepsilon}\sqrt{S_{ij}S_{ij} + \tilde{\Omega}_{ij}\tilde{\Omega}_{ij}}} \tag{3}$$

$$\tilde{\Omega}_{ij} = \overline{\Omega}_{ij} - \varepsilon_{ijk}\omega_k - 2\varepsilon_{ijk}\omega_k, \quad \overline{\Omega}_{ij} = \overline{\frac{1}{2}\left(\frac{\partial u_i}{\partial x_j} - \frac{\partial u_j}{\partial x_i}\right)}, \quad S_{ij} = \frac{1}{2}\left(\frac{\partial u_i}{\partial x_j} + \frac{\partial u_j}{\partial x_i}\right) \tag{4}$$

$$A_0 = 4.04, \quad A_s = \sqrt{6}\cos\left[\frac{1}{3}\cos^{-1}\left(\sqrt{6}\frac{S_{ij}S_{jk}S_{ki}}{\sqrt{S_{ij}S_{ij}}}\right)\right] \tag{5}$$

$$\frac{\partial}{\partial t}(\rho\varepsilon) + \frac{\partial}{\partial x_i}(\rho\varepsilon u_i) = \frac{\partial}{\partial x_j}\left[\left(\mu + \frac{\mu_t}{\sigma_\varepsilon}\right)\frac{\partial \varepsilon}{\partial x_j}\right] + \rho C_1 S\varepsilon - \rho C_2 \frac{\varepsilon^2}{k + \sqrt{\frac{\mu\varepsilon}{\rho}}} \tag{6}$$

$$C_1 = \max\left[0.43, \frac{\eta}{\mu + 5}\right], \quad \eta = S\frac{k}{\varepsilon}, \quad S = \sqrt{2S_{ij}S_{ij}}$$

The model constants are $\sigma_k = 1.0$, $\sigma_\varepsilon = 1.2$ and $C_2 = 1.9$.

In the Standard k-ω model ω is an inverse time scale that is associated with the turbulence (specific dissipation rate). The turbulent viscosity is calculated for the equation

$$\mu_t = \alpha^* \frac{\rho k}{\omega} \tag{7}$$

where the parameter α^* is a damping coefficient. For the high-Reynolds form of this model the damping coefficient equals 1. The equations for the k and ω are

$$\frac{\partial}{\partial t}(\rho k) + \frac{\partial}{\partial x_i}(\rho k u_i) = \frac{\partial}{\partial x_j}\left[\left(\mu + \frac{\mu_t}{\sigma_k}\right)\frac{\partial k}{\partial x_j}\right] + \mu_t S^2 - \rho\beta^* f_\beta k\omega \tag{8a}$$

$$\frac{\partial}{\partial t}(\rho\omega) + \frac{\partial}{\partial x_i}(\rho\omega u_i) = \frac{\partial}{\partial x_j}\left[\left(\mu + \frac{\mu_t}{\sigma_\omega}\right)\frac{\partial \omega}{\partial x_j}\right] + \alpha\frac{\omega}{k}\mu_t S^2 - \rho\beta_i f_\beta \omega^2 \tag{8b}$$

where

$$f_{\beta^*} = \begin{cases} 1 & \mathrm{X}_k \le 0 \\ \dfrac{1+680\,\mathrm{X}_k^2}{1+400\,\mathrm{X}_k^2} & \mathrm{X}_k > 0 \end{cases} \qquad \mathrm{X}_k = \frac{1}{\omega^3}\frac{\partial k}{\partial x_j}\frac{\partial \omega}{\partial x_j} \tag{9}$$

$$\beta^* = \beta^*_\infty \left[\frac{0.267 + (0.125\,\mathrm{Re}_t)^4}{1+(0.125\,\mathrm{Re}_t)^4} \right], \quad \mathrm{Re}_t = \frac{\rho k}{\mu \omega} \tag{10}$$

$$f_\omega = \frac{1+70\mathrm{X}_\omega}{1+80\mathrm{X}_\omega}, \quad \mathrm{X}_\omega = \left| \frac{\Omega_{ij}\Omega_{jk}S_{ki}}{\left(\beta^*_\infty \omega\right)^3} \right| \tag{11}$$

$$\alpha^* = \alpha^*_\infty \left(\frac{0.024 + 0.167\,\mathrm{Re}_t}{1+0.167\,\mathrm{Re}_t} \right), \alpha = \frac{\alpha_\infty}{\alpha^*} \left(\frac{0.111 + 0.339\,\mathrm{Re}_t}{1+0.339\,\mathrm{Re}_t} \right) \tag{12}$$

The model constants are $\alpha_\infty^* = 1.0$, $\alpha_\infty = 0.52$, $\beta_\infty^* = 0.09$, $\beta_i = 0.072$, $\sigma_k = 1.0$, $\sigma_\omega = 1.2$.

The Reynolds stress model closes the Reynolds-Averaged Navier-Stokes equations by solving additional transport equations for the six independent Reynolds stresses

$$\begin{aligned} &\frac{\partial}{\partial t}\left(\rho \overline{u_i' u_j'}\right) + \frac{\partial}{\partial x_k}\left(\rho u_k \overline{u_i' u_k'}\right) = \frac{n!}{r!(n-r)!} \\ &-\frac{\partial}{\partial x_k}\left[\rho \overline{u_i' u_j' u_k'} + \overline{p'\left(\delta_{kj}u_i' + \delta_{ik}u_j'\right)}\right] + \frac{\partial}{\partial x_k}\left[\mu \frac{\partial}{\partial x_k}\left(\overline{u_i' u_j'}\right)\right] - \\ &\rho\left(\overline{u_i' u_k'}\frac{\partial u_j}{\partial x_k} + \overline{u_j' u_k'}\frac{\partial u_i}{\partial x_k}\right) + \overline{p'\left(\frac{\partial u_i'}{\partial x_j} + \frac{\partial u_j'}{\partial x_i}\right)} - \\ &2\mu\overline{\frac{\partial u_i'}{\partial x_k}\frac{\partial u_j'}{\partial x_k}} - 2\rho\Omega_k\left(\overline{u_j' u_m'}\varepsilon_{ikm} + \overline{u_i' u_m'}\varepsilon_{jkm}\right) \end{aligned} \tag{13}$$

where $\varepsilon_{i,jkm}$ is Levi-Civita symbol. In our simulations we have used the Reynolds stress model with a linear pressure strain term.

Two-phase VOF (Volume of Fluid) model was used to simulate the free water level. To increase the water level in the channel, a 60 mm height sharp edge weir was placed at the end of the simulated section. The shape of the entrance section with the inclined top wall has been chosen to ensure that the inlet to the channel is fully flooded. A constant velocity profile was assumed at the channel inlet. The water from the channel drained through the bottom opening in an outlet chamber. The schematic view of the computation domain is shown in Fig. 2.

The direction of the flow is from the left to the right. The length of the simulated channel was 3500 mm, followed by a 600 mm calming chamber. The upstream edge of the obstacle was located 1500 mm from the inlet profile. The width of the channel was 400 mm but only half of the channel was modelled and the axis plane was treated as a symmetry boundary condition. The dimensions and the orientation of the bridge obstacle were the same as on the physical model (Fig. 4) except a small part close to a connection of the upstream pillar and the side wall. The boundary layers on the solid surfaces were meshed by a structured mesh and the rest of the computational domain was meshed by tetrahedral cells. Sizes of cells varied from 0.1 to 3.5 mm. All numerical simulations were performed as unsteady simulations using the influence of gravity. The flow discharge was the same as in the case of the physical model – 39 x 10^{-3} m^3 s^{-1}. On the beginning of the simulation the channel was filled by water up to a level 250 mm.

LABORATORY MEASUREMENTS

Measurements were performed in a laboratory flume at the Institute of Hydrodynamics of the Czech Academy of Sciences. Laboratory flume had a rectangular cross section shape, length equals 25 m and width 400 mm (Fig. 3). A downstream weir with horizontal jalousies was used to keep the water level on the height around 250 mm and the discharge was regulated on a value of 39 x 10^{-3} m^3 s^{-1}.

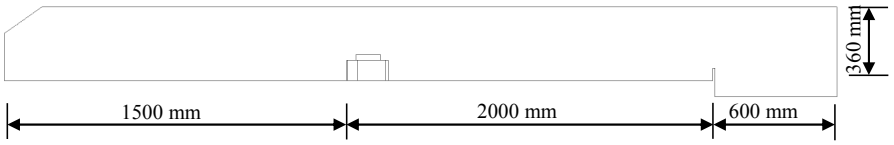

Fig. 2. Schematic view of the computational domain.

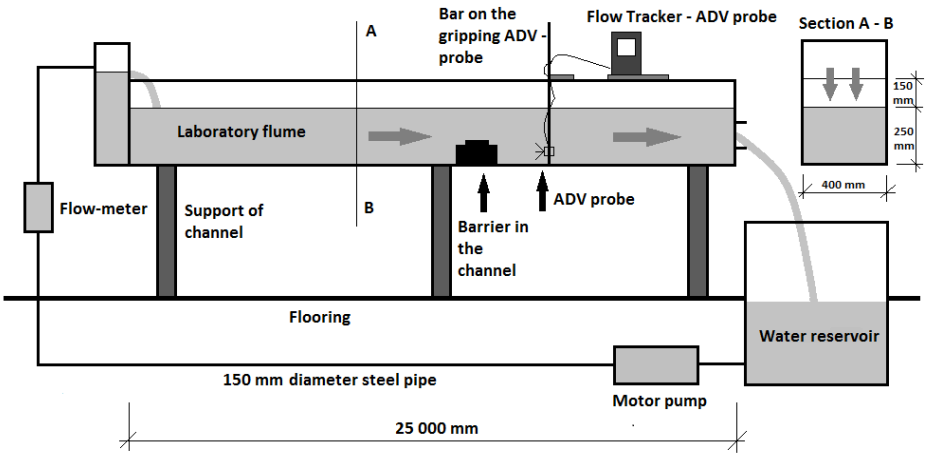

Fig. 3. Scheme of laboratory flume with the wooden barrier location.

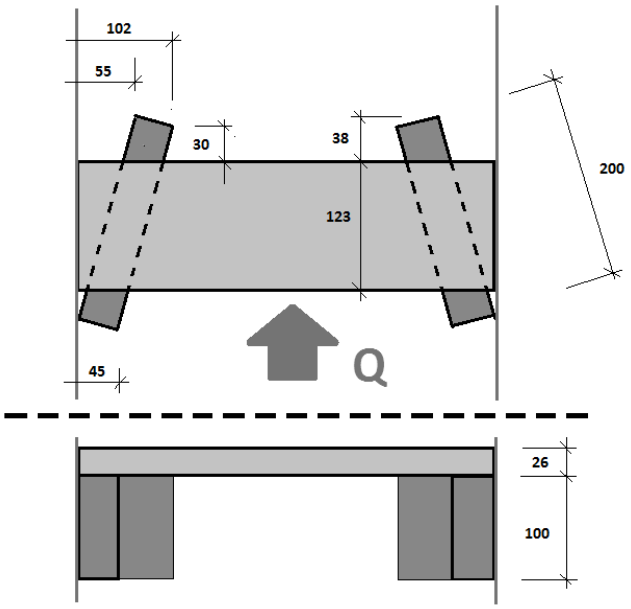

Fig. 4. Ground plan of obstacle and sight on the obstacle in the course of flow in laboratory flume.

As a measuring device there was used the ADV FlowTracker 3D probe. Many "aquatic" scientists employ ADV to characterise flow conditions (Carollo et al., 2002; Kim et al., 2000; Nikora et al., 1998). Compared to the thermal anemometry (hot film, hot wire, hot bead) and other invasive measurement techniques, like e.g. mechanical current-meters or electromagnetic sensors, the ADV has the advantage of being non-invasive, as the measuring volume is located some distance away from the actual probe. Acoustic instruments have relatively large sampling volumes, but they add the possibility of application in field conditions. In general, ADV are more straightforward to use, more robust, and easier to modify for field work than the other techniques. ADV use can limit mainly the accuracy of turbulence intensities, especially when making measurements close to the bed or in flows where large spatial gradients are present (Dombroski and Crimaldi, 2007).

The technique relies on the Doppler shift principle to measure the velocity of suspended scattering particles that are assumed to move passively with the flow. The ADV conducts 3 component current measurements in a sampling volume below the transmit-transducer. Sound bursts of known duration and frequency are emitted by the central transmitter and subsequently reflected back by suspended particles moving through the sampling volume. The reflected signals that are shifted in frequency (Doppler shift) are collected by the three receivers that surround the transmitter. The magnitude of the frequency shift is proportional to the velocity of the reflecting particles (Precht et al., 2006).

During the experiments it was applied so-called "General Mode" of ADV FlowTracker 3D probe (SonTek, 2009). This mode allows to measure velocity components in any measured point grid. In the first step, the measurements were carried out in profile, in which the flow is not disturbed – it means without any barrier. In the second phase, we placed a wooden barrier to the laboratory flume, which changed flow conditions and velocity component fields.

The obstacle was made from three prisms: two prisms on the flume bottom were stored obliquely at the angle 30° to the direction of flow of water in the flume. Bottom prisms have dimensions 50 x 100 x 200 mm. For these prisms (Fig. 4), we laid and attached perpendicularly to the flow direction upper prism with dimensions (26 x 123 x 400) mm. We measured the distribution of the velocity field at four profiles at a distance x_i = 70, 170, 300 and 900 mm from the barrier (Fig. 5) for information how velocity profile deformation damps down.

The measurement grid was created by different verticals along the flume width. All measurements were performed only in one half of cross-section profile because the flume and the obstacle were symmetrical by central axis. We selected the verticals in distance y_i = 70, 100, 130, 160, 190 and 220 mm from right side wall of the flume for profiles behind the obstacle, with the aim to take the velocity distribution in more details. Point velocity components v_x, v_y, v_z were measured at 7 different heights in each vertical. Heights of measured points in the verticals were z_i = 40, 80, 100, 120, 140, 160 and 180 mm from the bottom of the laboratory flume. The grid of measuring points in cross-section profiles was identical for all measurements and tests. The origin of the co-ordinate system is at the

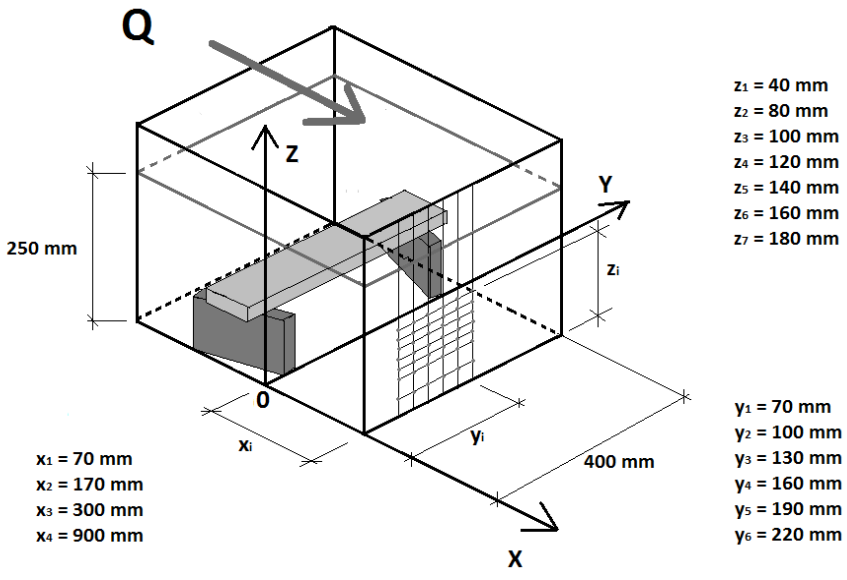

Fig. 5. Scheme of wooden obstacle in laboratory flume and location of measuring points of velocity components.

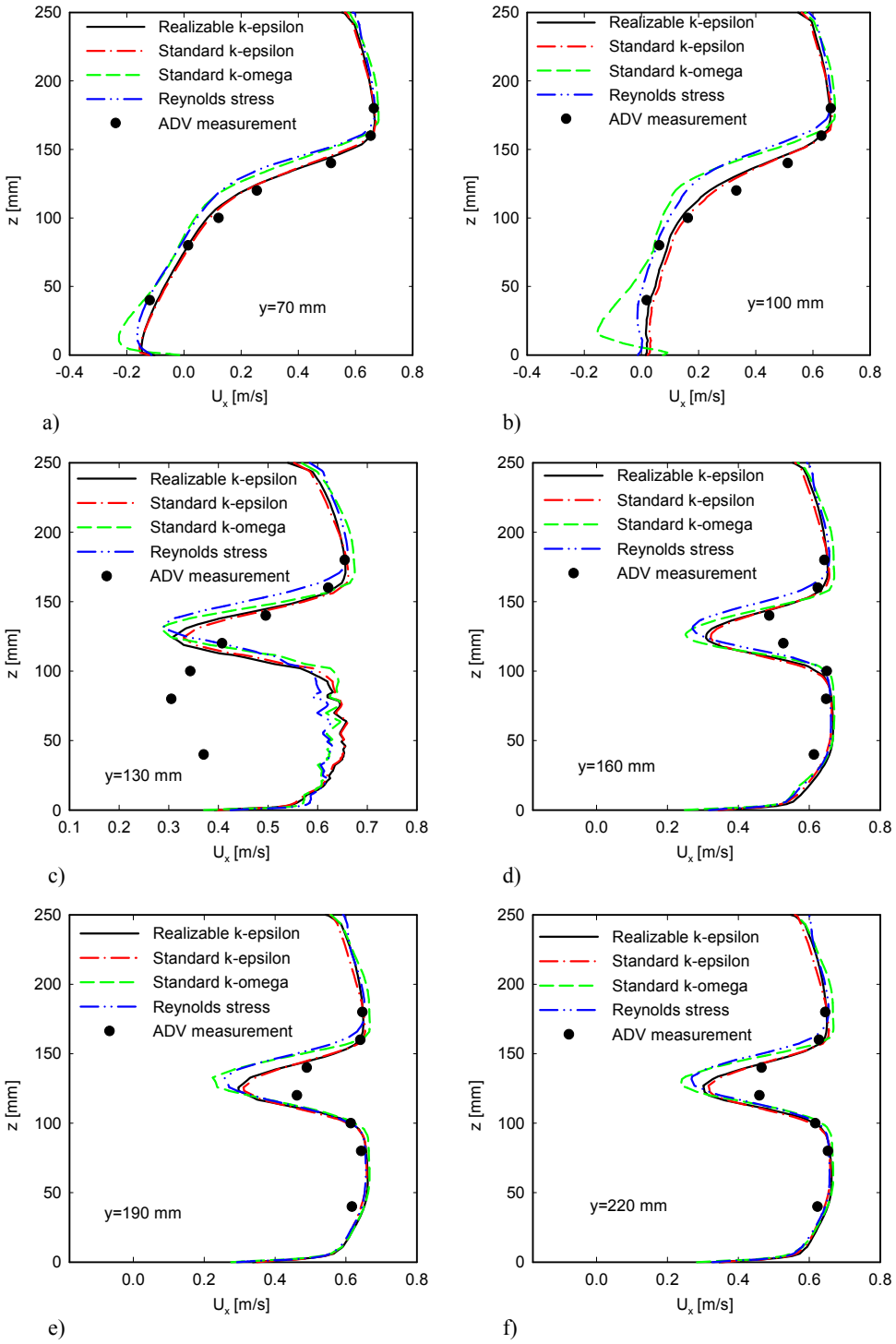

Fig. 6. Velocity profiles at the distance 70 mm behind the obstacle – a) y = 70 mm from the side wall, b) y = 100 mm, c) y = 130 mm, d) y = 160 mm, e) y = 190 mm, f) y = 220 mm.

bottom of the side wall of the channel. The longitudinal coordinate (x) starts at the position corresponding to the downstream edge of the obstacle.

Measurement time (t) was 240 seconds in each of the measuring grid point in the profile without barrier impact. Measurements results showed satisfactory stability of the probe. Because flow conditions behind the barrier are more complicated, the time of measurement for point velocity components in the profiles behind the barrier was increased to 300 seconds in each measured grid point.

RESULTS

The measured longitudinal velocity components were compared with the numerical simulations and the results are shown in Figs. 6–9.

Fig. 6 shows the measured and simulated velocity profiles at a distance of 70 mm behind the obstacle. In this figure we can see quite good agreement between the measured and simulated values of the longitudinal component of the velocity. The only exception is the velocity profile at y = 130 mm from the side-

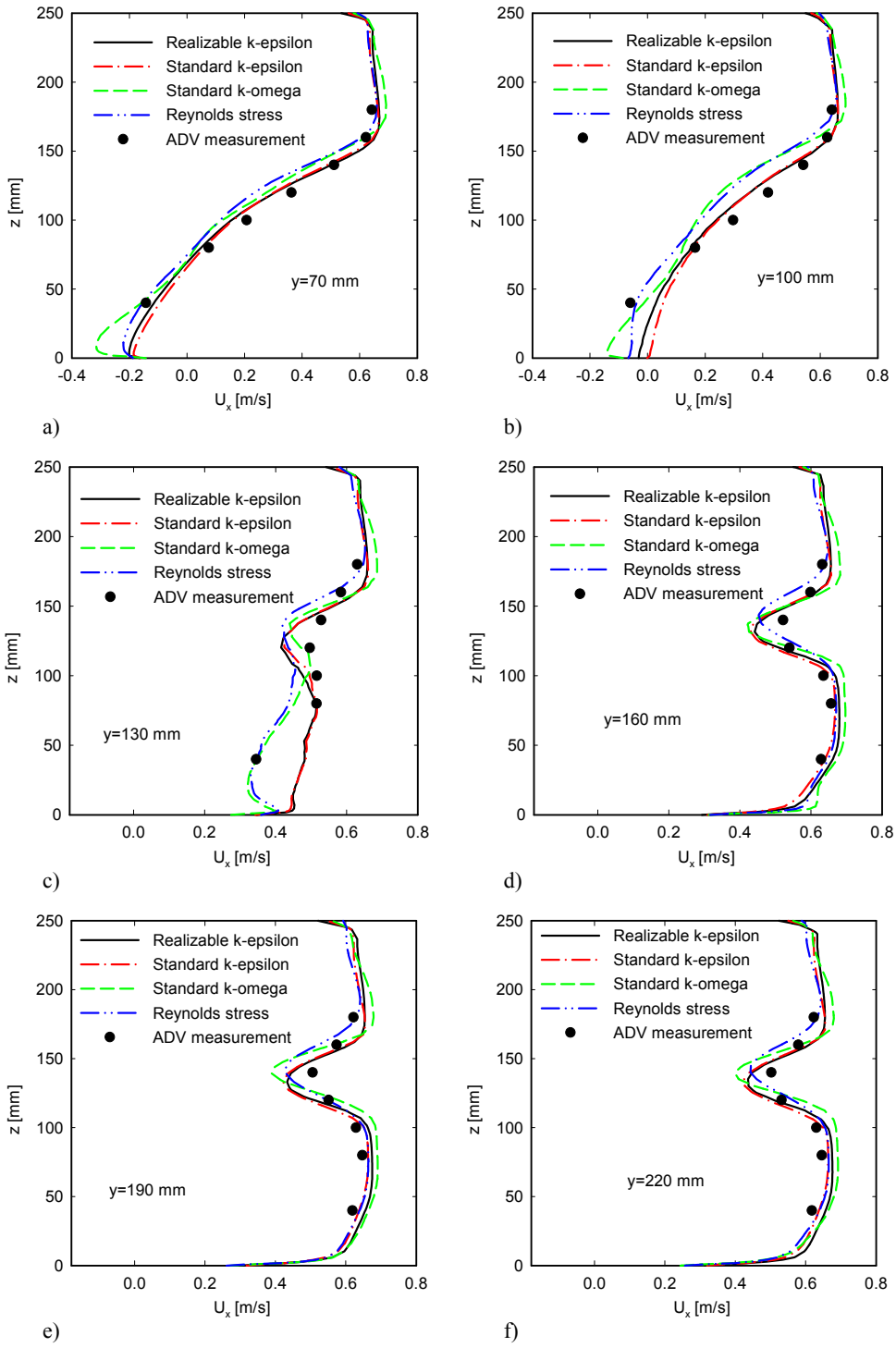

Fig. 7. Velocity profiles at the distance 170 mm behind the obstacle – a) y = 70 mm from the side wall, b) y = 100 mm, c) y = 130 mm, d) y = 160 mm, e) y = 190 mm, f) y = 220 mm.

wall where the simulated values already show the effect of the lower opening of the obstacle. This discrepancy can be caused on the one hand by the size of the ADV probe area being relatively large (in the order of tens of mm^3) and, on the other hand, by the large velocity component gradients in this area and also by velocity component fluctuations in measured volume during the measured period (Precht et al., 2006; Voulgaris and Trowbridge, 1998). Similar results were obtained for the velocity profiles measured at x = 170 mm. The results are shown in Fig. 7. Here, a relatively good match between the measured and simulated values of the longitudinal velocity component was also observed. However, with increasing distance from the obstacle, there are visible differences between measured and simulated data. Fig. 8 shows the velocity profiles measured at a distance of x = 300 mm. Differences between measured and simulated velocities can be observed mainly in the bottom part, close to the sidewall, where the measured velocities are significantly higher than the velocity determined from the simulation. In the case of the vertical at y = 160 mm from the sidewall the simulated velocities are higher. These differences are even

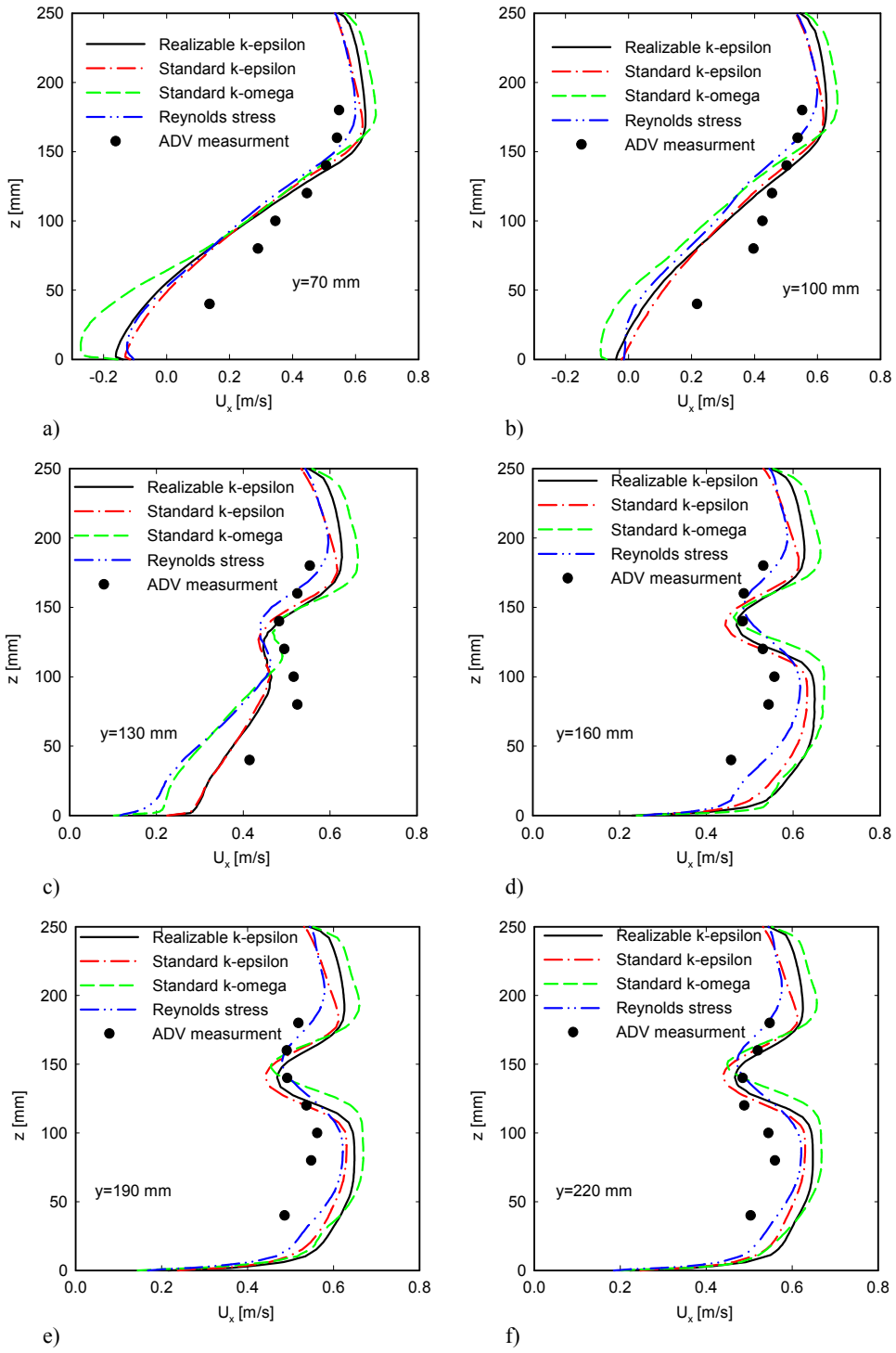

Fig. 8. Velocity profiles at the distance 300 mm behind the obstacle – a) y = 70 mm from the side wall, b) y = 100 mm, c) y = 130 mm, d) y = 160 mm, e) y = 190 mm, f) y = 220 mm.

more pronounced for the velocity profiles measured at the distance x = 900 mm, which are shown in Fig. 9. While the longitudinal velocities in the physical model are higher close to the side wall, towards the centre of the flume the measured velocities decrease. On the contrary the simulation still shows the influence of the bottom opening of the obstacle and therefore the highest velocities are observed in the centre part of the channel close to the bottom. Fig. 9 also shows the results of the measurement of the velocity profiles in case when the flume flow is unobstructed. It turns out that due to the obstacle there is a significant decrease in the velocity at the bottom part of the flume and even in this distance from the obstacle edge the impact of it does not disappear.

CONCLUSIONS

The paper presents the results of numerical simulations of velocity profile deformation behind the over flooded obstacle in the rectangular laboratory flume using the RANS models - Standard k-ε, Realizable k-ε, Standard k-ω and Reynolds stress

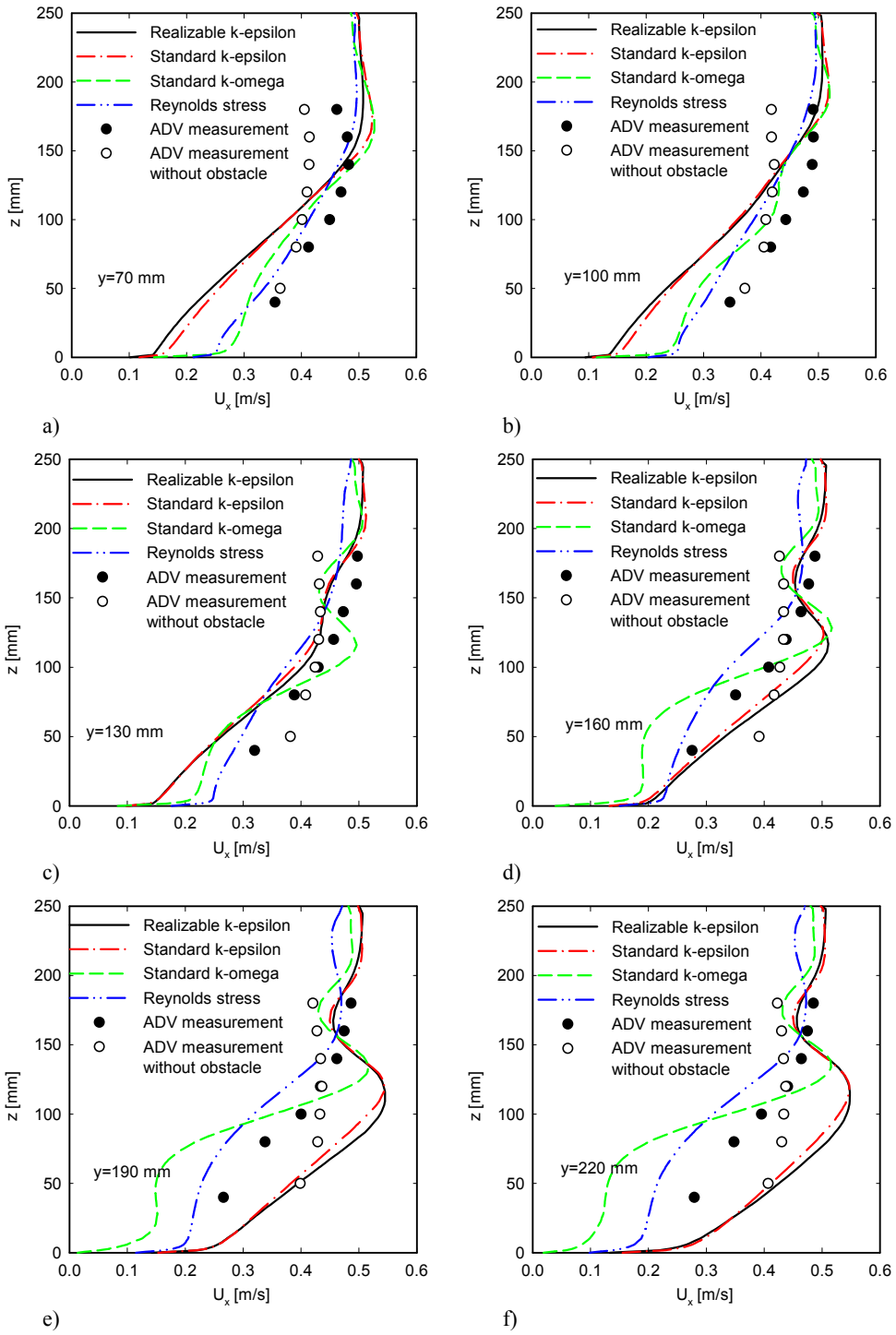

Fig. 9. Velocity profiles at the distance 900 mm behind the obstacle – a) y = 70 mm from the side wall, b) y = 100 mm, c) y = 130 mm, d) y = 160 mm, e) y = 190 mm, f) y = 220 mm.

models. In addition, the measurements by ADV device were performed on the physical model for verification of simulation results. Dimensions of simulated geometry matched dimensions on the physical model. It has been confirmed that simulation outputs of all models give usable results only in the area up to about 0.2 m behind the obstacle, which is approximately equivalent to double of the obstacle height and approximately equal to water depth. With the increasing distance from the obstacle, the differences between the simulation and the measured data increase and the chosen numerical approach no longer produces usable results.

Acknowledgements. The supports under project No. 15-18870S of the Grant Agency of the Czech Republic, RVO: 67985874 and VEGA -2-0058-15 are gratefully acknowledged. This publication is also the result of the project implementation ITMS 26240120004 Centre of excellence for integrated flood protection of land supported by the Research & Development Operational Programme funded by the ERDF.

REFERENCES

Baranya, S., Olsen, N.R.B., Stoesser, T., Sturm, T., 2012. Three-dimensional rans modeling of flow around circular piers using nested grids. Engineering Applications of Computational Fluid Mechanics, 6, 4, 648–662. http://doi.org/10.1080/19942060.2012.11015449

Carollo, F.G., Ferro, V., Termini, D., 2002. Flow velocity measurements in vegetated channels. J. Hydraul. Eng-ASCE, 128, 7, 664–673. ISSN 0733-9429.

Dombroski, D.E., Crimaldi, J., 2007. The accuracy of acoustic Doppler velocimetry measurements in turbulent boundary layer flows over a smooth bed. Limnology and Oceanography: Methods, 5, 23–33. ISSN 1541-5856.

Evangelista, S., Giovinco, G., Kocaman, S., 2017. A multi-parameter calibration method for the numerical simulation of morphodynamic problems. J. Hydrol. Hydromech., 65, 175–182. DOI: 10.1515/johh-2017-0014.

Frazao, S.S., Noel, B., Zech, Y., 2004. Experiments of dam-break flow in the presence of obstacle. http://www.impact-project.net/AnnexII_DetailedTechnicalReports/AnnexII_PartB_WP3/RF_Soares_et_al_Obstacle_B1-226.pdf

Janssen, F., Cardenas, M.B., Sawyer, A.H., Dammrich, T., Krietsch J., de Beer, D., 2012. A comparative experimental and multiphysics computational fluid dynamics study of coupled surface-subsurface flow in bed forms. Water Resources Research, 48, 8, 1–16. ISSN 1944-7973.

Keylock, C.J., Constantinescu, G., Hardy, R.J., 2012. The application of computational fluid dynamics to natural river channels: Eddy resolving versus mean flow approaches. Geomorphology, 179, 1–20. http://doi.org/10.1016/j.geomorph.2012.09. 006

Kerenyi, K., Sofu, T., Guo, J., 2008. Using supercomputers to determine bridge loads. Public Roads, 72, 2, Publication Number: FHWA-HRT-08-006. https://www.fhwa.dot.gov/publications/publicroads/ 08sep/05.cfm

Kim, S.C., Friedrichs, C.T., Maa, J.P.Y., Wright, L.D., 2000. Estimating bottom stress in tidal boundary layer from acoustic Doppler velocimeter data. J. Hydraul. Eng.-ASCE, 126, 6, 399–406. ISSN 0733-9429.

Kocaman, S., Ozmen-Cagatay, H., 2012. The effect of lateral channel contraction on dam break flows: Laboratory experiment. Journal of Hydrology, 432–433, 145–153. DOI: 10.1016/j.jhydrol.2012.02.035.

Laks, I., Szoszkiewicz K., Kałuża, T., 2017. Analysis of in situ water velocity distributions in the lowland river floodplain covered by grassland and reed marsh habitats - a case study of the bypass channel of Warta River (Western Poland). J. Hydrol. Hydromech., 65, 325–332. DOI: 10.1515/johh-2017-0021.

Mueller, D.S., Abad, J.D., García, C.M., Gartner, J.W., García, M.H., Oberg, K.A., 2007. Errors in acoustic profiler velocity measurements caused by flow disturbance. Journal of Hydraulic Engineering, 133, 12, 1411–1420. DOI: 10.1061/ASCE0733-94292007133:121411 C.

Nagata, N., Hosoda, T., Nakato, T., Muramoto, Y., 2005. Three-Dimensional Numerical Model for Flow and Bed Deformation around River Hydraulic Structures. Journal of Hydraulic Engineering, 131, 12, 14. ISSN 0733-9429.

Nikora, V.I., Suren, A.M., Brown, S.L.R., Biggs, B.J.F., 1998. The effects of the moss *Fissidens rigidulus* (*Fissidentaceae*: *Musci*) on near-bed flow structure in an experimental cobble bed flume. Limnol. Oceanogr, 43, 6, 1321–1331.

Olsen, N.R.B., 1999. Computational Fluid Dynamics in Hydraulic and Sedimentation Engineering. The Norwegian University of Science and Technology, 65 p. ISBN 82-7598-041-0.

Picek, T., Havlik, A., Mattas D., Mares, K., 2007. Hydraulic calculation of bridges at high water stages. Journal of Hydraulic Research, 45, 3, 400–406. doi.org/10.1080/00221686.2007.9521773

Precht, E., Janssen, F., Huettel, M., 2006. Near-bottom performance of the Acoustic Doppler Velocimeter (ADV) – a comparative study. Aquatic Ecology, 40, 481–492. DOI: 10.1007/s10452-004-8059-y.

Schmidt, S., Thiele, F., 2002. Comparison of numerical methods applied to the flow over wall-mounted cubes. Int. J. Heat Fluid Flow, 23, 3, 330–339. ISSN 0142-727X.

Shen, Y., Diplas, P., 2008. Application of two- and three-dimensional computational fluid dynamics models to complex ecological stream flows. Journal of Hydrology, 348, 1–2, 195–214. ISSN 0022-1694.

SonTek, 2009. FlowTracker Handheld ADV Technical Manual, Firmware Version 3.7, Software Version 2.30 – SonTek/YSI, San Diego, 2009, 126 p.

Stoesser, T., Kara, S., Sturm,W.T., Mulahasan, S., 2015. Flow dynamics through a submerged bridge opening with overtopping. Journal of Hydraulic Research, 53, 2, 186–195. ISSN 0022-1686.

Takashi, A., Sanehiro, W., Hiroshige, K., Masanori, A., Michitsugu, M., 2004. Development of flowrate measurement on open channel flow using ultrasonic Doppler method. In: Proc. 4th International Symposium on Ultrasonic Doppler Method for Fluid Mechanics and Fluid Engineering. Sapporo, pp. 33–36.

Versteegh, J., 1990. The numerical simulation of three-dimensional flow through or around hydraulic structures. PhD Thesis. TU Delft.

Voulgaris, G., Trowbridge, J.H., 1998. Evaluation of the acoustic Doppler velocimeter for turbulence measurements. Journal of Atmospheric and Oceanic Technology, 15, 272–289.

Zhang, H., Nakagawa, H., Kawaike, K., Baba, Y., 2009. Experiment and simulation of turbulent flow in local scour around a spur dyke. International Journal of Sediment Research, 24, 1, 33–45, ISSN 1001-6279.

NOMENCLATURE

μ_t	turbulent viscosity	(kg m^{-1} s^{-1})
ρ	density	(kg m^{-3})
k	turbulent kinetic energy	(m^2 s^{-2})
ε	dissipation rate of turbulent kinetic energy	(m^2 s^{-3})
u_i	i-velocity component	(m s^{-1})
u_i'	i-velocity component fluctuation	(m s^{-1})
x_i	i-coordinate	(m)
S_{ij}	strain rate tensor	(s^{-1})
Ω_{ij}	rate-of-rotation tensor	(s^{-1})
S	modulus of the strain tensor	(s^{-1})
ω	specific dissipation rate (ε/k)	(s^{-1})
ω_k, Ω_k	angular velocity	(s^{-1})

Received 31 October 2017
Accepted 23 March 2018

Note: Colour version of Figures can be found in the web version of this article.